
Single-Fiber Mechanics on the Nanoscale

DISSERTATION

zur Erlangung des akademischen Grades eines Doktors der Naturwissenschaften
(Dr. rer. nat.) im Fach Chemie der Fakultät für Biologie, Chemie und
Geowissenschaften der Universität Bayreuth.

Vorgelegt von

Daniel Kluge

geboren in Kulmbach

BAYREUTH 2013

Die vorliegende Arbeit wurde in der Zeit von Juli 2009 bis Juli 2013 am Lehrstuhl für Physikalische Chemie II unter der Betreuung von Herrn Prof. Dr. Andreas Fery an der Universität Bayreuth angefertigt.

Vollständiger Abdruck der von der Fakultät für Biologie, Chemie und Geowissenschaften der Universität Bayreuth genehmigten Dissertation zur Erlangung des akademischen Grades eines Doktors der Naturwissenschaften (Dr. rer. nat.).

Dissertation eingereicht am:	31. Juli 2013
Zulassung durch die Prüfungskommission:	19. August 2013
Wissenschaftliches Kolloquium:	18. November 2013
Amtierender Dekan:	Prof. Dr. Rhett Kempe

Prüfungsausschuss:

Prof. Dr. Andreas Fery (Erstgutachter)
Prof. Dr. Andreas Greiner (Zweitgutachter)
Prof. Dr. Jürgen Senker (Vorsitz)
Prof. Dr. Matthias Breuning

For every phenomenon, however complex,
someone will eventually come up with a simple and elegant theory.
This theory will be wrong.

ROTHCHILD'S RULE

Contents

Zusammenfassung	ix
Summary	xiii
List of Publications	xvii
List of Abbreviations and Symbols	xix
1 Introduction	1
1.1 Motivation: Fibers as Structural Elements on the Nanoscale	3
1.2 Aim of the Thesis	4
1.3 References	6
2 Synopsis	9
2.1 Outline	11
2.2 Nanomechanical Properties of Supramolecular Whiskers	11
2.3 Influence of the Molecular Structure and Morphology	13
2.4 Comparison of Self-Assembled and Electrospun Trisamide Fibers . . .	15
2.5 A Critical Assessment of Slack Effects in Nanobending Experiments .	17
2.6 Beyond Small Deformations	19
2.7 Extending the Material Library Beyond BTAs	21
2.8 Individual Contributions to Joint Publications	23
3 Status of the Field and Theoretical Background	25
3.1 Nanomechanical Characterization of Fibers	27
3.1.1 The Challenges of Nanomechanics	27
3.1.2 Bending	28
3.1.3 Uniaxial Tension	30
3.1.4 Nanoindentation	31
3.2 Beam Theory	33
3.2.1 Elastic Regime	33
3.2.2 Fixation and Boundary Conditions	35
3.2.3 Shearing	38
3.2.4 Large Deformations	39

3.3	Atomic Force Microscopy	42
3.3.1	General Setup	42
3.3.2	Imaging	43
3.3.3	Force Measurements	44
3.3.4	Calibration	45
3.3.5	Lateral Force Microscopy	46
3.4	Finite Element Analysis	49
3.4.1	An Introduction to the Finite Element Method	49
3.4.2	Finite Element Analysis for Nanofibers	52
3.5	Fibers Based on 1,3,5-Benzenetrisamides	54
3.5.1	Self-assembly of 1,3,5-Benzenetrisamides	54
3.5.2	Electrospinning of Trisamides	55
3.5.3	Applications of Trisamides	57
3.6	References	60
4	Nanomechanical Properties of Supramolecular Whiskers	71
4.1	Introduction	73
4.2	Results and Discussion	74
4.3	Conclusion	79
4.4	Experimental Section	80
4.5	Supporting Information	82
4.6	References	85
5	Influence of the Molecular Structure and Morphology	89
5.1	Introduction	91
5.2	Results and Discussion	93
5.2.1	Morphology	93
5.2.2	Bending experiments	94
5.2.3	Comparison of the systems	99
5.3	Conclusions	100
5.4	Experimental Section	101
5.5	Supporting Information	103
5.6	References	105
6	Comparison of Self-Assembled and Electrospun Trisamide Fibers	109
6.1	Introduction	111
6.2	Results and Discussion	113
6.3	Conclusions	118
6.4	Experimental Section	118
6.5	Supporting Information	121
6.6	References	124
7	A Critical Assessment of Slack Effects in Nanobending Experiments	127
7.1	Introduction	129
7.2	Results and Discussion	132
7.3	Conclusions	138

7.4	Experimental Section	139
7.5	Supporting Information	141
7.6	References	144
8	Perspectives I: Beyond Small Deformations	147
8.1	Introduction	149
8.2	Results and Discussion	150
8.2.1	Calibration	150
8.2.2	Friction influence	153
8.2.3	Small Deformation Measurements	154
8.2.4	Large Deformation Measurements	156
8.3	Conclusions	160
8.4	Experimental Section	161
8.5	References	162
9	Perspectives II: Extending the Material Library - Spider Silks	165
9.1	Introduction	167
9.2	Results and Discussion	168
9.2.1	Vertical Bending Measurements	168
9.2.2	Lateral Bending Measurements	172
9.3	Conclusions	175
9.4	Experimental Section	176
9.5	References	177
	Danksagung	I

Zusammenfassung

Diese Arbeit befasst sich mit der nanomechanischen Charakterisierung von 1,3,5-Benzoltriamidfasern (BTA Fasern). Zu diesem Zweck werden Biegeexperimente basierend auf der Rasterkraftmikroskopie (AFM) angewendet und weiterentwickelt. Ziel ist es, die linear elastischen Eigenschaften der Fasern zu bestimmen, insbesondere ihren Elastizitätsmodul. Weiterhin wird der Einfluss der Molekülstruktur und der Morphologie auf die mechanischen Eigenschaften untersucht und Fasern, die mittels 'top-down' und 'bottom-up' Techniken hergestellt worden sind, miteinander verglichen. Darüber hinaus beinhaltet die Arbeit theoretische Überlegungen zu den Modellen für die Auswertung der Biegeexperimente. Als weiterführende Perspektive wird ein experimenteller Aufbau diskutiert, der die mechanische Charakterisierung jenseits des elastischen Regimes ermöglicht, und die Anwendbarkeit der experimentellen Ansätze für andere Materialien aufgezeigt.

Nano- und mikroskopische Fasern, Stäbchen und vergleichbare eindimensionale Strukturen sind wichtige Bausteine in vielen Funktionsmaterialien. Beispiele sind Nanokomposite, Filter und Gerüste für die Gewebekonstruktion. Die Funktion faserbasierter Materialien ist oft eng mit den mechanischen Eigenschaften der Einzelfasern verknüpft. Folglich gibt es einen Bedarf nach einer zuverlässigen Charakterisierung der mechanischen Eigenschaften auf der Einzelfaserebene. Rasterkraftmikroskopische, nanomechanische Biegeexperimente sind unter den am häufigsten verwendeten Ansätzen, da sie eine zuverlässige Charakterisierung bei gleichzeitig moderatem Aufwand bei der Probenpräparation ermöglichen.

Eine hochinteressante Klasse von 1D Strukturen sind auf 1,3,5-Benzoltriamiden basierende supramolekulare Fasern. Diese Trisamide zeigen ein bemerkenswertes Selbstassemblierungsverhalten in kolumnare Strukturen. Zusätzlich kann die Morphologie dieser Aggregate über die Molekülstruktur der Trisamide maßgeschneidert werden. Weiterhin können sie ebenfalls mittels Elektrosponnen verarbeitet werden

und bieten somit zwei komplementäre Präparationswege über 'bottom-up' und 'top-down' Techniken. Dies ist eine außergewöhnliche Voraussetzung für die Ausbildung hierarchischer Strukturen mit echter Strukturkontrolle auf allen Hierarchieebenen, vom Einzelmolekül bis zum finalen Faserverbund.

Im ersten Teil dieser Arbeit werden nanomechanische Biegeexperimente an verschiedenen Typen von BTA Fasern vorgestellt. Insbesondere wird die Messmethode behandelt, die vereinfacht und verbessert wurde, um eine direkte Aufnahme von sogenannten Steifigkeitsprofilen entlang des kompletten freistehenden Segments einer Probe, die über einem Kanal positioniert wurde, zu ermöglichen. Diese Profile wurden benutzt, um die Randbedingungen (insbesondere die Fixierung der Faser auf dem Substrat) zu bestimmen. Die Kenntnis der Randbedingungen war von besonderer Bedeutung für die Auswahl des korrekten Modells, das das Faserverhalten während der mechanischen Deformation beschreibt. Die Experimente ermöglichten das erste Mal, direkt den Elastizitätsmodul selbstassemblierter BTA Fasern zu bestimmen. Der erhaltene Wert von 3 ± 1 GPa (der vergleichbar ist mit teilkristallinen Polymeren) war überraschend hoch angesichts der Tatsache, dass die Kohäsion der Fasern lediglich auf supramolekulare Wechselwirkungen wie Wasserstoffbrückenbindungen und π - π -Wechselwirkungen zurückzuführen ist, ohne dass intermolekulare kovalente Bindungen beteiligt sind.

Aufbauend auf diesen Ergebnissen wird in der Arbeit der Einfluss der Fasermorphologie und Molekülstruktur auf die mechanischen Eigenschaften untersucht. Zu diesem Zweck wurden drei BTAs mit unterschiedlicher Amidkonnektivität und unterschiedlicher Größe der Alkylsubstituenten verglichen. Alle Trisamide bildeten wohldefinierte Fasern aus, die signifikante Unterschiede im Durchmesser bis hin zu einer Größenordnung auswiesen. Wiederum wurden die mechanischen Eigenschaften mit Hilfe von rasterkraftmikroskopischen Biegeexperimenten bestimmt. Während die Biegesteifigkeit der Fasern aufgrund der unterschiedlichen Radien Unterschiede von bis zu drei Größenordnungen aufwies, zeigte die Berechnung des Elastizitätsmoduls, dass dies ein reiner Größeneffekt war und dass die Moduln aller Systeme ähnlich waren und im Bereich von 2-4 GPa lagen. Das bedeutet, dass eine Variation der molekularen Struktur erlaubt, die Fasermorphologie zu verändern ohne den Modul zu beeinflussen und es folglich ermöglicht, die Fasersteifigkeit über einen breiten Bereich einzustellen.

Der nächste Schritt war der Vergleich von BTA Fasern, die aus der selben Ausgangssubstanz einmal durch Selbstassemblierung (SA Fasern) und einmal durch Schmel-

zelektrospinnen (ES Fasern) erhalten wurden. Während Röntgendiffraktion zeigte, dass die Kristallstruktur der Fasern nicht durch die Präparationsmethode beeinflusst wurde, ließen rasterelektronenmikroskopische Messungen morphologische Unterschiede erkennen. Die SA Fasern bestanden aus fest verbundenen Bündeln einzelner Stränge, die ES Fasern waren glatt und homogen. Die Biegeexperimente zeigten jedoch, dass der Elastizitätsmodul E nicht signifikant durch den Präparationsprozess beeinflusst wurde. Obwohl die gemittelten Werte nahelegten, dass E_{SA} etwas niedriger war als E_{ES} , waren die Unterschiede klein und im Rahmen des Fehlers der Messmethode. Die Tatsache, dass die Größenordnung und Verteilung der Moduln vergleichbar waren, zeigt dass mechanisch robuste BTA Fasern über beide Ansätze hergestellt werden können. Dies eröffnet interessante Perspektiven hinsichtlich kontrollierter Bildung hierarchischer Strukturen mittels supramolekularer BTA Fasern mit hoher Flexibilität im Bezug auf die Strukturkontrolle.

Der zweite Teil der Arbeit behandelt Weiterentwicklungen der theoretischen Modelle und experimentellen Methoden. Im Hinblick auf theoretische Gesichtspunkte wurde der Effekt einer durchhängenden Faser auf nanomechanische Biegeexperimente untersucht. Finite Elemente Simulationen zeigten, dass ein steigendes Verhältnis von Durchhangtiefe zu Faserradius zu einer apparenten Erhöhung der Fasersteifigkeit, sowohl im Bereich kleiner als auch großer Deformationen, führt, und damit zu einer Überschätzung des Elastizitätsmoduls. Weiterhin veränderte es die Form des Steifigkeitsprofils. Die Konsequenz ist eine Missinterpretation der experimentellen Randbedingungen, wie wiederum eine weitere Überschätzung des Elastizitätsmoduls um bis zu eine Größenordnung zur Folge hat. Die Simulationen legten nahe, dass eine laterale Belastung der Faser (d.h. senkrecht zur Durchhangsrichtung) nur leicht vom Durchhängen beeinflusst wird. Somit können laterale Experimente eine experimentelle Lösung sein, um bei Proben, bei denen das Durchhängen ein Problem darstellt, zuverlässigere Ergebnisse zu produzieren.

In Hinblick auf die experimentellen Methoden werden in der Arbeit Experimente vorgestellt, die die Charakterisierung der mechanischen Eigenschaften über den linear elastischen Bereich hinaus ermöglichen. Durch eine laterale statt einer vertikalen Belastung können große Deformationen erreicht werden. Bei diesen erfährt die Faser eine Kombination aus Biegung und Zug und eine entsprechende Auswertung wird aufgezeigt. Innerhalb des elastischen Regimes zeigten die Daten gute Übereinstimmung mit den vertikalen Experimenten. Deformation bis zum Bruch erlaubte die erstmalige Bestimmung der Biegefestigkeit eines BTA Fasertyps. Mit weiteren Verbesserungen hinsichtlich der Kalibrierung und Befestigung der Fasern ermög-

licht die Kombination von vertikalen und lateralen Messungen an genau der selben Stelle die mechanische Charakterisierung im linearen Bereich und darüber hinaus mit herausragender Verlässlichkeit.

Der zweite Teil der Arbeit schließt mit der Demonstration der Anwendbarkeit der entwickelten Biegeexperimente auf elektroverspinnene Fasern aus Spinnenseidenproteinen, die mittels biotechnologischer Methoden gewonnen wurden. Während vertikale Biegeexperimente zwar prinzipiell möglich waren, ließen ihre Ergebnisse keine eindeutigen Schlussfolgerungen zu. Die meisten Proben zeigten einen scheinbaren Modul der unrealistisch hoch war und ihre Form der Steifigkeitsprofile ließ sich nicht durch klassische balktentheoretische Modelle für die Randbedingungen erklären. Obwohl diese Messungen nicht ausgewertet werden konnten, demonstrierten sie die Fähigkeit der Biegeexperimente, nicht-ideales Verhalten zu identifizieren, und folglich ihre Zuverlässigkeit. Zusätzliche laterale Experimente zeigten keine solch dramatischen Abweichungen von den theoretischen Modellen und erlaubten, auf Einzelfaserebene eine klare Erhöhung des Elastizitätsmoduls und der Biegefestigkeit durch Nachbehandlung mit Methanol zu zeigen.

Summary

This thesis deals with the nanomechanical characterization of 1,3,5-benzenetrisamide (BTA) fibers. For that purpose, bending experiments based on atomic force microscopy (AFM) are applied and further developed. The main goal is determining the fibers' linear elastic properties, especially Young's modulus. In addition, the influence of the molecular structure and morphology on the mechanical properties is investigated and fibers prepared by top-down and bottom-up techniques are compared. Beyond that, the thesis includes theoretical considerations concerning the models used for evaluation of the bending tests. As a further perspective, an experimental setup that allows a mechanical characterization beyond the elastic regime is discussed and the applicability of the experimental approaches to other materials is demonstrated.

Nano- and microscale fibers, rods, and comparable one-dimensional (1D) structures are important building blocks in many functional materials. Examples include nanocomposites, filters, and tissue engineering scaffolds. The function of fiber based materials is often closely related to the mechanical properties of the individual fibers. As a consequence, there is a need for a reliable characterization of the mechanical properties on the single fiber scale. Nanomechanical AFM bending experiments are among the most frequently used approaches since they allow a reliable characterization and require only moderate effort in terms of sample preparation.

A very exciting class of 1D structures are supramolecular fibers based on 1,3,5-benzenetrisamides. These trisamides show a remarkable self-assembly behavior into columnar structures. In addition, the morphology of these assemblies can be tailored via the molecular structure of the trisamides. Furthermore, they can also be processed via electrospinning, thus offering two complementary preparation pathways by bottom-up and top-down techniques. This is an exceptional prerequisite for the formation of hierarchical structures with true structural control on all levels of hierarchy, from the single molecule to the final fiber assembly.

The first part of this work presents nanomechanical bending experiments on various types of BTA fibers. It especially focuses on the measurement technique, which was facilitated and improved to allow the straightforward acquisition of stiffness profiles along the whole free-standing segment of a sample that was positioned over a channel. These profiles were used to determine the boundary conditions (in particular the fixation of the fiber on the substrate). Knowledge of the boundary conditions was of major importance for choosing the correct model that described the fiber behavior during the bending deformation. The experiments allowed for the first time to directly measure Young's modulus of self-assembled BTA fibers. The obtained value of 3 ± 1 GPa (which is comparable to semi-crystalline polymers) was surprisingly high, considering the fact that the cohesion of the fibers is purely due to supramolecular interactions like hydrogen bonding and π - π -stacking, without any intermolecular covalent bonds.

Building on these results, this work investigates the influence of the fibers' morphology and molecular structure on their mechanical properties. For that purpose, we compared three BTA compounds with differences regarding the connectivity of the amide moieties and the size of the alkyl substituents. All trisamides formed well-defined fibers that exhibited significant differences in diameters of up to one order of magnitude. We again determined the mechanical properties with AFM bending experiments. While the flexural rigidity of the fibers showed a difference of up to three orders of magnitude due to the differences in diameter, calculation of Young's modulus revealed that these differences were a pure size effect and that the moduli of all systems were similar and in the range of 2-4 GPa. This means that variation of the molecular structure allows changing the fibers' morphology without affecting their modulus and consequently, allows tuning their stiffness over a wide range.

The next step was the comparison of BTA fibers obtained from the same compound, but prepared by self-assembly (SA fibers) and melt electrospinning (ES fibers). While X-ray diffraction (XRD) showed that the crystal structure of the fibers was not influenced by the preparation method, SEM measurements revealed morphological differences. The SA fibers consisted of firmly connected bundles of individual strands, the ES fibers were smooth and homogeneous. The bending experiments, however, showed that Young's modulus E was not significantly affected by changing the preparation process. Although the average values suggested that E_{SA} was slightly lower than E_{ES} , the difference was small and within the error of the measurements. The fact that the order of magnitude and distributions of the moduli were comparable, demonstrates that mechanically robust BTA fibers can be obtained by both ap-

proaches. This opens interesting perspectives for the controlled formation of hierarchical structures using supramolecular BTA fibers with great flexibility in terms of structural control.

The second part of the thesis addresses further developments of the theoretical models and experimental approaches. In terms of theory, we studied the effect of a slack fiber (i.e., a fiber that is not lying straight over the channel, but has a slight curvature towards the substrate) on nanomechanical bending experiments. Our finite element (FE) simulations showed that an increasing slack-to-radius ratio leads to an apparent stiffening within the small- and large-deformation regime and therefore, to an overestimation of Young's modulus. In addition, it altered the shape of the stiffness profile. The consequence is a misinterpretation of the experimental boundary conditions which causes further overestimation of Young's modulus by over one order of magnitude. Our simulations suggested that lateral loading of the fiber (i.e., perpendicular to the slack direction) is only slightly affected by the slack and can therefore provide an experimental solution to deal with samples where slack is an issue and to produce more reliable results.

In terms of experimental approaches, the thesis also presents experiments that allow the characterization of mechanical properties beyond the linear elastic regime. By applying a lateral instead of a vertical load, large deformations of the fibers can be achieved. At large deformations, the fiber experiences a combination of bending and tension, and an appropriate evaluation is considered. In the elastic regime, the lateral data showed good agreement with the vertical experiments. Deforming the fibers until failure for the first time allowed estimating the bending strength of a BTA fiber type. With further improvements in terms of cantilever calibration and sample fixation, the possibility to combine vertical and lateral bending on exactly the same position allows characterization of the mechanical properties within and beyond the linear elastic regime with outstanding reliability.

The second part of the thesis concludes with the demonstration of the applicability of the developed bending experiments to electrospun fibers prepared from genetically engineered spider silk proteins. While vertical bending experiments were possible, they produced very inconclusive results. Most samples showed an apparent modulus that was unrealistically high and shapes of the stiffness profile that could not be explained by the classical beam theory boundary conditions. Although these measurements could not be evaluated, they demonstrated the capability of bending experiments to identify non-ideal behavior and therefore, their reliability. Addi-

tional lateral bending experiments, however, did not show such dramatic deviations from the theoretical models and allowed to clearly identify the increase of Young's modulus and flexural strength by a post-treatment with methanol on the single fiber level.

List of Publications

1. **D. Kluge**, F. Abraham, S. Schmidt, H.-W. Schmidt, A. Fery, NANOMECHANICAL PROPERTIES OF SUPRAMOLECULAR SELF-ASSEMBLED WHISKERS DETERMINED BY AFM FORCE MAPPING. *Langmuir* **2010**, *26*, 3020-3023.
2. **D. Kluge**, J. C. Singer, J. W. Neubauer, F. Abraham, H.-W. Schmidt, A. Fery, INFLUENCE OF THE MOLECULAR STRUCTURE AND MORPHOLOGY OF SELF-ASSEMBLED 1,3,5-BENZENETRISAMIDE NANOFIBERS ON THEIR MECHANICAL PROPERTIES. *Small* **2012**, *16*, 2563-2570.
3. **D. Kluge**, J. C. Singer, B. R. Neugirg, J. W. Neubauer, H.-W. Schmidt, A. Fery, TOP-DOWN MEETS BOTTOM-UP: A COMPARISON OF THE MECHANICAL PROPERTIES OF MELT ELECTROSPUN AND SELF-ASSEMBLED 1,3,5-BENZENETRISAMIDE FIBERS. *Polymer* **2012**, *53*, 5754-5759.
4. D. Kunz, J. Erath, **D. Kluge**, H. Thurn, B. Putz, A. Fery, J. Brey, IN-PLANE MODULUS OF SINGULAR 2:1-CLAY LAMELLAE APPLYING A SIMPLE WRINKLING TECHNIQUE. *ACS Applied Materials & Interfaces* **2013**, *5*, 5851-5855.
5. **D. Kluge**, D. Ruffoni, A. Fery, A CRITICAL ASSESSMENT OF SLACK EFFECTS IN NANOBENDING EXPERIMENTS. Initially submitted to *Journal of Applied Physics*.

List of Abbreviations and Symbols

Abbreviations

1D	One-dimensional
2D	Two-dimensional
AFM	Atomic force microscopy, atomic force microscope
BTA	1,3,5-Benzenetrisamide
CNT	Carbon nanotube
DCBM	Double clamped beam model
DSC	Differential scanning calorimetry
ES	Electrospun
ESM	Element stiffness matrix
FE	Finite element
FEA	Finite element analysis
FEM	Finite element method
FIB	Focused ion beam
GSM	Global stiffness matrix
HFIP	1,1,1,3,3,3-hexafluoro-2-propanol
HMN	2,2,4,4,6,8,8-heptamethylnonane
InvOLS	Inverse optical lever sensitivity
<i>i</i> -PP	Isotactic polypropylene
LFM	Lateral force microscopy
MA	Major ampullate (gland)
MEMS/NEMS	Micro-/nano electro mechanical systems
MOF	Metal organic framework
PAN	Polyacrylonitrile
PDS	Photo diode signal
PLLA	Poly(L-lactic acid)

SA	Self-assembled
SEM	Scanning electron microscopy
SPM	Scanning probe microscopy
SSBM	Simply supported beam model
SWCNT	Single-walled carbon nanotube
XRD	X-ray diffraction

Symbols

A	Young's modulus
d	Diameter
D	Distance between probe and sample
$d_{n,i}$	Distance to the neutral axis in i -direction
δ	Deformation, deflection
E	Young's modulus
ϵ_i	Strain in i -direction
EI	Flexural rigidity
F	Force
f_s	Shape factor
G	Shear modulus
h	Tip height
H	Lateral lever arm
I	Area moment of inertia
k	Spring constant
K	Elemental stiffness
κ	Curvature
L	Length of the free-standing segment
M	Bending moment
ν	Poisson's ratio
ϕ	Torsional angle
Q_f	Quality factor
r	Radius
ρ	Radius of curvature
s	Slack depth

S_ϕ	Torsional sensitivity
S_x	Lateral sensitivity
$\sigma_{b,max}$	Bending (flexural) strength
σ_f	Fracture strength
σ_i	Stress in i -direction
σ_y	Yield stress
t	Thickness
u	Deformation in x -direction
v	Deformation in y -direction
ΔV_ϕ	Torsional PDS in volt
w	Deformation in z -direction
Z	Piezo displacement in z -direction

Introduction

1.1 Motivation: Fibers as Structural Elements on the Nanoscale

Emerging technologies inspire the creativity of scientists and artists alike, with nanotechnology being a prominent recent example on the boundary between science and fiction. A miniaturization contest not unlike the one suggested in Richard Feynman's influential lecture *There's Plenty of Room at the Bottom* (1959) is part of the main plot in Nikolai Leskov's story *The Steal Flea* (1881). The latter is one of the first works of fiction that mentioned man-made structures which are not even visible anymore at five million times magnification, and microscopic technologies also appear in the work of Arthur C. Clarke (*The Next Tenants*, 1956). While the controversial ideas of futurist K. Eric Drexler¹ can be found in the critically acclaimed novel *The Diamond Age* by Neal Stephenson (1995), Whitesides and Smalley pointed out the severe physical and chemical limitations of nanotechnology in a Drexlerian understanding.^{2,3} However, observing how science fiction and nanotechnology have influenced each other has also revealed unexpected similarities in their way of envisioning the future.⁴

As a scientist, it's neither necessary to wait for the distant future nor to tend to the manipulation of individual atoms to benefit from nanotechnological advances. Even on scales that are, strictly speaking, not nano (meaning with at least one or more dimension between 1 and 100 nm), the development of devices such as the atomic force microscope (AFM) has opened up exciting new research fields, as they allow the characterization of materials on small scales with unprecedented precision. While there is a multitude of fascinating physical phenomena that can be studied, this work focuses primarily on mechanical properties.

The recent progress in micro- and nanomechanics has for example provided extended insight into the properties of biological structures.⁵⁻⁷ It has also allowed studying how cells adapt to and respond to mechanical stresses or the mechanical properties of their surroundings.⁸⁻¹¹ These studies are in the border region of classical engineering and molecular mechanics,^{7,12} and a deeper understanding requires the combination of advanced experimental and theoretical approaches.

Many of these biological materials are part of larger hierarchical structures.¹³⁻¹⁵ A fundamental function of those natural structures is providing mechanical support and protection.¹⁵ Therefore, they often possess exceptional mechanical proper-

ties which are a direct consequence of their microstructure.¹⁶ Studying these concepts allows chemists and materials scientists to draw inspiration for the design and development of new artificial materials, which is sometimes termed 'bionics' or 'biomimetics'.¹⁷ The possibilities and the power of clever material design are impressively demonstrated by mechanical metamaterials, even though they are not inspired by biological examples.¹⁸

A fundamental structural element in hierarchical materials are fibers, beams, rods, and comparable one-dimensional (1D) objects,¹³ meaning that one dimension is large (sometimes even continuous) compared to the other two.^a Consequently, they are also used in a large number of artificial materials with manifold applications. Their mechanical properties, for example, play an important role in nanocomposites, which are often based on the smart combination of individual fibers or a fiber network embedded in a matrix with complementary mechanical properties. In terms of nanocomposites, carbon nanotubes (CNTs) are the most commonly applied 1D material,^{19,20} but also cellulose nanowhiskers^{21,22} and in few cases, electrospun fibers²³ have been used.

Electrospinning is especially well-suited for the preparation of soft matter fibers with diameters ranging from several nanometers to a few micrometers.²⁴ Consequently, there is a large number of functional structures based on electrospun fibers.²⁵ One important field is filtration, where nanofibers can increase the efficiency and introduce selectivity and functionality.²⁶ Other examples are biomedical applications such as drug delivery and wound dressings, that utilize the combination of mechanical stability, high surface-to-volume ratio, and biodegradability.^{27,28} Especially tissue engineering scaffolds based on electrospun nanofibers have received a lot of attention.²⁹ In contrast to the electrospun materials, metal nanowires and other (semi)conductive 1D structures are mostly formed by bottom-up techniques. They offer promising applications for electronic, optoelectronic, electrochemical, and electromechanical devices as interconnects and functional units.³⁰

1.2 Aim of the Thesis

The previous section has demonstrated that nano- and microfibers are highly relevant for a large number of scientific fields. In addition, all previously mentioned

^aAlthough the terms 'fiber' and 'beam' are mostly used throughout this thesis for the sake of simplicity, the general concepts are of course also applicable to other 1D structures.

functional structures require a suitable mechanical stability, either because the structure itself has a mechanical function (such as nanocomposites or fibrillar scaffolds), or because it has to withstand a certain amount of forces during usage (such as filters). As a consequence, there is a need for a reliable characterization of the mechanical properties on the single fiber scale.

A promising approach are AFM bending experiments. In analogy to a macroscopic bending experiment, the samples are deposited on structured substrates and deformed with a microscopic cantilever which simultaneously measures the respective forces. These measurements do not only allow calculation of the mechanical properties, but also the determination of the experimental boundary conditions which are crucial for a correct interpretation of the mechanical behavior.

The main system that is studied within the scope of this thesis are alkyl substituted 1,3,5-benzenetrisamides (BTAs). They are a very exciting class of molecules that show a remarkable self-assembly behavior into columnar supramolecular structures. The morphology of these assemblies can be tailored via the molecular structure of the trisamides. In addition, they can also be processed via electrospinning, thus allowing the combination of bottom-up and top-down techniques. This is an exceptional prerequisite for the formation of hierarchical structures with true structural control on all levels of hierarchy, from the single molecule to the final fiber assembly.

Consequently, the aim of the thesis is divided into two closely interconnected aspects, the nanomechanical characterization of the trisamides and the further development of the necessary experimental techniques. In terms of the BTA fibers, the first step is reliably determining their linear elastic properties, especially Young's modulus. In addition, the influence of the molecular structure and morphology on the mechanical properties is investigated. Furthermore, BTA fibers prepared by self-assembly and electrospinning are compared to find out whether using different preparation pathways affects their mechanics.

Beyond that, the thesis includes theoretical considerations concerning the models used for evaluation of the bending tests. In addition, the experimental approach is further expanded by implementing large deformation measurements up to failure of the fiber. Finally, the applicability of the experimental approaches to other materials, such as engineered spider silk protein fibers, is demonstrated.

1.3 References

- [1] K. E. Drexler, *Engines of Creation*, Anchor Books, New York, NY, **1986**.
- [2] G. M. Whitesides, *Scientific American* **2001**, *285*, 78–83.
- [3] R. E. Smalley, *Scientific American* **2001**, *285*, 76–77.
- [4] C. Toumey, *Nature Nanotechnology* **2008**, *3*, 180–181.
- [5] A. Vinckier, G. Semenza, *Febs Letters* **1998**, *430*, 12–16.
- [6] S. Kasas, G. Dietler, *Pflugers Archiv-European Journal of Physiology* **2008**, *456*, 13–27.
- [7] T. P. J. Knowles, M. J. Buehler, *Nature Nanotechnology* **2011**, *6*, 469–479.
- [8] D. E. Discher, P. Janmey, Y. L. Wang, *Science* **2005**, *310*, 1139–1143.
- [9] F. Rehfeldt, A. J. Engler, A. Eckhardt, F. Ahmed, D. E. Discher, *Advanced Drug Delivery Reviews* **2007**, *59*, 1329–1339.
- [10] R. Weinkamer, P. Fratzl, *Materials Science & Engineering C - Materials for Biological Applications* **2011**, *31*, 1164–1173.
- [11] B. Trappmann, J. E. Gautrot, J. T. Connelly, D. G. T. Strange, Y. Li, M. L. Oyen, M. A. C. Stuart, H. Boehm, B. J. Li, V. Vogel, J. P. Spatz, F. M. Watt, W. T. S. Huck, *Nature Materials* **2012**, *11*, 642–649.
- [12] J. Howard, *Cellular and Molecular Bioengineering* **2008**, *1*, 24–32.
- [13] A. K. Mohanty, M. Misra, G. Hinrichsen, *Macromolecular Materials and Engineering* **2000**, *276*, 1–24.
- [14] I. Burgert, *American Journal of Botany* **2006**, *93*, 1391–1401.
- [15] P. Fratzl, R. Weinkamer, *Progress in Materials Science* **2007**, *52*, 1263–1334.
- [16] S. A. Wainwright, B. WD, C. JD, G. JM, *Mechanical design in organisms*, Princeton University Press, Princeton, NJ, **1982**.
- [17] P. Fratzl, *Journal of the Royal Society Interface* **2007**, *4*, 637–642.
- [18] B. Xu, F. Arias, S. T. Brittain, X. M. Zhao, B. Grzybowski, S. Torquato, G. M. Whitesides, *Advanced Materials* **1999**, *11*, 1186–1189.
- [19] O. Breuer, U. Sundararaj, *Polymer Composites* **2004**, *25*, 630–645.
- [20] M. Moniruzzaman, K. I. Winey, *Macromolecules* **2006**, *39*, 5194–5205.
- [21] S. J. Eichhorn, A. Dufresne, M. Aranguren, N. E. Marcovich, J. R. Capadona, S. J. Rowan, C. Weder, W. Thielemans, M. Roman, S. Renneckar, W. Gindl, S. Veigel, J. Keckes, H. Yano, K. Abe, M. Nogi, A. N. Nakagaito, A. Mangalam, J. Simonsen, A. S. Benight, A. Bismarck, L. A. Berglund, T. Peijs, *Journal of Materials Science* **2010**, *45*, 1–33.
- [22] A. D. Liu, A. Walther, O. Ikkala, L. Belova, L. A. Berglund, *Biomacromolecules* **2011**, *12*, 633–641.

- [23] Z. M. Huang, Y. Z. Zhang, M. Kotaki, S. Ramakrishna, *Composites Science and Technology* **2003**, *63*, 2223–2253.
- [24] A. Greiner, J. H. Wendorff, *Angewandte Chemie-International Edition* **2007**, *46*, 5670–5703.
- [25] C. Burger, B. S. Hsiao, B. Chu, *Annual Review of Materials Research* **2006**, *36*, 333–368.
- [26] R. S. Barhate, S. Ramakrishna, *Journal of Membrane Science* **2007**, *296*, 1–8.
- [27] D. Liang, B. S. Hsiao, B. Chu, *Advanced Drug Delivery Reviews* **2007**, *59*, 1392–1412.
- [28] S. Agarwal, J. H. Wendorff, A. Greiner, *Polymer* **2008**, *49*, 5603–5621.
- [29] C. P. Barnes, S. A. Sell, E. D. Boland, D. G. Simpson, G. L. Bowlin, *Advanced Drug Delivery Reviews* **2007**, *59*, 1413–1433.
- [30] Y. N. Xia, P. D. Yang, Y. G. Sun, Y. Y. Wu, B. Mayers, B. Gates, Y. D. Yin, F. Kim, Y. Q. Yan, *Advanced Materials* **2003**, *15*, 353–389.

Synopsis

2.1 Outline

Chapter 3 gives a brief overview of the status of the field and basic theoretical backgrounds. The central part of the thesis is the nanomechanical characterization of benzenetrisamide based fiber materials. It is discussed in three individual publications that are presented in Chapters 4 through 6, which are already published. Chapter 7 considers experimental irregularities using finite element (FE) simulations and is submitted for publication. The Chapters 8 and 9 are to date unpublished and further extend the concepts of the thesis in terms of complementary characterization techniques and other materials. In the following, the connection between these individual Chapters is highlighted and the main results are summarized. Finally, the individual contributions of each coauthor to the joint publications are specified.

2.2 Nanomechanical Properties of Supramolecular Whiskers

Chapter 4 especially focuses on nanomechanical bending experiments using the atomic force microscope (AFM) (Figure 2.1(a)), which are the central experimental approach in this thesis. These experiments are carried out in analogy to a standard macroscopic three-point bending test. For a correct interpretation of the data, it is essential to determine the experimental boundary conditions, i.e., the fixation of the sample on the substrate. The two most common models assume that the fiber is either fully clamped (double clamped beam model, DCBM) or only loosely supported by the substrate (simply supported beam model, SSBM). We facilitated and improved the existing measurement technique by incorporation of the force mapping mode, which allowed the straightforward acquisition of stiffness profiles along the whole free-standing segment of the sample (Figure 2.1(b)). These profiles can be used to directly determine the boundary conditions and calculate the flexural rigidity (and with knowledge of the cross section, Young's modulus) of a free-standing fiber segment.

The presented approach allowed for the first time to directly measure Young's modulus of self-assembled 1,3,5-benzenetrisamide (BTA) fibers (Figure 2.2). These trisamides form supramolecular, columnar structures with enormous aspect ratios

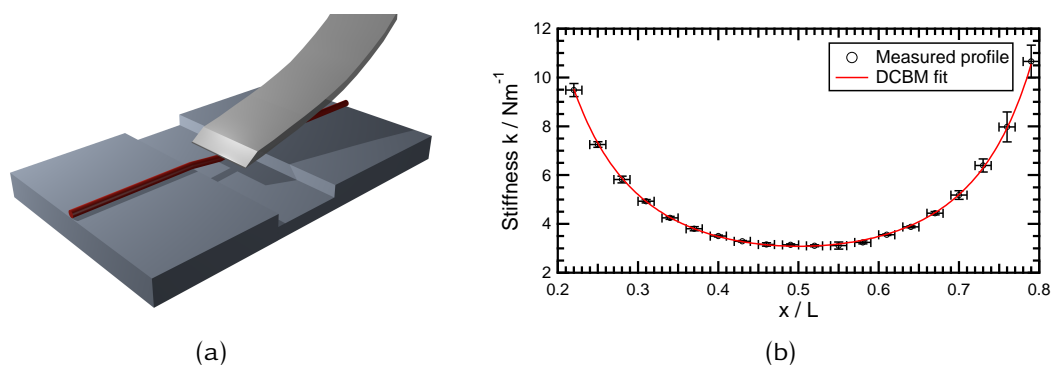


Figure 2.1 (a) Schematic setup of an AFM bending experiment. (b) Exemplary stiffness profile of a free-standing fiber segment (taken from Chapter 6).

due to well-defined intermolecular hydrogen bonds. We determined their flexural rigidity using bending experiments. Since their cross sections were not circular, we imaged each investigated fiber individually with the AFM to be able to calculate Young's modulus. We obtained a value of 3 ± 1 GPa, which is comparable to semi-crystalline polymers. This was a surprising and striking result, considering the fact that the cohesion of the fibers is purely due to supramolecular interactions like hydrogen bonding and π - π -stacking, without any intermolecular covalent bonds. This work demonstrated for the first time that BTAs are a mechanically robust building block for the formation of supramolecular structures.

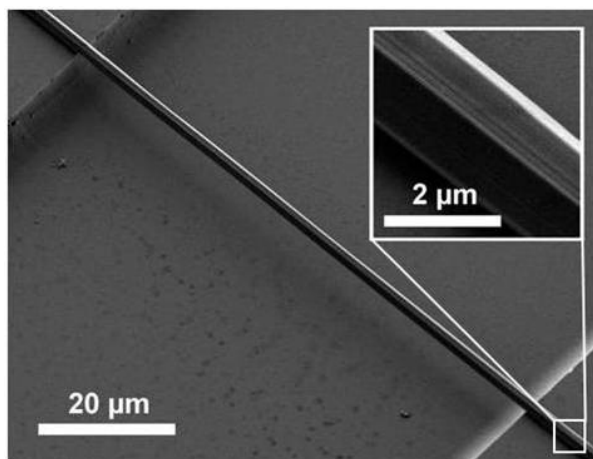


Figure 2.2 Free-standing BTA fiber positioned over a channel of a structured glass substrate (Chapter 4).

2.3 Influence of the Molecular Structure and Morphology

Directly building on these results, the publication in Chapter 5 investigates the influence of the fibers' morphology and molecular structure on their mechanical properties. Their assembly behavior strongly depends on the connectivity of the amide moieties to the central core and on the constitution of the peripheral groups. Consequently, BTAs offer the possibility to tailor desired properties, which makes them very interesting for bottom-up approaches. We compared three BTA compounds with different amide connectivity and different size of the alkyl substituents. To interpret the mechanical properties of the structurally different BTAs, we first investigated the morphology of the self-assembled nanofibers using scanning electron microscopy (SEM) (Figure 2.3). All trisamides formed well-defined fibers that exhibited significant differences in diameters of up to one order of magnitude, ranging from $0.21 \pm 0.08 \mu\text{m}$ to $2 \pm 1 \mu\text{m}$.

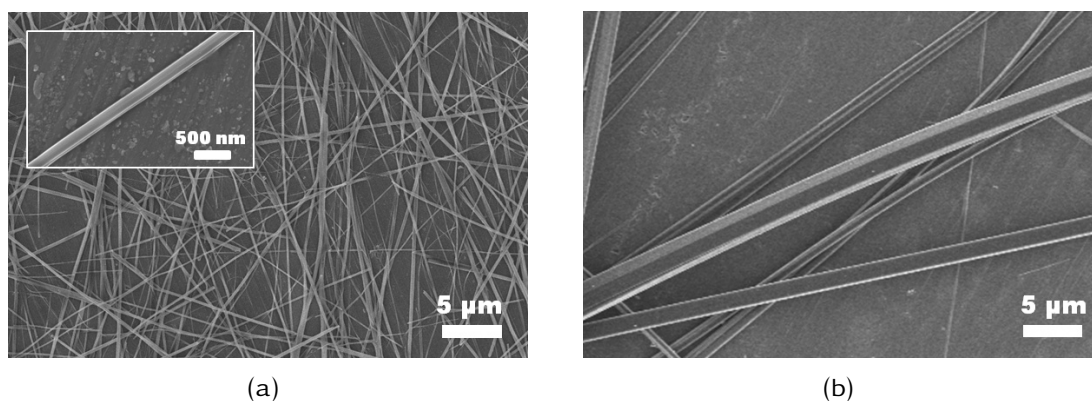


Figure 2.3 SEM images of BTA fibers with the (a) smallest and (b) largest diameters obtained (Chapter 5).

We determined the mechanical properties using the nanomechanical AFM bending experiments introduced in Chapter 4. To directly compare the different measurements, we expanded the previously described approach by normalizing the stiffness profiles with respect to the fiber diameter and length of the free-standing segment. We could identify two contributions to the apparent mechanical properties, the difference arising from the different thicknesses of the individual nanofiber types and additional changes of the material properties. The flexural rigidity of the fibers showed a difference of up to three orders of magnitude (Figure 2.4(a)). This was

a consequence of the increased diameters of the investigated nanofibers, since the rigidity is proportional to the fourth power of the radius.

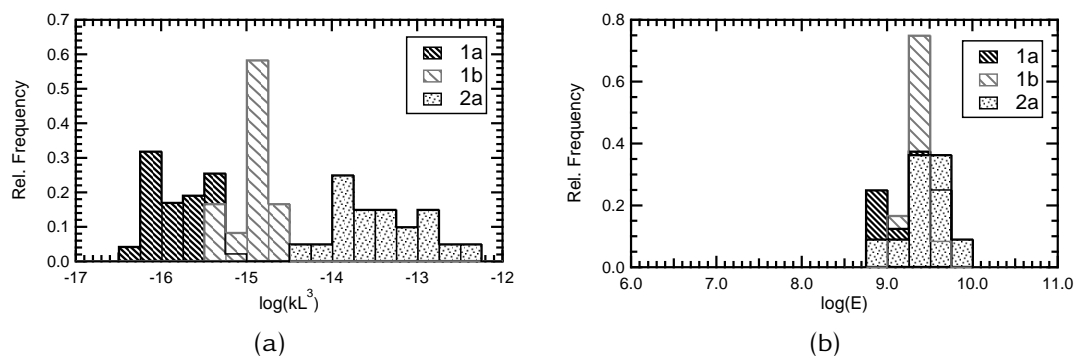


Figure 2.4 (a) Apparent flexural rigidity of all investigated nanofiber segments. The stiffness was measured at the midpoint of the free-standing segments. Please note that the x axis has a logarithmic scaling. The rigidity of **1b** is one to two, and of **2a** is up to three orders of magnitude higher than that of **1a**. (b) Distribution of the calculated modulus for all three investigated systems. The results for all systems are comparable (Chapter 5).

Calculation of Young's modulus as described in Chapter 4 revealed that these differences were a pure size effect, without equivalent changes of the material properties (Figure 2.4(b)). The moduli of all systems were comparable, ranging from 2.1 ± 0.1 GPa to 3.3 ± 0.3 GPa. This suggests that the influence of the investigated molecular structures on the mechanical properties is small, most likely because the intermolecular interactions are dominated by the three hydrogen bonds. The consequence is that variation of the molecular structure allows tailoring the fibers' morphology without affecting their modulus and thus, allows tuning their stiffness over a wide range. The results of this Chapter are a first step towards the application of self-assembled BTA nanofibers as components for bottom-up functional materials with tailored properties from the nano- to the microscale.

2.4 Comparison of Self-Assembled and Electrospun Trisamide Fibers

In addition to self-assembly from solution, BTA fibers can also be obtained via melt electrospinning, thus offering two complementary preparation pathways by bottom-up and top-down techniques. Chapter 6 compares electrospun (ES) and self-assembled (SA) fibers obtained from the same compound and demonstrates that both approaches lead to mechanically robust BTA fibers. X-ray diffraction (XRD) revealed that the crystal structure of the fibers was not influenced by the preparation method. SEM measurements, however, clearly showed morphological differences. While the SA fibers possessed a hierarchical structure, consisting of firmly connected bundles of individual strands, the ES fibers showed a smooth and homogeneous structure (Figure 2.5).

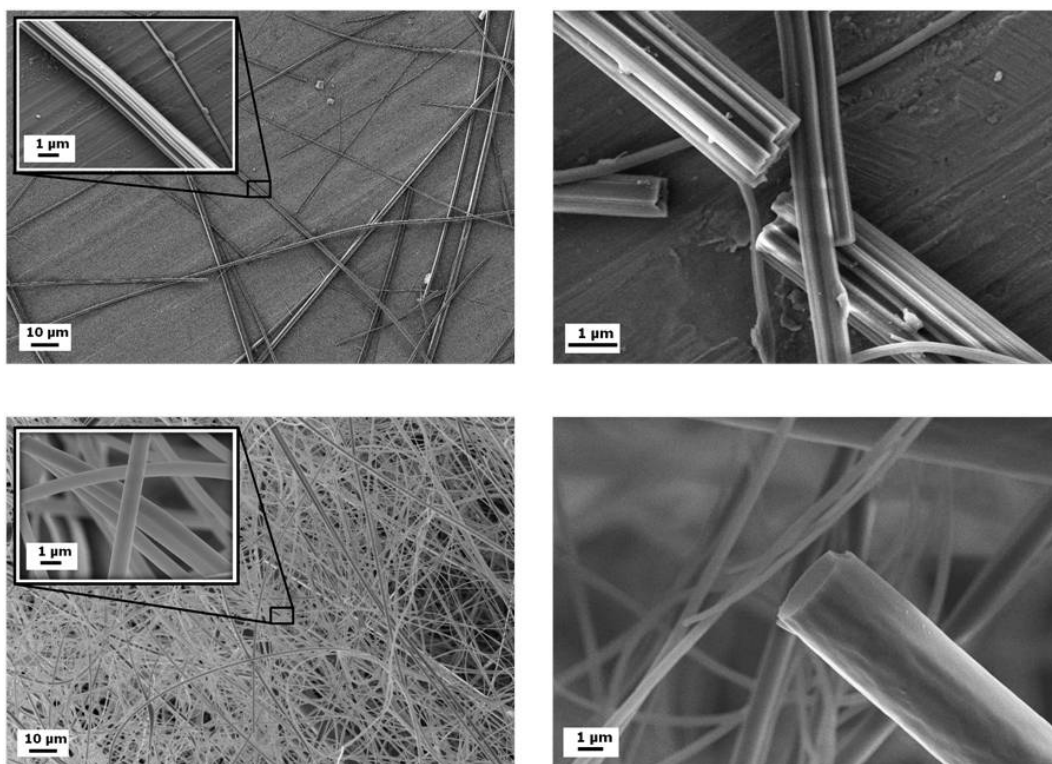


Figure 2.5 Top: SEM micrograph of the SA-fibers (left) and of a fracture section (right). Bottom: SEM micrograph of the ES-fibers of 1 (left) and of a fracture section (right). More detailed structures of the fibers are shown in the insets (Chapter 6).

AFM bending experiments, which probe the mechanical behavior on the length scale of the whole assembly, revealed that Young's modulus E was not significantly affected by changing the preparation process. While the average values suggested

that E_{SA} (3.6 ± 0.4 GPa) was slightly lower than E_{ES} (4.7 ± 0.6 GPa), the difference was small and within the error of the measurements. The important result was that the order of magnitude and distributions of the moduli were comparable (Figure 2.6), demonstrating that mechanically robust BTA fibers can be obtained by both approaches.

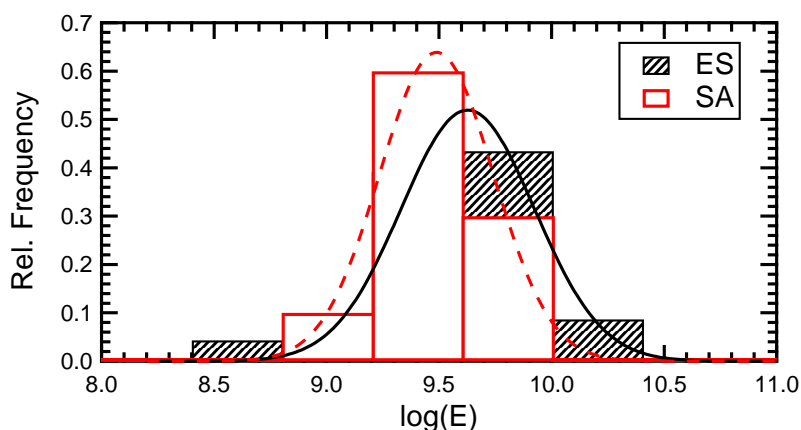


Figure 2.6 Distribution of the Young's moduli of SA-fibers (open bars, dashed line) and ES-fibers (hatched bars, solid line) (Chapter 6).

The findings of Chapters 4 through 6 open interesting perspectives for the controlled formation of hierarchical structures using supramolecular BTA fibers. First of all, they possess surprisingly high elastic constants in the lower GPa range, despite the absence of intermolecular covalent bonds. In addition, they can be obtained using bottom-up *and* top-down approaches, thus allowing the combination of their complementary advantages for one materials class. Furthermore, the molecular structure can be used to fine-tune the morphology of the individual fibers without significantly affecting their modulus. Consequently, they offer the possibility of a true structural control on all levels of hierarchy, from the single molecule over the individual fibers up to future applications in nonwovens.

2.5 A Critical Assessment of Slack Effects in Nanobending Experiments

The previous chapters demonstrate that AFM bending experiments are a reliable tool for the nanomechanical characterization of fibers. A prerequisite, however, is the correct identification and interpretation of the boundary conditions. For some measurements (e.g., Chapter 9), we found stiffness profile shapes that could not be described by any of the common beam theory models or by a mixture of those. Therefore, there was a need to elucidate the possible sources of such a behavior.

While most of the work in the literature has focused on non-ideal conditions at the fiber supports, Chapter 7 investigates the effect of a slack fiber, which represents an irregularity at the midsection. Our goal was to estimate how a certain degree of slack will affect the apparent mechanical properties and present guidelines on how to detect such influences and avoid a misinterpretation of the results. Since this effect is difficult to study experimentally (in the sense that a well-defined and systematically varied slack cannot be readily introduced), we used finite element (FE) analysis to simulate stiffness profiles for fibers with various degrees of slacking. We found that the slack produced a misleading shape of the stiffness profile (Figure 2.7). The dominating effect for the profile change was the slack-to-radius ratio. For moderate slack depths (comparable to the radius), the shape of the stiffness profile resembled the simply supported beam model, although the fiber was firmly clamped in the simulations. Evaluation using the SSBM however would lead to an overestimation of Young's modulus by over one order of magnitude.

In addition, we also investigated large-deformation-measurements. Experimentally, those measurements are often realized by applying the load in the substrate plane. To see how this affects the measurements, we performed simulations with vertical loading (i.e., in the same direction as the slack) and lateral loading (i.e., perpendicular to the slack, Figure 2.8). The simulations revealed that lateral measurements were not significantly influenced by the slack, no matter if performed within the small-deformation regime or the large-deformation regime. Therefore, they could be an experimental solution to deal with samples where slack is an issue.

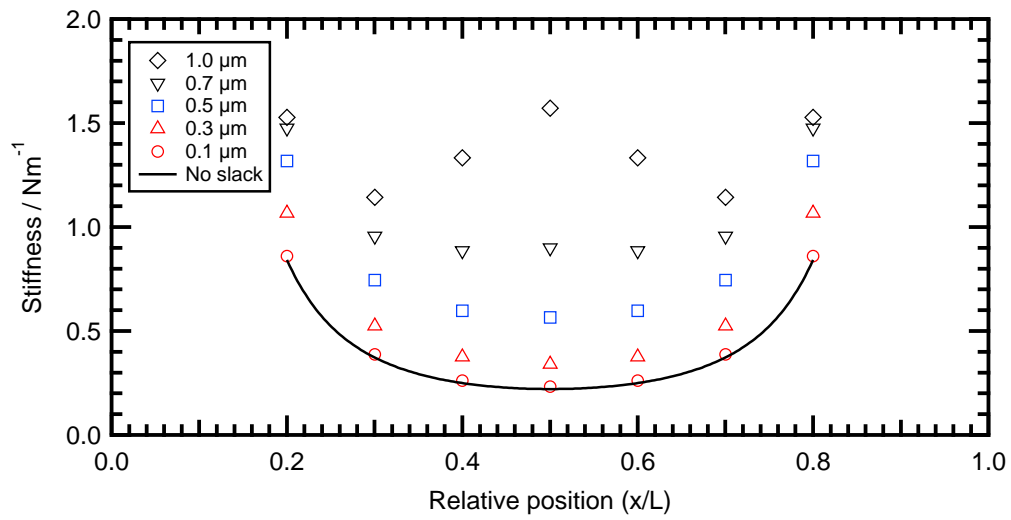


Figure 2.7 Stiffness profiles obtained from the FE simulations. For the sake of clarity, not all simulated profiles are shown here. (Chapter 7)

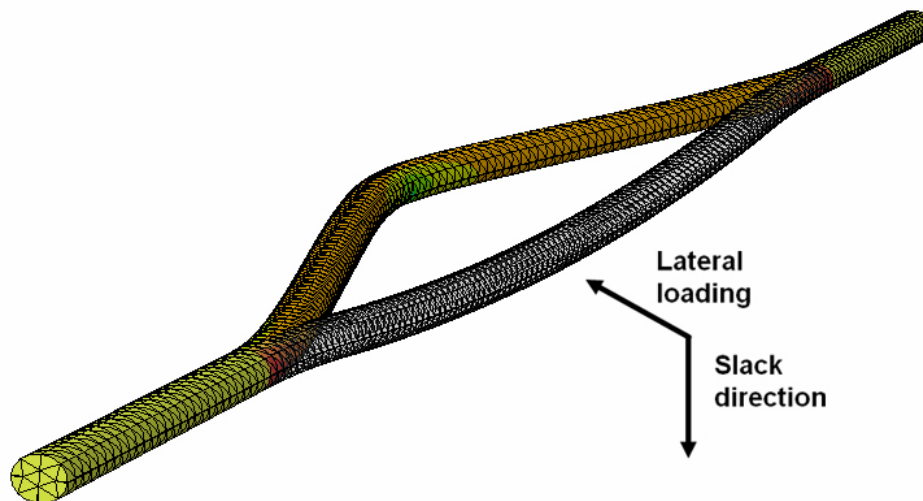


Figure 2.8 Volume element model used for studying the effect of loading the fiber in and perpendicular to the slack direction (Chapter 7).

2.6 Beyond Small Deformations

All previous chapters mainly focused on the linear elastic properties of the fibers. However, for many applications, also properties beyond the linear elastic regime are important. A possible approach to study these with bending experiments is discussed in Chapter 8. By applying a lateral instead of a vertical deformation, the fibers can be deformed until failure. In this setup, the fiber experiences a combination of bending and tension, and an appropriate evaluation is considered.

As the first important step for a quantitative evaluation of these measurements, a lateral calibration approach of the AFM setup is presented. In contrast to vertical measurements, the lateral calibration is more complicated, less precise, and although several approaches have been reported in the literature, there are no standard techniques so far. In our approach, the lateral sensitivity is determined in the same manner as the vertical sensitivity, using the slope of the measured signal in the constant compliance regime when applying forces to a hard substrate (Figure 2.9). Using the vertical steps in the structured glass substrates that are also used for the bending experiments ensured that the cantilever hits the calibration substrate at almost the same position as the fibers in the measurements, thus keeping the lever arm (i.e., the distance of the contact point to the reflective side of the cantilever) constant. The lateral spring constant was calculated from the geometry of the cantilever.

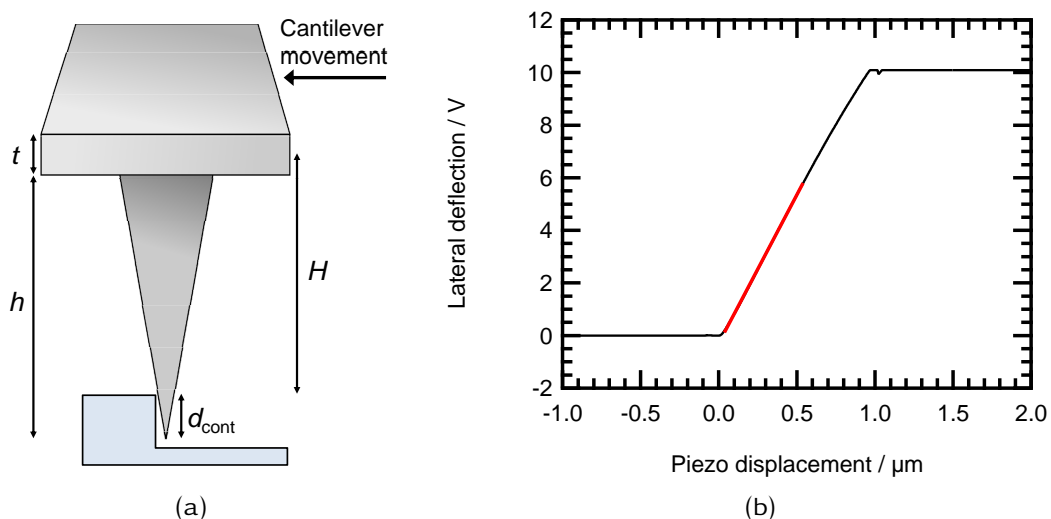


Figure 2.9 (a) Sketch of the lateral sensitivity calibration using the step of the structured glass substrates. (b) Lateral deflection-displacement curve obtained by pushing the cantilever against the undeformable substrate (Chapter 8).

We compared vertical and lateral measurements on BTA fibers in the small-deformation regime and found a good agreement between both deformation modes, although the lateral measurements were much more prone to scatter, most likely due to the unavoidable uncertainty of the lateral calibration. Building up on these results, we performed large deformation measurements until failure (Figure 2.10). Only the very thin fibers of one trisamide system could reliably be broken, since thicker fibers detached from the substrate before fracture. Nevertheless, we were able to estimate the flexural strength of the investigated system, which was comparable to that of Nylon.

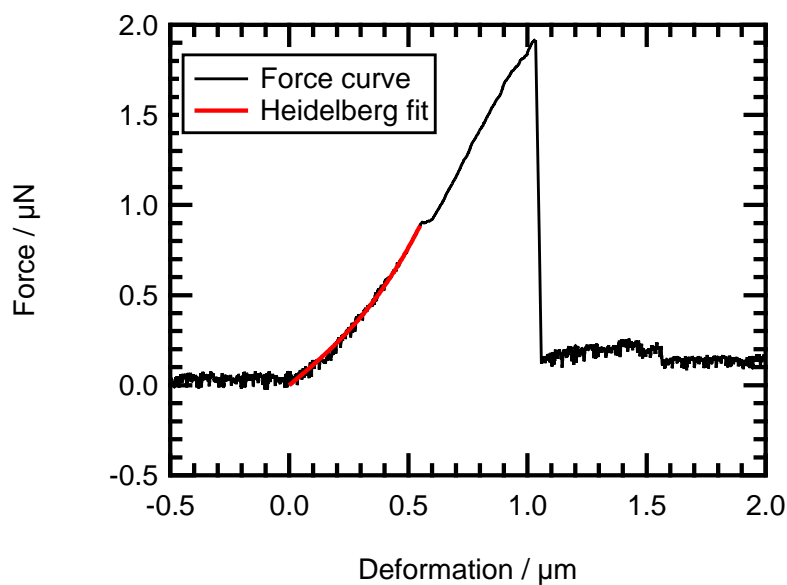


Figure 2.10 Example of a lateral force curve until failure. The nonlinear part in the beginning describes a purely elastic behavior of the material, but includes geometric nonlinearities (Chapter 8).

The work in this chapter demonstrates that lateral experiments can be a powerful addition to the vertical bending setup, but there remain some drawbacks that have to be addressed in future work. The most fundamental requirement in order to apply the lateral experiments to a wide variety of fibers is a suitable approach for a fixation on the substrate. In addition, the lateral calibration remains a major error source despite the presented improvements. Once these issues are solved, the possibility to combine vertical and lateral bending on exactly the same position allows characterization of the mechanical properties within and beyond the linear elastic regime with outstanding reliability.

2.7 Extending the Material Library Beyond BTAs

Although supramolecular BTA fibers are the main focus of the thesis, the developed concepts and techniques of course can also be applied to other materials. Chapter 9 presents a study on electrospun fibers of recombinant spider silk proteins. Due to their good biocompatibility, biodegradability, and low immune reaction, spider silks are a promising material for scaffolding in tissue engineering applications and as wound dressings. Since spiders cannot be farmed on a large scale due to their predatory and cannibalistic nature, the recombinant production of genetically engineered silk proteins is an alternative.

We investigated fibers prepared from a genetically engineered silk protein using the vertical and lateral bending tests described in the previous chapters. Although the vertical force-deformation curves on the free-standing segments showed a linear behavior, the experiments produced very inconsistent results with large deviations between the individual fibers. Generally, the SSBM showed better agreement with the data, contrary to the impression during handling of the samples under the optical microscope that suggested a firm fixation of the fibers on the substrate. In addition, the apparent Young's modulus was unrealistically high. While we could identify the inhomogeneous cross section of the fibers as a possible source of error, it could not explain the shape of the stiffness profile, and control experiments on fibers which did not show the inhomogeneities showed comparable results (Figure 2.11). This strongly suggested that the observed behavior must not be attributed to real supported boundary conditions.

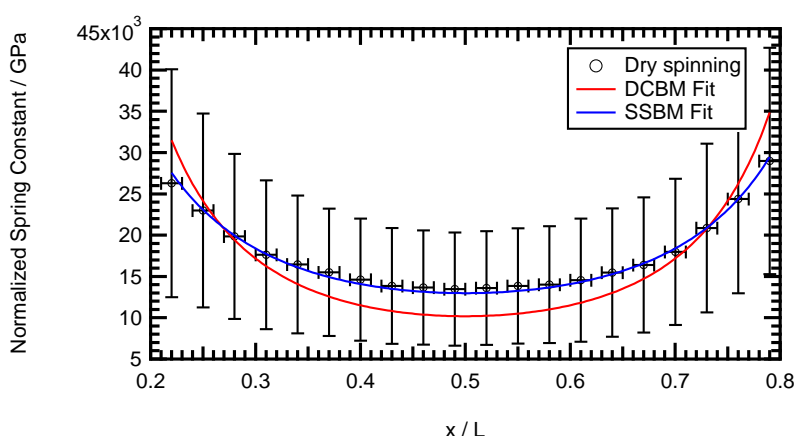


Figure 2.11 Exemplary stiffness profile of the control experiments on dry spun fibers silk fibers. Although the SSBM fits better, the common models cannot describe the shape of the profile (Chapter 9).

In addition to the vertical bending tests, we also employed a lateral setup as described in Chapter 8. In contrast to the vertical tests, the lateral data showed a very good agreement with the predicted behavior and evaluation of the elastic properties yielded realistic values of Young's modulus with a reasonable amount of scatter. This strongly resembles the behavior of a slack fiber reported in Chapter 7, but further experimental investigation is necessary to provide a conclusive explanation. Despite the limitations, the lateral measurements allowed comparing silk fibers with and without post-treatment by methanol vapor. This treatment is known to induce a transformation from a predominantly α -helical secondary structure to a β -sheet rich structure, and we could clearly see a difference in the elastic properties of the treated and untreated fibers (Figure 2.12).

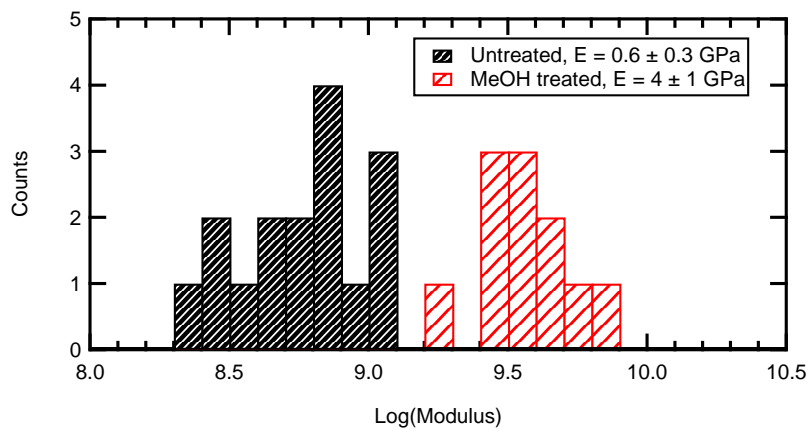


Figure 2.12 Distribution of Young's modulus determined from the lateral bending experiments for untreated (black) and methanol treated (red) silk fibers (Chapter 9).

Regardless of the issues, this chapter demonstrates that a mechanical investigation of other materials via bending experiments is possible, that they can identify non-ideal behavior and therefore, produce reliable results. Especially lateral large deformation experiments are a promising approach for further mechanical studies.

2.8 Individual Contributions to Joint Publications

The experimental work and findings presented in the thesis are the result of collaboration with fellow researchers. In the following, the individual contributions of each coworker are specified.

Chapter 4 is published in *Langmuir* **2010**, *26(5)*, 3020-3023 under the title *Nanomechanical Properties of Supramolecular Self-Assembled Whiskers Determined by AFM Force Mapping* by Daniel Kluge, Frank Abraham, Stephan Schmidt, Hans-Werner Schmidt, and Andreas Fery. I carried out all of the bending experiments, evaluated the data, programmed the evaluation procedures, performed parts of the SEM imaging, and wrote the publication. Frank Abraham performed the sample preparation, parts of the SEM imaging, and wrote the publication. Stephan Schmidt was involved in scientific discussions and corrected the manuscript. Hans-Werner Schmidt and Andreas Fery supervised the project, corrected the manuscript and were involved in scientific discussions.

Chapter 5 is published in *Small* **2012**, *16*, 2563-2570 under the title *Influence of the Molecular Structure and Morphology of Self-Assembled 1,3,5-Benzenetrisamide Nanofibers on their Mechanical Properties* by Daniel Kluge, Julia C. Singer, Jens W. Neubauer, Frank Abraham, Hans-Werner Schmidt, and Andreas Fery. I carried out a part of the bending experiments, evaluated the AFM data, programmed the evaluation procedures, and wrote the paper. Julia C. Singer performed the fiber preparation, morphological characterization, and wrote the paper. Jens W. Neubauer performed and evaluated a part of the bending experiments within the scope of his bachelor thesis under my guidance. Frank Abraham prepared a part of the self-assembled nanofibers. Hans-Werner Schmidt and Andreas Fery supervised the project, corrected the manuscript and were involved in scientific discussions.

Chapter 6 is published in *Polymer* **2012**, *53*, 5754-5759 under the title *Top-down meets bottom-up: A comparison of the mechanical properties of melt electrospun and self-assembled 1,3,5-benzenetrisamide fibers* by Daniel Kluge, Julia C. Singer, Benedikt R. Neugirg, Jens W. Neubauer, Hans-Werner Schmidt, and Andreas Fery. I oversaw the bending experiments, evaluated the AFM data, programmed the evaluation procedures, and wrote the paper. Julia C. Singer performed the fiber preparation, morphological characterization, and wrote the paper. Jens W. Neubauer performed and partially evaluated the bending experiments on the self-assembled fibers within the scope of his bachelor thesis under my guidance. Benedikt R. Neugirg performed

and partially evaluated the bending experiments on the electrospun fibers under my guidance. Hans-Werner Schmidt and Andreas Fery supervised the project, corrected the manuscript and were involved in scientific discussions.

Chapter 7 was initially submitted for publication in *Journal of Applied Physics* under the title *A Critical Assessment of Slack Effects in Nanobending Experiments* by Daniel Kluge, Davide Ruffoni, and Andreas Fery. I performed all FEM simulations and evaluated the data. Davide Ruffoni and Andreas Fery supervised the project, corrected the manuscript and were involved in scientific discussions. At the date of publication of this thesis, the chapter is intended to be published as part of a larger upcoming paper, including further experimental work.

Status of the Field and Theoretical Background

3.1 Nanomechanical Characterization of Fibers

3.1.1 The Challenges of Nanomechanics

The advancing miniaturization of building elements allows the design of novel functional structures with exceptional properties. However, even if the bulk properties of a material are already known, the increased importance of defects and inhomogeneities on the nanoscale makes probing the individual structural elements necessary. Especially tailored high-end materials often cannot be characterized with macroscopic tests, since they lack the required sensitivity. Therefore, there is a growing need for simple, versatile and reliable nanomechanical characterization techniques. While mechanical testing on such small scales is always difficult, nano- and microfibers pose some special challenges:

- During sample preparation, the fibers have to be manipulated, aligned and fixated with high precision and without unintentionally damaging the fibers or inducing stresses and strains prior to mechanical testing.
- *In situ* observation of the experiment is difficult and requires optical microscopy or even electron microscopy techniques. The latter are limited to conductive samples since on such small scale, the sputtered conductive layer could alter the mechanical properties.
- The mechanical testing itself requires high precision and resolution for both forces and displacements. Therefore, typical testing systems cannot be used and the measurements are often performed using atomic force microscopy (AFM, see Section 3.3).

There has been continuing effort and success in the last few years in overcoming these difficulties, summarized in comprehensive reviews on nanomechanics in general by *Withers et al.*,¹ *Aston et al.*,² and, with an exclusive focus on the mechanical testing of nanofibers by *Tan et al.*,³ as well as a book chapter dealing with the characterization of polymer nanostructures with AFM by *Kim et al.*⁴ Although many of the experimental techniques were further developed and fine-tuned since then, the three major approaches for quasi-static mechanical testing of fibers are still bending experiments, uniaxial tensile tests and indentation measurements. Besides, there are also dynamic approaches which are mostly based on probing the resonant frequency of free-standing fibers and which will not be further discussed here.

3.1.2 Bending

Nanomechanical bending experiments are one of the most frequently used approaches since they allow a reliable characterization and require only moderate effort in terms of sample preparation. The principal setup is shown in Figure 3.1. The fiber is placed on a substrate with well-defined gaps like channels or holes and the load is typically applied to the fiber using commercial AFMs or equivalent devices. Most measurements are evaluated with continuum mechanical beam bending theory, especially since for fibers with a diameter larger than 100 nm, surface effects, such as surface tension, long range interactions, and a chemically different surface layer, are typically negligible.⁵⁻⁷

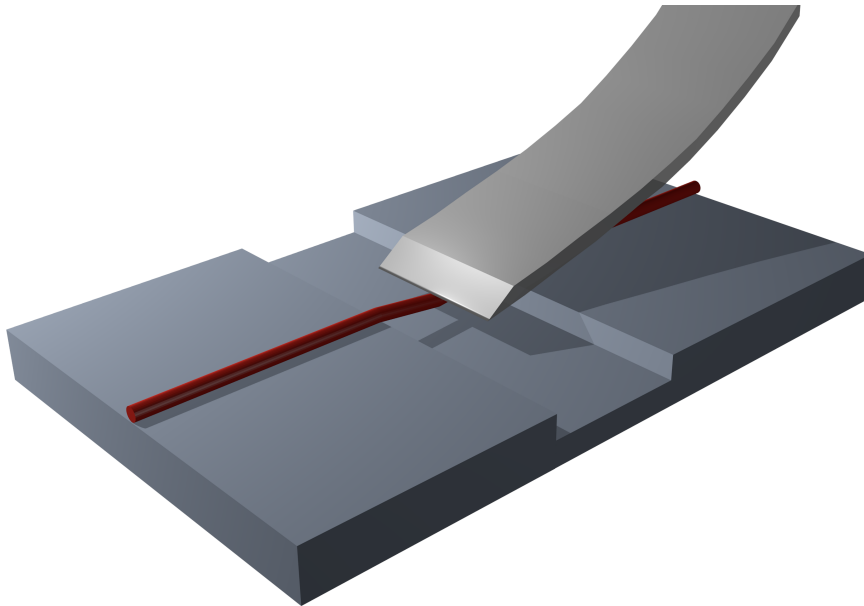


Figure 3.1 Schematic setup of a micromechanical bending experiment on fibers via AFM.

Nevertheless, several important prerequisites have to be considered for a correct interpretation of the data, which are easier to control on the macroscopic scale. First of all, indentation of the fiber during bending must be avoided to ensure that the force-deformation behavior consists of pure bending. Second, the fixation of the fiber on the substrate plays an important role. Finally, the fibers should lie straight and perpendicular over the gaps in the substrate, but without prestress. Since not all of these parameters can be completely controlled, sometimes it is necessary to incorporate them into the theoretical model used for evaluation, which will be discussed in Section 3.2 and Chapter 7.

One of the first investigations of nanoscopic fibers with bending experiments was the determination of Young's modulus of β -chitin fibers.⁸ Today, fibers consisting of a wide variety of materials and with diameters of a few nanometers up to several microns have been studied. The materials can be grouped into three main fields of research, (carbon) nanotubes, metal or metal oxide nanowires, and soft matter fibers. These fields have distinct scientific questions which may involve different underlying physical principles and samples of vastly different sizes.

An interesting aspect to note is that although all three fields apply bending experiments for a nanomechanical characterization, surprisingly little of the results and findings are referenced within the respective other communities. One reason might be that the focus of the individual groups is sometimes very different. In the soft matter community that often deals with novel materials, mostly Young's modulus and comparable continuum mechanical characteristics are of interest, whereas, especially for nanowires, often the influence of defects is more important since the materials are well-established. Whatever the reasons, the consequence is that achievements within one community are typically slow to be recognized by the others. Therefore, there is still potential for further improving the experiments by combining the results of the different fields.

Since nanotubes possess remarkable properties but a very small size, a true nanomechanical characterization is highly relevant. Due to the difficult sample handling, bending experiments have proven to be a very convenient approach to study the mechanical properties of CNTs and CNT ropes^{9,10} as well as the effect of a mechanical deformation on their electrical characteristics.¹¹ Recently, also boron nitride nanotubes were investigated.¹² For the same reasons, bending experiments have also been widely applied for the mechanical characterization of metal and metaloxide nanowires and nanobelts.^{5,13-22}

Bending experiments are also very important within the soft matter community for the characterization of (bio)polymer nanofibers, and especially for biological systems as the samples often have a given size and do not tolerate harsh measurement conditions (e.g., ultra high vacuum). Experiments on biological samples and biopolymers included microtubules,²³ native, modified and electrospun collagen fibrils,²⁴⁻²⁷ intermediate filaments,^{28,29} amyloid fibrils,³⁰ different types of cellulose fibrils,³¹⁻³³ and even gecko setae.³⁴ Studies on synthetic polymers are often focused on electrospun fibers and included poly(L-lactic acid) (PLLA) nanofibers,³⁵ electrospun polyacrylonitrile (PAN) fibers,³⁶ polymer nanowires,³⁷ and poly(vinyl alcohol)

nanofibers reinforced with ferritin.³⁸ The concept was even further extended to particle bridges.^{39,40} However, especially for synthetic polymers, there are also other characterization methods available. The controlled fabrication of nanofibers via electrospinning allows the application of uniaxial tensile tests (see Section 3.1.3) and if the polymers can be produced in larger quantities, there is often no need for a nanoscopic mechanical characterization of the material.

While bending experiments are typically associated with small and elastic deformations, they have also been employed to study the large-deformation regime. It should be noted, however, that correct interpretation of these measurements requires significantly more complex theories (see 3.2.4) which have not been applied in every case.⁴¹ In addition, those measurements are typically performed in a lateral setup, which introduces additional experimental difficulties (see Section 3.3.5). The first studies employing large deformations have been performed on SiC nanorods and CNTs.⁴² Other publications included carbon nanotube ropes,^{43,44} electrospun polymer-nanotube composite nanofibers,⁴⁵ electrospun collagen and fibrinogen fibers,^{46,47} fibrin fibers,⁴⁸ and intermediate filaments.²⁹ While there is a large number of studies on metal- and metal oxide nanowires, nanobelts, and nanobeams,^{49–60} the work of *Heidelberg* et al. includes the most comprehensive description of the large-deformation behavior of nanowires.⁴¹

3.1.3 Uniaxial Tension

The big advantage of uniaxial tension measurements is the straightforward acquisition of stress-strain curves. However, there are several difficulties for nanofibers:^{3,61} First of all, sample preparation requires direct manipulation of the fiber and therefore carries the risk of damaging the sample. Second, gripping is difficult and often requires gluing the fiber to a support. This can influence the measurements due to pull-out of the fiber or finite elasticity of the glue. Finally, misalignment of the loading direction to the fiber axis can cause additional bending moments and stresses which can lead to misinterpretation of the data. Therefore, setups for uniaxial tension are often much more sophisticated than bending experiments. A possible approach is sketched in Figure 3.2. In some of the first studies, a comparable setup was combined with electron microscopy to measure the tensile properties of carbon nanotubes.^{62–64} Besides, experiments were performed on various types of electrospun polymers.^{65–71} Here, sample preparation can often be facilitated by depositing

the fibers in a support frame, so that commercially available high-precision tensile devices can be employed.

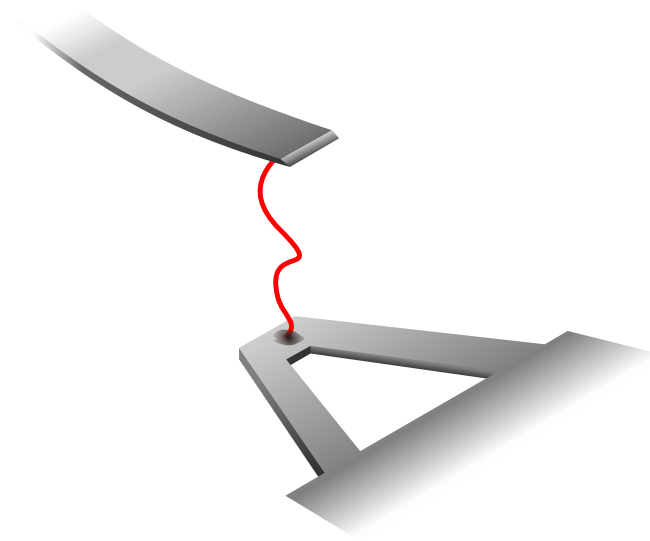


Figure 3.2 Schematic setup of a possible uniaxial tension experiment based on the description by *Tan et al.*³ The fiber is glued between two AFM cantilevers with different spring constants. The stiff triangular cantilever is used to apply a strain to the fiber while the other one acts as force sensor.

It is important to differentiate between tension in general, and a pure uniaxial tension. For uniaxial tension, the tensile stresses are homogeneously distributed throughout the test specimen, while bending leads to an inhomogeneous stress distribution of compressive and tensile stresses.⁷² At large bending deformations, additional homogeneously distributed tensile stresses may also become significant (see Section 3.2.4 and Chapter 8).

3.1.4 Nanoindentation

Indentation is based on pressing a hard probe with a defined geometry into the sample and extracting the mechanical properties from the force-indentation curve. The principle can be seen in Figure 3.3. The measurements are evaluated with suitable theories of contact mechanics, depending on the nature and complexity of the systems.^{73,74} Nanoindentation measurements are mostly performed at high loads where adhesion forces play a minor role and thus, the measurements are often described with an extended Hertzian or Oliver-Pharr model.⁷⁴⁻⁷⁷

It has been demonstrated that nanoindentation measurements can be used for the mechanical characterization of thin fibers.⁷⁸⁻⁸⁰ They have the main advantage of

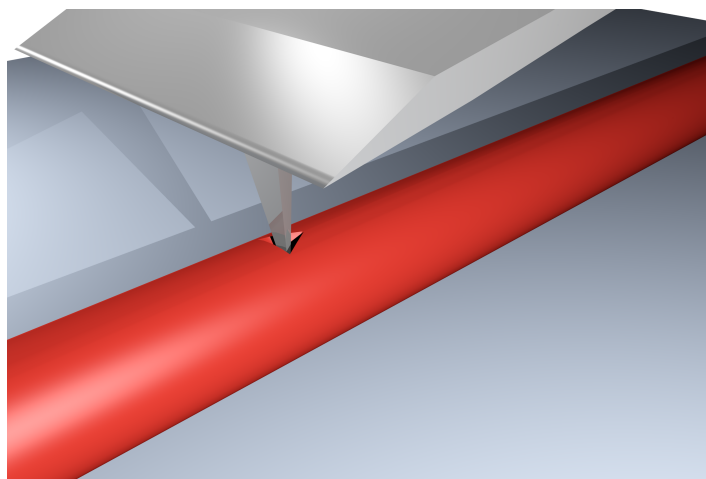


Figure 3.3 Schematic setup of an AFM based indentation experiment on a nanofiber.

much easier sample preparation compared to bending and tension, since the fibers can simply be deposited on a flat, hard substrate. However, there are several issues with this approach.^{3,80} First of all, the fibers may be compressed so far that the underlying substrate influences the measurement and Young's modulus is overestimated. For thin samples, this effect becomes important when the indentation depth is larger than 5–10 % of the sample thickness, which results in a lower fiber diameter limit of around 200 nm.⁷³ Second, for indenters with a sharp tip, the curved shape of the fiber can also pose a problem due to the ill-defined contact area and slippage of the tip.^{3,80} Therefore, nanoindentation is most commonly performed on thin films (especially polymers) and biological samples.^{73,75,81–84}

An important thing to keep in mind is that the determined mechanical properties do not necessarily have to correspond with bending and tension measurements: For an isotropic material, the Young's modulus determined by indentation measurements will yield the same result as the other approaches. Many fibers, however, are more likely to show transverse isotropy.⁸⁵ Here, the elastic modulus in the axial direction (longitudinal elastic modulus) will be different from the elastic modulus perpendicular to the fiber axis (transverse elastic modulus).^{34,86} Therefore, indentation measurements on nanofibers should be regarded as a complementary approach rather than as replacement for bending and tensile tests.

3.2 Beam Theory

Although bending on the nanoscale is experimentally by far more challenging than on the macroscopic scale, the general mechanical concepts are the same and *beam theory* is frequently used to evaluate the measurements. A detailed description of beam theory can be found in textbooks of mechanical engineering. The major part of this chapter is a summary of the concepts that are relevant for the experimental work in the thesis and is mainly based on the books by *Gere* and *Ugural*.^{72,87} Note however that the notation (especially the definition of the coordinate system) deviates slightly from the engineering standards in order to be consistent with the standards of AFM.

Since beam theory is a continuum mechanical approach, there will be limitations for fibers with very small diameters that can no longer be treated as a continuous material. In addition, phenomena like thermal fluctuations are normally not included in macroscopic continuum mechanical theories. Especially surface effects start to have a significant influence for fibers with a diameter below 100 nm.⁵⁻⁷ Since the fibers investigated in this work were relatively thick (with diameters from ≈ 150 nm to above 1 μm), the fundamental models and predictions of classical beam theory were considered sufficient in the majority of cases.

3.2.1 Elastic Regime

A transverse load that is applied to a beam will result in a bending moment M and the beam will bend into a curved shape which is called the *deflection curve*. The deformation of a beam with a uniform cross section under *pure bending* is depicted in Figure 3.4. In pure bending, the shear forces are zero and cross sections remain plane and normal to the longitudinal axis.⁷² In general, it is assumed that the beam is symmetric to the (xz) plane (therefore, bending can be reduced to a quasi-2D-problem) and *slender*, which means that its length is large compared to its maximum cross-sectional dimension.

Let us consider a beam subjected to a positive bending moment as depicted in Figure 3.4. Internally, the top part of the beam will be shortened due to the curvature while the lower part will be elongated, which corresponds to *longitudinal strains* ϵ_x . In between, a surface is situated that does not change in length, which is called the *neutral surface* and its intersection with the (xz) plane is called the *neutral axis*. The

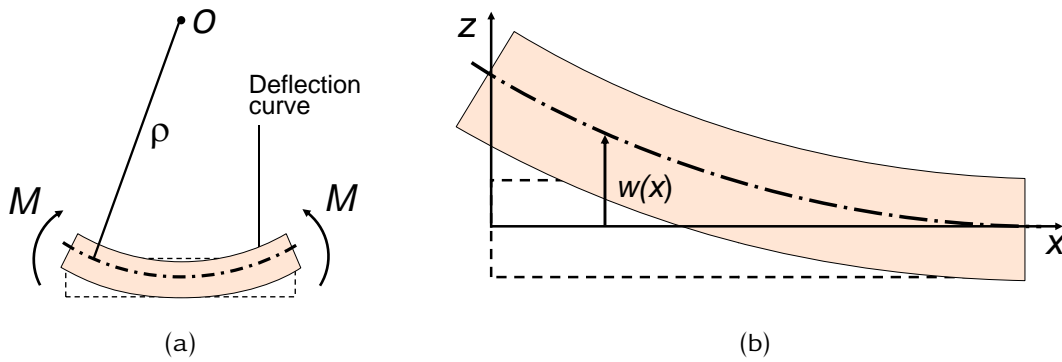


Figure 3.4 Pure bending of a beam. (a) Deformed shape of a beam as a result of the bending moments M acting on its ends. The deformation is strongly exaggerated. (b) Enlarged end of the beam. Since the beam is assumed symmetric to the (xz) -plane, bending is reduced to a quasi-2D-problem.

deflection curve is defined by the location of this surface. Its distance from the center of curvature O is called the *radius of curvature* ρ . The curvature itself is denoted $\kappa = \rho^{-1}$. The relation between strain and curvature is

$$\epsilon_x = -\kappa d_{n,z} \quad (3.1)$$

where $d_{n,z}$ is the distance to the neutral surface. For a linear elastic, isotropic material that follows Hooke's law, the corresponding normal stresses acting on the cross section are therefore given by:

$$\sigma_x = E\epsilon_x = -E\kappa d_{n,z} \quad (3.2)$$

An important result of this equation is that the stresses vary linearly with the distance $d_{n,z}$ from the neutral surface and change from maximum compressive to maximum tensile from the top to the bottom of the beam. In addition, the stresses can be correlated with the bending moment to calculate the moment-curvature equation:⁷²

$$M = \kappa EI \quad (3.3)$$

The product EI is called the *flexural rigidity* and consists of Young's modulus E and the *area moment of inertia* I of the cross section. I is a purely geometric parameter and depends on the axis around which the beam is curved and therefore on the direction

of loading. For example, a load in the z direction will lead to curvature around the y axis and therefore, I_y is needed for the calculations. It is defined as

$$I_y = \int_A z^2 dA \quad (3.4)$$

where A is the area of the cross section. Combining Equations (3.2) and (3.3) yields the *flexure formula*, which relates the stresses to the bending moment:

$$\sigma_x = -\frac{Md_{n,z}}{I} \quad (3.5)$$

For practical applications, it is also important to calculate the *deflection* of the beam. The deflection w is defined as the z component of the displacement of an arbitrary point on the neutral surface in the distance x from the beam end. For small deflections of the beam, the relation between curvature and deflection can be expressed as⁷²

$$\kappa = \frac{d^2w}{dx^2} \quad (3.6)$$

Combining this with Equation (3.3) yields

$$\frac{d^2w}{dx^2} = \frac{M}{EI} \quad (3.7)$$

This is the governing *differential equation of the deflection curve* of a beam, sometimes also called the *Bernoulli-Euler law* of technical bending theory.⁸⁷ Integrating this equation with known bending moment M and flexural rigidity EI allows calculation of the beam's full deflection curve.⁷²

3.2.2 Fixation and Boundary Conditions

Depending on the fixation of the beam, there are different boundary conditions for which Equation (3.7) has to be solved. While it is relatively easy to determine and control the boundary conditions for a macroscopic bending test, things get significantly more complicated on the nanoscale. However, knowledge of the boundary conditions is essential for a correct interpretation of the mechanical behavior. Often,

an important issue is determining the proper model for the fixation of a microscopic 1D object on the substrate during bending.¹⁵

The two most commonly applied models are a beam that is firmly fixed on the substrate and a beam that is only supported by the substrate (see Figure 3.5). The corresponding models are often denoted as *double clamped beam model* (DCBM) and *simply supported beam model* (SSBM). Since the ends of the beam are only loosely supported in the SSBM case, they are free to rotate and are therefore lifted off the substrate when the beam is loaded in its mid-section.

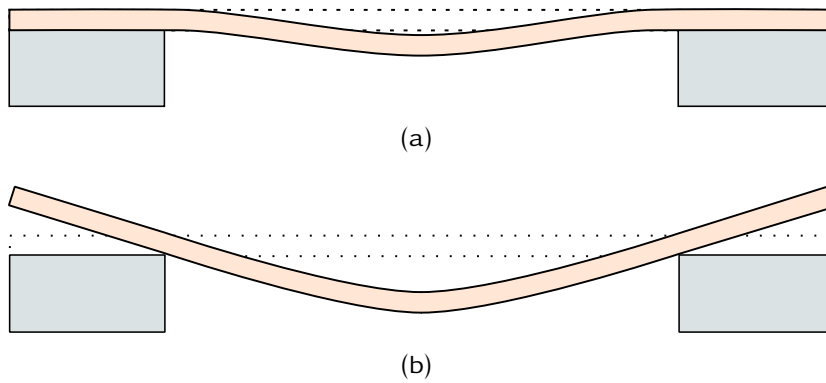


Figure 3.5 Common models for the boundary conditions of a beam under pure bending. (a) The double clamped beam model (DCBM) assumes that the ends are firmly attached to the supports. (b) The simply supported beam model (SSBM) assumes that the ends of the beam are only loosely lying on the supports and are therefore free to rotate.

It is easy to determine the (symmetric) boundary conditions for both cases. For the DCBM, the deflection and the slope are zero at the ends of the beam. The origin of the x axis is set to one end of the beam, so the x coordinate of this end is 0, the other is equal to the length of the free-standing segment (which is equal to the distance between the supports) L . This results in:

$$w(0) = 0 \qquad w(L) = 0 \qquad (3.8)$$

$$\left. \frac{dw}{dx} \right|_0 = 0 \qquad \left. \frac{dw}{dx} \right|_L = 0 \qquad (3.9)$$

For the SSBM, only the deflection must be zero because the beam is able to rotate and therefore w has a finite slope. However, the bending moment also has to vanish, so that

$$w(0) = 0 \qquad w(L) = 0 \qquad (3.10)$$

$$M(0) = EI \frac{d^2 w}{dx^2} \Big|_0 = 0 \qquad M(L) = EI \frac{d^2 w}{dx^2} \Big|_L = 0 \qquad (3.11)$$

Finding a correct expression for the acting bending moments M and solving Equation (3.7) for specific boundary conditions is not straightforward. Detailed examples can be found in the literature.⁷² For the DCBM, the solution is^{14,25}

$$w(x) = \frac{F(L-x)^3 x^3}{3L^3 EI} \qquad (3.12)$$

and for the SSBM^{14,15}

$$w(x) = \frac{F(L-x)^2 x^2}{3LEI} \qquad (3.13)$$

When calculating the deformation at the midpoint for both cases, one obtains:

$$w(x) = \frac{FL^3}{192EI} \qquad (3.14)$$

for the DCBM and

$$w(x) = \frac{FL^3}{48EI} \qquad (3.15)$$

for the SSBM, respectively. It is obvious that the deformation at a given force is four times larger for the SSBM. The reason is that there is no additional curvature at the ends, because they are lifted off the substrate, which significantly reduces the stresses within the beam. Therefore, a simple 3-point bending test where the load is only applied and the deformation is only observed at the midpoint of the beam, is not sufficient to reliably determine the mechanical properties on the nanoscale. However, Equations 3.12 and 3.13 show that the model also influences the *shape* of the deflection curve, which presents a possibility to determine the boundary conditions by performing spatially resolved force measurements along the free-standing segment of the beam.

For AFM force measurements, it is sometimes easier to determine the stiffness instead of the absolute deformation of the sample. Rearranging Equations 3.12 and 3.13 accordingly yields

$$k(x) = \frac{3L^3 EI}{(L-x)^3 x^3} \quad (3.16)$$

for the DCBM and

$$k(x) = \frac{3LEI}{(L-x)^2 x^2} \quad (3.17)$$

for the SSBM.^{25,88} By determining the stiffness on multiple positions along the free-standing segment, a *stiffness profile* is obtained. The shape of this profile can be used to verify the boundary conditions and to calculate the flexural rigidity EI by fitting the equations to the measured profile. Since the length of the channel is known, EI is the only free parameter in the fit. When the area moment of inertia I is known (e.g., by AFM measurements of the fiber cross section), the fiber's Young's modulus E can be directly calculated from the stiffness profile.

With the increasing importance of bending experiments for the nanomechanical characterization of 1D structures, determining the boundary conditions has gained growing research interest. The influence of the boundary conditions was investigated by dynamic⁸⁹ and static^{6,14,19} bending measurements and its importance is still pointed out in very recent publications.¹² There are several detailed studies by the *Aston* group concerning the boundary conditions for nanobending experiments.^{1,15,16,37} Besides the commonly used models of complete clamping and loose support, they also investigated the effect of a fixation with finite stiffness.⁹⁰ In this thesis, the effect of the boundary conditions and their investigation via force mapping is further discussed in Chapter 4.

3.2.3 Shearing

The discussion so far was limited to pure bending. However, for thicker beams, larger deflections or highly anisotropic materials, there may be a significant contribution of shear forces within the beam which leads to *nonuniform bending* and a Timoshenko-Beam like behavior.^{72,91} In the literature, this issue is often addressed

by defining a bending modulus E_b , which is related to Young's modulus E and the shear modulus G via:^{23,25,28}

$$\frac{1}{E_b} = \frac{1}{E} + \frac{1}{G} \cdot \frac{3f_s d^2}{L^2} \quad (3.18)$$

for a double clamped cylinder. Here, d is the diameter and L is the length of the suspended segment. f_s is a shape factor that equals 10/9 for solid cylinders.²⁸ The derivation of Equation (3.18) uses the fact that the area moment of inertia I and the cross-sectional area A are both functions of the fiber's radius.⁹¹ However, for more arbitrary cross sections, this is not necessarily the case, and Equation (3.18) becomes

$$\frac{1}{E_b} = \frac{1}{E} + \frac{1}{G} \cdot 48 \frac{f_s I}{AL^2} \quad (3.19)$$

which is used in Chapter 5.

For isotropic materials, small deflections and quasi-static experiments (i.e. low deformation speed), the contribution of shearing is only a few percent and can be neglected⁸⁷ and $E_{bend} = E$. For highly anisotropic materials, this is only valid if the aspect ratio $\frac{L}{d}$ fulfills the requirement:^{10,26}

$$\frac{L}{d} \geq 8 \sqrt{\frac{E}{G}} \quad (3.20)$$

If shearing contributes to the bending behavior of a specific sample, there will be a linear dependency of $1/E_b$ on d^2/L^2 as suggested by Equation (3.18), which can be used to calculate E and G from the data.^{23,25}

3.2.4 Large Deformations

The characterization of nanofibers at large deformations is often performed in a lateral bending setup (see Section 3.1.2). In this setup, the fiber experiences an additional tension due to a total increase in length at large deformations. The measured forces will therefore be a combination of bending and tension: For small deformations, bending forces are dominant. For large deformations, the experiment can be considered as quasi-uniaxial stretching and tension forces are dominant. The proper

mathematical description of this interplay is rather complicated.^{41,43,45} For the sake of clarity, let us consider the approximate solution for the resulting force F_{center} at the midpoint of the fiber by *Heidelberg et al.*⁴¹

$$F_{\text{center}} = \frac{192EI}{L^3} \Delta v_{\text{center}} + \frac{8EA}{L^3} \Delta v_{\text{center}}^3 \quad (3.21)$$

In this equation, Δv_{center} is the absolute displacement of the fiber in y direction, E is Young's modulus, and A is the cross-sectional area of the fiber. For a lateral deformation, the area moment of inertia about the z axis I_z is needed since the fiber is deformed in the y direction. The first, linear term is the regular bending force. The second, cubic term is the tensile force acting on the fiber which becomes significant for deformations at the midpoint of the free-standing segment that are larger than the radius of the fiber.⁴¹ Therefore, the force-deformation curve measured in a bending experiment will no longer be linear at large deformations, even if the material still behaves linearly elastic.

Equation (3.21) still assumes a linear elastic material behavior. If a material, for example, behaves elastoplastically, it starts to show plastic deformations when the stress exceeds the yield stress σ_y . Since the bending stresses are not homogeneously distributed, the outer regions of the beam will show plastic deformation while an *elastic core* remains linearly elastic.⁷² The point where the material starts to deviate from the linear elastic models can be identified as the *yield point* if no other effects (such as slipping of the fixations) occur.

Further deformation until failure allows calculation of the *fracture strength* σ_f . Let us first consider a beam that breaks at small deformations and that does therefore not experience additional tensile stresses. It is important to remember that the stress distribution in bending is not homogeneous. Instead, the stress increases with distance to the neutral axis and is either of compressive or tensile type (see Section 3.2.1). Since fracture of the fiber is caused by failure at the region of highest stress, it is not important to exactly determine the whole stress distribution, but only the maximum stress at break which is equal to the *bending or flexural strength* σ_b . The relationship between the bending stress and the bending moment is given by Equation (3.5).

$$\sigma_x = -\frac{Md_{n,\max}}{I}$$

The maximum moment resulting from a concentrated load F on a double-clamped beam is given by:⁹²

$$M_{\max} = -\frac{2Fx^2(L-x)^2}{L^3} \quad (3.22)$$

Here, x is the position where the load is applied, and L is the length of the free-standing segment. When applying the load at the midpoint of the free-standing segment where $x = L/2$, the equation facilitates to

$$M_{\max} = -\frac{FL}{8} \quad (3.23)$$

Combining this result with Equation (3.5) and considering that the maximum bending stress will occur at the maximum distance from the neutral surface yields an expression for the bending strength:⁴⁹

$$\sigma_{b,\max} = \frac{FL}{8I}d_{n,\max} \quad (3.24)$$

In reality, the calculation of a nanofiber's fracture strength can become quite complicated. Additional tensile stresses due to elongation of the whole beam will be homogeneously distributed within the beam. Therefore, the bending and tension components of the force described by Equation (3.21) have to be treated separately to calculate the resulting stresses. It depends on the sample, which contributions are dominant and which models have to be applied. An example where the individual stress contributions have been calculated can be found in Chapter 8.

3.3 Atomic Force Microscopy

3.3.1 General Setup

Nanomechanical characterization requires the precise measurement of forces and deformations on the nanoscale. This can be achieved using the *Atomic Force Microscope* (AFM). It was introduced in 1986 by *Binnig, Quate* and *Gerber*.⁹³ Although it was originally based on the setup of the *Scanning Tunneling Microscope* (STM),⁹⁴ the principle of the AFM is to use the deflection of a spring as a measure of the acting forces. Today, AFM has become one of the most versatile and most commonly applied methods for investigating objects and forces on the nanoscale.^{95,96} A major advantage over electron microscopy is that measurements can be performed under ambient conditions in air and even in (aqueous) solvents. On the downside, the investigation is limited to the sample surface. A typical setup is illustrated in Figure 3.6.

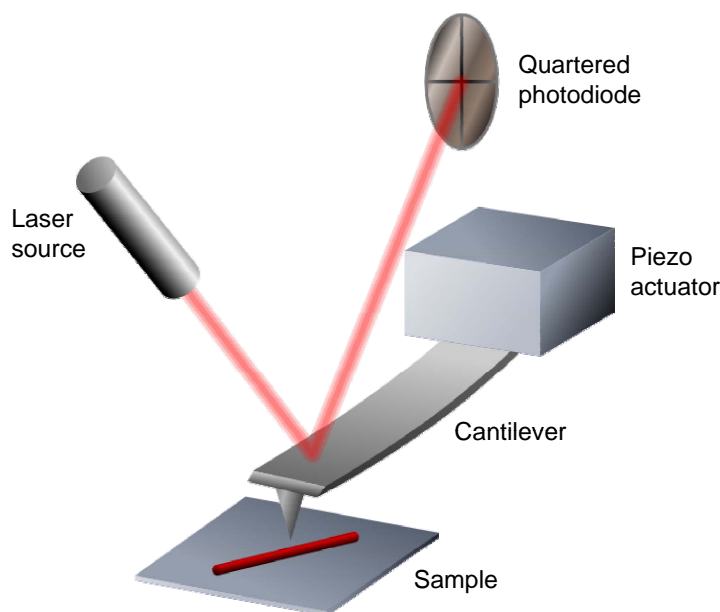


Figure 3.6 Illustration of a typical AFM setup.

All techniques which can be summarized as *scanning probe microscopy* (SPM)⁹⁷ are based on the interaction of the sample with a probe. As the name implies, AFM is used to measure forces. They can be of diverse nature (see 3.3.3) and either attractive or repulsive.^{74,98} The probe is commonly a sharp Si or Si₃N₄ tip or a colloidal glass

bead which is attached to a cantilever spring. Any interactions will lead to a deflection of the cantilever, which is commonly measured with the *optical lever* method.⁹⁸ Here, a laser beam is focused on the backside of the cantilever and reflected to a *quartered photo diode* which serves as position sensor. Deflection of the cantilever leads to a change of intensities in the individual quarters which is used to calculate the *vertical* and *lateral deflection*. The *x*-, *y*- and *z*-movement of the probe relative to the sample is controlled by piezo actuators. In many cases, an optical microscope is integrated into the setup to facilitate positioning of the laser beam on the cantilever and which allows monitoring the sample during measurements.

3.3.2 Imaging

The most widely-used application of AFM is imaging small scale samples. The simplest approach is bringing the cantilever into contact with the sample (*contact mode*) and either recording the deflection directly (*constant height*) or keeping it constant by using a feedback-loop (*constant force*) and processing the feedback signal into an image. Beyond that, dynamic approaches like the *intermittent contact mode* have become especially relevant for imaging soft samples, since minimizing the contact between tip and sample (and thereby especially shear forces) allows preventing damage and increasing resolution.^{95,99}

There are two important drive modes for dynamic measurements:⁹⁹ Most measurements in air or liquids use *amplitude modulation*. Here, the cantilever is excited near its resonant frequency and the oscillation amplitude is kept constant by a feedback loop.¹⁰⁰ In addition to the height image, the phase shift of the oscillation can be used to evaluate the energy dissipation,¹⁰¹ which also allows drawing conclusions about the mechanical properties of the sample.⁹⁹ In *frequency modulation*, the shift of the resonance frequency is recorded.¹⁰² This mode is often used for measurements in ultra-high vacuum and can probe the repulsive regime of the tip-sample interaction.

The resolution of scanning probe techniques is not limited by diffraction as in optical microscopy. Instead, the geometry of the probe limits the quality of the image. *Convolution* of the sample and the tip geometry becomes a considerable issue for samples with lateral dimensions in the same order of magnitude as the cantilever tip radius (which is typically around 10 nm). Therefore, there are ongoing efforts to correct AFM images for convolution effects.^{103,104}

3.3.3 Force Measurements

A fundamental capability of AFM is the detection and measurement of forces on the nanoscale, often referred to as *force spectroscopy*.⁷⁴ Typical examples include electrostatic forces, van der Waals forces, steric forces and capillary forces. There are numerous review articles and textbooks that explain the theories of intermolecular, interparticle and interfacial forces as well as the interpretation of the corresponding AFM measurements.^{74,105,106} In addition, *single molecule force spectroscopy* allows the measurement of molecular interactions¹⁰⁷ and protein mechanics¹⁰⁸ by attaching one or several molecules to the probe (which can also happen randomly simply by adhesion when approaching the sample until contact and retracting) and evaluating the forces involved in detachment, unfolding and rupture.

Furthermore, also the continuum mechanical properties of the sample can be investigated, which will be the focus of this thesis. Prominent examples include biological samples (which immensely profit from the AFM's capability to measure in liquids) and polymeric thin films.^{84,109} In many of these approaches, the AFM is used as a device for sensitive indentation measurements (see also Section 3.1.4).

In force spectroscopy experiments, the force is typically measured as a function of the piezo displacement in the z -direction Z (*force-displacement curve*). In order to calculate the true distance D between probe and sample, the deflection of the cantilever δ_c and the deformation of the sample δ_s have to be taken into account.⁷⁴

$$D = Z - (\delta_c + \delta_s) \quad (3.25)$$

The continuum mechanical properties of samples are measured in the contact regime ($D = 0$). Therefore, Equation 3.25 can be simplified and rewritten to express the force as a function of the sample deformation (*force-deformation curve*). To calculate the deflection of the cantilever, it can be treated as a Hookean spring:

$$\delta_c = \frac{F}{k_c} \quad (3.26)$$

The result is:

$$\delta_s = Z - \frac{F}{k_c} \quad (3.27)$$

Instead of using the slope of the force-deformation curve, the stiffness of the sample can also be directly evaluated with a model of coupled springs.^{37,110}

$$\frac{1}{k_t} = \frac{1}{k_s} + \frac{1}{k_c} \quad (3.28)$$

Here, k_s is the stiffness of the sample and k_t is the coupled stiffness which is equal to the slope of the force-displacement curve. Solving Equation 3.28 for k_s leads to:

$$k_s = \frac{k_c k_t}{k_c - k_t} \quad (3.29)$$

3.3.4 Calibration

For a quantitative evaluation of AFM force measurements, the photodiode signal (PDS) has to be converted to an actual force. The *calibration* usually involves two steps as depicted in Figure 3.7: First, the signal in volt is converted to an actual deflection of the cantilever in nm using the *inverse optical lever sensitivity* (InvOLS), the ratio of cantilever deflection to photodiode signal. The sensitivity is obtained from the slope in the constant compliance regime of a force curve on a hard substrate.⁷⁴

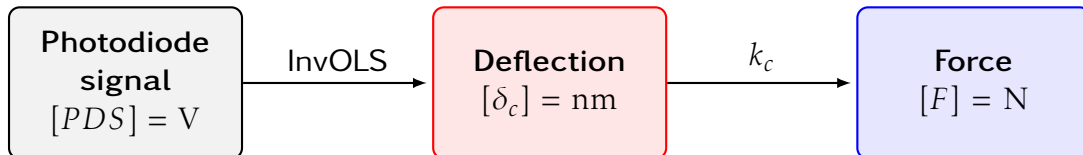


Figure 3.7 The typical steps of the AFM force measurement calibration.

While the spring constant of the cantilever can in principle be calculated from its geometry, it requires precise knowledge of its plan dimensions, its thickness and especially of the material properties and is therefore susceptible to error.⁷⁴ As a consequence, a variety of more sophisticated approaches have been developed which shall only be briefly summarized here. The *thermal noise* method uses thermal fluctuations to determine the cantilever's spring constant, resonant frequency, and the quality factor Q_f , which provides information concerning the dampening.¹¹¹ The method introduced by *Sader et al.*¹¹² has undergone several improvements and now only relies on the resonant frequency, the quality factor and the plan dimensions of the cantilever.^{113,114} The method proposed by *Cleveland et al.* determines the

spring constant of the cantilever by measuring the resonant frequency before and after adding a small mass to the end of the cantilever.¹¹⁵

3.3.5 Lateral Force Microscopy

Regular AFM force measurements are carried out in the direction perpendicular to the surface. In addition, it is also possible to perform measurements parallel to the surface, where the photodiode detects the lateral deflection of the cantilever. This is often called *lateral force microscopy* (LFM) and was first employed by *Mate* et al. to study the friction force of a tungsten tip on a graphite surface.¹¹⁶ One of the main applications of LFM is nanotribology, i.e., the investigation of friction, lubrication and wear on the nanoscale.¹¹⁷ The general setup is shown in Figure 3.8. The application of lateral deformations for bending experiments will be discussed in Chapter 8.

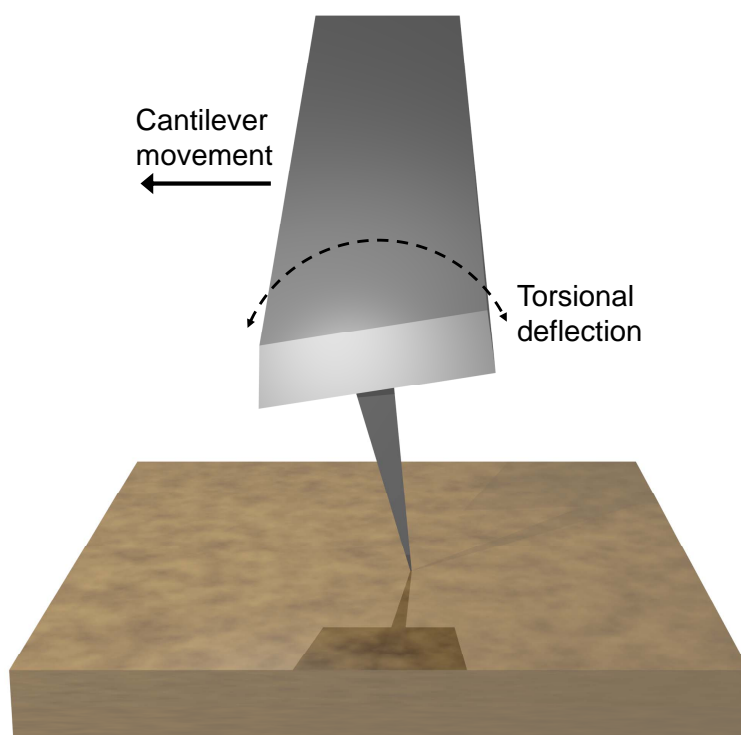


Figure 3.8 Schematic LFM setup.

One major limitation of LFM is that the calibration is more complicated and less precise than for the vertical setup. As in regular force spectroscopy experiments, it normally consists of two steps: First, the photodiode signal in volt is converted into a displacement of the cantilever tip in nm using the lateral optical lever sensitivity.

The actual forces can be calculated from this deflection with knowledge of the lateral spring constant. Alternatively, a conversion factor is determined that allows to directly calculate the force from the signal in volt. To date, there are many different approaches in the literature, but in contrast to vertical experiments, there is no standard technique for a successful and reliable calibration, as even the best approaches involve uncertainties of around 50%. A very comprehensive review on lateral force calibration was recently published by *Munz*.¹¹⁸

Special care should be taken concerning the terminology, in particular the use of the terms *lateral* and *torsional*. This work follows the terminology of *Munz*¹¹⁸ where *torsional sensitivity* and *torsional spring constant* refer to an angular torsion of the cantilever in rad, whereas *lateral sensitivity* and *lateral spring constant* refer to an actual displacement of the cantilever tip in nm (see also Figure 3.9).

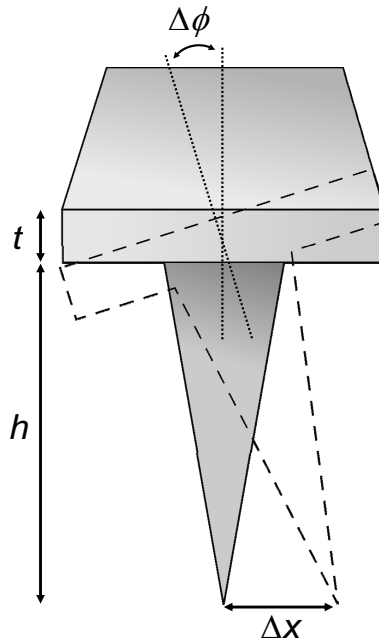


Figure 3.9 Definition of the important quantities for LFM.

The torsional angle $\Delta\phi$ and the lateral displacement Δx are related through the lever arm H of the cantilever:

$$\Delta x = H\Delta\phi \quad (3.30)$$

In a regular LFM setup (e.g., for friction measurements), it is defined as the tip length h plus half of the cantilever thickness t :

$$H = h + \frac{t}{2} \quad (3.31)$$

Depending on the experimental setup, the calculation of the lever arm can be more complicated for bending experiments (see Chapter 8). In summary, the important quantities for LFM are defined as:

Torsional sensitivity: S_ϕ	$\Delta V_\phi = S_\phi \Delta\phi$	$[S_\phi] = \text{Vrad}^{-1}$
Lateral sensitivity: S_x	$\Delta V_\phi = S_x \Delta x$	$[S_x] = \text{Vnm}^{-1}$
Lateral spring constant: k_x	$F_{\text{lat}} = k_x \Delta x$	$[k_x] = \text{Nm}^{-1}$

3.4 Finite Element Analysis

The *Finite Element Method* (FEM) is an indispensable tool for engineers and physicists alike and provides a numerical technique for the approximate solution of differential equations. Therefore, it can be applied to virtually *all* sorts of physical problems like heat transfer, electrical and magnetic fields, fluid flow, and acoustic problems, to name just a few. However, its origin and also its main application in this thesis is the analysis of structural mechanics. Especially in this context, it is often termed *Finite Element Analysis* (FEA). Section 3.4.1 is supposed to provide a very brief introduction into the basic principles of FEA and focuses solely on elasticity theory. It is mainly based on the books by Rieg et al.¹¹⁹ and Henwood et al.,¹²⁰ as well as on the Abaqus 6.11 user manual.¹²¹ In addition, Section 3.4.2 provides a short overview of nanofiber studies in the literature that employed the FEM.

3.4.1 An Introduction to the Finite Element Method

Implicit methods

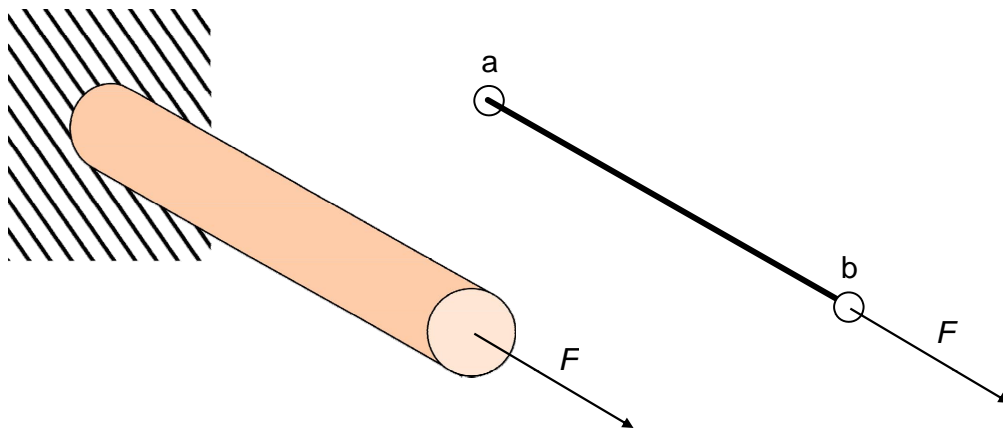


Figure 3.10 A rod with a fixed end and an applied load on the other end and its FE representation as one truss element with two nodes.

A simple yet illustrative example to demonstrate the principle concept of FEA is a rod that is firmly fixed on one end and to which a load is applied on the other end (Figure 3.10). Such a problem can be modeled using a *truss element* with two *nodes*, *a* and *b*. The *external force* *F* will lead to internal stresses and therefore to an *internal*

force F_{int} . For small deformations of a linear elastic material, it can be calculated according to Hooke's law:

$$F_{\text{int}} = \sigma A = EA\epsilon = EA \frac{u_b - u_a}{L} \quad (3.32)$$

The expression $\frac{EA}{L}$ is called the *elemental stiffness* K . In equilibrium, the external forces acting on each node must be balanced out by internal forces. This equilibrium condition can be written as:

$$F_a = Ku_a - Ku_b \quad (3.33)$$

$$F_b = Ku_b - Ku_a \quad (3.34)$$

The same equation system can be written in matrix form as

$$\begin{Bmatrix} F_a \\ F_b \end{Bmatrix} - \begin{bmatrix} K & -K \\ -K & K \end{bmatrix} \begin{Bmatrix} u_a \\ u_b \end{Bmatrix} = 0 \quad (3.35)$$

The expression

$$\begin{bmatrix} K & -K \\ -K & K \end{bmatrix}$$

is called *element stiffness matrix* (ESM) for an individual element or *global stiffness matrix* (GSM) if multiple elements are present. To illustrate this, let us extend the modeling of the rod under tension to two truss elements with a total of three nodes a , b , and c . The equilibrium condition can then be written as

$$\begin{Bmatrix} F_a \\ F_b \\ F_c \end{Bmatrix} - \begin{bmatrix} K_1 & -K_1 & 0 \\ -K_1 & (K_1 + K_2) & -K_2 \\ 0 & -K_2 & K_2 \end{bmatrix} \begin{Bmatrix} u_a \\ u_b \\ u_c \end{Bmatrix} = 0 \quad (3.36)$$

When all elements are of equal elemental stiffness, the GSM in Equation (3.36) can be rewritten as

$$\begin{Bmatrix} F_a \\ F_b \\ F_c \end{Bmatrix} - \left(\frac{EA}{L} \right) \begin{bmatrix} 1 & -1 & 0 \\ -1 & 2 & -1 \\ 0 & -1 & 1 \end{bmatrix} \begin{Bmatrix} u_a \\ u_b \\ u_c \end{Bmatrix} = 0 \quad (3.37)$$

Most FEA programs first determine the displacements u_i by simultaneously solving the equation system (3.36). Once the displacements are known, the internal forces (i.e. stresses) are calculated.

No matter how complicated the FE model, this *implicit* approach for structural mechanical analysis is always comparable and can be summarized as follows:¹¹⁹

1. Definition of the FE structure
2. Calculation of the ESMs
3. Generating the GSM by addition of the individual ESMs (*compilation*)
4. Definition of the boundary conditions (forces, constraints, displacements, etc.)
5. Iterative solution of the equation system yields the displacements u_i of the individual nodes
6. Calculation of the internal forces and stresses

Implicit approaches are also capable of solving nonlinear problems. For that purpose, the total prescribed displacements, loads, etc., are divided into multiple steps (*incrementation*) and a solution is calculated for each step. Since the size of the increments of course affects the outcome of the simulation, it is important to choose proper algorithms for the (adaptive) incrementation. However, discussion of these algorithms is beyond the scope of this work.

Explicit Methods

Although they were not applied in this thesis, *explicit dynamic methods* should also be briefly mentioned here. Instead of solving the whole equation system at once, they calculate the propagation of a *stress wave* over several time increments. To illustrate this, let us again consider the rod under tension, but now with three elements (Figure 3.11). In the first time increment, the concentrated load leads to an acceleration $\frac{d^2 u_a}{dt^2}$ and a velocity $\frac{du_a}{dt}$ of node a , which in turn leads to a strain rate $\frac{d\epsilon_A}{dt}$ in element A . The total strain can be calculated by integrating the strain rate through the time.

The other nodes do not move since there are no forces acting on them in the first increment.

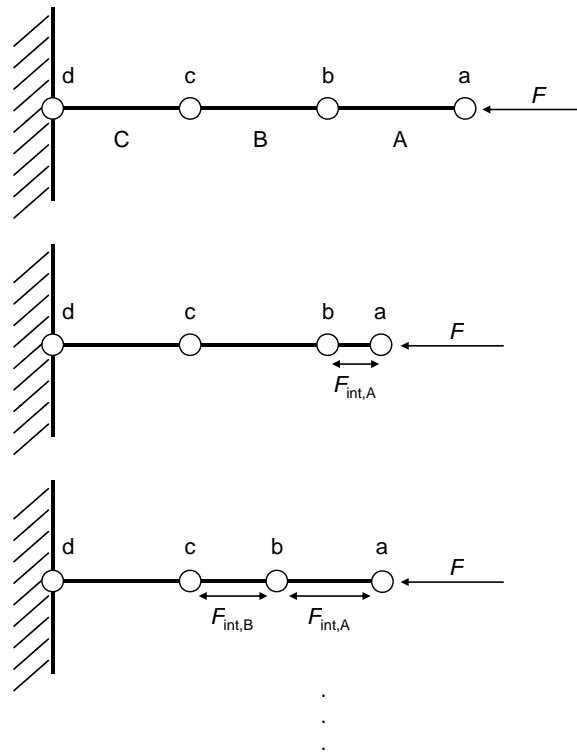


Figure 3.11 Illustration of an explicit FEA model at the beginning of the first, second, and third time increment.

In the second increment, the stresses resulting from the strain ϵ_A in the first increment result in internal forces on the nodes of element *A*. These stresses are used to calculate a dynamic equilibrium of nodes *a* and *b*. This now also leads to stresses in element *B*. The whole process is continued until the desired total time is reached.

This example shows the main difference between implicit and explicit methods. While implicit methods attempt a simultaneous solution of the whole equation system, explicit methods consecutively calculate the dynamic equilibrium for each element over defined time increments. Therefore, explicit approaches are especially well suited to calculate dynamic or highly nonlinear problems.

3.4.2 Finite Element Analysis for Nanofibers

In terms of computational methods, the nanoscale lies in the border region of what can be described with large atomistic and molecular models, respectively, and con-

tinuum models like FEA.¹²² An important topic is the relation between microstructure and mechanical properties. For example, the results from atomistic or molecular dynamics simulations can be used to model coarse-grained structural elements like springs.¹²³ FE models can then be used to simulate the behavior of these structural elements and also bridge the gap to the macroscopic properties without necessarily assuming a complete continuum.^{123,124}

In the field of nanofibers and comparable 1D-objects, FEA was for example used to study design criteria for MEMS/NEMS devices,¹²⁵ the deformation of cellulose nanocrystals,^{126,127} and temperature effects on the elastic properties of SWCNTs.¹²⁸ In several cases, FE models were also used as a complementary tool for bending measurements on metal and metaloxide nanowires,^{49,58,129–131} CNTs,^{132–134} microtubules,¹³⁵ amyloid fibrils,¹³⁶ and to study the bending mechanics of cytoskeletal bundles.¹³⁷

In general, FE simulations can provide valuable information when studying objects on a small scale, since they allow investigating parameters that are otherwise not accessible on such a small scale. However, when applied in a continuum mechanical approach, the limitations (concerning, e.g., surface effects and thermal fluctuations) have to be kept in mind for small objects (see also 3.1.2).⁷

3.5 Fibers Based on 1,3,5-Benzenetrisamides

3.5.1 Self-assembly of 1,3,5-Benzenetrisamides

Alkyl substituted 1,3,5-benzenetrisamides (BTAs) are a very exciting class of molecules that show a remarkable self-assembly behavior. Due to the resulting exceptional physical properties (see Section 3.5.3), their self-assembly and structural aspects have recently attracted increasing research interest.^{138–140} Supramolecular BTA architectures consist of helical columnar stacks with enormous aspect ratios.^{141,142} In general, the self-assembly of BTAs from solution into an ordered 1D structure is governed by the three well-defined intermolecular hydrogen bonds between the amide groups of adjacent molecules.^{141,143,144} However, the molecular structure offers manifold possibilities to further influence the self-assembly behavior and tailor the structure and the properties and there are ongoing efforts using advanced spectroscopy techniques to characterize their structure and also its influence when used as a nucleating agent.^{145,146} The two essential aspects, the connectivity of the amide groups to the central core and the constitution of the peripheral alkyl groups, will be discussed in the following.

There is a difference between BTAs based on trimesic acid (A) and 1,3,5-triaminobenzene (B, see Figure 3.12). According to *Wegner et al.*, all amide functions of type A are pointing in the same direction, which leads to helically arranged, strong hydrogen-bonds.¹⁴⁷ They also found that the hydrogen bond length in columns formed by type B are longer and hence weaker than in type A. This was also supported by *Albuquerque et al.*, who found that the inverse connectivity of the amide group in type B increases the planarization within the monomer unit compared to type A, introduces asymmetry, and decreases the macrodipole.¹⁴⁸ In addition, solid state NMR experiments combined with Car-Parrinello Molecular Dynamics simulations showed that the amide functions within the column of B can be asymmetrically arranged, which further weakens the aggregation.¹⁴⁷ However, *Schmidt et al.* demonstrated that there are also trisamides of type B where all carbonyl groups point in the same direction.¹⁴⁵

The constitution of the peripheral alkyl groups also influences the self-assembly behavior and solid-state properties.¹⁴⁹ For example, BTAs based on A with linear alkyl substituents show discotic liquid crystalline behavior when the chain length exceeds C_6 .^{150–154} In addition, it was found that branched side chains lead to a stabilization

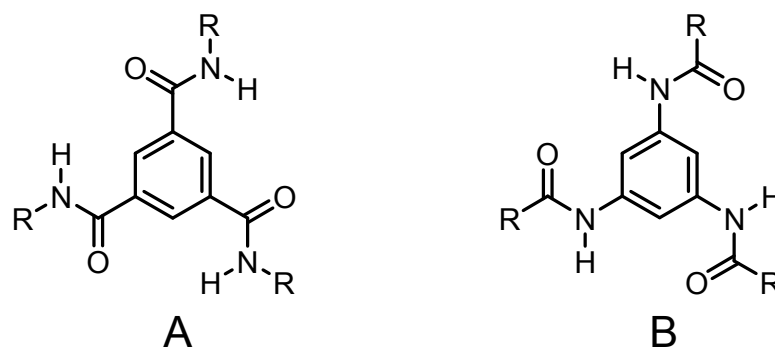


Figure 3.12 The chemical structure of trisamides based on trimesic acid (A) and 1,3,5-triaminobenzene (B).

of the aggregation.^{149,154} *Stals* et al. found that BTAs based on B only show thermotropic liquid crystalline behavior with chiral substituents.¹⁴⁴

3.5.2 Electrospinning of Trisamides

Recently, *Singer* et al. discovered that BTAs can also be shaped into fibrous structures using melt electrospinning.¹⁵⁵ Electrospinning is a typical top-down technique for the formation of polymer fibers, and is especially well-suited for the preparation of thin fibers (with diameters ranging from several nanometers to a few micrometers) from solutions and melts.^{156–158} Other common top-down techniques are melt blow spinning^{159,160} and centrifugal spinning.¹⁶¹

A review about the principles of electrospinning and its applications was recently published by *Greiner* et al.¹⁵⁶ The setup consists of a thin nozzle through which the polymer solution or melt is pumped (see Figure 3.13). At the same time, the nozzle serves an electrode, through which charges are induced in the liquid to create a strong electric field (typically 100–500 kV m⁻¹). The collector plate for the fibers is connected to the counter electrode. When a drop of liquid is pressed through the nozzle, the applied potential induces a cone-shaped deformation of the drop towards the counter electrode, the so-called Taylor cone.¹⁶² When the electrostatic repulsive forces within the cone's surface overcome the surface tension, a jet of liquid shoots out towards the counter electrode and forms fibers on its way by the evaporation of the solvent or solidifying of the melt.^{163,164} Although it may seem at first glance like a straightforward and simple technique, electrospinning is highly complex due to the interplay of several physical instability processes during jet formation.^{164–167}

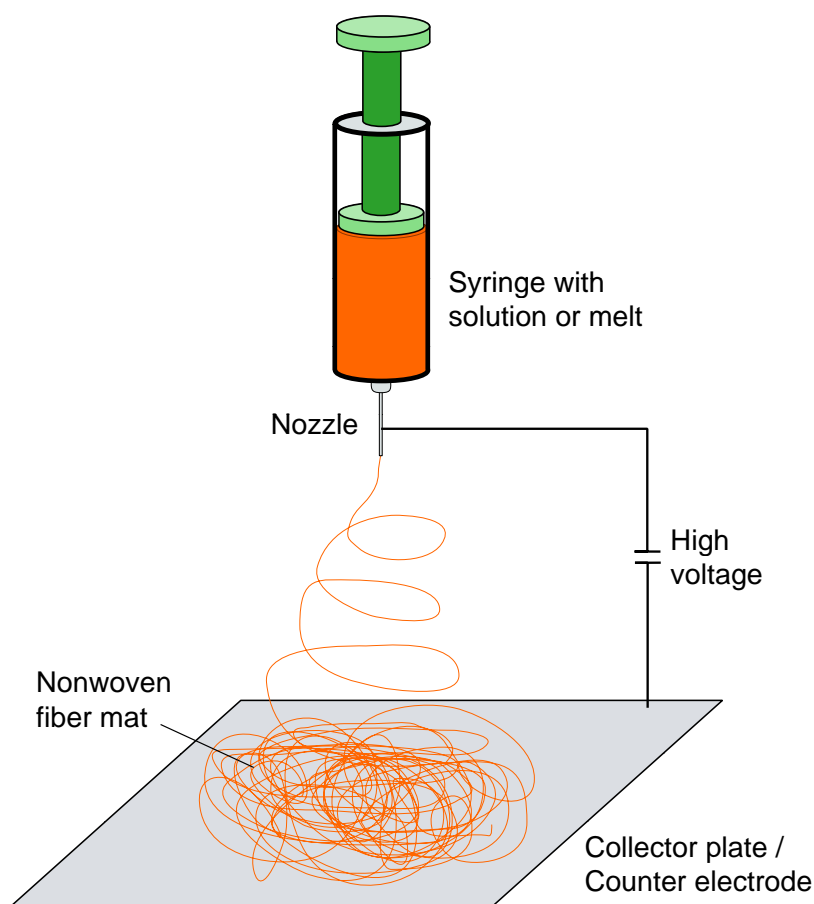


Figure 3.13 Sketch of a typical electrospinning setup.

In the case of polymers, chain entanglements prevent the jet from breaking up into individual droplets as often observed for low molecular weight substances (*electrospraying*). However, a high molecular weight is not a mandatory prerequisite for electrospinning, as long as strong intermolecular interactions are present and sufficient for stabilizing the jet.^{168,169} Therefore, the ability of trisamides to form macrodipoles during their supramolecular organization in an external electric field makes them promising precursors for electrospinning.^{170–172} In addition, as explained in Section 3.5.1, trisamide melts can show a complex mesophase behavior.^{147,149,154,155} Singer et al. utilized this effect and demonstrated that fibers of self-assembling 1,3,5-benzenetrisamides can be melt electrospun from the nematic liquid crystalline phase and even from the optical isotropic melt.¹⁵⁵ Exemplary morphologies of self-assembled and electrospun trisamide fibers can be seen in Figure 3.14.

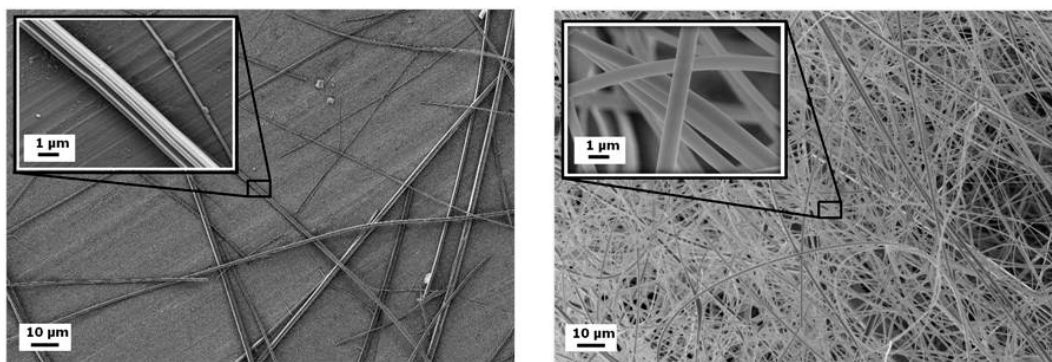


Figure 3.14 Exemplary morphologies of trisamide fibers formed by self-assembly (left) and electrospinning (right) using the same starting compound (see Chapter 6).¹⁷³

3.5.3 Applications of Trisamides

BTAs are a highly versatile class of molecules and have been the focus of numerous scientific studies. They are probably best known and also commercially used as additives for polymers, for example as nucleating agents and/or clarifiers for polyvinylidene fluoride¹⁷⁴ and isotactic polypropylene (*i*-PP).^{138,175–177} Beyond that, they also show a large number of exceptional physical properties that can directly be attributed to their remarkable self-assembly behavior. This makes them highly interesting for the design of novel materials with an extremely wide variety of possible applications.¹⁴⁰

The trivalent interactions allow BTAs to act as supports for various kinds of ligands and subsequent aggregation then leads to polyvalent molecular wires.¹⁷⁸ For example, BTAs were used as scaffolds to connect bioactive units with flexible linkers for potential biomedical applications.^{178–180} They were also successfully employed in gadolinium-based contrast agents for magnetic resonance imaging (MRI).¹⁸¹ Furthermore, BTAs with suitable side chains can lead to interpenetrating metal organic frameworks (MOFs) upon complexation with metal ions.¹⁴⁰

While in those cases, the BTAs were more used as a means to an end, there have also been studies of materials where the BTAs themselves play a more dominant role. For example, it is possible to obtain aggregates that show a remnant polarization and a high surface potential.¹⁴⁰ It has been demonstrated that BTAs are able to improve the properties of electret materials.^{182–186} The possibility to form macrodipoles makes them interesting for organic thin film transistors, photovoltaic cells and OLEDs.^{148,187}

Focusing more on their self-assembly properties, acid-modified BTAs were also combined with polypropylene imine dendrimers to form liquid crystalline materials with a well-ordered superlattice that may become interesting as mesoporous membranes with selective transport properties.¹⁸⁸ In addition, they allow the thermoreversible physical gelation of a variety of organic solvents,^{153,189–192} and also hydrogelation^{193–196}

A question that has lately become relevant is whether it is possible to prepare mechanically stable BTA-based materials. There have been studies on their formation of supramolecular materials, whether on their own,¹⁹⁷ or by end-capping or copolymerizing the BTAs with low-molecular weight telechelic polymers.^{142,197} In addition, *Misslitz* et al. demonstrated the possibility to use supramolecular nanofiber webs in nonwoven scaffolds for air filtration.¹⁹⁸ This approach has several potential benefits: First of all, self-assembly of the nanofiber web inside the support opens up the pathway from surface filtration to volume filtration. Second, the thermoreversible assembly of the nanofibers is a promising approach for allowing a simple release of the residue and regeneration of the filter.

Although their mechanical properties play a crucial role for such applications, there have been no comprehensive mechanical studies of individual BTA nanofibers to this date. Therefore, the nanomechanical characterization techniques presented within this thesis have been applied to numerous trisamide fibers consisting of different core structures, substituents (see Figure 3.15) and prepared by self-assembly and electrospinning. A complete overview of the trisamide fibers studied in this work can be found in Table 3.1. This provided the possibility to characterize the nanomechanical properties of the individual supramolecular aggregates and to determine whether, and how, influencing the self-assembly behavior via the core structure and substituents, or changing the preparation route completely to electrospinning, will affect the mechanics.

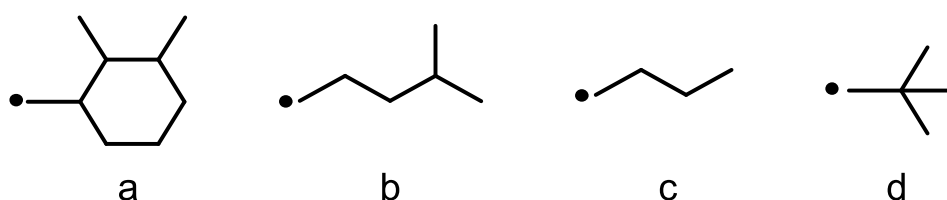


Figure 3.15 Trisamide substituents investigated within this thesis.

The previous sections have demonstrated that BTAs offer the exceptional possibility to combine all advantages of top-down (electrospinning) and bottom-up (self-

Table 3.1 Overview of the trisamides investigated within this thesis.

Core type	Substituent	Preparation	Discussed in Chapter
A	2,3-dimethyl-cyclohexyl (a)	self-assembly	5,8
A	3-methylbutyl (b)	self-assembly	5
A	propyl (c)	self-assembly	6
A	propyl (c)	electrospinning	6
B	<i>tert</i> -butyl (d)	self-assembly	4,5,8

assembly) techniques for fiber formation. As a consequence, they allow unprecedented structural control on all levels of hierarchy from the molecular structure to the single fibers and fiber fleeces. The BTAs combine this feature with outstanding physical and chemical properties that make them highly interesting for a wide range of applications. Understanding their mechanical properties is another essential step towards the tailored design of novel BTA-based materials.

3.6 References

- [1] J. R. Withers, D. E. Aston, *Advances in Colloid and Interface Science* **2006**, *120*, 57–67.
- [2] D. E. Aston, J. R. Bow, D. N. Gangadean, *International Materials Reviews* **2013**, *58*, 167–202.
- [3] E. P. S. Tan, C. T. Lim, *Composites Science and Technology* **2006**, *66*, 1102–1111.
- [4] S.-K. Kim, H. Lee in *Applied Scanning Probe Methods IX*, (Eds.: M. Tomitori, B. Bhushan, H. Fuchs), Nano Science and Technology, Springer Berlin Heidelberg, **2008**, Chapter 12, pp. 311–328.
- [5] G. Y. Jing, H. L. Duan, X. M. Sun, Z. S. Zhang, J. Xu, Y. D. Li, J. X. Wang, D. P. Yu, *Physical Review B* **2006**, *73*, 235409.
- [6] J. He, C. M. Lilley, *Applied Physics Letters* **2008**, *93*, 263108.
- [7] C. Li, Z. J. Zheng, J. L. Yu, C. W. Lim, *Acta Mechanica Sinica* **2011**, *27*, 713–719.
- [8] W. Xu, P. J. Mulhern, B. L. Blackford, M. H. Jericho, I. Templeton, *Scanning Microscopy* **1994**, *8*, 499–506.
- [9] J. P. Salvetat, J. M. Bonard, N. H. Thomson, A. J. Kulik, L. Forro, W. Benoit, L. Zuppiroli, *Applied Physics A - Materials Science & Processing* **1999**, *69*, 255–260.
- [10] J. P. Salvetat, G. A. D. Briggs, J. M. Bonard, R. R. Bacsa, A. J. Kulik, T. Stockli, N. A. Burnham, L. Forro, *Physical Review Letters* **1999**, *82*, 944–947.
- [11] T. W. Tombler, C. W. Zhou, L. Alexseyev, J. Kong, H. J. Dai, L. Lei, C. S. Jayanthi, M. J. Tang, S. Y. Wu, *Nature* **2000**, *405*, 769–772.
- [12] A. E. Tanur, J. Wang, A. L. Reddy, D. N. Lamont, Y. K. Yap, G. C. Walker, *J Phys Chem B* **2013**, *117*, 4618–25.
- [13] A. San Paulo, J. Bokor, R. T. Howe, R. He, P. Yang, D. Gao, C. Carraro, R. Maboudian, *Applied Physics Letters* **2005**, *87*, 053111.
- [14] W. J. Mai, Z. L. Wang, *Applied Physics Letters* **2006**, *89*, 073112.
- [15] Y. X. Chen, B. L. Dorgan, D. N. Mcilroy, D. E. Aston, *Journal of Applied Physics* **2006**, *100*, 104301.
- [16] Y. X. Chen, I. Stevenson, R. Pouy, L. D. Wang, D. N. Mcilroy, T. Pounds, M. G. Norton, D. E. Aston, *Nanotechnology* **2007**, *18*, 135708.
- [17] V. Cimalla, C. C. Rohlig, J. Pezoldt, M. Niebelschutz, O. Ambacher, K. Bruckner, M. Hein, J. Weber, S. Milenkovic, A. J. Smith, A. W. Hassel, *Journal of Nanomaterials* **2008**.
- [18] H. Zhang, J. Tang, L. Zhang, B. An, L. C. Qin, *Applied Physics Letters* **2008**, *92*, 173121.

- [19] X. W. Deng, V. R. Joseph, W. J. Mai, Z. L. Wang, C. F. J. Wu, *Proceedings of the National Academy of Sciences of the United States of America* **2009**, *106*, 11845–11850.
- [20] C. C. Röhlig, M. Niebelschutz, K. Brueckner, K. Tonisch, O. Ambacher, V. Cimalla, *Physica Status Solidi B-Basic Solid State Physics* **2010**, *247*, 2557–2570.
- [21] B. Varghese, C. H. Sow, C. T. Lim, *Nanoscience and Nanotechnology Letters* **2010**, *2*, 268–281.
- [22] Y.-J. Kim, K. Son, I.-C. Choi, I.-S. Choi, W. I. Park, J.-I. Jang, *Advanced Functional Materials* **2011**, *21*, 279–286.
- [23] A. Kis, S. Kasas, B. Babic, A. J. Kulik, W. Benoit, G. A. D. Briggs, C. Schonenberger, S. Catsicas, L. Forro, *Physical Review Letters* **2002**, *89*, 248101.
- [24] A. J. Heim, T. J. Koob, W. G. Matthews, *Biomacromolecules* **2007**, *8*, 3298–3301.
- [25] L. Yang, C. F. C. Fitie, K. O. V. D. Werf, M. L. Bennink, P. J. Dijkstra, J. Feijen, *Biomaterials* **2008**, *29*, 955–962.
- [26] L. Yang, K. O. V. D. Werf, C. F. C. Fitie, M. L. Bennink, P. J. Dijkstra, J. Feijen, *Biophysical Journal* **2008**, *94*, 2204–2211.
- [27] D. R. Stamov, T. A. K. Nguyen, H. M. Evans, T. Pfohl, C. Werner, T. Pompe, *Biomaterials* **2011**, *32*, 7444–7453.
- [28] C. Guzman, S. Jeney, L. Kreplak, S. Kasas, A. J. Kulik, U. Aebi, L. Forro, *Journal of Molecular Biology* **2006**, *360*, 623–630.
- [29] L. Kreplak, H. Herrmann, U. Aebi, *Biophysical Journal* **2008**, *94*, 2790–2799.
- [30] J. F. Smith, T. P. J. Knowles, C. M. Dobson, C. E. Macphee, M. E. Welland, *Proceedings of the National Academy of Sciences of the United States of America* **2006**, *103*, 15806–15811.
- [31] G. Guhados, W. K. Wan, J. L. Hutter, *Langmuir* **2005**, *21*, 6642–6646.
- [32] Q. Cheng, S. Wang, *Composites Part A: Applied Science and Manufacturing* **2008**, *39*, 1838–1843.
- [33] S. Iwamoto, W. H. Kai, A. Isogai, T. Iwata, *Biomacromolecules* **2009**, *10*, 2571–2576.
- [34] G. Huber, S. Orso, R. Spolenak, U. G. K. Wegst, S. Enders, S. N. Gorb, E. Arzt, *International Journal of Materials Research* **2008**, *99*, 1113–1118.
- [35] E. P. S. Tan, C. T. Lim, *Applied Physics Letters* **2004**, *84*, 1603–1605.
- [36] S. Y. Gu, Q. L. Wu, J. Ren, G. J. Vancso, *Macromolecular Rapid Communications* **2005**, *26*, 716–720.
- [37] S. Shanmugham, J. W. Jeong, A. Alkhateeb, D. E. Aston, *Langmuir* **2005**, *21*, 10214–10218.

- [38] M. K. Shin, S. I. Kim, S. J. Kim, S.-K. Kim, H. Lee, *Applied Physics Letters* **2006**, *88*, 193901–3.
- [39] X. Y. Ling, I. Y. Phang, W. Maijenburg, H. Schonherr, D. N. Reinhoudt, G. J. Vancso, J. Huskens, *Angewandte Chemie-International Edition* **2009**, *48*, 983–985.
- [40] X. Y. Ling, I. Y. Phang, H. Schonherr, D. N. Reinhoudt, G. J. Vancso, J. Huskens, *Small* **2009**, *5*, 1428–1435.
- [41] A. Heidelberg, L. T. Ngo, B. Wu, M. A. Phillips, S. Sharma, T. I. Kamins, J. E. Sader, J. J. Boland, *Nano Letters* **2006**, *6*, 1101–1106.
- [42] E. W. Wong, P. E. Sheehan, C. M. Lieber, *Science* **1997**, *277*, 1971–1975.
- [43] D. A. Walters, L. M. Ericson, M. J. Casavant, J. Liu, D. T. Colbert, K. A. Smith, R. E. Smalley, *Applied Physics Letters* **1999**, *74*, 3803–3805.
- [44] G. T. Kim, G. Gu, U. Waizmann, S. Roth, *Applied Physics Letters* **2002**, *80*, 1815–1817.
- [45] D. Almecija, D. Blond, J. E. Sader, J. N. Coleman, J. J. Boland, *Carbon* **2009**, *47*, 2253–2258.
- [46] C. R. Carlisle, C. Coulais, M. Guthold, *Acta Biomaterialia* **2010**, *6*, 2997–3003.
- [47] C. R. Carlisle, C. Coulais, M. Namboothiry, D. L. Carroll, R. R. Hantgan, M. Guthold, *Biomaterials* **2009**, *30*, 1205–1213.
- [48] W. Liu, C. R. Carlisle, E. A. Sparks, M. Guthold, *Journal of Thrombosis and Haemostasis* **2010**, *8*, 1030–1036.
- [49] S. Sundararajan, B. Bhushan, *Sensors and Actuators a-Physical* **2002**, *101*, 338–351.
- [50] S. Sundararajan, B. Bhushan, T. Namazu, Y. Isono, *Ultramicroscopy* **2002**, *91*, 111–118.
- [51] T. Namazu, Y. Isono, *Sensors and Actuators a-Physical* **2003**, *104*, 78–85.
- [52] B. Wu, A. Heidelberg, J. J. Boland, *Nature Materials* **2005**, *4*, 525–529.
- [53] B. Wu, A. Heidelberg, J. J. Boland, J. E. Sader, X. M. Sun, Y. D. Li, *Nano Letters* **2006**, *6*, 468–472.
- [54] L. T. Ngo, D. Almecija, J. E. Sader, B. Daly, N. Petkov, J. D. Holmes, D. Erts, J. J. Boland, *Nano Letters* **2006**, *6*, 2964–2968.
- [55] H. Ni, X. D. Li, *Nanotechnology* **2006**, *17*, 3591–3597.
- [56] H. Ni, X. D. Li, H. S. Gao, *Applied Physics Letters* **2006**, *88*, 043108.
- [57] B. Wen, J. E. Sader, J. J. Boland, *Physical Review Letters* **2008**, *101*, 175502.
- [58] C. Zou, G. Jing, D. Yu, Y. Xue, H. Duan, *Physics Letters A* **2009**, *373*, 2065–2070.
- [59] E. Celik, I. Guven, E. Madenci, *Nanotechnology* **2011**, *22*, 155702.

- [60] G. Stan, S. Krylyuk, A. V. Davydov, I. Levin, R. F. Cook, *Nano Letters* **2012**, *12*, 2599–2604.
- [61] M. A. Haque, M. T. A. Saif, *Experimental Mechanics* **2003**, *43*, 248–255.
- [62] M. F. Yu, M. J. Dyer, G. D. Skidmore, H. W. Rohrs, X. K. Lu, K. D. Ausman, J. R. V. Ehr, R. S. Ruoff, *Nanotechnology* **1999**, 244–252.
- [63] M. F. Yu, B. S. Files, S. Arepalli, R. S. Ruoff, *Physical Review Letters* **2000**, *84*, 5552–5555.
- [64] M. F. Yu, O. Lourie, M. J. Dyer, K. Moloni, T. F. Kelly, R. S. Ruoff, *Science* **2000**, *287*, 637–640.
- [65] E. P. S. Tan, C. N. Goh, C. H. Sow, C. T. Lim, *Applied Physics Letters* **2005**, *86*, 073115.
- [66] R. Inai, M. Kotaki, S. Ramakrishna, *Nanotechnology* **2005**, *16*, 208–213.
- [67] S. Y. Chew, T. C. Hufnagel, C. T. Lim, K. W. Leong, *Nanotechnology* **2006**, *17*, 3880–3891.
- [68] E. Zussman, M. Burman, A. L. Yarin, R. Khalfin, Y. Cohen, *Journal of Polymer Science Part B-Polymer Physics* **2006**, *44*, 1482–1489.
- [69] D. Jaeger, J. Schischka, J. Bagdahn, R. Jaeger, *Journal of Applied Polymer Science* **2009**, *114*, 3774–3779.
- [70] M. B. Bazbouz, G. K. Stylios, *Journal of Polymer Science Part B-Polymer Physics* **2010**, *48*, 1719–1731.
- [71] C. L. Pai, M. C. Boyce, G. C. Rutledge, *Polymer* **2011**, *52*, 2295–2301.
- [72] J. Gere, B. Goodno, *Mechanics of Materials*, Cengage Learning, London, 7th ed., **2008**.
- [73] J. Domke, M. Radmacher, *Langmuir* **1998**, *14*, 3320–3325.
- [74] H.-J. Butt, B. Cappella, M. Kappl, *Surface Science Reports* **2005**, *59*, 1–152.
- [75] M. R. Vanlandingham, S. H. Mcknight, G. R. Palmese, J. R. Elings, X. Huang, T. A. Bogetti, R. F. Eduljee, J. W. Gillespie, *Journal of Adhesion* **1997**, *64*, 31–59.
- [76] G. M. Pharr, W. C. Oliver, F. R. Brotzen, *Journal of Materials Research* **1992**, *7*, 613–617.
- [77] W. C. Oliver, G. M. Pharr, *Journal of Materials Research* **2004**, *19*, 3–20.
- [78] J. G. Park, S. H. Lee, B. Kim, Y. W. Park, *Applied Physics Letters* **2002**, *81*, 4625–4627.
- [79] F. Ko, Y. Gogotsi, A. Ali, N. Naguib, H. H. Ye, G. L. Yang, C. Li, P. Willis, *Advanced Materials* **2003**, *15*, 1161–1165.
- [80] E. P. S. Tan, C. T. Lim, *Applied Physics Letters* **2005**, *87*, 123106.
- [81] B. Bhushan, X. D. Li, *International Materials Reviews* **2003**, *48*, 125–164.
- [82] C. A. Schuh, *Materials Today* **2006**, *9*, 32–40.

- [83] D. M. Ebenstein, L. A. Pruitt, *Nano Today* **2006**, *1*, 26–33.
- [84] D. Passeri, M. Rossi, E. Tamburri, M. L. Terranova, *Analytical and Bioanalytical Chemistry* **2013**, *405*, 1463–1478.
- [85] R. D. Kriz, W. W. Stinchcomb, *Experimental Mechanics* **1979**, *19*, 41–49.
- [86] G. Stan, C. V. Ciobanu, P. M. Parthangal, R. F. Cook, *Nano Letters* **2007**, *7*, 3691–3697.
- [87] A. C. Ugural, *Mechanics of Materials*, Wiley-VCH, 1st ed., **2007**.
- [88] D. Kluge, F. Abraham, S. Schmidt, H. W. Schmidt, A. Fery, *Langmuir* **2010**, *26*, 3020–3023.
- [89] S. Cuenot, C. Fretigny, S. Demoustier-Champagne, B. Nysten, *Journal of Applied Physics* **2003**, *93*, 5650–5655.
- [90] D. Gangadean, D. N. Mcilroy, B. E. Faulkner, D. E. Aston, *Nanotechnology* **2010**, *21*, 225704.
- [91] J. M. Gere, S. P. Timoshenko in *Mechanics of Materials*, Chapman & Hall, London, 3rd, **1991**, p. 692.
- [92] W. C. Young, R. G. Budynas, *Roark's Formulas for Stress and Strain*, The McGraw-Hill Companies, Inc., New York, NY, 7th ed., **2002**.
- [93] G. Binnig, C. Quate, C. Gerber, *Physical Review Letters* **1986**, *56*, 930–933.
- [94] G. Binnig, H. Rohrer, *Helvetica Physica Acta* **1982**, *55*, 726–735.
- [95] F. J. Giessibl, *Reviews of Modern Physics* **2003**, *75*, 949–983.
- [96] P. Samori, *Journal of Materials Chemistry* **2004**, *14*, 1353–1366.
- [97] W. A. Hofer, A. S. Foster, A. L. Shluger, *Rev. Mod. Phys.* **2003**, *75*, 1287–1331.
- [98] B. Cappella, G. Dietler, *Surface Science Reports* **1999**, *34*, 1–104.
- [99] R. Garcia, R. Perez, *Surface Science Reports* **2002**, *47*, 197–301.
- [100] Q. Zhong, D. Inniss, K. Kjoller, V. B. Elings, *Surface Science* **1993**, *290*, L688–L692.
- [101] J. P. Cleveland, B. Anczykowski, A. E. Schmid, V. B. Elings, *Applied Physics Letters* **1998**, *72*, 2613–2615.
- [102] T. R. Albrecht, P. Grutter, D. Horne, D. Rugar, *Journal of Applied Physics* **1991**, *69*, 668–673.
- [103] D. Tranchida, S. Piccarolo, R. A. C. Deblieck, *Measurement Science and Technology* **2006**, *17*, 2630–2636.
- [104] A. T. Winzer, C. Kraft, S. Bhushan, V. Stepanenko, I. Tessmer, *Ultramicroscopy* **2012**, *121*, 8–15.
- [105] H. J. Butt, M. Kappl, K. Graf, *Physics and Chemistry of Interfaces*, Wiley-VCH, Berlin, 2nd ed., **2006**.
- [106] J. N. Israelachvili, *Intermolecular and Surface Forces*, Academic Press, San Diego, 3rd ed., **2011**.

- [107] T. Hugel, M. Seitz, *Macromolecular Rapid Communications* **2001**, *22*, 989–1016.
- [108] T. E. Fisher, A. F. Oberhauser, M. Carrion-Vazquez, P. E. Marszalek, J. M. Fernandez, *Trends in Biochemical Sciences* **1999**, *24*, 379–384.
- [109] W. R. Bowen, R. W. Lovitt, C. J. Wright, *Biotechnology Letters* **2000**, *22*, 893–903.
- [110] D. Kunz, E. Max, R. Weinkamer, T. Lunkenbein, J. Breu, A. Fery, *Small* **2009**, *5*, 1816–1820.
- [111] J. L. Hutter, J. Bechhoefer, *Review of Scientific Instruments* **1993**, *64*, 3342–3342.
- [112] J. E. Sader, I. Larson, P. Mulvaney, L. R. White, *Review of Scientific Instruments* **1995**, *66*, 3789–3798.
- [113] J. E. Sader, J. W. M. Chon, P. Mulvaney, *Review of Scientific Instruments* **1999**, *70*, 3967–3969.
- [114] C. P. Green, H. Lioe, J. P. Cleveland, R. Proksch, P. Mulvaney, J. E. Sader, *Review of Scientific Instruments* **2004**, *75*, 1988–1996.
- [115] J. P. Cleveland, S. Manne, D. Bocek, P. K. Hansma, *Review of Scientific Instruments* **1993**, *64*, 403–405.
- [116] C. M. Mate, G. M. McClelland, R. Erlandsson, S. Chiang, *Physical Review Letters* **1987**, *59*, 1942–1945.
- [117] B. Bhushan, J. N. Israelachvili, U. Landman, *Nature* **1995**, *374*, 607–616.
- [118] M. Munz, *Journal of Physics D: Applied Physics* **2010**, *43*, 063001.
- [119] F. Rieg, R. Hackenschmidt, B. Alber-Laukant, *Finite Elemente Analyse für Ingenieure*, Hanser, München, 4th ed., **2012**.
- [120] D. Henwood, J. Bonet, *Finite Elements - a Gentle Introduction*, MacMillan Press Ltd, London, 1st ed., **1996**.
- [121] Abaqus 6.11 Documentation, Dassault Systèmes, **2011**.
- [122] T. P. J. Knowles, M. J. Buehler, *Nature Nanotechnology* **2011**, *6*, 469–479.
- [123] M. Deriu, S. Enemark, M. Soncini, F. Montecvecchi, A. Redaelli, *Journal of Materials Science* **2007**, *42*, 8864–8872.
- [124] H. Tang, M. J. Buehler, B. Moran, *Annals of Biomedical Engineering* **2009**, *37*, 1117–1130.
- [125] B. Bhushan, G. B. Agrawal, *Ultramicroscopy* **2003**, *97*, 495–507.
- [126] R. R. Lahiji, X. Xu, R. Reifengerger, A. Raman, A. Rudie, R. J. Moon, *Langmuir* **2010**, *26*, 4480–4488.
- [127] A. Pakzad, J. Simonsen, P. A. Heiden, R. S. Yassar, *Journal of Materials Research* **2012**, *27*, 528–536.
- [128] X. Chen, X. Wang, B. Y. Liu, *Journal of Reinforced Plastics and Composites* **2009**, *28*, 551–569.

- [129] H. K. Ni, Q. A. Zou, X. Fu, S. Wu, H. Wang, T. Xue, *Chinese Physics Letters* **2010**, *27*, 116801.
- [130] E. Celik, I. Guven, E. Madenci, *Theoretical and Applied Fracture Mechanics* **2011**, *55*, 185–191.
- [131] J. Yvonnet, A. Mitrushchenkov, G. Chambaud, Q. C. He, *Computer Methods in Applied Mechanics and Engineering* **2011**, *200*, 614–625.
- [132] X. Y. Wang, X. Wang, *Composites Part B-Engineering* **2004**, *35*, 79–86.
- [133] X. Guo, A. Y. T. Leung, X. Q. He, H. Jiang, Y. Huang, *Composites Part B-Engineering* **2008**, *39*, 202–208.
- [134] C. Fang, A. Kumar, S. Mukherjee, *Journal of Applied Mechanics - Transactions of the ASME* **2011**, *78*, 034502.
- [135] S. Kasas, A. Kis, B. M. Riederer, L. Forro, G. Dietler, S. Catsicas, *Chemphyschem* **2004**, *5*, 252–257.
- [136] Z. P. Xu, R. Paparcone, M. J. Buehler, *Biophysical Journal* **2010**, *98*, 2053–2062.
- [137] M. Bathe, C. Heussinger, M. Claessens, A. R. Bausch, E. Frey, *Biophysical Journal* **2008**, *94*, 2955–2964.
- [138] M. Kristiansen, P. Smith, H. Chanzy, C. Baerlocher, V. Gramlich, L. Mccusker, T. Weber, P. Pattison, M. Blomenhofer, H.-W. Schmidt, *Crystal Growth & Design* **2009**, *9*, 2556–2558.
- [139] I. A. W. Filot, A. R. A. Palmans, P. A. J. Hilbers, R. A. V. Santen, E. A. Pidko, T. F. A. Greef, *The Journal of Physical Chemistry B* **2010**, *114*, 13667–13674.
- [140] S. Cantekin, T. F. A. D. Greef, A. R. A. Palmans, *Chemical Society Reviews* **2012**, *41*, 6125–6137.
- [141] M. P. Lightfoot, F. S. Mair, R. G. Pritchard, J. E. Warren, *Chemical Communications* **1999**, 1945–1946.
- [142] J. Roosma, T. Mes, P. Leclere, A. R. A. Palmans, E. W. Meijer, *Journal of the American Chemical Society* **2008**, *130*, 1120–1121.
- [143] M. M. J. Smulders, A. P. H. J. Schenning, E. W. Meijer, *Journal of the American Chemical Society* **2008**, *130*, 606–611.
- [144] P. J. M. Stals, J. C. Everts, R. D. Bruijn, I. A. W. Filot, M. M. J. Smulders, R. Martin-Rapun, E. A. Pidko, T. F. A. D. Greef, A. R. A. Palmans, E. W. Meijer, *Chemistry - A European Journal* **2010**, *16*, 810–821.
- [145] M. Schmidt, J. J. Wittmann, R. Kress, D. Schneider, S. Steuernagel, H. W. Schmidt, J. Senker, *Crystal Growth & Design* **2012**, *12*, 2543–2551.
- [146] M. Schmidt, J. J. Wittmann, R. Kress, H.-W. Schmidt, J. Senker, *Chemical Communications* **2013**, *49*, 267–269.
- [147] M. Wegner, D. Dudenko, D. Sebastiani, A. R. A. Palmans, T. F. A. Greef, R. Graf, H. W. Spiess, *Chemical Science* **2011**, *2*, 2040–2049.

- [148] R. Q. Albuquerque, A. Timme, R. Kress, J. Senker, H.-W. Schmidt, *Chemistry - A European Journal* **2013**, *19*, 1647–1657.
- [149] P. J. M. Stals, M. M. J. Smulders, R. Martín-Rapún, A. R. A. Palmans, E. W. Meijer, *Chemistry - A European Journal* **2009**, *15*, 2071–2080.
- [150] Y. Matsunaga, Y. Nakayasu, S. Sakai, M. Yonenaga, *Molecular Crystals and Liquid Crystals* **1986**, *141*, 327–333.
- [151] Y. Matsunaga, N. Miyajima, Y. Nakayasu, S. Sakai, M. Yonenaga, *Bulletin of the Chemical Society of Japan* **1988**, *61*, 207–10.
- [152] Y. Harada, Y. Matsunaga, *Bulletin of the Chemical Society of Japan* **1988**, *61*, 2739–41.
- [153] J. J. van Gorp, J. A. J. M. Vekemans, E. W. Meijer, *Journal of the American Chemical Society* **2002**, *124*, 14759–14769.
- [154] A. Timme, R. Kress, R. Q. Albuquerque, H.-W. Schmidt, *Chemistry - A European Journal* **2012**, *18*, 8329–8339.
- [155] J. C. Singer, R. Giesa, H.-W. Schmidt, *Soft Matter* **2012**, *8*, 9972–9976.
- [156] A. Greiner, J. H. Wendorff, *Angewandte Chemie-International Edition* **2007**, *46*, 5670–5703.
- [157] A. Baji, Y. W. Mai, S. C. Wong, M. Abtahi, P. Chen, *Composites Science and Technology* **2010**, *70*, 703–718.
- [158] D. W. Hutmacher, P. D. Dalton, *Chemistry-an Asian Journal* **2011**, *6*, 44–56.
- [159] C. J. Ellison, A. Phatak, D. W. Giles, C. W. Macosko, F. S. Bates, *Polymer* **2007**, *48*, 3306–3316.
- [160] D. H. Tan, C. F. Zhou, C. J. Ellison, S. Kumar, C. W. Macosko, F. S. Bates, *Journal of Non-Newtonian Fluid Mechanics* **2010**, *165*, 892–900.
- [161] R. T. Weitz, L. Harnau, S. Rauschenbach, M. Burghard, K. Kern, *Nano Letters* **2008**, *8*, 1187–1191.
- [162] G. Taylor, *Proceedings of the Royal Society of London Series A - Mathematical and Physical Sciences* **1964**, *280*, 383–397.
- [163] M. Cloupeau, B. Prunet-Foch, *Journal of Electrostatics* **1989**, *22*, 135–159.
- [164] A. L. Yarin, S. Koombhongse, D. H. Reneker, *Journal of Applied Physics* **2001**, *90*, 4836–4846.
- [165] D. H. Reneker, A. L. Yarin, H. Fong, S. Koombhongse, *Journal of Applied Physics* **2000**, *87*, 4531–4547.
- [166] A. L. Yarin, S. Koombhongse, D. H. Reneker, *Journal of Applied Physics* **2001**, *89*, 3018–3026.
- [167] M. M. Hohman, M. Shin, G. Rutledge, M. P. Brenner, *Physics of Fluids* **2001**, *13*, 2201–2220.
- [168] M. G. McKee, J. M. Layman, M. P. Cashion, T. E. Long, *Science* **2006**, *311*, 353–355.

- [169] M. T. Hunley, M. G. Mckee, P. Gupta, G. L. Wilkes, T. E. Long, *MRS Proceedings* **2006**, 948.
- [170] A. Sakamoto, D. Ogata, T. Shikata, O. Urakawa, K. Hanabusa, *Polymer* **2006**, 47, 956–960.
- [171] I. Tomatsu, C. F. C. Fitié, D. Byelov, W. H. Jeu, P. C. M. M. Magusin, M. Wübhenhorst, R. P. Sijbesma, *The Journal of Physical Chemistry B* **2009**, 113, 14158–14164.
- [172] C. Kulkarni, S. K. Reddy, S. J. George, S. Balasubramanian, *Chemical Physics Letters* **2011**, 515, 226–230.
- [173] D. Kluge, J. C. Singer, B. R. Neugirg, J. W. Neubauer, H.-W. Schmidt, A. Fery, *Polymer* **2012**, 53, 5754–5759.
- [174] F. Abraham, H.-W. Schmidt, *Polymer* **2010**, 51, 913–921.
- [175] M. Blomenhofer, S. Ganzleben, D. Hanft, H.-W. Schmidt, M. Kristiansen, P. Smith, K. Stoll, D. Mäder, K. Hoffmann, *Macromolecules* **2005**, 38, 3688–3695.
- [176] F. Abraham, S. Ganzleben, D. Hanft, P. Smith, H.-W. Schmidt, *Macromolecular Chemistry & Physics* **2010**, 211, 171–181.
- [177] J. Varga, K. Stoll, A. Menyhárd, Z. Horváth, *Journal of Applied Polymer Science* **2011**, 121, 1469–1480.
- [178] M. K. Muller, L. Brunsveld, *Angewandte Chemie-International Edition* **2009**, 48, 2921–2924.
- [179] C. Appelt, A. K. Schrey, J. A. Soderhall, P. Schmieder, *Bioorganic & Medicinal Chemistry Letters* **2007**, 17, 2334–2337.
- [180] Y. M. Chabre, D. Giguere, B. Blanchard, J. Rodrigue, S. Rocheleau, M. Neault, S. Rauthu, A. Papadopoulos, A. A. Arnold, A. Imberty, R. Roy, *Chemistry-a European Journal* **2011**, 17, 6545–6562.
- [181] P. Besenius, J. L. M. Heynens, R. Straathof, M. M. L. Nieuwenhuizen, P. H. H. Bomans, E. Terreno, S. Aime, G. J. Strijkers, K. Nicolay, E. W. Meijer, *Contrast Media & Molecular Imaging* **2012**, 7, 356–361.
- [182] N. Mohmeyer, B. Müller, N. Behrendt, J. Hillenbrand, M. Klaiber, X. Zhang, P. Smith, V. Altstädt, G. M. Sessler, H.-W. Schmidt, *Polymer* **2004**, 45, 6655–6663.
- [183] N. Mohmeyer, H.-W. Schmidt, P. M. Kristiansen, V. Altstädt, *Macromolecules* **2006**, 39, 5760–5767.
- [184] N. Mohmeyer, N. Behrendt, X. Zhang, P. Smith, V. Altstädt, G. M. Sessler, H.-W. Schmidt, *Polymer* **2007**, 48, 1612–1619.
- [185] D. P. Erhard, R. Giesa, V. Altstädt, H.-W. Schmidt, *Journal of Applied Polymer Science* **2010**, 115, 1247–1255.
- [186] D. P. Erhard, D. Lovera, W. Jenninger, J. Wagner, V. Altstädt, H.-W. Schmidt, *Macromolecular Chemistry & Physics* **2010**, 211, 2179–2186.

- [187] C. F. C. Fitié, W. S. C. Roelofs, P. C. M. M. Magusin, M. Wübbenhorst, M. Kemerink, R. P. Sijbesma, *Journal of Physical Chemistry B* **2012**, *116*, 3928–3937.
- [188] C. F. C. Fitié, I. Tomatsu, D. Byelov, W. H. D. Jeu, R. P. Sijbesma, *Chemistry of Materials* **2008**, *20*, 2394–2404.
- [189] Y. Yasuda, E. Iishi, H. Inada, Y. Shiota, *Chemistry Letters* **1996**, 575–576.
- [190] K. Hanabusa, C. Koto, M. Kimura, H. Shirai, A. Kakehi, *Chemistry Letters* **1997**, 429–430.
- [191] S. Y. Ryu, S. Kim, J. Seo, Y.-W. Kim, O.-H. Kwon, D.-J. Jang, S. Y. Park, *Chemical Communications* **2004**, 70–71.
- [192] N. Mohmeyer, H.-W. Schmidt, *Chemistry - A European Journal* **2007**, *13*, 4499–4509.
- [193] A. Bernet, M. Behr, H.-W. Schmidt, *Soft Matter* **2011**, *7*, 1058–1065.
- [194] D. K. Kumar, D. A. Jose, P. Dastidar, A. Das, *Chemistry of Materials* **2004**, *16*, 2332–2335.
- [195] N. E. Shi, H. Dong, G. Yin, Z. Xu, S. H. Li, *Advanced Functional Materials* **2007**, *17*, 1837–1843.
- [196] N. Shi, G. Yin, M. Han, Z. Xu, *Colloids and Surfaces B: Biointerfaces* **2008**, *66*, 84–89.
- [197] T. Mes, M. M. J. Smulders, A. R. A. Palmans, E. W. Meijer, *Macromolecules* **2010**, *43*, 1981–1991.
- [198] H. Misslitz, K. Kreger, H.-W. Schmidt, *Small* **2013**, *9*, 2053–2058.

Nanomechanical Properties of Supramolecular Whiskers

Reproduced with permission from:

D. Kluge, F. Abraham, S. Schmidt, H.-W. Schmidt, A. Fery, NANOMECHANICAL PROPERTIES OF SUPRAMOLECULAR SELF-ASSEMBLED WHISKERS DETERMINED BY AFM FORCE MAPPING. *Langmuir* **2010**, *26*, 3020-3023.

© 2010 American Chemical Society.

ABSTRACT

In this Letter, we investigate the nanomechanical properties of self-assembled 1,3,5-benzenetrisamide whiskers with atomic force microscopy (AFM) bending experiments. We use force mapping to acquire spatially resolved force measurements over the full length of a whisker segment spanning a channel of a structured glass substrate. This allows validation of the experimental boundary conditions directly from the AFM data and a reliable determination of Young's modulus. The presented technique can be generalized for the mechanical characterization of other one-dimensional materials.

4.1 Introduction

In the past decades, micro- and nanoscopic one-dimensional (1D) objects such as fibers, rods, and whiskers have become increasingly important in materials science. Their potential is demonstrated by nature, where these small-scale objects contribute significantly to the combination of exceptional mechanical properties and functionality of hierarchical structures.^{1–6} Nanotechnological approaches to natural and artificial fiber- and whisker-based materials offer diverse applications for tissue engineering, for filtration, in composite materials, or as drug carriers.^{7–10}

While the physical and chemical properties of such materials have to meet high requirements to be suitable for a specific application, the most fundamental property for all of these applications is the mechanical stability. In order to investigate their mechanical properties, approaches beyond standard characterization methods for macroscopic materials are necessary. A comprehensive review was recently published by *Tan and Lim*,¹¹ presenting the most common techniques: indentation measurements, tensile tests, and bending experiments.

In this work, we focus on bending experiments using atomic force microscopy (AFM). These experiments are carried out in analogy to a standard macroscopic three-point bending test. However, it is easy to understand that, at smaller scales, it is difficult to determine the exact boundary conditions of the experiment, meaning the way the sample is supported by the substrate. We use *force mapping* to achieve spatially resolved force measurements over the full length of the suspended whisker.

This approach on bending experiments allows the precise investigation of the experimental boundary conditions without any complementary techniques. We discuss the importance of these boundary conditions for a reliable evaluation of the flexural rigidity and Young's modulus. The knowledge of the elastic properties is important to estimate the suitability of the whiskers for future applications.

Recently, alkyl substituted 1,3,5-benzenetrisamides (Figure 4.1) have received considerable attention because of their pronounced self-assembly behavior. In liquids, they can induce thermoreversible physical gelation of a variety of organic solvents.^{12,13} More recently, we reported that substituted 1,3,5-benzenetrisamides represent a highly versatile family of novel nucleating and/or clarifying agents for isotactic polypropylene (*i*-PP).^{14,15} In addition, it has been shown that trialkyl-1,3,5-benzenetricarboxamides with *n*-alkyl moieties $> C_6$ display discotic liquid-crystalline behavior.¹⁶⁻¹⁸ This behavior results from the formation of supramolecular nanowhiskers or columnar structures due to well-defined intermolecular hydrogen bonds between the 1,3,5-trisamide molecules.^{19,20} Structural aspects of 1,3,5-benzenetrisamides were reported by *Kristiansen et al.*²¹

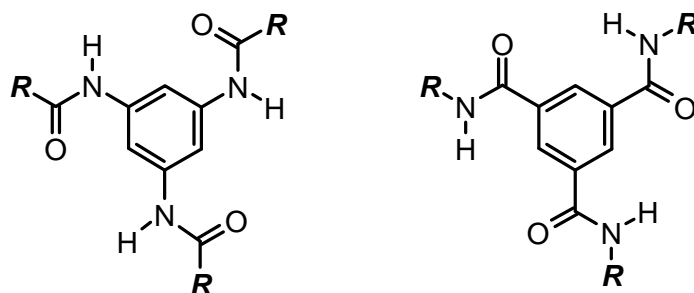


Figure 4.1 Chemical structure of two types of 1,3,5-benzenetrisamides.

4.2 Results and Discussion

We used the substituted benzenetrisamide 1,3,5-tris(2,2-dimethylpropionylamino)benzene (Figure 4.1, left, R = *tert*-butyl) to prepare supramolecular organic nanowhiskers. We were able to control the assemblies' final morphology by recrystallization of the trisamide in the high-boiling hydrocarbon solvent 2,2,4,4,6,8,8-heptamethylnonane (HMN). Dissolving the additive at defined concentrations (typically between 50 and 600 ppm) at 240 °C in a sealed high pressure differential scanning calorimetry (DSC) pan and then cooling at 10 K/min to room temperature gave

suspensions of well-defined whiskers in HMN. With increasing concentration and slower cooling rates, the whiskers' average diameter increased. At larger whisker diameters, sometimes hollow structures appeared.^a For the mechanical measurements of individual whiskers, the suspension was transferred to structured glass substrates and the solvent was completely evaporated under high vacuum.

Figure 4.2(a) shows a scanning electron microscopy (SEM) overview micrograph of uniform and very long whiskers with aspect ratios exceeding 1000:1. These whiskers were prepared at a concentration of 50 ppm and a cooling rate of 10 K/min. The whiskers in Figure 4.2(b) were prepared at a concentration of 300 ppm (cooling rate: 10 K/min). The higher magnification confirms a hexagonal structure of the whiskers. The whiskers were cut with a focused ion beam (FIB) and it was revealed that whiskers prepared under these conditions and with this diameter are hollow. The SEM micrograph in Figure 4.2(c) shows a free-standing trisamide whisker positioned over a channel of a structured glass substrate. This setup was used for the bending measurements.

Bending experiments have successfully been used for the characterization of biological samples,^{22–27} carbon nanotubes,^{28–32} inorganic materials like nanowires and -belts,^{33–37} polymer nanofibers,^{38–41} and artificial membranes.^{42,43} The general setup of a bending experiment is shown in Figure 4.3. The fiber is suspended over well-defined microgaps (such as channels, holes, etc.) and is pushed into these gaps by a microfabricated cantilever. The AFM allows precise movement of the cantilever and measurement of the respective forces. The mechanical properties of the sample can be calculated from the force-deformation data using beam theory.⁴⁴

To ensure that the whiskers are not indented by the AFM probe while performing the bending experiments, we compared force-deformation curves acquired on the plain substrate, on the whisker supported by the substrate, and on the free-standing whisker. Under the applied loads, the deformation of the free-standing whisker was in the linear elastic regime. No significant deformation was visible in case of the supported whisker, which proves the absence of indentation (Figure 4.4).

*Chen et al.*³³ have demonstrated the importance of the experimental boundary conditions for a correct evaluation of the mechanical properties. In many cases, it is assumed that the sample is firmly fixed on the substrate due to adhesion.^{30,45} In order to ensure this, several groups have put high efforts into fixing the ends (e.g., by

^aThe influence of the hollow structure on the mechanical properties is discussed in the Supporting Information SI 4.2 and turns out to be insignificant in this case.

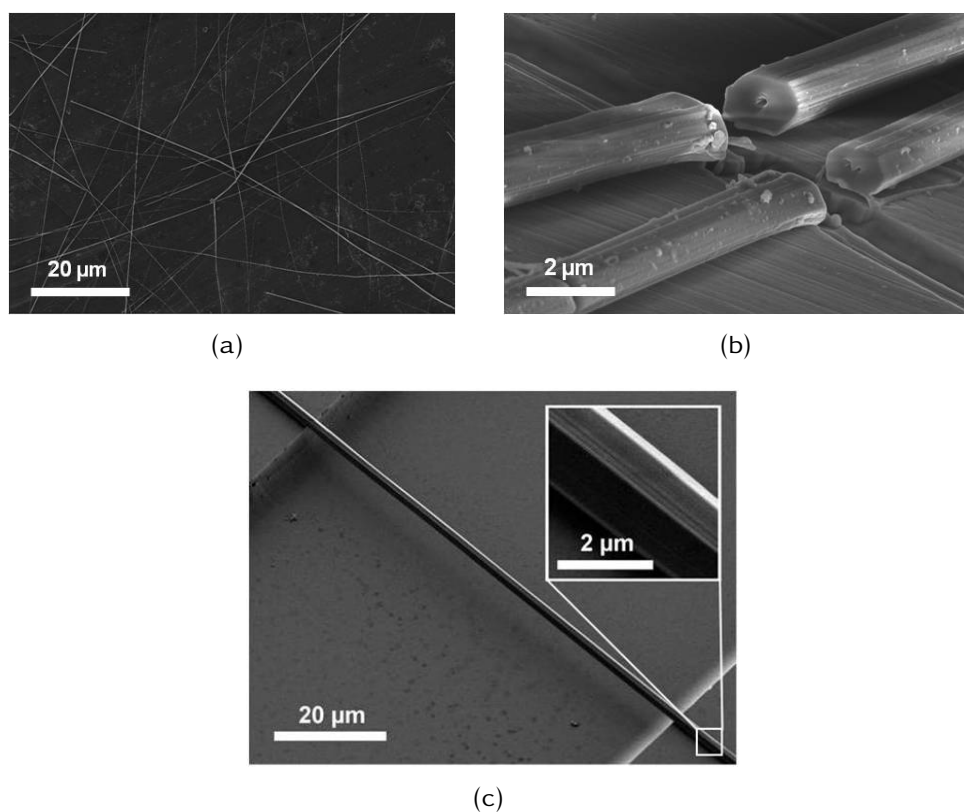


Figure 4.2 SEM micrographs of 1,3,5-benzenetrisamide whiskers. (a) Overview of whiskers obtained at a concentration of 50 ppm (cooling rate 10 K/min). (b) Cross section of whiskers with larger diameters prepared at a concentration of 300 ppm (cooling rate 10 K/min). (c) Free-standing whisker (600 ppm, cooling rate 10 K/min) positioned over a channel of a structured glass substrate (channel width of 90 μm).

electron or ion beam induced deposition of Pt^{35,46} or W³⁷ bridges). However, the experiments were still based on an assumption of the boundary conditions. There are only few reported cases where the actual boundary conditions of the experiments have been investigated by using the dependency of the mechanical properties on the loading position.^{33,35,39} The importance of acquiring additional spatial information when investigating mechanical properties can be seen by the recent development of commercial techniques such as the Digital Pulsed Force Mode (WITec) and the Peak-Force Quantitative Nanomechanical Property Mapping (Veeco) that allow an *in situ* combination of spatial mapping and quantitative nanomechanical measurements.

Our approach realizes this combination by applying the widely used force mapping function of the AFM for the actual bending tests. Force mapping is the acquisition of force-displacement measurements at each pixel of an AFM image.^{47,48} With this procedure, a property of interest (e.g., hardness or adhesion) can be mapped to the

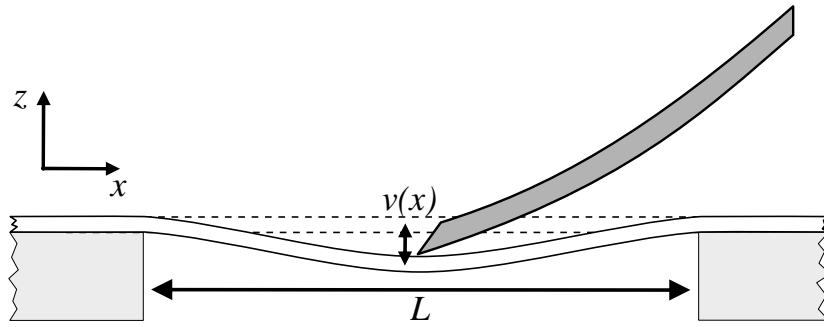


Figure 4.3 Schematic setup of the bending experiments. v is the deflection of the fiber, and L is the length of the suspended segment.

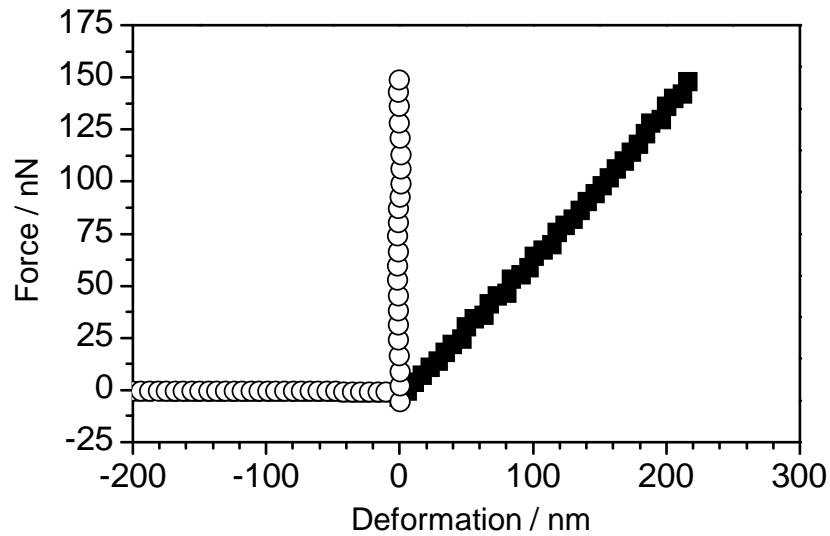


Figure 4.4 AFM force-deformation measurements on different segments of one whisker. (O) Segment supported by the substrate. (■) Free-standing segment over the channel. The segment supported by the substrate shows no significant deformation, which proves the absence of indentation.

sample by evaluation of the force measurements. However, our main interest was not to image the sample, but to perform spatially resolved bending experiments. This provides a way of investigating the bending behavior under different loading positions, which allows determining the boundary conditions of the experiments directly from the AFM measurements.

We evaluated the force-displacement curves with a self-written procedure in IGOR Pro (Wavemetrics) to obtain the apparent spring constant k_{app} of the sample. To account for the contribution of the cantilever spring constant k_c to k_{app} , we applied a model of coupled springs^{39,49} and obtained the actual whisker spring constant $k_w = k_c k_{app} / (k_c - k_{app})$. The resulting force map yields a profile of the whisker spring

constants along the free standing segment of the whisker in the direction of the whisker axis. The shape of the profile depends on the boundary conditions of the experiment³³ and can be calculated using beam theory. Hence, the boundary conditions can be obtained by fitting different models to the experimental data.

The two most common models are the double clamped beam model (DCBM), where the ends of the sample are firmly fixed to the substrate, and the simply supported beam model (SSBM), where the ends of the sample may freely rotate as response to the applied load.^{33,35,44} The respective equations for the spring constants are

$$k_w(x) = \frac{3L^3EI}{(L-x)^3x^3} \quad (4.1)$$

for the DCBM and

$$k_w(x) = \frac{3LEI}{(L-x)^2x^2} \quad (4.2)$$

for the SSBM.^{27,35} In both equations, L is the length of the suspended segment, and x is the position where the load is applied. The product of Young's modulus E and the area moment of inertia I is the flexural rigidity. Both equations were fitted to the data with EI as the only free parameter. The comparison of both fits in Figure 4.5 clearly shows that the clamped boundary fit represents the data best, and thus, the whisker was indeed firmly fixed on the substrate by adhesion.

Using the fitted flexural rigidities, E can be calculated when I is known. In order to obtain I , we imaged the whiskers on the hard substrate and determined their precise dimensions. Since the lower part of the whiskers was not accessible by AFM, we completed the missing areas with a hexagonal shape so that the cross section was consistent with the morphology known from the SEM measurements. With this topographical data we calculated I using the program *Fmom*. In comparison with simplified geometries, we found that an elliptical model (using the height and width as obtained by AFM) can be used as a good approximation (see the Supporting Information SI 4.4).

The so obtained average modulus is 3.2 ± 1.4 GPa, which is comparable to that of semicrystalline polymers. While the order of magnitude is a reasonable result, the exact numerical value has to be considered carefully, since all AFM bending experiments share intrinsic uncertainties due to the cantilever calibration, the modeling of the cross section, and the possible inhomogeneities of the material. We also investigated the effect of shearing during bending for the experiments and found no

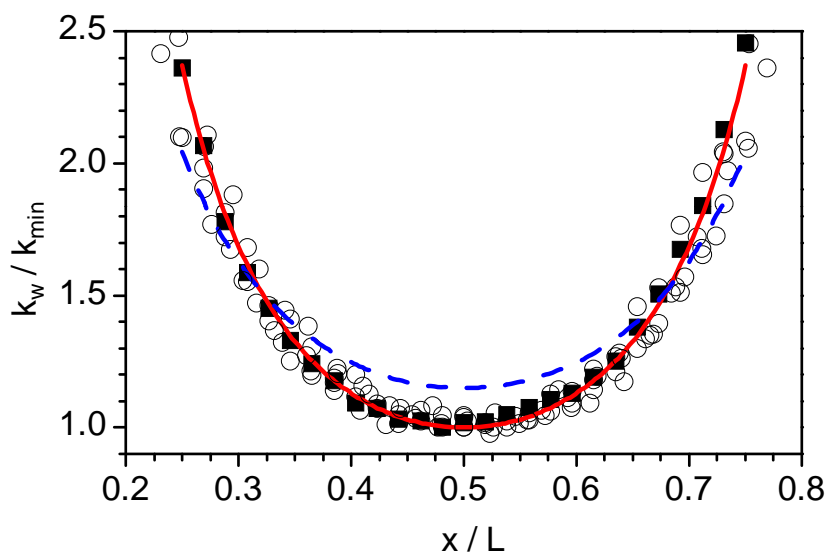


Figure 4.5 Normalized profile of the corrected spring constants. Solid squares: Data of one measurement on a whisker. Solid line: Data fitted with the DCBM. Dashed line: Data fitted with the SSBM. Open circles: Data from measurements on other whiskers. It can be clearly seen that the DCBM is a valid assumption and that all experimental data is in good agreement with the calculated profile.

visible contribution (see the Supporting Information SI 4.5). Therefore, the obtained modulus does not need to be corrected to account for shearing. Since the detailed influence of the self-assembled structure on the nanomechanical response to bending has yet to be investigated, E has to be treated as an apparent value as is common in the literature.⁵⁰

4.3 Conclusion

We presented an approach on AFM bending experiments that uses the force mapping function of the instrument to perform spatially resolved deformations over the full length of a freely suspended one-dimensional sample. The advantage of this approach is that it allows a determination of the experimental boundary conditions directly from the AFM data. We used this method for a mechanical characterization of supramolecular organic whiskers based on 1,3,5-benzenetrisamides. For our experiments, a double-clamped beam model was valid. We obtained the flexural rigidity and Young's modulus of the whiskers, which was comparable to that of semicrystalline polymers. Further investigations will focus on the influence of the molecular structure on the bending behavior to establish structure-property relationships. Our

work points out that AFM bending experiments provide a powerful way to perform mechanical investigations that bridge the gap between the molecular and the macroscopic scale.

4.4 Experimental Section

Whisker preparation. The detailed synthesis of the trisamide is described in the Supporting Information SI 4.1. Suspensions of the trisamide with defined concentrations (300 and 600 ppm) were prepared by dissolving the respective amount in 2,2,4,4,6,8,8-heptamethylnonane under nitrogen blanket. For the controlled assembly, 20 μL of a suspension was transferred to a stainless steel high pressure pan of a Diamond differential scanning calorimeter (Perkin Elmer, Waltham, MA). The temperature program started with annealing for 10 min at 240°C and then cooling with 10 K/min to room temperature. The samples for the bending experiments were prepared by adding 10 μL of the final suspension to structured glass substrates (GeSiM, Großerkmannsdorf) and evaporating the solvent.

AFM Measurements. A Nanowizard I atomic force microscope (JPK Instruments AG, Berlin) was used for all AFM measurements. A Zeiss Axiovert 200 (Zeiss, Jena) microscope was used in order to choose an appropriate segment of the whiskers (uniform, undamaged, and perpendicular to the channels of the substrate) for the force measurements. After careful calibration of the cantilever with the thermal noise method,⁵¹ force-displacement measurements were performed over the whole free-standing segment of the whisker using the force mapping mode. The resolution was chosen to measure at least 10 lines along the whisker with each line consisting of a minimum of 40 measurements. This yielded a point distance ranging from 0.5 μm (channel width 20 μm) to 2 μm (channel width 90 μm). The approach set point was set in the range of 20-100 nN with a typical value of 50 nN. The maximum applied force was between 100 nN and 200 nN, with a typical value of 150 nN. For the force measurements, tipless cantilevers (CSC12/tipless/AlBS and NSC12/tipless/AlBS by Mikromasch, Estonia and AppNano Forta-TL-50 by Applied NanoStructures, Inc., Santa Clara, CA; spring constants 0.5-1.5 N/m) were used. Imaging of the whiskers in order to determine their dimensions was done on the segments supported by the substrate in the intermittent contact mode with high resolution cantilevers (DP15/GP/AlBS, Mikromasch, Estonia).

Scanning Electron Microscopy (SEM). The samples were sputtered using platinum (1.0 nm) in a Cressington sputter coater 208HR to enhance conductivity. SEM micrographs were recorded on a Zeiss LEO 1530 FESEM (Zeiss, Jena) instrument. The FIB cross-sectional imaging was performed on a Zeiss 1540 EsB CrossBeam microscope, using DSC aluminum pans as substrates.

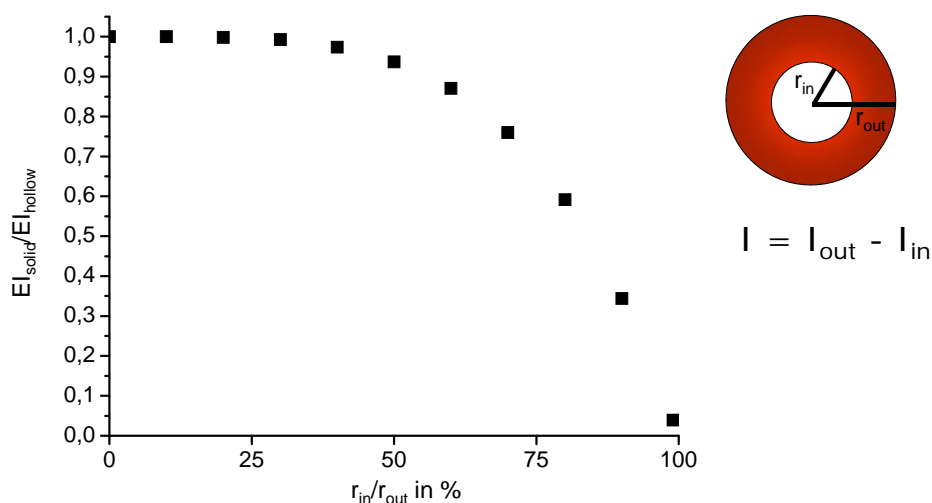
Acknowledgments

This work received financial support from the Deutsche Forschungsgemeinschaft (SFB 840, TP B8) and the BMBF project 'Bionics'. We thank Werner Reichstein and Alexandra Schweikart for their assistance with the SEM measurements and Prof. Jürgen Dankert for the permission of using Fmom. D.K. acknowledges the support of the Elite Network of Bavaria.

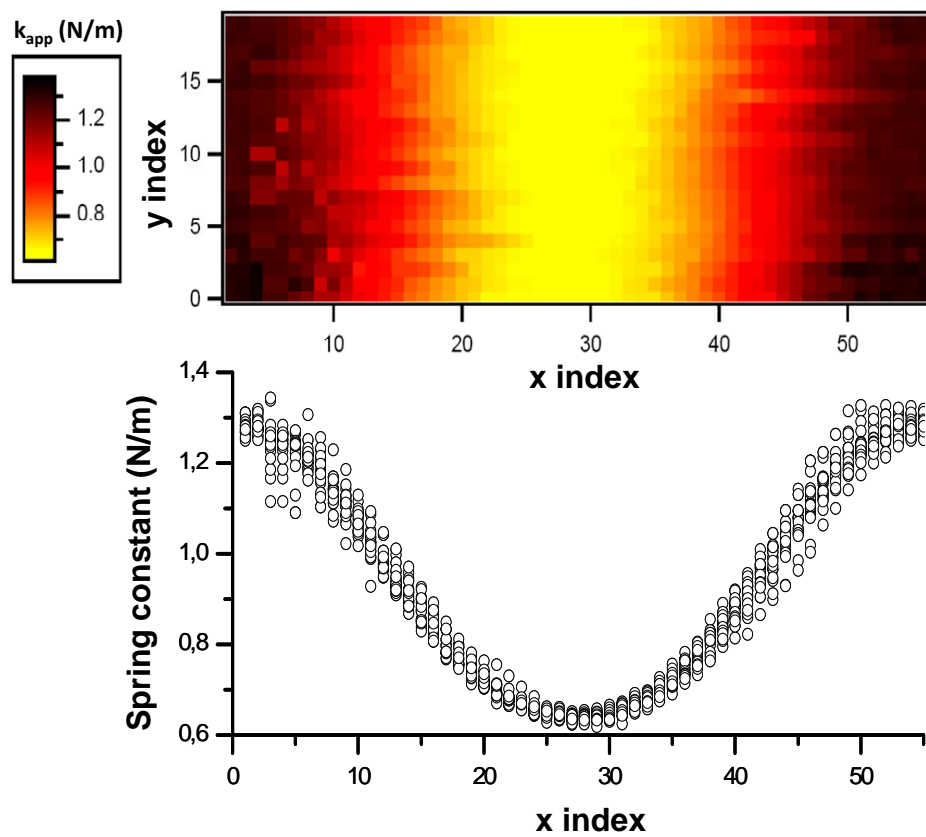
4.5 Supporting Information

SI 4.1 Synthesis of 1,3,5-tris(2,2-dimethylpropionylamino)benzene.

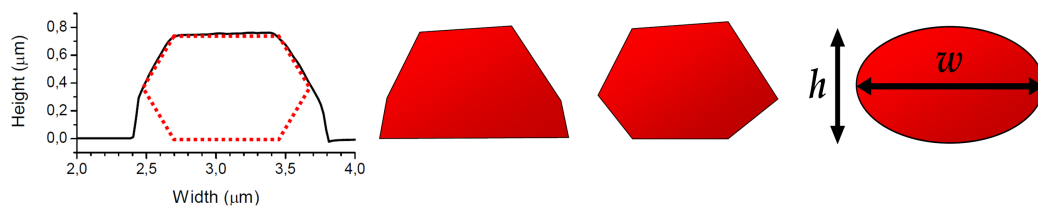
Pivaloyl chloride was added at 0°C under nitrogen to a mixture of dried N-methylpyrrolidone, pyridine as base, LiCl and the 1,3,5-triaminobenzene hydrochloride. The reaction mixture was heated to 60°C and maintained at this temperature for 48 hours. After cooling, the reaction mixture was precipitated into a five-fold excess of ice water. The precipitate was filtered off, dried under vacuum for 24 h (30°C, 0.1 mbar) and recrystallized from THF. Reaction Batch: 19.0 g (0.157 mol) 2,2-dimethylpropionyl chloride, 11.0 g (0.047 mol) 1,3,5-triaminobenzene hydrochloride, 500 mL NMP, 100 ml pyridine, 0.1 g LiCl. Recrystallization from THF, Yield: 7.1 g (0.019 mmol), 40 %. Characterization: ¹H-NMR (DMSO-d₆): δ = 1.20 (s, 27H); 7.60 (s, 3H); 9.15 (s, 3H, N-H), MS (70 eV), m/z (%): 375 (M⁺, 15); 291 (15); 207 (8); 57 (100); 41 (12). TGA: T_m: - (sublimation), T_{-10wt.%}: 374°C (10 K/min, N₂).



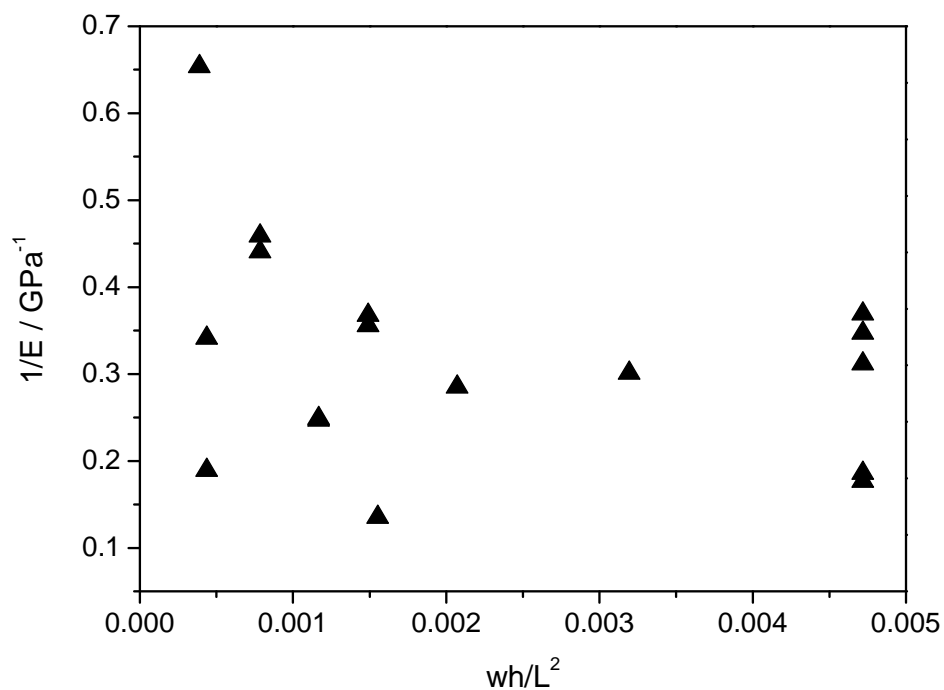
SI 4.2 Calculated relative rigidity $EI_{\text{solid}}/EI_{\text{hollow}}$ as a function of an increasingly hollow structure. For the sake of clearness, we used a circular cross section for the calculation. The whiskers with the largest holes ever observed had an inner diameter that was smaller than half of the outer diameter. Therefore the largest $r_{\text{in}}/r_{\text{out}}$ was 50%, which causes a decrease of rigidity of only around 6%. Since even this maximum decrease is smaller than the error of the measurements, the occurrence of holes can be neglected for the evaluation of the mechanical properties.



SI 4.3 Exemplary force map and the respective profile plot of the uncorrected spring constants. Please note that the individual lines of the force map (from left to right) were shifted for the sake of clearness to account for the convolution with the cantilever shape.



SI 4.4 Comparison of models for the cross section used in order to obtain the area moment of inertia I . From left to right: a) Cross section as determined by AFM imaging. The dotted line illustrates the hexagonal shape that cannot be fully determined by AFM since the cantilever cannot image below the broadest segment. b) Model for F_{mom} using the full shape of the AFM cross section, leading to a possible overestimation of I and subsequently a underestimation of Young's modulus E . Obtained value: $E = 2.9 \pm 1.5 \text{ GPa}$. c) Model for F_{mom} using the assumed hexagonal lower part, leading to a possible overestimation of Young's modulus. Obtained value: $E = 3.2 \pm 1.4 \text{ GPa}$. d) Elliptical approximation. Obtained value: $E = 3.7 \pm 1.6 \text{ GPa}$. On comparison it is clear that while each model has certain inaccuracies, the deviations are small and within the error ranges.



SI 4.5 Investigation of the influence of shearing on Young's modulus as proposed by *Kis et al.*²⁵ Each point represents a measurement on a fiber segment. w is the width and h the height of the fibers as obtained by AFM imaging. L is the length of the free standing segment. If shearing played a significant role during bending, the modulus should decrease with increasing wh/L^2 ratio.

4.6 References

- [1] I. Burgert, *American Journal of Botany* **2006**, *93*, 1391–1401.
- [2] P. Fratzl, I. Burgert, H. S. Gupta, *Physical Chemistry Chemical Physics* **2004**, *6*, 5575–5579.
- [3] P. Fratzl, R. Weinkamer, *Progress in Materials Science* **2007**, *52*, 1263–1334.
- [4] A. K. Mohanty, M. Misra, G. Hinrichsen, *Macromolecular Materials and Engineering* **2000**, *276*, 1–24.
- [5] L. Römer, T. Scheibel, *Prion* **2008**, *2*, 154–161.
- [6] T. Scheibel, *Current Opinion in Biotechnology* **2005**, *16*, 427–433.
- [7] C. P. Barnes, S. A. Sell, E. D. Boland, D. G. Simpson, G. L. Bowlin, *Advanced Drug Delivery Reviews* **2007**, *59*, 1413–1433.
- [8] C. Burger, B. S. Hsiao, B. Chu, *Annual Review of Materials Research* **2006**, *36*, 333–368.
- [9] S. Y. Chew, T. C. Hufnagel, C. T. Lim, K. W. Leong, *Nanotechnology* **2006**, *17*, 3880–3891.
- [10] Z. M. Huang, Y. Z. Zhang, M. Kotaki, S. Ramakrishna, *Composites Science and Technology* **2003**, *63*, 2223–2253.
- [11] E. P. S. Tan, C. T. Lim, *Composites Science and Technology* **2006**, *66*, 1102–1111.
- [12] K. Hanabusa, C. Koto, M. Kimura, H. Shirai, A. Kakehi, *Chemistry Letters* **1997**, 429–430.
- [13] Y. Yasuda, E. Iishi, H. Inada, Y. Shiota, *Chemistry Letters* **1996**, 575–576.
- [14] M. Blomenhofer, S. Ganzleben, D. Hanft, H.-W. Schmidt, M. Kristiansen, P. Smith, K. Stoll, D. Mäder, K. Hoffmann, *Macromolecules* **2005**, *38*, 3688–3695.
- [15] F. Abraham, S. Ganzleben, D. Hanft, P. Smith, H.-W. Schmidt, *Macromolecular Chemistry & Physics* **2010**, *211*, 171–181.
- [16] Y. Harada, Y. Matsunaga, *Bulletin of the Chemical Society of Japan* **1988**, *61*, 2739–41.
- [17] Y. Matsunaga, Y. Nakayasu, S. Sakai, M. Yonenaga, *Molecular Crystals and Liquid Crystals* **1986**, *141*, 327–333.
- [18] Y. Matsunaga, N. Miyajima, Y. Nakayasu, S. Sakai, M. Yonenaga, *Bulletin of the Chemical Society of Japan* **1988**, *61*, 207–10.
- [19] M. P. Lightfoot, F. S. Mair, R. G. Pritchard, J. E. Warren, *Chemical Communications* **1999**, 1945–1946.
- [20] J. Roosma, T. Mes, P. Leclere, A. R. A. Palmans, E. W. Meijer, *Journal of the American Chemical Society* **2008**, *130*, 1120–1121.

- [21] M. Kristiansen, P. Smith, H. Chanzy, C. Baerlocher, V. Gramlich, L. Mccusker, T. Weber, P. Pattison, M. Blomenhofer, H.-W. Schmidt, *Crystal Growth & Design* **2009**, *9*, 2556–2558.
- [22] C. R. Carlisle, C. Coulais, M. Namboothiry, D. L. Carroll, R. R. Hantgan, M. Guthold, *Biomaterials* **2009**, *30*, 1205–1213.
- [23] Q. Cheng, S. Wang, *Composites Part A: Applied Science and Manufacturing* **2008**, *39*, 1838–1843.
- [24] C. Guzman, S. Jeney, L. Kreplak, S. Kasas, A. J. Kulik, U. Aebi, L. Forro, *Journal of Molecular Biology* **2006**, *360*, 623–630.
- [25] A. Kis, S. Kasas, B. Babic, A. J. Kulik, W. Benoit, G. A. D. Briggs, C. Schonenberger, S. Catsicas, L. Forro, *Physical Review Letters* **2002**, *89*, 248101.
- [26] W. Xu, P. J. Mulhern, B. L. Blackford, M. H. Jericho, I. Templeton, *Scanning Microscopy* **1994**, *8*, 499–506.
- [27] L. Yang, K. O. V. D. Werf, C. F. C. Fitié, M. L. Bennink, P. J. Dijkstra, J. Feijen, *Biophysical Journal* **2008**, *94*, 2204–2211.
- [28] G. T. Kim, G. Gu, U. Waizmann, S. Roth, *Applied Physics Letters* **2002**, *80*, 1815–1817.
- [29] J. P. Salvetat, J. M. Bonard, N. H. Thomson, A. J. Kulik, L. Forro, W. Benoit, L. Zuppiroli, *Applied Physics A - Materials Science & Processing* **1999**, *69*, 255–260.
- [30] J. P. Salvetat, G. A. D. Briggs, J. M. Bonard, R. R. Bacsa, A. J. Kulik, T. Stockli, N. A. Burnham, L. Forro, *Physical Review Letters* **1999**, *82*, 944–947.
- [31] T. W. Tomblor, C. W. Zhou, L. Alexseyev, J. Kong, H. J. Dai, L. Lei, C. S. Jayanthi, M. J. Tang, S. Y. Wu, *Nature* **2000**, *405*, 769–772.
- [32] E. W. Wong, P. E. Sheehan, C. M. Lieber, *Science* **1997**, *277*, 1971–1975.
- [33] Y. X. Chen, B. L. Dorgan, D. N. Mcilroy, D. E. Aston, *Journal of Applied Physics* **2006**, *100*, 104301.
- [34] G. Y. Jing, H. L. Duan, X. M. Sun, Z. S. Zhang, J. Xu, Y. D. Li, J. X. Wang, D. P. Yu, *Physical Review B* **2006**, *73*, 235409.
- [35] W. J. Mai, Z. L. Wang, *Applied Physics Letters* **2006**, *89*, 073112.
- [36] T. Namazu, Y. Isono, *Sensors and Actuators a-Physical* **2003**, *104*, 78–85.
- [37] H. Zhang, J. Tang, L. Zhang, B. An, L. C. Qin, *Applied Physics Letters* **2008**, *92*, 173121.
- [38] S. Y. Gu, Q. L. Wu, J. Ren, G. J. Vancso, *Macromolecular Rapid Communications* **2005**, *26*, 716–720.
- [39] S. Shanmugham, J. W. Jeong, A. Alkhateeb, D. E. Aston, *Langmuir* **2005**, *21*, 10214–10218.
- [40] M. K. Shin, S. I. Kim, S. J. Kim, S.-K. Kim, H. Lee, *Applied Physics Letters* **2006**, *88*, 193901–3.

- [41] E. P. S. Tan, C. T. Lim, *Applied Physics Letters* **2004**, *84*, 1603–1605.
- [42] C. Y. Jiang, S. Markutsya, Y. Pikus, V. V. Tsukruk, *Nature Materials* **2004**, *3*, 721–728.
- [43] S. Markutsya, C. Y. Jiang, Y. Pikus, V. V. Tsukruk, *Advanced Functional Materials* **2005**, *15*, 771–780.
- [44] A. C. Ugural, *Mechanics of Materials*, Wiley-VCH, 1st ed., **2007**.
- [45] G. Y. Jing, H. Ji, W. Y. Yang, J. Xu, D. P. Yu, *Applied Physics a-Materials Science & Processing* **2006**, *82*, 475–478.
- [46] A. Heidelberg, L. T. Ngo, B. Wu, M. A. Phillips, S. Sharma, T. I. Kamins, J. E. Sader, J. J. Boland, *Nano Letters* **2006**, *6*, 1101–1106.
- [47] D. R. Baselt, J. D. Baldeschwieler, *Journal of Applied Physics* **1994**, *76*, 33–38.
- [48] M. Radmacher, J. P. Cleveland, M. Fritz, H. G. Hansma, P. K. Hansma, *Biophysical Journal* **1994**, *66*, 2159–2165.
- [49] D. Kunz, E. Max, R. Weinkamer, T. Lunkenbein, J. Breu, A. Fery, *Small* **2009**, *5*, 1816–1820.
- [50] J. R. Withers, D. E. Aston, *Advances in Colloid and Interface Science* **2006**, *120*, 57–67.
- [51] J. L. Hutter, *Langmuir* **2005**, *21*, 2630–2632.

Influence of the Molecular Structure and Morphology

Reproduced with permission from:

D. Kluge, J. C. Singer, J. W. Neubauer, F. Abraham, H.-W. Schmidt, A. Fery, INFLUENCE OF THE MOLECULAR STRUCTURE AND MORPHOLOGY OF SELF-ASSEMBLED 1,3,5-BENZENETRISAMIDE NANOFIBERS ON THEIR MECHANICAL PROPERTIES. *Small* **2012**, *16*, 2563-2570.

© 2012 Wiley-VCH Verlag GmbH & Co. KGaA, Weinheim.

ABSTRACT

The influence of molecular structure on the mechanical properties of self-assembled 1,3,5-benzenetrisamide nanofibers is investigated. Three compounds with different amide connectivity and different alkyl substituents are compared. All the trisamides form well-defined fibers and exhibit significant differences in diameters of up to one order of magnitude. Using nanomechanical bending experiments, the rigidity of the nanofibers shows a difference of up to three orders of magnitude. Calculation of Young's modulus reveals that these differences are a size effect and that the moduli of all systems are similar and in the lower GPa range. This demonstrates that variation of the molecular structure allows changing of the fibers' morphology, whereas it has a minor influence on their modulus. Consequently, the stiffness of the self-assembled nanofibers can be tuned over a wide range – a crucial property for applications as versatile nano- and micromechanical components.

5.1 Introduction

Functional materials with a defined nanostructure have become one of the most promising research fields for advanced applications such as tissue engineering, drug delivery, micro-/ nanoelectromechanical systems (MEMS/NEMS), and filtration.¹⁻³ In these materials, one-dimensional (1D) objects like nanofibers or nanorods play an important role since they often define or reinforce their structure – as individual rods or threads or as a part of complex hierarchical networks.^{4,5}

Naturally, a lot of effort has been put into the development and efficient preparation of 1D nanostructures and structured materials in general.⁵⁻⁷ However, regardless of their preparation, the macroscopic properties of these materials are always determined by their structure on much smaller length scales. As a consequence, there is an ever growing interest in systems where, already on the molecular level, structure-property correlations can be understood and controlled.

Recently, 1,3,5-benzenetrisamides (BTAs) have attracted great research interest because of their supramolecular aggregation into helical columnar stacks with enormous aspect ratios.^{8,9} In general, the growth of BTA molecules into an ordered 1D structure is stabilized by threefold hydrogen bonding.¹⁰⁻¹² The specific self-assembly behavior, however, strongly depends on the connectivity of the amide moi-

eties to the central core. Thus, we must differentiate between BTA based on trimesic acid **1** and 1,3,5-triaminobenzene **2** (Figure 5.1). All amide-functions of type **1** are pointing in the same direction, which results in helically arranged, strong hydrogen bonds.¹³ Compared to type **1**, the hydrogen bond length in columns formed by BTA molecules of type **2** are longer and hence weaker. Solid-state NMR experiments combined with Car-Parrinello Molecular Dynamics simulations showed that in the solid state, the amide functions within the column of **2** are asymmetrically arranged, thus leading in total to a weaker aggregation.¹³

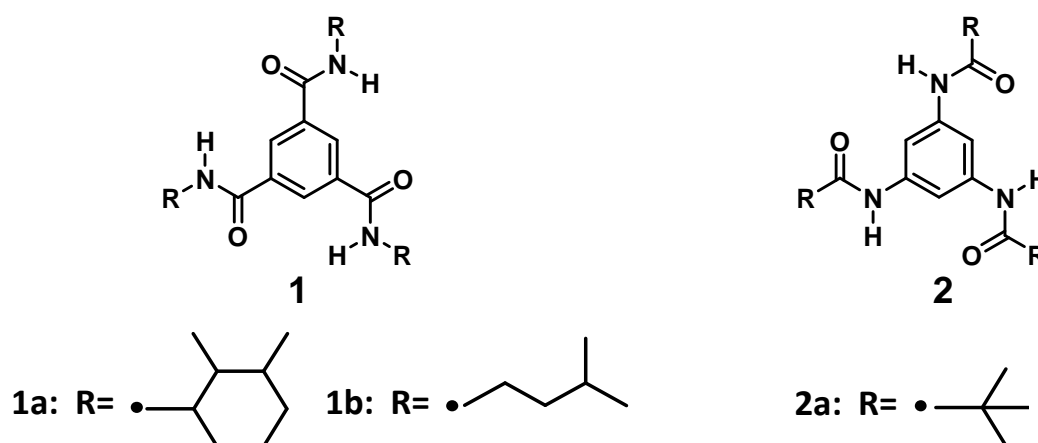


Figure 5.1 Chemical structure of BTAs based on trimesic acid (**1**) and 1,3,5-triaminobenzene (**2**).

The self-assembly behavior in solution and the solid-state properties of BTAs also depend dramatically on the constitution of the peripheral groups.¹⁴ Even subtle changes of the side chains can influence the aggregation behavior and properties of BTA. Starting with a linear C₆-alkyl chain, **1** shows discotic liquid-crystalline behavior.^{15–19} The aggregation in the mesophase is stabilized utilizing branched side chains.^{14,18} BTAs of type **2** show thermotropic liquid-crystal behavior only with chiral substituents.¹²

Consequently, BTAs offer the possibility to tailor desired properties. Well-defined BTA fibers were tailored to serve as organo-^{19–23} and hydrogelators,^{24–27} supramolecular materials,^{28,29} nucleating agents for polyvinylidene fluoride,³⁰ and were designed to improve the properties of electret materials.^{31–35} Both BTAs based on trimesic acid and on 1,3,5-triaminobenzene were intensively studied as polymer processing aids³⁶ and nucleating agents for isotactic polypropylene (i-PP).^{9,37–39} Varga et al. recently used **1a** as a new type of β-nucleating agent for i-PP.³⁹

While there are many studies on the application of BTAs, only little is known about their mechanical properties. In a previous study we showed that fibers obtained from **2a** self-assembled from 2,2,4,4,6,8,8-heptamethylnonane (HMN) possess a significant mechanical stability.⁴⁰ The reported stability and the possibility to tailor their properties makes BTA nanofibers very interesting for bottom-up approaches and demands further mechanical investigations. However, there are no experimental reports on the effect of the molecular structure on the mechanical properties to this date. Investigating the mechanical properties of 1D materials on this scale requires approaches beyond typical macroscopic characterization techniques. Amongst other methods (e.g., indentation and tensile tests), nanomechanical bending experiments are recognized for their reliability, straightforward sample preparation, and applicability to a wide variety of systems.^{41,42} In the past, bending experiments were used for the mechanical investigation of polymer nanofibers,^{43–45} biological materials,^{46–50} carbon nanotubes (CNTs),^{51,52} nanowires,^{53–55} and even complex structures like particle bridges.^{56,57} In a previous study of BTA fibers, we performed bending experiments using atomic force microscopy (AFM).⁴⁰ The presented experiments allowed us to identify the correct type of sample fixation directly from the AFM data, and thus to reliably measure the Young's modulus of the investigated fibers.

Herein, we study the influence of the molecular structure of self-assembled BTA nanofibers on their morphology and mechanical properties. For that purpose, we investigate the fibers of three different BTA structures, with respect to the connectivity of the amide moieties and the size of the alkyl substituents. We briefly discuss morphological aspects and, using AFM bending experiments, determine the stiffness of the fibers and calculate their Young's modulus. Furthermore, we compare our results with predictions and findings in the literature.

5.2 Results and Discussion

5.2.1 Morphology

To interpret the mechanical properties of the structurally different BTAs, we first investigated the morphology of the self-assembled nanofibers. A scanning electron microscopy (SEM) overview image of the dried samples is shown in Figure 5.2. The

nanofibers of **1a** have an average diameter d of $0.21 \pm 0.08 \mu\text{m}$. The narrow size distribution (Figure 5.2(a), right) illustrates the homogenous formation of the stacked structure. Moreover, all self-assembled fibers exhibit an immense aspect ratio of more than 500:1. The inset in Figure 5.2(a) shows the morphology of a single nanofiber. The diameter and the straight and uniform structure are maintained over the whole length. Compound **1b** self-assembles into long aggregates with an average diameter of $0.4 \pm 0.2 \mu\text{m}$. Compound **1a** with substituted cycloaliphatic groups forms smaller fibers than **1b** with branched alkyl substituents, thus demonstrating the influence of the peripheral substituents on the self-assembly behavior. A significantly larger fiber diameter, accompanied by a wider distribution, is formed by **2a** ($d = 2 \pm 1 \mu\text{m}$).

5.2.2 Bending experiments

For the AFM bending experiments, the nanofibers were transferred to glass substrates structured with lithographically prepared channels to achieve a free-standing configuration. Figure 5.3(a) shows a schematic representation of the deformation set-up. A representative SEM image of suspended fibers can be found in the Supporting Information (SI 5.1). As a first step, we ensured that there was no indentation or compression of the nanofibers contributing to the bending experiments. Therefore, we recorded force-deformation curves on the supported segments of the samples. A typical measurement can be seen in Figure 5.3(b). There was no significant deformation visible for the typically applied loads.

For the actual bending experiments, we performed force-distance measurements on 30 to 40 positions along the free-standing nanofiber segments. The stiffness at the respective position was calculated from the slope of the force-distance curve. Towards the midpoint of the channel the measured stiffness decreased, and hence we obtained stiffness profiles along the whole free-standing segment Figure 5.3(c).

From the shape of the profiles, we determined the boundary conditions (i.e., the type of fixation) of each segment and the modulus of the nanofiber using models of classical beam theory.⁵⁸ A detailed discussion of the importance of the boundary conditions, of the analytical models, and of the experimental procedure can be found in the literature.⁴⁰ The two most commonly applied models are the double-clamped beam model (DCBM), where the ends of the sample are firmly fixed, and the simply supported beam model (SSBM), where the ends are assumed to rotate freely.^{53,58,59}

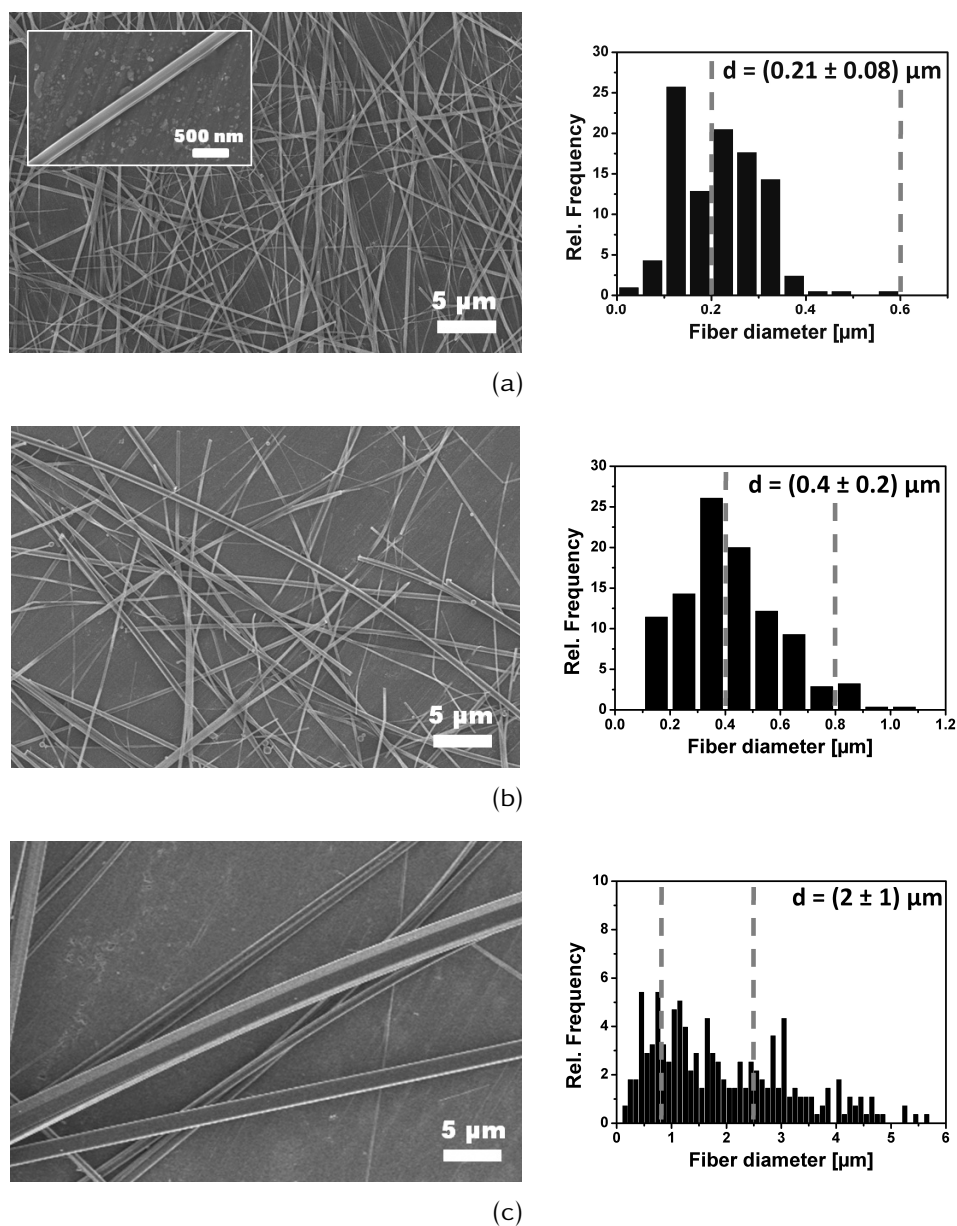


Figure 5.2 (a) SEM image and size distribution of nanofibers of **1a**. The average diameter d is $0.21 \pm 0.08 \mu\text{m}$. The SEM overview image and the inset highlight the narrow size distribution and homogeneous structure of the nanofibers. (b) SEM image and size distribution of nanofibers of **1b** ($d = 0.4 \pm 0.2 \mu\text{m}$). (c) SEM image and size distribution of fibers of **2a** ($d = 2 \pm 1 \mu\text{m}$). The vertical dashed lines in the histograms indicate the minimal and maximal size of each fiber type for which successful AFM bending measurements were performed.

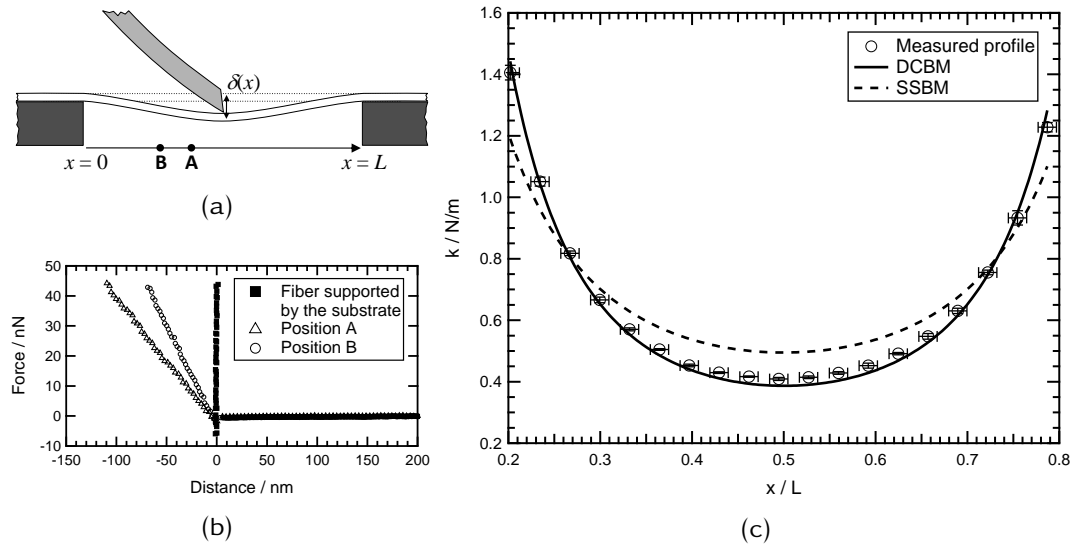


Figure 5.3 (a) Sketch of the experimental setup. (b) Exemplary force deformation curves obtained on the bare substrate, around the middle of the supported segment (A) and at an intermediate position between edge and midpoint (B). (c) Exemplary stiffness profile of a supported segment of 1a. The data was obtained by averaging over 6 measurements on the same segment and fitted with the DCBM (solid line) and SSBM (dashed line). The DCBM is clearly valid.

We observed both types of behavior and could clearly distinguish between both cases. However, effects like a slight slackness of the sample or defects at the fixation points can lead to profiles that resemble a SSBM-type behavior although the ends are clamped, and hence can lead to an inaccurate interpretation of the data. On the contrary, when a profile matches the DCBM, the experimental conditions have to be in perfect agreement with the modeled clamped conditions, and therefore the interpretation is much more reliable. To avoid uncertainties, we decided to use only segments that clearly corresponded to the DCBM for the calculation of the modulus.

For the DCBM, the stiffness $k(x)$ at a given position x is

$$k(x) = \frac{3L^3EI}{(L-x)^3x^3} \quad (5.1)$$

Here, L is the length of the free-standing segment and x is the position where the load is applied, with $0 \leq x \leq L$. EI is the flexural rigidity and defined as the product of the modulus E and the area moment of inertia I . The measured profiles were fitted with EI as the only free parameter. To obtain E , we imaged each individual nanofiber with AFM and calculated I from the respective cross sections. This is a

highly important step, since the flexural rigidity scales quartic with the diameter of the samples. By imaging each individual investigated nanofiber and calculating the correct area moment of inertia, our evaluation of the mechanical data is not based on any assumptions concerning size and shape of the cross section. An exemplary cross section can be found in the Supporting Information (SI 5.2).

It can be seen from Equation (5.1) that the spring constants of multiple nanofiber segments can be normalized so that one obtains

$$k_{\text{norm}}(x) = \frac{3E}{\left(1 - \frac{x}{L}\right)^3 \left(\frac{x}{L}\right)^3} \quad (5.2)$$

with

$$k_{\text{norm}}(x) = \frac{k(x)L^3}{I} \quad (5.3)$$

We averaged the normalized spring constants of all investigated nanofiber segments and fitted the data with Equation (5.2) (Figure 5.4). The resulting modulus for **1a** was 2.3 ± 0.3 GPa. In the same way, we determined the Young's moduli of **1b** (2.1 ± 0.1 GPa) and **2a** (3.3 ± 0.3 GPa). The quality of the fit shows the excellent agreement of the deformation profiles with the DCBM. Therefore, the error bars are a direct measure of the uncertainty of the determined Young's modulus which is caused by defects and inhomogeneities of the self-assembled nanofibers and by uncertainties of the measurements. Those may be attributed to the error of the AFM cantilever spring constant (<10%), the channel width (<5%) and the determined area moment of inertia (<20%).

Since the molecular structure suggests highly anisotropic mechanical properties for the nanofibers, the effect of anisotropy should also be discussed. When bent, the upper part of a beam is subjected to compression while the lower part is subjected to extension. This leads to additional shear forces within the beam that become important in anisotropic materials when the length-to-radius ratio of the bent segment becomes $\frac{L}{R} \leq 4\sqrt{\frac{E}{G}}$.⁶⁰ In this case, shearing can be accounted for by defining an apparent bending modulus E_b that is related to the true elastic modulus E and the shear modulus G via^{45,47}

$$\frac{1}{E_b} = \frac{1}{E} + 12f_s \frac{R^2}{L^2} \frac{1}{G} \quad (5.4)$$

for samples with a circular cross section. L is the length and R the radius of the free-standing segment, f_s is the form factor of shear, which is related to the sample's cross section (e.g., 10/9 for a cylinder).⁶¹ For more arbitrary cross sections, the area

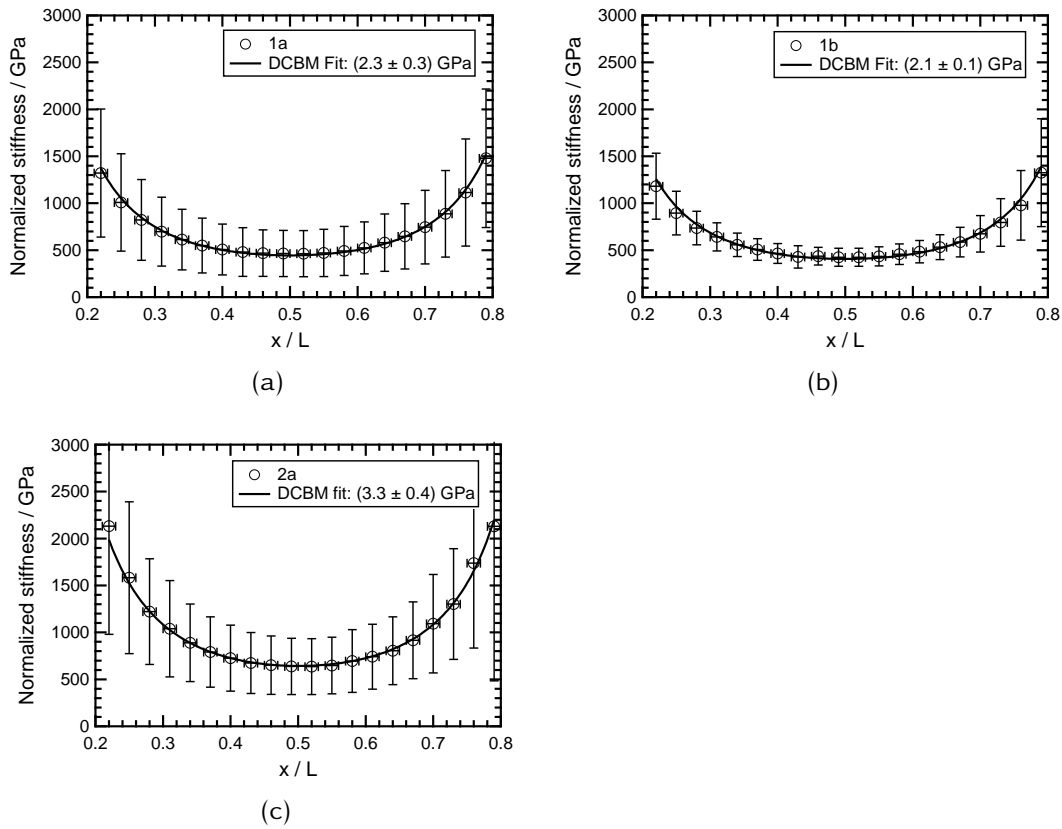


Figure 5.4 Results of the spatially resolved bending experiments. The shape of all profiles shows excellent agreement with the DCBM. The larger size of the error bars compared to the individual measurements (as seen in Figure 5.3(c)) is a consequence and a direct measure of the distribution and uncertainty of the determined moduli amongst individual specimen of one sample.

and second moment of area cannot be expressed by the radius and therefore

$$\frac{1}{E_b} = \frac{1}{E} + 48f_s \frac{I}{AL^2} \frac{1}{G} \quad (5.5)$$

In any way, if shearing plays a dominant role, G and consequently E can be determined from the slope of $1/E_b$ versus $I/(AL^2)$. However, for all investigated systems, no significant influence of shearing could be observed (Supporting Information SI 5.3). Therefore, the anisotropy is only of minor importance for the bending behavior under our measurement conditions, and the determined values can be regarded as the true Young's moduli in the axial direction of the nanofibers.

5.2.3 Comparison of the systems

To determine the effect of the molecular structure on the mechanical properties, we have to differentiate between two effects: The difference arising from the different thicknesses of the individual nanofiber types and additional changes of the material properties. First, we compared the stiffness of the free-standing nanofiber segments (Figure 5.5(a)). Since the measurements had to be performed on different channel widths, we normalized the stiffness with respect to the channel width to obtain the apparent flexural rigidity, irrespective of the boundary conditions found during evaluation of the modulus. The rigidity of the free-standing segments of **1b** was one to two orders of magnitude higher than that of **1a**. For **2a**, it was up to three orders of magnitude higher. This increase is a consequence of the increased diameters of the investigated nanofibers, since the rigidity is proportional to the fourth power of the radius.

In contrast, the modulus is comparable for all systems. For **1a**, we found a modulus of 2.3 ± 0.3 GPa, for **1b** 2.1 ± 0.1 GPa and for **2a** (3.3 ± 0.3 GPa). These values are in good agreement with those found for electrospun polyamide fibers.⁶² The result of **2a** also confirms a study where self-assembled aggregates of the same molecule were prepared under different preparation conditions and a modulus of 3 ± 1 GPa was found.⁴⁰ Therefore, the change of stiffness by up to three orders of magnitude can clearly be identified as a pure size effect without equivalent changes of the material properties. This is a rather surprising finding, since it suggests that the influence of the investigated molecular structures on the mechanical properties is small. In addition to the absolute value, we also investigated the distribution of the individual moduli which was also comparable for all systems (Figure 5.5(b)).

From a molecular point of view, there are several contributions to the mechanical stability of the BTA aggregates. The formation of intracolumnar hydrogen bonds and the intercolumnar interactions governed by macrodipoles are most important.^{18,63} The size and nature of the substituents (linear, branched, cyclic) play an additional role. The calculations of *Stals* et al. on the effect of the amide connectivity on the aggregate stability suggest that BTAs based on trimesic acid **1** are able to form stronger hydrogen bonds.¹² Therefore one would expect that **1a** and **1b** have a higher elastic modulus than **2a**. However, our measurements indicate a slightly higher modulus of **2a** compared to **1a** and **1b**. There are two explanations for our findings. If the volume of the substituent is increased, the intercolumnar distance becomes larger. Consequently, the strength of the macrodipole interactions is lowered. Concomitantly,

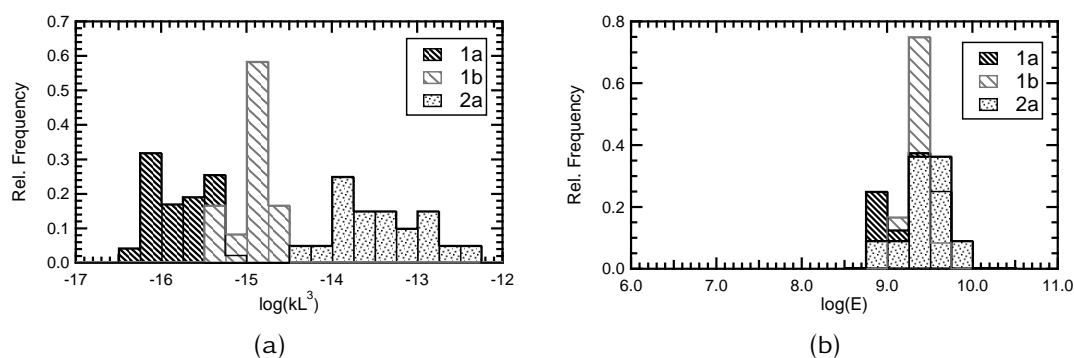


Figure 5.5 (a) Apparent flexural rigidity of all investigated nanofiber segments. The stiffness was measured at the midpoint of the free-standing segments. Please note that the x axis has a logarithmic scaling. The rigidity of **1b** is one to two, and of **2a** is up to three orders of magnitude higher than that of **1a**. (b) Distribution of the calculated modulus for all three investigated systems. The results for all systems are comparable.

the number of columns per cross-sectional area decreases. Both effects contribute to the lower modulus of **1a** and **1b** compared to **2a**.

5.3 Conclusions

We have compared self-assembled nanofibers of three BTA derivatives with different molecular structures. We recorded SEM images to investigate their morphological differences and found that **1a** forms nanofibers with an average diameter of $0.21 \pm 0.08 \mu\text{m}$, followed by the nanofibers of **1b** with an average diameter of $0.4 \pm 0.2 \mu\text{m}$. The fibers of **2a** had an average diameter of $2 \pm 1 \mu\text{m}$, with a much wider distribution. We compared the mechanical properties as determined via nanomechanical AFM bending experiments of all systems and found that the flexural rigidity of **1b** is one to two, and of **2a** is up to three orders of magnitude higher than that of **1a**. We calculated the modulus of all three systems and obtained $2.3 \pm 0.3 \text{ GPa}$ for **1a**, $2.1 \pm 0.1 \text{ GPa}$ for **1b**, and $3.3 \pm 0.3 \text{ GPa}$ for **2a**. This showed that the dramatic difference of the stiffness was purely a size effect. In conclusion, our findings demonstrate that while the molecular structure alters the morphology and therefore the absolute stiffness of the self-assembled nanofibers, the elastic modulus of all systems is similar, even over a large range of sizes from about 100 nm to 3 μm . This allows tuning the stiffness of the nanofibers. The results of our study are a first step towards the application of self-assembled BTA nanofibers as components

for bottom-up functional materials with tailored properties from the nano- to the microscale.

5.4 Experimental Section

Synthesis of the 1,3,5-trisamides. **1a**, **1b** and **2a** were synthesized as described in the literature.^{64–66}

Nanofiber preparation. Compound **1a** or **2a** (600 ppm) in 2,2,4,4,6,8,8-heptamethylnonane (HMN) was dissolved under reflux at 240 °C and cooled to room temperature. This suspension (200 μL) was transferred to a custom-made high-pressure pan and heated to 240 °C for 10 min in the dropping point cell FP83HT from Mettler Toledo. By cooling from 240 °C to 30 °C at 20 Kmin^{-1} (controlled with the Mettler Toledo central processor FP90), a controlled self-assembly into fibers was achieved. For the preparation of **1b**, a solution (500 ppm) was treated like described above. The cooling rate was 5 Kmin^{-1} . The samples for the bending experiments were prepared by wetting structured glass substrates (GeSiM GmbH, Gro erkmannsdorf, Germany; channel widths 5 and 10 μm for **1a**, 10 μm for **1b**, and 30 μm for **2a**) with blank HMN (15 μL), adding the nanofiber suspension (0.5 μL), and allowing the samples to dry overnight.

SEM imaging. For preparation of the SEM samples, the nanofiber suspensions (5 μL) were placed in DSC aluminum pans and the solvent was evaporated under reduced pressure. The samples were sputtered with platinum (2.0 nm) in a Cressington sputter coater 208HR to enhance conductivity. SEM images were recorded on a Zeiss LEO 1530 FESEM instrument (Zeiss, Jena, Germany). For the size distributions, over 200 individual nanofibers of each system were evaluated.

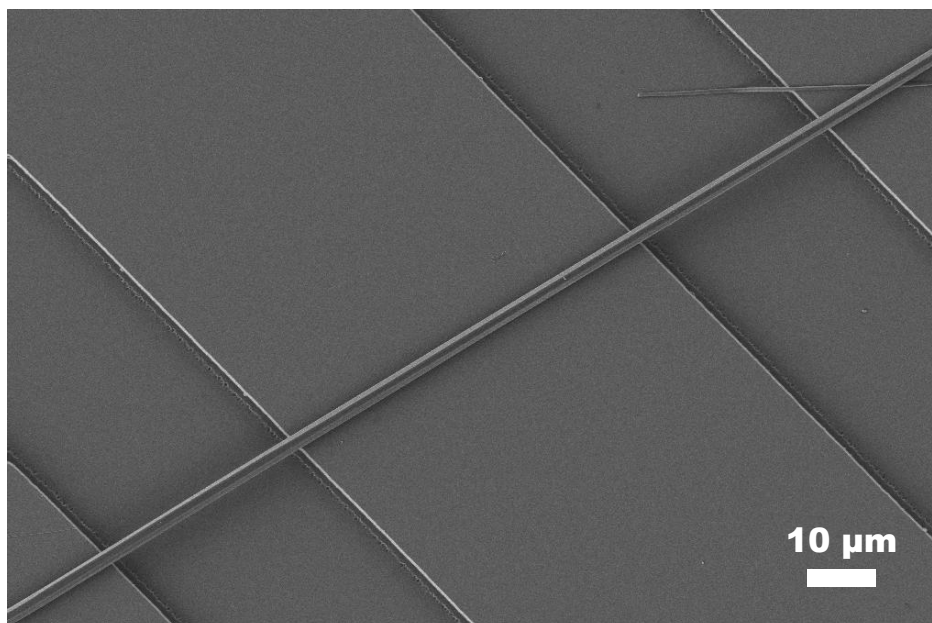
AFM measurements. All AFM measurements were performed on a Nanowizard I apparatus (JPK Instruments AG, Berlin, Germany), combined with a Zeiss Axiovert 200 microscope and a Zeiss LD A-Plan[®] Ph1 objective lens (20x, numerical aperture 0.3, working distance 4.3 mm). The bending experiments were performed as previously reported,⁴⁰ using tipless NSC12/AIBS cantilevers (μMasch , Tallinn, Estonia). For **1a**, the typical load was 50 nN, which resulted in typical deformations of 100–200 nm at the midpoint. In addition, 50 force-distance measurements with a maximum load of 150 nN were performed on 10 individual nanofibers on segments supported by the substrate, to prove that there was no unwanted compression of

the nanofibers during the bending experiments. For the measurements on **1b**, the typical load was around 30 nN. For **2a**, the loads were between 50 and 100 nN in order to achieve comparable deformations. None of the systems showed unwanted compression under the tested loads of up to 150 nN. The dimensions of the mechanically investigated nanofibers were determined on the segments supported by the substrates in intermittent contact mode with sharp imaging cantilevers (Olympus OMCL-AC160TS, Atomic Force, Mannheim, Germany). All data were processed and evaluated using self-written procedures in Igor Pro 6 (Wavemetrics Inc., Portland, USA). For the calculation of Young's modulus, the data from 96 measured profiles on 16 nanofibers of **1a**, 72 profiles on 10 nanofibers of **1b** and 66 profiles on 10 fibers of **2a** were used.

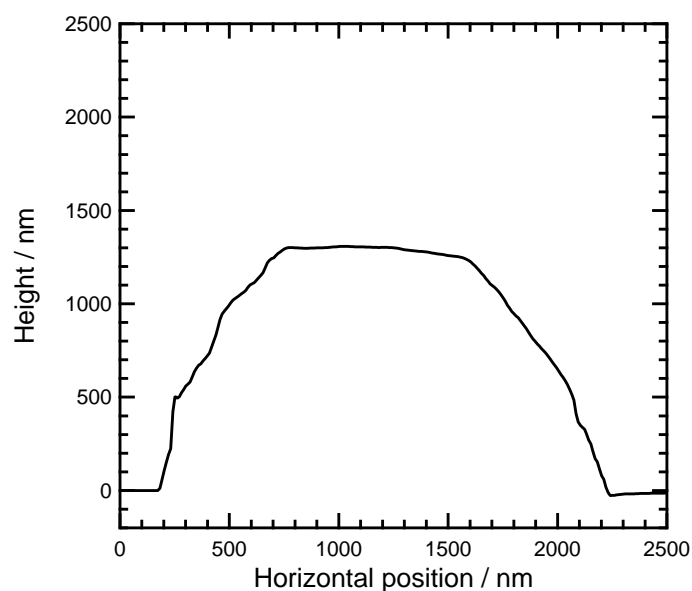
Acknowledgements

This work received financial support from the German Science Foundation (Deutsche Forschungsgemeinschaft) within the SFB 840, project B8. We thank Sandra Ganzleben for the synthesis of the 1,3,5-benzenetrisamides and Benedikt Neugirg for his contribution to the experimental part of this work. DK, JCS and JWN acknowledge the support of the Elite Network of Bavaria.

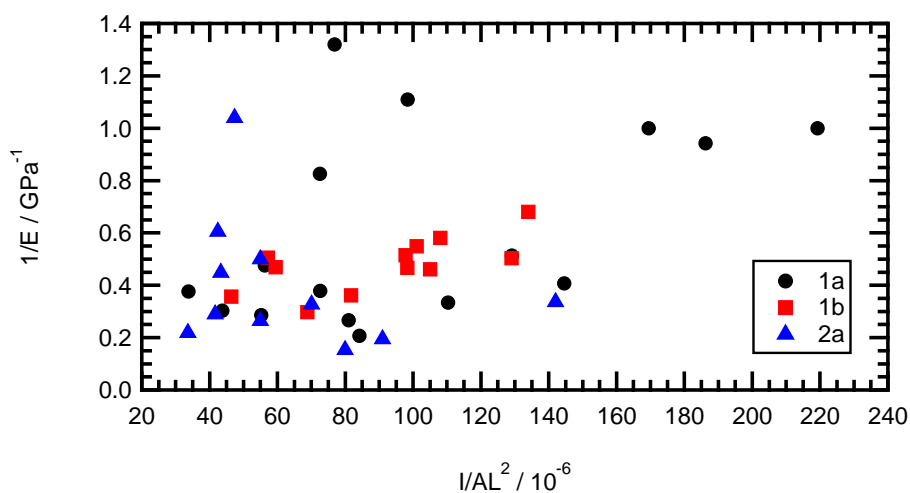
5.5 Supporting Information



SI 5.1 Representative SEM image of a fiber of **2a** deposited on a structured glass substrate: The fiber is free-standing in the channel areas, while it is supported on the elevated areas.



SI 5.2 Exemplary cross section of a fiber of **2a** as obtained by AFM imaging. It can be seen that the cross section deviates from a cylindrical shape. Therefore, we imaged each individual investigated fiber and calculated the area moment of inertia I directly from the AFM-image in order to calculate Young's modulus.



SI 5.3 Investigation of the shearing influence on the measured moduli. The data was calculated using Equation (5.5). It can be seen that for **1a** and **2a**, no influence of shearing can be observed. Only for **1b**, a slope of the data points can be seen which, although ill-defined, could be attributed to shearing. However, the contribution is too small for a reliable determination of G which can be seen from the scatter of the data. Therefore, even if shearing contributes to the measurements of **1b**, the contribution is insignificantly small and the calculated bending modulus E_b can be regarded as the true Young's modulus E .

5.6 References

- [1] S. Agarwal, J. H. Wendorff, A. Greiner, *Polymer* **2008**, *49*, 5603–5621.
- [2] R. S. Barhate, S. Ramakrishna, *Journal of Membrane Science* **2007**, *296*, 1–8.
- [3] P. Moriarty, *Reports on Progress in Physics* **2001**, *64*, 297–381.
- [4] P. Fratzl, R. Weinkamer, *Progress in Materials Science* **2007**, *52*, 1263–1334.
- [5] Y. N. Xia, P. D. Yang, Y. G. Sun, Y. Y. Wu, B. Mayers, B. Gates, Y. D. Yin, F. Kim, Y. Q. Yan, *Advanced Materials* **2003**, *15*, 353–389.
- [6] J. H. Fendler, F. C. Meldrum, *Advanced Materials* **1995**, *7*, 607–632.
- [7] A. Greiner, J. H. Wendorff, *Angewandte Chemie-International Edition* **2007**, *46*, 5670–5703.
- [8] I. A. W. Filot, A. R. A. Palmans, P. A. J. Hilbers, R. A. V. Santen, E. A. Pidko, T. F. A. Greef, *The Journal of Physical Chemistry B* **2010**, *114*, 13667–13674.
- [9] M. Kristiansen, P. Smith, H. Chanzy, C. Baerlocher, V. Gramlich, L. Mccusker, T. Weber, P. Pattison, M. Blomenhofer, H.-W. Schmidt, *Crystal Growth & Design* **2009**, *9*, 2556–2558.
- [10] M. P. Lightfoot, F. S. Mair, R. G. Pritchard, J. E. Warren, *Chemical Communications* **1999**, 1945–1946.
- [11] M. M. J. Smulders, A. P. H. J. Schenning, E. W. Meijer, *Journal of the American Chemical Society* **2008**, *130*, 606–611.
- [12] P. J. M. Stals, J. C. Everts, R. D. Bruijn, I. A. W. Filot, M. M. J. Smulders, R. Martín-Rapún, E. A. Pidko, T. F. A. D. Greef, A. R. A. Palmans, E. W. Meijer, *Chemistry - A European Journal* **2010**, *16*, 810–821.
- [13] M. Wegner, D. Dudenko, D. Sebastiani, A. R. A. Palmans, T. F. A. Greef, R. Graf, H. W. Spiess, *Chemical Science* **2011**, *2*, 2040–2049.
- [14] P. J. M. Stals, M. M. J. Smulders, R. Martín-Rapún, A. R. A. Palmans, E. W. Meijer, *Chemistry - A European Journal* **2009**, *15*, 2071–2080.
- [15] Y. Harada, Y. Matsunaga, *Bulletin of the Chemical Society of Japan* **1988**, *61*, 2739–41.
- [16] Y. Matsunaga, Y. Nakayasu, S. Sakai, M. Yonenaga, *Molecular Crystals and Liquid Crystals* **1986**, *141*, 327–333.
- [17] Y. Matsunaga, N. Miyajima, Y. Nakayasu, S. Sakai, M. Yonenaga, *Bulletin of the Chemical Society of Japan* **1988**, *61*, 207–10.
- [18] A. Timme, R. Kress, R. Q. Albuquerque, H.-W. Schmidt, *Chemistry - A European Journal* **2012**, *18*, 8329–8339.
- [19] J. J. van Gorp, J. A. J. M. Vekemans, E. W. Meijer, *Journal of the American Chemical Society* **2002**, *124*, 14759–14769.
- [20] K. Hanabusa, C. Koto, M. Kimura, H. Shirai, A. Kakehi, *Chemistry Letters* **1997**, 429–430.

- [21] N. Mohmeyer, H.-W. Schmidt, *Chemistry - A European Journal* **2007**, *13*, 4499–4509.
- [22] S. Y. Ryu, S. Kim, J. Seo, Y.-W. Kim, O.-H. Kwon, D.-J. Jang, S. Y. Park, *Chemical Communications* **2004**, 70–71.
- [23] Y. Yasuda, E. Iishi, H. Inada, Y. Shirota, *Chemistry Letters* **1996**, 575–576.
- [24] A. Bernet, M. Behr, H.-W. Schmidt, *Soft Matter* **2011**, *7*, 1058–1065.
- [25] D. K. Kumar, D. A. Jose, P. Dastidar, A. Das, *Chemistry of Materials* **2004**, *16*, 2332–2335.
- [26] N. E. Shi, H. Dong, G. Yin, Z. Xu, S. H. Li, *Advanced Functional Materials* **2007**, *17*, 1837–1843.
- [27] N. Shi, G. Yin, M. Han, Z. Xu, *Colloids and Surfaces B: Biointerfaces* **2008**, *66*, 84–89.
- [28] T. Mes, M. M. J. Smulders, A. R. A. Palmans, E. W. Meijer, *Macromolecules* **2010**, *43*, 1981–1991.
- [29] J. Roosma, T. Mes, P. Leclere, A. R. A. Palmans, E. W. Meijer, *Journal of the American Chemical Society* **2008**, *130*, 1120–1121.
- [30] F. Abraham, H.-W. Schmidt, *Polymer* **2010**, *51*, 913–921.
- [31] D. P. Erhard, R. Giesa, V. Altstädt, H.-W. Schmidt, *Journal of Applied Polymer Science* **2010**, *115*, 1247–1255.
- [32] D. P. Erhard, D. Lovera, W. Jenninger, J. Wagner, V. Altstädt, H.-W. Schmidt, *Macromolecular Chemistry & Physics* **2010**, *211*, 2179–2186.
- [33] N. Mohmeyer, N. Behrendt, X. Zhang, P. Smith, V. Altstädt, G. M. Sessler, H.-W. Schmidt, *Polymer* **2007**, *48*, 1612–1619.
- [34] N. Mohmeyer, B. Müller, N. Behrendt, J. Hillenbrand, M. Klaiber, X. Zhang, P. Smith, V. Altstädt, G. M. Sessler, H.-W. Schmidt, *Polymer* **2004**, *45*, 6655–6663.
- [35] N. Mohmeyer, H.-W. Schmidt, P. M. Kristiansen, V. Altstädt, *Macromolecules* **2006**, *39*, 5760–5767.
- [36] K. Stoll, K. Hoffmann, B. Rotzinger, H.-W. Schmidt, Process for Improving the Flow Properties of Polymer Melts, WO 2007039471, **2007**.
- [37] F. Abraham, S. Ganzleben, D. Hanft, P. Smith, H.-W. Schmidt, *Macromolecular Chemistry & Physics* **2010**, *211*, 171–181.
- [38] M. Blomenhofer, S. Ganzleben, D. Hanft, H.-W. Schmidt, M. Kristiansen, P. Smith, K. Stoll, D. Mäder, K. Hoffmann, *Macromolecules* **2005**, *38*, 3688–3695.
- [39] J. Varga, K. Stoll, A. Menyhárd, Z. Horváth, *Journal of Applied Polymer Science* **2011**, *121*, 1469–1480.
- [40] D. Kluge, F. Abraham, S. Schmidt, H. W. Schmidt, A. Fery, *Langmuir* **2010**, *26*, 3020–3023.
- [41] E. P. S. Tan, C. T. Lim, *Composites Science and Technology* **2006**, *66*, 1102–1111.

- [42] J. R. Withers, D. E. Aston, *Advances in Colloid and Interface Science* **2006**, *120*, 57–67.
- [43] M. K. Shin, S. I. Kim, S. J. Kim, S.-K. Kim, H. Lee, *Applied Physics Letters* **2006**, *88*, 193901–3.
- [44] E. P. S. Tan, C. T. Lim, *Applied Physics Letters* **2004**, *84*, 1603–1605.
- [45] L. Yang, C. F. C. Fitie, K. O. V. D. Werf, M. L. Bennink, P. J. Dijkstra, J. Feijen, *Biomaterials* **2008**, *29*, 955–962.
- [46] C. Guzman, S. Jeney, L. Kreplak, S. Kasas, A. J. Kulik, U. Aebi, L. Forro, *Journal of Molecular Biology* **2006**, *360*, 623–630.
- [47] A. Kis, S. Kasas, B. Babic, A. J. Kulik, W. Benoit, G. A. D. Briggs, C. Schonenberger, S. Catsicas, L. Forro, *Physical Review Letters* **2002**, *89*, 248101.
- [48] S. Orso, U. Wegst, E. Arzt, *Journal of Materials Science* **2006**, *41*, 5122–5126.
- [49] D. R. Stamov, T. A. K. Nguyen, H. M. Evans, T. Pfohl, C. Werner, T. Pompe, *Biomaterials* **2011**, *32*, 7444–7453.
- [50] W. Xu, P. J. Mulhern, B. L. Blackford, M. H. Jericho, I. Templeton, *Scanning Microscopy* **1994**, *8*, 499–506.
- [51] J. P. Salvetat, G. A. D. Briggs, J. M. Bonard, R. R. Bacsá, A. J. Kulik, T. Stockli, N. A. Burnham, L. Forro, *Physical Review Letters* **1999**, *82*, 944–947.
- [52] E. W. Wong, P. E. Sheehan, C. M. Lieber, *Science* **1997**, *277*, 1971–1975.
- [53] Y. X. Chen, B. L. Dorgan, D. N. Mcilroy, D. E. Aston, *Journal of Applied Physics* **2006**, *100*, 104301.
- [54] B. Wu, A. Heidelberg, J. J. Boland, *Nature Materials* **2005**, *4*, 525–529.
- [55] H. Zhang, J. Tang, L. Zhang, B. An, L. C. Qin, *Applied Physics Letters* **2008**, *92*, 173121.
- [56] X. Y. Ling, I. Y. Phang, W. Maijenburg, H. Schonherr, D. N. Reinhoudt, G. J. Vancso, J. Huskens, *Angewandte Chemie-International Edition* **2009**, *48*, 983–985.
- [57] X. Y. Ling, I. Y. Phang, H. Schonherr, D. N. Reinhoudt, G. J. Vancso, J. Huskens, *Small* **2009**, *5*, 1428–1435.
- [58] J. Gere, B. Goodno, *Mechanics of Materials*, Cengage Learning, London, 7th ed., **2008**.
- [59] W. J. Mai, Z. L. Wang, *Applied Physics Letters* **2006**, *89*, 073112.
- [60] L. Yang, K. O. V. D. Werf, C. F. C. Fitie, M. L. Bennink, P. J. Dijkstra, J. Feijen, *Biophysical Journal* **2008**, *94*, 2204–2211.
- [61] J. M. Gere, S. P. Timoshenko in *Mechanics of Materials*, Chapman & Hall, London, 3rd, **1991**, p. 692.
- [62] C. L. Pai, M. C. Boyce, G. C. Rutledge, *Polymer* **2011**, *52*, 2295–2301.
- [63] A. Sakamoto, D. Ogata, T. Shikata, O. Urakawa, K. Hanabusa, *Polymer* **2006**, *47*, 956–960.

- [64] D. Mäder, K. Hoffmann, H.-W. Schmidt, WO 03102069 A1, **2003**.
- [65] H.-W. Schmidt, M. Blomenhofer, K. Stoll, H.-R. Meier, WO 2004072168 A2, **2004**.
- [66] H.-W. Schmidt, P. Smith, M. Blomenhofer, WO 02/46300 A2, **2002**.

Comparison of Self-Assembled and Electrospun Trisamide Fibers

Reproduced with permission from:

D. Kluge, J. C. Singer, B. R. Neugirg, J. W. Neubauer, H.-W. Schmidt, A. Fery, TOP-DOWN MEETS BOTTOM-UP: A COMPARISON OF THE MECHANICAL PROPERTIES OF MELT ELECTROSPUN AND SELF-ASSEMBLED 1,3,5-BENZENETRISAMIDE FIBERS. *Polymer* **2012**, *53*, 5754-5759.

© 2012 Elsevier Ltd.

ABSTRACT

1,3,5-Benzenetrisamides (BTAs) are a prominent class of low-molecular weight compounds in supramolecular chemistry. They are well-known to self-assemble into micro- and nanofibers in a bottom-up approach. At the same time, BTAs are also suitable for top-down processing by melt electrospinning. In this work, we demonstrate for the first time that both approaches lead to mechanically robust BTA fibers. We compare self-assembled and electrospun fibers of N,N',N''-tripropyl-1,3,5-benzenetricarboxamide on multiple length scales. X-ray diffraction (XRD) reveals the same crystal structure independently from the preparation method. Using scanning electron microscopy (SEM), we observe significantly different morphologies of both fiber types on the sub-micron-scale. However, atomic force microscopy (AFM) bending experiments show that despite differences in morphology, Young's modulus is comparable for both types and in the lower GPa range (3-5 GPa). Thus, both top-down and bottom-up techniques with their complementary features in terms of accessible structures and potential applications are available for this class of materials.

6.1 Introduction

The controlled fabrication of well-defined microscopic fibrillar structures has become one of the main topics in materials science.¹⁻³ Networks and nonwovens based on these structures possess exceptional properties, such as high surface area, possibility for easy functionalization and superior mechanical strength.⁴ These are promising features for applications such as tissue engineering, drug delivery, sensors, micro-/nanoelectromechanical systems (MEMS/NEMS), and filtration.³⁻⁷ Especially fibers of sub-micron or nanoscale diameters are of interest due to their surface to volume ratio and the possibility to form structures with small mesh-sizes. Two approaches are feasible to access these length scales: Bottom-up approaches rely on the self-assembly of smaller units (even single molecules) to hierarchical structures.^{8,9} Top-down approaches, such as electrospinning, shape the materials directly into the desired structure. Especially for fibers and nonwovens, a great variety of structures has been demonstrated.¹⁰

Both techniques are complementary in various ways: Since self-assembly allows simultaneous formation and growth of many fibers in a given volume, it is preferable

in terms of processing times, especially for upscaling. In addition, if the processing conditions are chosen well, smaller fiber diameters are accessible in a more simple fashion than in electrospinning.^{8,11} On the downside, self-assembled fibers have smaller length and random orientation since they grow from many nuclei.

The advantage of electrospinning is that fibers can easily be formed with macroscopic length and well-defined orientation on macroscopic length scales. This even allows the controlled formation of superstructures at the micrometer level and above. However, the processing times are longer since electrospinning is a sequential process, in which the time necessary to form fibers is proportional to the total fiber length. To offer the highest flexibility, it would be desirable to switch from one to the other approach for the same class of materials - especially for the formation of hierarchically organized structures which span multiple length scales.

Lately, the self-assembly of 1,3,5-benzenetrisamides (BTAs) into fibrillar structures has attracted increasing research interest.^{12,13} The benzene core realizes a planar and symmetric moiety and three amide groups allow the formation of strong hydrogen bonds between adjacent molecules resulting in supramolecular architectures.¹⁴ BTAs are well-known as nucleating agents for polyvinylidene fluoride and polypropylene.¹⁵⁻¹⁸ Moreover, they are applied as organo- and hydrogelators,¹⁹⁻²² as additives to improve the charge storage capability of electret materials²³ and as supramolecular materials.^{24,25}

In addition to their bottom-up properties, we recently reported on the melt electrospinning of various BTAs and 1,3,5-cyclohexanetrisamides into defined fine fibers with a narrow size distribution.²⁶ Although a high molecular mass polymer is not essential for obtaining uniform electrospun fibers,²⁷ electrospinning of low molecular weight substances is still unusual. BTAs form macrodipoles along the main axis of the column during the supramolecular assembly process within external electric fields and consequently offer excellent preconditions for electrospinning.²⁸⁻³⁰ The melt electrospinning of BTAs is an exciting new top-down approach for self-assembling systems. It offers the possibility to overcome the strict limitation of the self-assembly conditions and consequently opens up a wide field of new applications for BTAs.

For all applications, a reasonable mechanical stability is an essential prerequisite. However, regardless by which means the BTA fibers are prepared, the mechanical characterization on a micron- or sub-micron scale requires sophisticated methods. A powerful technique are nanomechanical bending experiments, which have

been used for the mechanical investigation of polymer nanofibers,^{31–33} biological materials,^{34–38} CNTs,^{39,40} and nanowires.^{41–43} In previous studies, we performed bending experiments on BTA micro- and nanofibers obtained via controlled self-assembly from nonpolar solvents. The experiments demonstrated that their molecular architecture allows control over the fiber morphology without decreasing their mechanical stability.^{44,45}

In this work, we address the question whether the properties of BTA fibers are affected by using a top-down approach instead of a bottom-up approach. For that purpose, we prepare fibers of the same 1,3,5-benzenetricarboxamide via self-assembly from solution and melt electrospinning. This allows us for the first time to compare crystal structure, morphology and nano-mechanical properties of BTA fibers prepared from the same material.

6.2 Results and Discussion

For the comparison, we prepared fibers of *N,N',N''*-tripropyl-1,3,5-benzenetricarboxamide **1** (Figure 6.1) via bottom-up (in the following termed SA-fibers) as well as top-down techniques (in the following termed ES-fibers). The SA-fibers were produced via controlled self-assembly by cooling of a solution of **1** in 2,2,4,4,6,8,8-heptamethylnonane (HMN). As top-down approach, we used melt electrospinning.

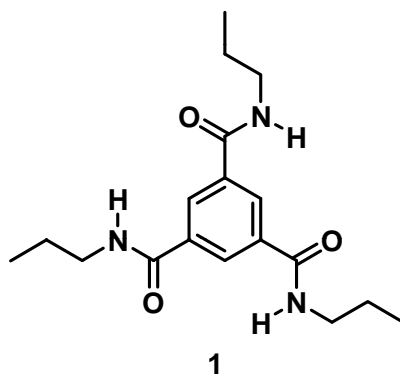


Figure 6.1 Chemical structure of *N,N',N''*-tripropyl-1,3,5-benzenetricarboxamide (**1**).

In order to investigate structural features on the Ångström-scale, we performed XRD measurements on chopped fibers. The X-ray diffractograms of both systems are identical, indicating the same crystal structure (Figure 6.2, see also Supporting Informa-

tion SI 6.1). The peaks of the SA fibers show a narrower full width at half maximum, what is expected since a higher degree of crystallinity is typically achieved by the bottom-up process. Due to hydrogen bonds, **1** packs in a primitive cubic [4⁶]-pcu supramolecular three dimensional network. The molecules are located in planes, which are stacked along the *c* axis.⁴⁶ While it is on first glance surprising that the electrospun material shows an as well-developed crystalline order as the self-assembled material, we demonstrated in previous work that ES-fibers are not formed from a molecular liquid state but from a melt which still consists of short columnar pre-aggregates.^{26,47} Thus the crystallization process is greatly accelerated due to the pre-aggregation of single molecules and leads to a poly-crystalline state.

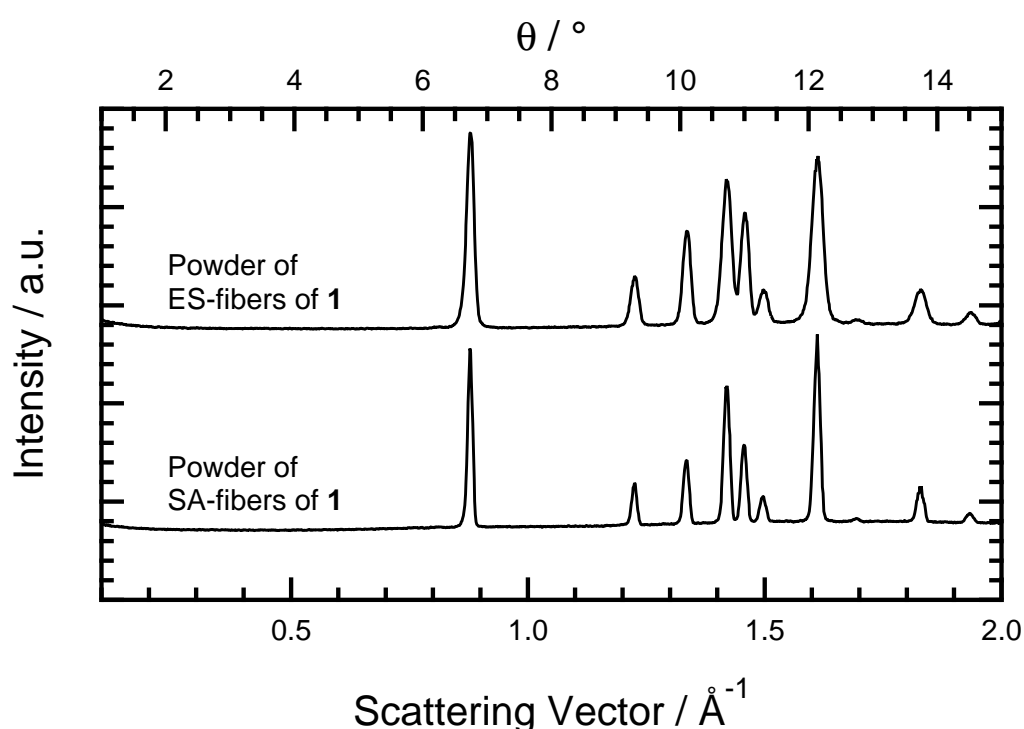


Figure 6.2 X-ray diffractograms of SA- and ES-fibers in powder form.

The microscopic morphology of the fibers was investigated via SEM. The average diameter of the SA- and ES-fibers, respectively, was $1.2 \pm 0.7 \mu\text{m}$ and $0.8 \pm 0.2 \mu\text{m}$ (size distribution diagrams see SI 6.2 and SI 6.3). Although the diameters of SA- and ES-fibers are comparable, the morphology of both systems shows significant differences. SA-fibers possess a hierarchical structure: they consist of bundles of individual strands that have an average diameter of about 100 nm (see inset of Figure 6.3, top, left). This bundle substructure is also visible in the irregular fracture sections of the SA-fibers (Figure 6.3, top, right). In contrast, ES-fibers exhibit a homogeneous, smooth surface without defects or pronounced surface features (Figure 6.3, bottom,

left). Even fracture sections of the ES-fibers are very smooth without any detailed sub-structure or obvious defects (Figure 6.3, bottom, right).

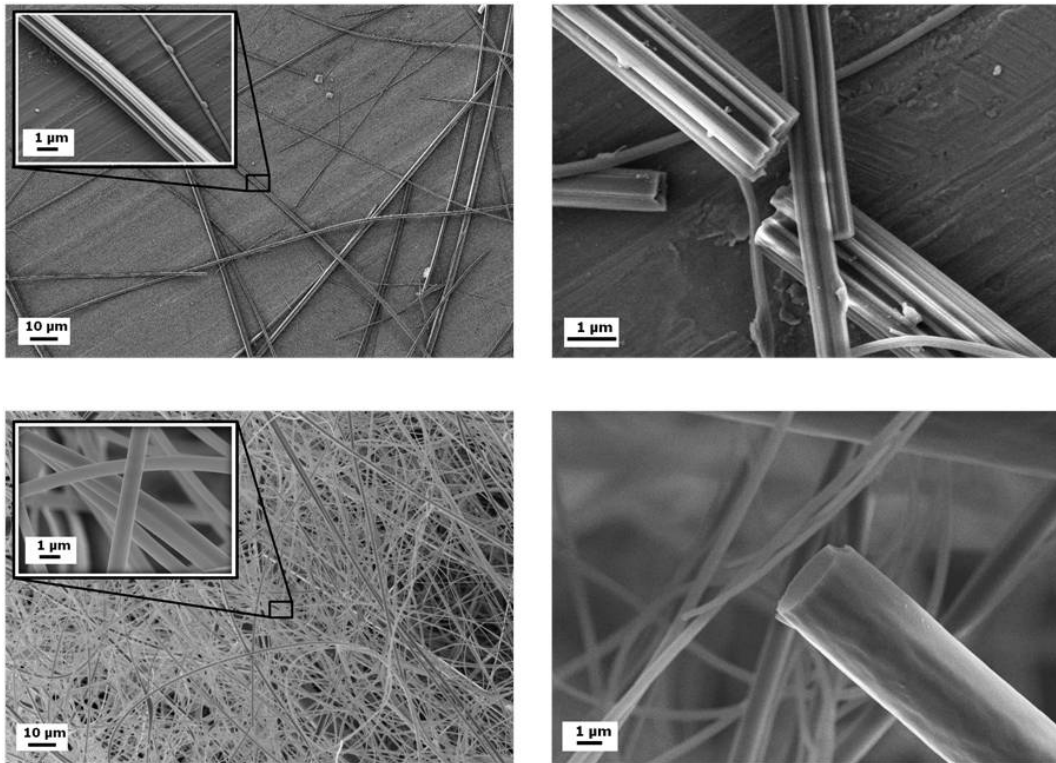


Figure 6.3 Top: SEM micrograph of the SA-fibers (left) and of a fracture section (right). Bottom: SEM micrograph of the ES-fibers of 1 (left) and of a fracture section (right). More detailed structures of the fibers are shown in the insets.

These differences in the microscopic morphology arise from the significantly different methods used to generate the two investigated fiber types. The crystallization process of the SA-fibers is much slower, allowing the development of larger crystals which then bundle into fibers. This explains the broader diameter distribution found for SA-fibers. In contrast, during electrospinning, ES-fibers are obtained from molten material, resulting in a homogenous strand.

In order to evaluate the mechanical properties of both systems, we performed nanomechanical bending experiments using an atomic force microscope (AFM). A detailed description of the theoretical background and experimental procedures can be found elsewhere.⁴⁴ Both fiber types were transferred to microstructured glass substrates (Figure 6.4) to achieve a free-standing configuration (Figure 6.5(a)). In this configuration, no deformation was observed when applying a vertical load to the segments supported by the substrate (Figure 6.5(b)). Therefore, only bending defor-

mations are measured when applying a load to the free-standing segments over the gap and the results can be evaluated with classical beam theory.⁴⁸

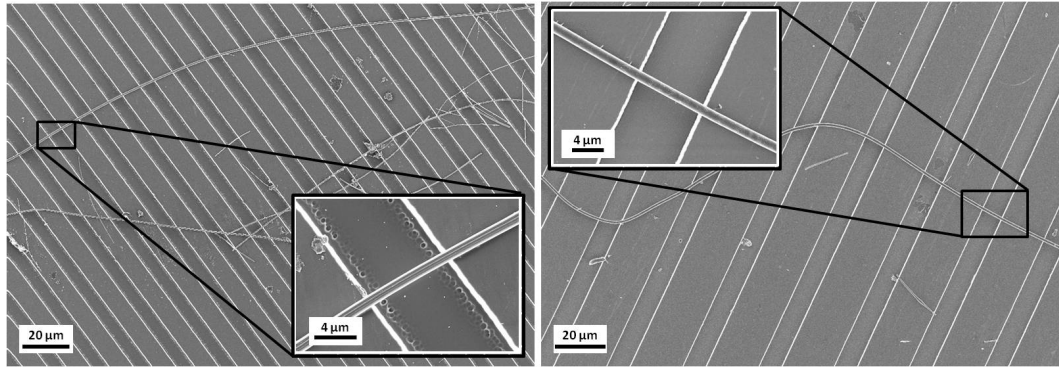


Figure 6.4 SA-fibers (left) and ES-fibers (right) on microstructured glass substrates for AFM bending experiments.

We recorded stiffness profiles by measuring the stiffness $k(x)$ at several positions x along the free-standing segment (Figure 6.5(c)) and calculated Young's modulus E of each investigated segment by fitting the profiles with the double-clamped beam model Equation (6.1).^{41,44,48}

$$k(x) = \frac{3L^3EI}{(L-x)^3 x^3} \quad (6.1)$$

Here, L is the length of the free-standing segment and I is the area moment of inertia. We imaged each investigated sample with the AFM to obtain the correct fiber thickness and shape to avoid errors as I shows quartic scaling with the radius.

Since Young's modulus is a material property, it is possible to normalize the profiles of all investigated SA- and ES-fibers, respectively, to calculate the averaged values.⁴⁵ The resulting Young's moduli were $E_{SA} = 3.6 \pm 0.4$ GPa and $E_{ES} = 4.7 \pm 0.6$ GPa (see SI 6.4 for more detailed data). In addition, we calculated the modulus of each fiber individually and determined the distributions (Figure 6.5(d)). While the ES-fibers show a slightly higher average modulus than the SA-fibers, the distributions are similar for both systems. We also investigated if shearing affects the measurements, but found no influence (see SI 6.5).

Our experiments show that the moduli of SA- and ES-fibers are in the same range and comparable to those of (semi)crystalline or glassy polymers like PVC and PMMA, common fiber materials like nylon and electrospun collagen fibers.^{33,49} The elastic properties of the fibers are also in good agreement with BTAs with different molecular structure where Young's moduli between 2 and 4 GPa have been

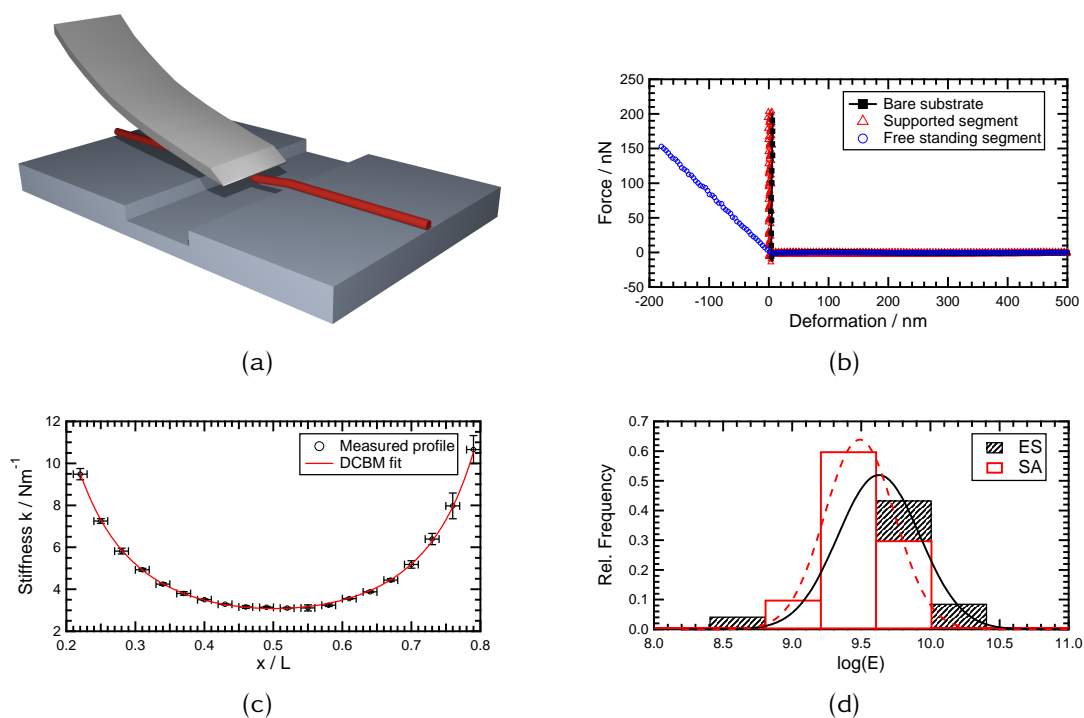


Figure 6.5 (a) Schematic setup of the bending experiments. (b) Force-deformation measurements on bare glass substrates (black squares), substrate-supported (red triangles) and free-standing segments (blue circles) of ES-fibers. (c) Stiffness profile of a free-standing ES-fiber segment fitted with the DCBM. (d) Distribution of the Young's moduli of SA-fibers (open bars, dashed line) and ES-fibers (hatched bars, solid line).

observed.^{44,45} In order to understand the mechanical similarity of these morphologically quite different SA- and ES-fibers, one has to look at the underlying principles behind the mechanics. In both systems, intermolecular hydrogen bonds and π -stacking are responsible for the formation and cohesion of the fibers. Likewise, the ensemble of these noncovalent interactions determines the response to mechanical stresses. Therefore, despite differences in their morphology, it is reasonable that SA- and ES-fibers possess comparable elastic properties. Although the distributions of the moduli are rather broad, we observed a tendency towards a slightly lower modulus of the SA-fibers compared to the ES-fibers. This can be explained by their bundle-substructure which is more likely prone to defects. However, the effect is small and within the range of sample deviations and the error of the measurements. The important finding is that both fiber types show a remarkable mechanical stability despite the small molecule size and the absence of covalent interactions.

6.3 Conclusions

In this study we demonstrated for the first time that mechanically robust BTA fibers can be accessed via bottom-up and top-down approaches. We prepared self-assembled (SA) and melt electrospun (ES) fibers from the same compound **1** and obtained fibers with an average diameter of $1.2 \pm 0.7 \mu\text{m}$ and $0.8 \pm 0.2 \mu\text{m}$ for SA- and ES-fibers, respectively. On the Ångström-scale, XRD measurements show the same crystal structure of the fibers, independently of the preparation method. On the microscopic scale, SEM measurements however clearly revealed morphological differences: The self-assembled fibers possessed a hierarchical structure, consisting of firmly connected bundles of individual strands, while melt electrospun fibers showed a smooth and homogeneous structure. AFM bending experiments, which probe the mechanical behavior on the length scale of the whole assembly, revealed that Young's modulus E was not significantly affected by changing the preparation process. While the order of magnitude and distributions of the moduli were comparable, the average values suggested that E_{SA} ($3.6 \pm 0.4 \text{ GPa}$) was slightly lower than E_{ES} ($4.7 \pm 0.6 \text{ GPa}$) due to the bundle-substructure of the SA-fibers which is more likely prone to defects. However, the difference was small and within the error range of measurements. Still, our results prove that mechanically robust BTA fibers can be obtained by bottom-up as well as top-down approaches.

These findings open interesting perspectives for structure formation from BTAs. First, the relatively high elastic constants in the lower GPa range that are found for both approaches demonstrate that the fibrillar structures are mechanically robust regardless of how they are formed, qualifying them as a platform for hierarchical structure formation. Second, the results show that BTAs are shapeable into fibers with both approaches. This is interesting, since bottom-up and top-down approaches have complementary advantages and disadvantages, as discussed in the introduction. Now with this system, the best of the bottom up and top-down approaches can be combined for one materials class and used for creating hierarchically structured nonwovens for example for filter applications.

6.4 Experimental Section

Material. N,N',N''-tripropyl-1,3,5-benzenetricarboxamide **1** was synthesized according to the literature.⁵⁰ The melting temperature of **1** is 289°C and was deter-

mined in a Perkin Elmer Diamond DSC (heating rate: 10 K/min, nitrogen flow: 20 mL/min). The temperature at a 10% weight loss is 351 °C. The measurement was performed in a Mettler SDTA 851 TGA at 10 K/min (nitrogen flow: 60 mL/min). Isothermal TGA runs at the spinning temperature (290 °C) under nitrogen atmosphere were performed to verify the thermal stability of **1** during the period of the electrospinning process. **1** shows a weight loss below 5 wt.% for 55 minutes.

SA-fiber preparation. In 2,2,4,4,6,8,8-heptamethylnonane (HMN) 600 ppm of **1** were dissolved under reflux at 240 °C and cooled to room temperature. To ensure a controlled self-assembly behavior, 200 µL of the suspension were heated in a custom designed high pressure pan to 240 °C for 10 minutes in the Dropping Point Cell FP83HT from METTLER TOLEDO followed by cooling to 30 °C with 5 K/min (controlled with the METTLER TOLEDO Central Processor FP90). For the bending experiments, identical structured glass substrates were wetted with 10 µL of blank HMN, 0.5 µL of the fiber suspension were added and the samples were allowed to dry overnight.

ES-fiber preparation. The melt electrospinning experiments were carried out as described elsewhere.²⁶ **1** was equilibrated in a syringe with an inner needle diameter of 0.6 mm for three minutes at its melting point at 290 °C (temperature of the heated cylinder around the syringe body in the melt electrospinning set-up) before applying high voltage of -30 kV. The distance between needle tip and collector was 6 cm and the feeding rate 500 µL/h. The electrospun material was collected on a single 12 mm diameter aluminum SEM stub with a carbon tab which was mounted on top of the collector plate. The melt electrospinning experiment was carried out during 15 minutes. For the bending experiments, the fibers were transferred to structured glass substrates (GeSiM GmbH, Grosserkmannsdorf, Germany; channel widths 20, 30 and 40 µm, respectively) by gently bringing the SEM stub and the substrates in contact.

XRD-Measurements. The XRD-measurements in the angle range of $\theta = 0.5^\circ - 15^\circ$ were carried out on a Huber Guinier diffractometer 600. To get Cu $K_{\alpha 1}$ radiation ($\lambda = 154.051$ pm) it is equipped with a Huber germanium monochromator 61. An extra slit diaphragm reduces the broadening of the primary beam due to scattering in air. The samples were prepared in soda glass capillaries (1.5 - 2 mm diameter) from powder.

Scanning Electron Microscopy. For preparation of the SA-fiber SEM samples, 5 µL of the HMN-suspension were put in aluminum pans and the solvent was evaporated

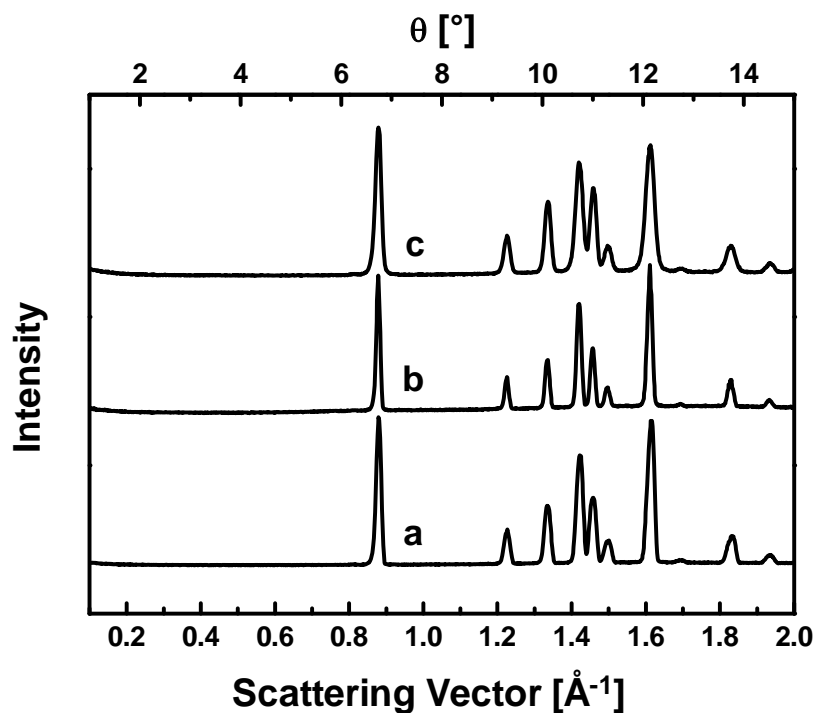
under reduced pressure. ES-fibers of **1** were directly spun onto a SEM specimen stub with a carbon tab. All samples were sputtered with platinum (2.0 nm) in a Cressington sputter coater 208HR. The SEM micrographs were recorded on a Zeiss ULTRA plus FESEM (Zeiss, Jena, Germany). To obtain a reliable size distribution, 250 individual SA- and ES-fibers, respectively, were evaluated using AxioVision LE Software (Carl Zeiss AG, Germany). The histograms can be found in the Supporting Information SI 6.2 and SI 6.3.

AFM measurements. All AFM measurements were performed on a Nanowizard I (JPK Instruments AG, Berlin, Germany). The bending experiments were performed as previously reported.⁴⁴ Details about the used cantilever types and applied loads can be found in the Supporting Information SI 6.6.

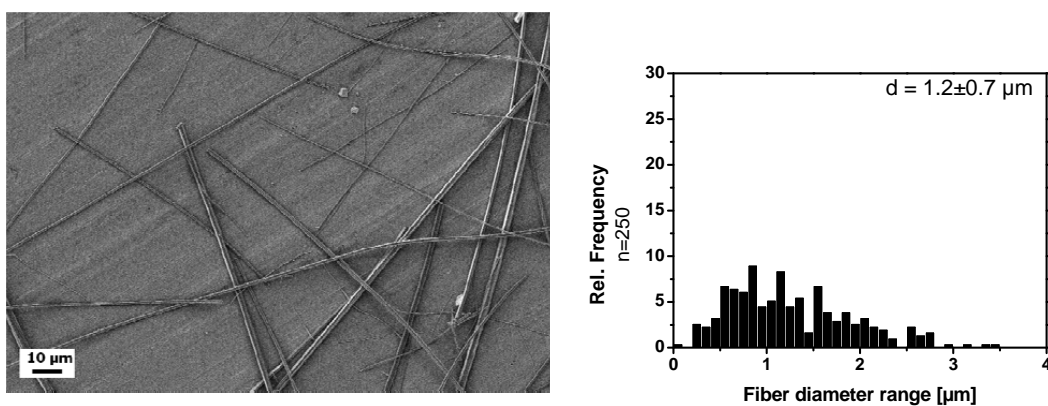
Acknowledgments

This work received financial support from the German Research Foundation (Deutsche Forschungsgemeinschaft) within the SFB 840, project B8. We thank Doris Hanft for help with the synthesis of the 1,3,5-benzenetrisamide, Martina Heider and Dr. Beate Förster from Bayreuth Institute of Macromolecular Research for support with the SEM images and Andreas Timme and Marina Behr for the XRD measurements. DK, JCS, BN and JWN acknowledge the support of the Elite Network of Bavaria.

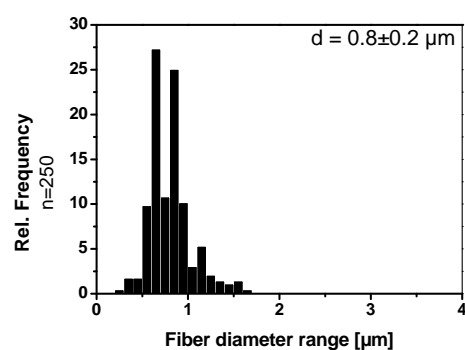
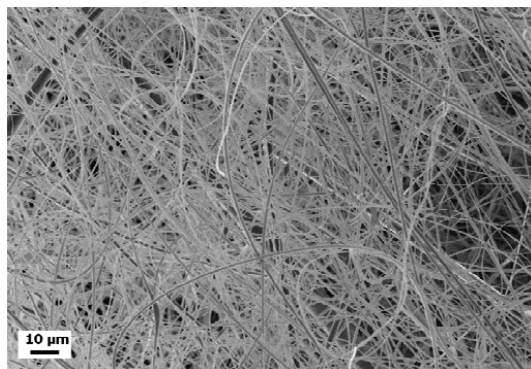
6.5 Supporting Information



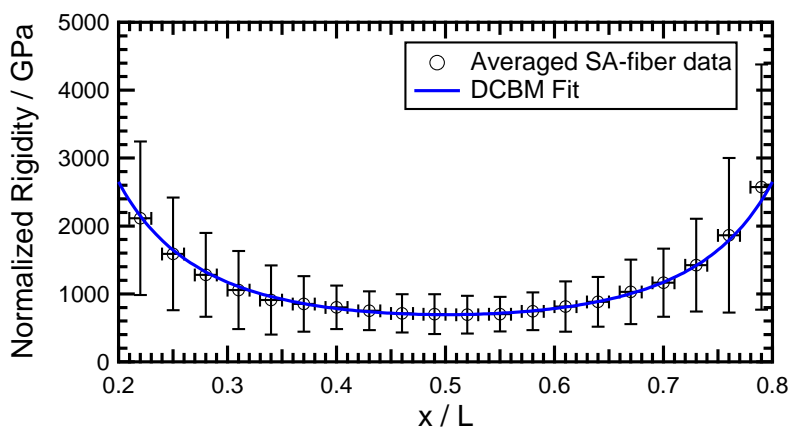
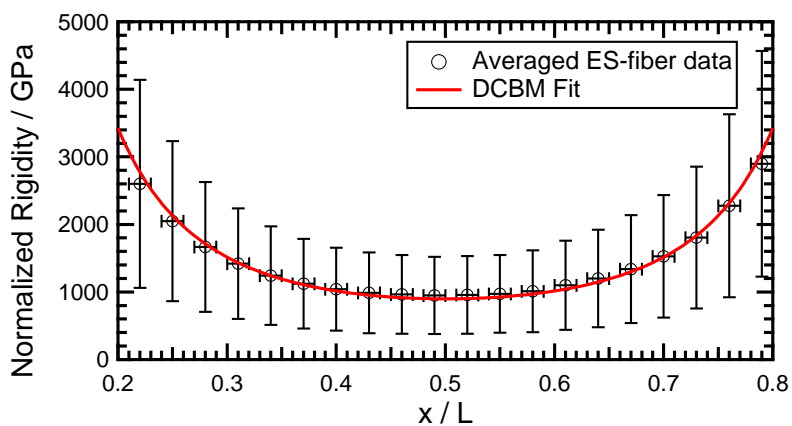
SI 6.1 X-ray diffractograms of 1: a) Powder obtained by recrystallization from dimethylformamide; b) Powdery self-assembled fibers and c) Powdery melt electro-spun fibers.



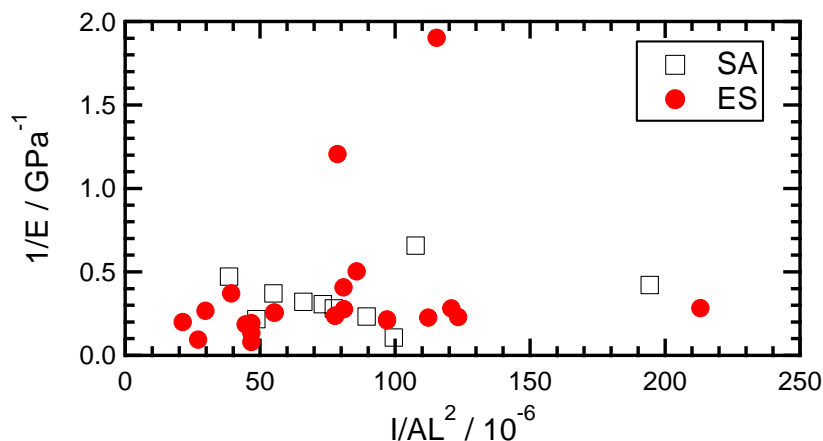
SI 6.2 SEM image and histogram of self-assembled fibers of 1, obtained by self-assembly from 2,2,4,4,6,8,8-heptamethylnonane (600 ppm of 1).



SI 6.3 SEM image and histogram of melt electrospun fibers of **1**. Spinning parameters: Applied voltage: -30 kV; Temperature: 290°C; Flow rate: 500 $\mu\text{L}/\text{h}$; Distance needle tip - ground plate: 6 cm; Needle ID: 0.6 mm.



SI 6.4 Evaluation of all normalized ES-fiber and SA-fiber bending profiles and fit with the double clamped beam model. Detailed information about the normalization procedures can be found in the literature.⁴⁵



SI 6.5 Shearing influence. More details on the theoretical background of the shearing investigation can be found in the literature.^{33,45} Briefly, if shearing occurs, the apparent measured modulus decreases with increasing ratio of fiber thickness to fiber length. Therefore, one would expect to see a linear increase in the plot of $1/E$ versus I/AL^2 (where the second is a measure for the thickness-to-length ratio for fibers with arbitrary cross sections). Since we found no such dependency, we can conclude that shearing does not significantly affect our measurements

SI 6.6 Experimental parameters of the AFM measurements.

For the bending experiments, we used tipless NSC12/AIBS cantilevers (μ Masch, Tallinn, Estonia). The typical loads were 50 nN (SA-fibers) and 150 nN (ES-fibers), which resulted in typical deformations of 100 nm (SA-fibers) and 200 nm (ES-fibers) at the midpoint of the free standing segment. In addition, force-distance measurements with a maximum load of 50 nN (SA-fibers) and 150 nN (ES-fibers) were performed on sample segments supported by the substrate to proof that there was no unwanted compression of the fibers during the bending experiments. The systems showed no unwanted compression under the tested loads. The dimensions of the mechanically investigated samples were determined on the segments supported by the substrates in intermittent contact mode with sharp imaging cantilevers (Olympus OMCL-AC160TS, Atomic Force, Mannheim, Germany). All data was processed and evaluated using self-written procedures in Igor Pro 6 (Wavemetrics Inc., Portland, USA). For the calculation of Young's modulus, the data from 10 free-standing segments on a total of 9 SA-fibers and 23 segments on a total of 18 ES-fibers and were used.

6.6 References

- [1] Y. N. Xia, P. D. Yang, Y. G. Sun, Y. Y. Wu, B. Mayers, B. Gates, Y. D. Yin, F. Kim, Y. Q. Yan, *Advanced Materials* **2003**, *15*, 353–389.
- [2] C. Kuttner, M. Tebbe, H. Schlaad, I. Burgert, A. Fery, *ACS Applied Materials & Interfaces* **2012**, *4*, 3485–3492.
- [3] S. Agarwal, J. H. Wendorff, A. Greiner, *Polymer* **2008**, *49*, 5603–5621.
- [4] K. Jayaraman, M. Kotaki, Y. Z. Zhang, X. M. Mo, S. Ramakrishna, *Journal of Nanoscience and Nanotechnology* **2004**, *4*, 52–65.
- [5] R. S. Barhate, S. Ramakrishna, *Journal of Membrane Science* **2007**, *296*, 1–8.
- [6] M. P. Lutolf, J. A. Hubbell, *Nature Biotechnology* **2005**, *23*, 47–55.
- [7] P. Moriarty, *Reports on Progress in Physics* **2001**, *64*, 297–381.
- [8] N. Kimizuka, *Self-Assembly of Supramolecular Nanofibers*, (Ed.: T. Shimizu), Springer-Verlag Berlin, Berlin, **2008**, pp. 1–26.
- [9] L. C. Palmer, S. I. Stupp, *Accounts of Chemical Research* **2008**, *41*, 1674–1684.
- [10] A. Greiner, J. H. Wendorff, *Angewandte Chemie-International Edition* **2007**, *46*, 5670–5703.
- [11] D. W. Hutmacher, P. D. Dalton, *Chemistry-an Asian Journal* **2011**, *6*, 44–56.
- [12] I. A. W. Filot, A. R. A. Palmans, P. A. J. Hilbers, R. A. V. Santen, E. A. Pidko, T. F. A. Greef, *The Journal of Physical Chemistry B* **2010**, *114*, 13667–13674.
- [13] M. Kristiansen, P. Smith, H. Chanzy, C. Baerlocher, V. Gramlich, L. Mccusker, T. Weber, P. Pattison, M. Blomenhofer, H.-W. Schmidt, *Crystal Growth & Design* **2009**, *9*, 2556–2558.
- [14] M. P. Lightfoot, F. S. Mair, R. G. Pritchard, J. E. Warren, *Chemical Communications* **1999**, 1945–1946.
- [15] F. Abraham, S. Ganzleben, D. Hanft, P. Smith, H.-W. Schmidt, *Macromolecular Chemistry & Physics* **2010**, *211*, 171–181.
- [16] F. Abraham, H.-W. Schmidt, *Polymer* **2010**, *51*, 913–921.
- [17] M. Blomenhofer, S. Ganzleben, D. Hanft, H.-W. Schmidt, M. Kristiansen, P. Smith, K. Stoll, D. Mäder, K. Hoffmann, *Macromolecules* **2005**, *38*, 3688–3695.
- [18] M. Schmidt, J. J. Wittmann, R. Kress, D. Schneider, S. Steuernagel, H. W. Schmidt, J. Senker, *Crystal Growth & Design* **2012**, *12*, 2543–2551.
- [19] A. Bernet, M. Behr, H.-W. Schmidt, *Soft Matter* **2011**, *7*, 1058–1065.
- [20] K. Hanabusa, C. Koto, M. Kimura, H. Shirai, A. Kakehi, *Chemistry Letters* **1997**, 429–430.
- [21] D. K. Kumar, D. A. Jose, P. Dastidar, A. Das, *Chemistry of Materials* **2004**, *16*, 2332–2335.
- [22] Y. Yasuda, E. Iishi, H. Inada, Y. Shirota, *Chemistry Letters* **1996**, 575–576.

- [23] N. Mohmeyer, N. Behrendt, X. Zhang, P. Smith, V. Altstädt, G. M. Sessler, H.-W. Schmidt, *Polymer* **2007**, *48*, 1612–1619.
- [24] T. Mes, M. M. J. Smulders, A. R. A. Palmans, E. W. Meijer, *Macromolecules* **2010**, *43*, 1981–1991.
- [25] J. Roosma, T. Mes, P. Leclere, A. R. A. Palmans, E. W. Meijer, *Journal of the American Chemical Society* **2008**, *130*, 1120–1121.
- [26] J. C. Singer, R. Giesa, H.-W. Schmidt, *Soft Matter* **2012**, *8*, 9972–9976.
- [27] M. T. Hunley, M. G. Mckee, P. Gupta, G. L. Wilkes, T. E. Long, *MRS Proceedings* **2006**, *948*.
- [28] C. Kulkarni, S. K. Reddy, S. J. George, S. Balasubramanian, *Chemical Physics Letters* **2011**, *515*, 226–230.
- [29] A. Sakamoto, D. Ogata, T. Shikata, O. Urakawa, K. Hanabusa, *Polymer* **2006**, *47*, 956–960.
- [30] I. Tomatsu, C. F. C. Fitié, D. Byelov, W. H. Jeu, P. C. M. M. Magusin, M. Wübbenhorst, R. P. Sijbesma, *The Journal of Physical Chemistry B* **2009**, *113*, 14158–14164.
- [31] M. K. Shin, S. I. Kim, S. J. Kim, S.-K. Kim, H. Lee, *Applied Physics Letters* **2006**, *88*, 193901–3.
- [32] E. P. S. Tan, C. T. Lim, *Applied Physics Letters* **2004**, *84*, 1603–1605.
- [33] L. Yang, C. F. C. Fitié, K. O. V. D. Werf, M. L. Bennink, P. J. Dijkstra, J. Feijen, *Biomaterials* **2008**, *29*, 955–962.
- [34] C. Guzman, S. Jeney, L. Kreplak, S. Kasas, A. J. Kulik, U. Aebi, L. Forro, *Journal of Molecular Biology* **2006**, *360*, 623–630.
- [35] A. Kis, S. Kasas, B. Babic, A. J. Kulik, W. Benoit, G. A. D. Briggs, C. Schonenberger, S. Catsicas, L. Forro, *Physical Review Letters* **2002**, *89*, 248101.
- [36] S. Orso, U. Wegst, E. Arzt, *Journal of Materials Science* **2006**, *41*, 5122–5126.
- [37] D. R. Stamov, T. A. K. Nguyen, H. M. Evans, T. Pfohl, C. Werner, T. Pompe, *Biomaterials* **2011**, *32*, 7444–7453.
- [38] W. Xu, P. J. Mulhern, B. L. Blackford, M. H. Jericho, I. Templeton, *Scanning Microscopy* **1994**, *8*, 499–506.
- [39] J. P. Salvetat, G. A. D. Briggs, J. M. Bonard, R. R. Bacsá, A. J. Kulik, T. Stockli, N. A. Burnham, L. Forro, *Physical Review Letters* **1999**, *82*, 944–947.
- [40] E. W. Wong, P. E. Sheehan, C. M. Lieber, *Science* **1997**, *277*, 1971–1975.
- [41] Y. X. Chen, B. L. Dorgan, D. N. Mcilroy, D. E. Aston, *Journal of Applied Physics* **2006**, *100*, 104301.
- [42] B. Wu, A. Heidelberg, J. J. Boland, *Nature Materials* **2005**, *4*, 525–529.
- [43] H. Zhang, J. Tang, L. Zhang, B. An, L. C. Qin, *Applied Physics Letters* **2008**, *92*, 173121.

- [44] D. Kluge, F. Abraham, S. Schmidt, H. W. Schmidt, A. Fery, *Langmuir* **2010**, *26*, 3020–3023.
- [45] D. Kluge, J. C. Singer, J. W. Neubauer, F. Abraham, H.-W. Schmidt, A. Fery, *Small* **2012**, *8*, 2563–2570.
- [46] C. A. Jiménez, J. B. Belmar, L. Ortíz, P. Hidalgo, O. Fabelo, J. Pasán, C. Ruiz-Pérez, *Crystal Growth & Design* **2009**, *9*, 4987–4989.
- [47] A. Timme, R. Kress, R. Q. Albuquerque, H.-W. Schmidt, *Chemistry - A European Journal* **2012**, *18*, 8329–8339.
- [48] J. Gere, B. Goodno, *Mechanics of Materials*, Cengage Learning, London, 7th ed., **2008**.
- [49] J. Brandrup, E. H. Immergut, E. A. Grulke, A. Abe, D. R. Bloch, *Polymer Handbook, Vol. 1*, John Wiley & Sons, Inc., Hoboken, New Jersey, **1999**, pp. V/162–V/167.
- [50] H.-W. Schmidt, P. Smith, M. Blomenhofer, WO 02/46300 A2, **2002**.

A Critical Assessment of Slack Effects in Nanobending Experiments

Reproduced from:

D. Kluge, D. Ruffoni, A. Fery, A CRITICAL ASSESSMENT OF SLACK EFFECTS IN NANOBENDING EXPERIMENTS. Initially submitted to *Journal of Applied Physics* and intended to be published as part of a larger upcoming paper.

ABSTRACT

Bending experiments using atomic force microscopy (AFM) are an important tool for the nanomechanical characterization of fibers. Since these measurements are often evaluated with rather simple models of beam theory, the importance of the correct identification and interpretation of the experimental boundary conditions has been repeatedly pointed out in the literature. However, most of the work so far has focused on non-ideal conditions at the fiber supports. In this work, we investigate the effect of a slack fiber, which represents an irregularity at the midsection, on its nanomechanical behavior. Using finite element (FE) analysis, we demonstrate that the slack produces a stiffening as well as a misleading shape of the stiffness profile which can lead to an overestimation of Young's modulus by over one order of magnitude. In addition, we propose an alternative experimental setup where the fiber is loaded perpendicular to the slack direction as a method for evaluating the nanomechanical properties of fibers that is robust against slack.

7.1 Introduction

Micro- and nanoscopic one-dimensional (1D) objects such as nanofibers, -wires, and -rods are important structural elements in materials science.¹⁻³ Their properties are of interest in many scientific topics, including (but not limited to) micro-/nano electro mechanical systems (MEMS/NEMS),² tissue engineering,⁴ biomedical applications,¹ biological systems,⁵ filtration,^{6,7} and supramolecular materials.⁸⁻¹⁰ Determining and understanding the nanomechanical properties of the individual 1D objects is an important step towards the design of novel functional materials. A central approach for the nanomechanical characterization of fibrillar structures are bending tests on free-standing fibers.¹¹ Typical experimental setups use structured substrates for the fiber preparation and atomic force microscopy (AFM) for the measurement of forces and deformations (Figure 7.1). For data evaluation, classical beam theory is applied.¹²

It has been demonstrated that careful determination of the boundary conditions is essential for a reliable evaluation of the mechanical properties.¹³ This can be achieved by recording a deformation or stiffness profile along the free-standing fiber segment.^{9,13,14} The shape of this profile can be used to verify the boundary conditions. A very important point is, for example, whether the fiber is firmly attached

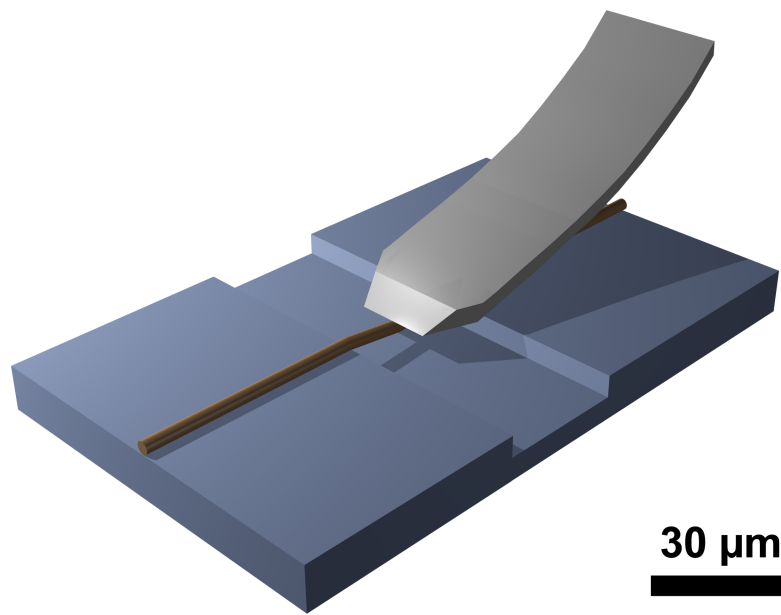


Figure 7.1 Typical AFM-setup for nanomechanical bending experiments.

to or only loosely supported by the substrate, which is typically described by two models: The double clamped beam model (DCBM) and the simply supported beam model (SSBM).¹⁴ The respective equations for the stiffness profiles are

$$k(x) = \frac{3L^3EI}{(L-x)^3 x^3} \quad (7.1)$$

for the DCBM and

$$k(x) = \frac{3LEI}{(L-x)^2 x^2} \quad (7.2)$$

for the SSBM, where $k(x)$ is the stiffness at the respective position x , E is Young's modulus, I is the area moment of inertia and L is the length of the free-standing segment. There are also more complex models that consider a finite stiffness of the fixation,¹⁵ or incorporate geometrical parameters, such as a non-perpendicular alignment of the fiber on the channel.¹⁶ However, most research has only focused on the behavior of the fiber at its supports.^{13–18} The influence on the bending behavior of non-ideal geometry of the fiber in the mid-region, such as the presence of a slack, has not been studied so far. In fact, such defects are often experimentally inaccessible due to the small scale of the problems. In those cases, computer simulations can be a helpful tool. Depending on their size, nanofibers can be described with large

atomistic and molecular models, respectively, or continuum-based approaches like finite element (FE) analysis.⁵

In the field of nanofibers and comparable 1D objects, FE models have been used to study design criteria for MEMS/NEMS devices,¹⁹ the properties of cellulose fibrils and nanocrystals,^{20,21} and have already been a complementary tool for bending measurements in several cases. Examples include metal and metaloxide nanowires,^{22–25} CNTs,^{26–28} microtubules,²⁹ amyloid fibrils,³⁰ the bending mechanics of cytoskeletal bundles,³¹ and they have even provided further insight into ill-defined boundary conditions at the edge of the fiber.¹⁸ It is important to point out that continuum mechanical FE models have certain limitations in describing the behavior of nano-objects (concerning, e.g., surface effects and thermal fluctuations).³² Nevertheless, they provide a fast and computational inexpensive way to analyze problems where those effects play a minor role.

In this work, we investigate the effect of a slack fiber (Figure 7.2) on nanobending experiments. Our goal is not to establish a complete theoretical description of this problem, but to estimate how a certain degree of slack will affect the apparent linear and non-linear mechanical properties and to present guidelines on how to detect such influences in order to avoid a misinterpretation of the results. For that purpose, we simulate stiffness profiles by means of FE analysis for fibers with various degrees of slacking. Using classical beam theory, we evaluate the stiffness profiles to estimate the error when determining Young's modulus from such experiments if the slack is neglected. In addition, we examine whether alternative experimental setups can be used to circumvent these issues.

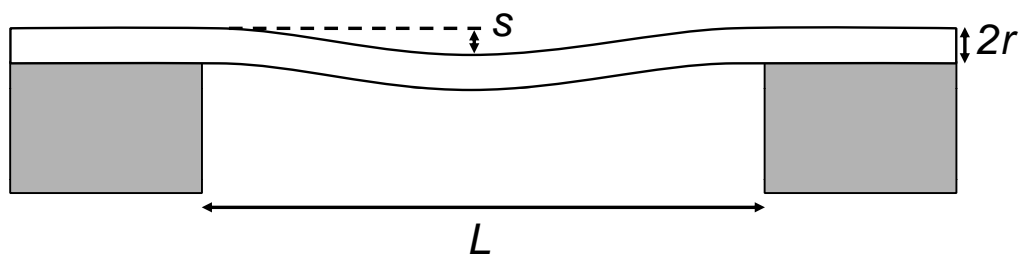


Figure 7.2 Sketch of a free-standing fiber segment with a slack mid-section. L is the length of the free-standing segment, r is the radius of the fiber and s is the maximum depth of the slack at the mid-point of the fiber.

7.2 Results and Discussion

The presence of a slack in the fiber had a clear effect on the fiber stiffness (Figure 7.3). For small slack depths s ($s < 0.3 \mu\text{m}$), the shape of the stiffness profiles corresponded to the DCBM, since the beam in the simulations was fully clamped. However, with increasing slack depth, the absolute stiffness increased and we found a flattening of the profiles up to a point (starting at a depth of around $0.7 \mu\text{m}$) where the stiffness in the mid region of the free-standing segment ($0.4 L$ to $0.6 L$) was even higher than in the border regions.

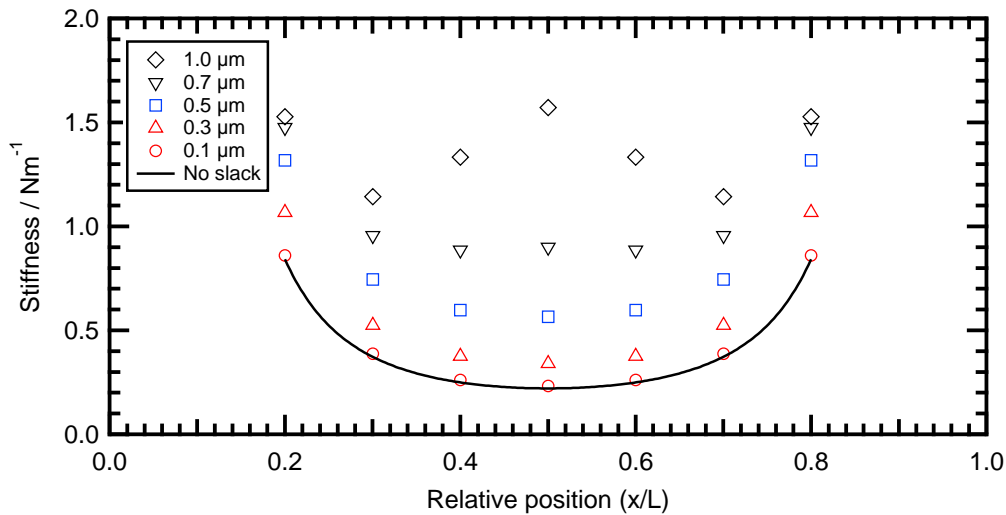


Figure 7.3 Stiffness profiles obtained from the FE simulations. For the sake of clarity, not all simulated profiles are shown here.

Nanomechanical bending experiments that use the shape of the profile to evaluate the mechanical properties can easily identify such extreme cases and therefore, we limited the evaluation to the experimentally relevant range up to a slack of $0.7 \mu\text{m}$. However, moderate slack depths have a more subtle influence on the profile that may lead to misinterpretation of the data. In order to estimate the error that arises if slack is present in the experiments but not accounted for during the evaluation, we applied the conventional DCBM model (which correctly represents the fixation used in the FE analysis, but neglects the slack) and calculated the apparent Young's modulus E_{app} . Since the slack would have led to an overestimation of Young's modulus in all simulations, we defined an overestimation factor f_o as the ratio of E_{app} and the actual modulus that we defined in the simulations, E_{sim} :

$$f_o = \frac{E_{\text{app}}}{E_{\text{sim}}} \quad (7.3)$$

Since the stiffness of the fiber increased with increasing slackness, the overestimation of Young's modulus by the DCBM model also increased and led to a maximum overestimation of a factor 2 (Figure 7.4).

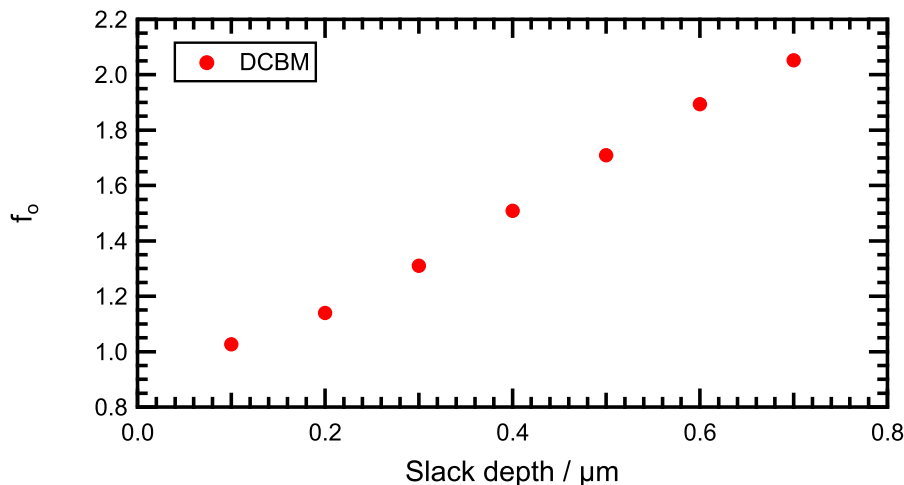


Figure 7.4 Overestimation f_o of the apparent Young's modulus E_{app} when evaluating the stiffness profiles with the DCBM.

In addition, the presence of slack also changed the shape of the stiffness profile, which turned out to be an additional source for misinterpretation of the experimental results. Although the simulated fiber was clamped at both sides, the stiffness profiles showed a SSBM-like shape when increasing the slack depth (Figure 7.5). In order to quantify this effect, one can look at the relative error of the fit of the stiffness profile using both analytical models (Equations 7.1 and 7.2). For slack depths $s > 0.3 \mu\text{m}$, the SSBM started to show much better agreement with the data (Figure 7.6). However, as the SSBM assumes only a supported fiber, evaluating the profiles with this model resulted in a drastic overestimation of Young's modulus by a factor of 10.

In summary, the slackness gives rise to two sources of error. The first is an apparent stiffening which, at small deformations, may lead to an overestimation of a factor 2. The second is a shape change of the stiffness profile that causes a misinterpretation of the boundary conditions as well as an overestimation of Young's modulus by one order of magnitude.

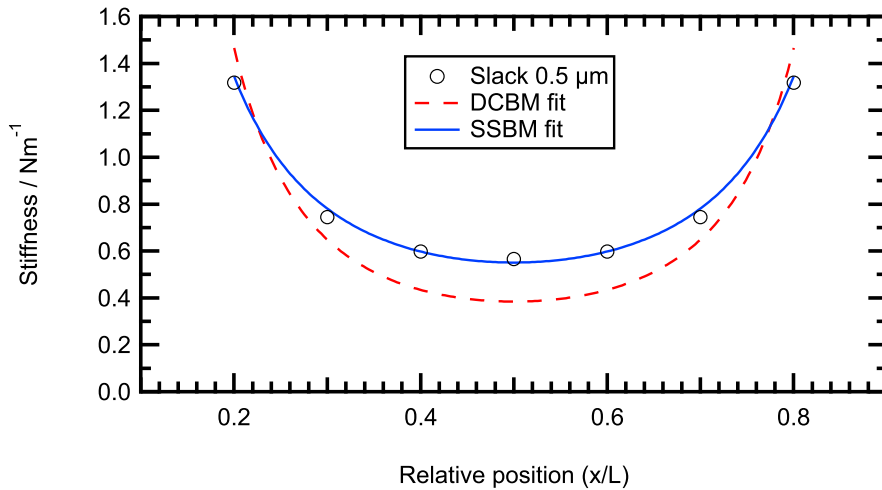


Figure 7.5 Exemplary fit of a profile obtained for moderate slack depth with the DCBM and SSBM. Although the shape of the profile clearly corresponds to the SSBM, Young's modulus is overestimated by a factor of 10.

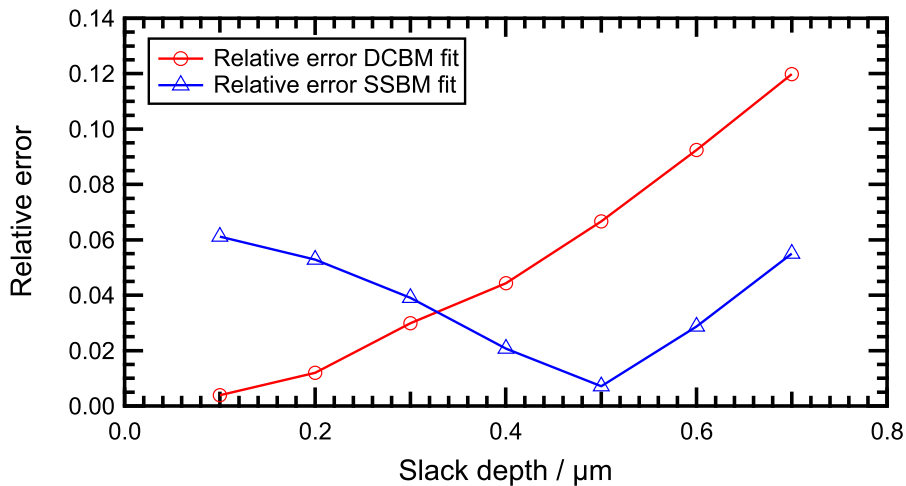


Figure 7.6 Relative error of the DCBM/SSBM fits that were used to determine E_{app} . The DCBM error increases with increasing slack, while the SSBM error initially decreases, which will lead to misinterpretation of the data as an apparent SSBM-case for moderate slack depths.

Up to this point, we only considered a fixed model with absolute values of L , r and s . Obviously, the influence of the slack will depend on the relations between these three parameters. Although an increasing slack-to-length ratio resulted in slight stiffening, we found that the dominating influence was the slack-to-radius ratio (Figure 7.7). Simple variation of the length-to-radius ratio did not cause significant changes of the profile (Supporting Information SI 7.3).

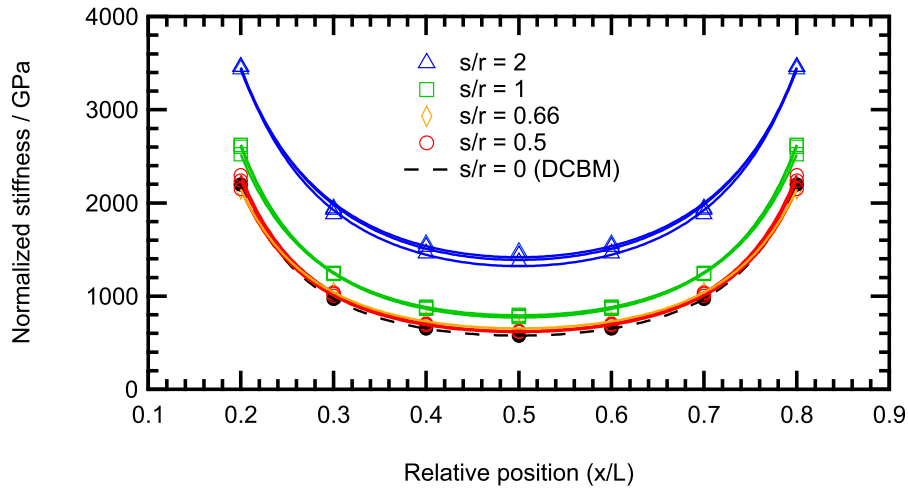


Figure 7.7 Stiffness profiles with various combinations of L , r , and s . The s/r ratio is the dominating influence. Note that because the absolute stiffness is dependent on the diameter and length of the free-standing segment, the data was normalized to the length of the free-standing segment and the area moment according to Kluge et al.⁹ to directly show the slack influence. The different curves with the same symbols are simulations with the same s/r ratio but with different L/r ratios.

We also characterized the influence of the slack in large-deformation measurements. Normally, bending experiments are performed within the small-deformation regime, since strictly speaking, commonly applied Euler-Bernoulli beam theory is only valid for deformations \ll radius.¹² However, *Heidelberg* et al. proposed a model that also considers large deformations.³³ Here, being mostly interested in the influence of the slack, we only used the approximate solution to the bending problem:

$$F_{\text{center}} = \frac{192EI}{L^3} \Delta v_{\text{center}} + \frac{8EA}{L^3} \Delta v_{\text{center}}^3 \quad (7.4)$$

where F_{center} is the force applied at the midpoint of the fiber, Δv_{center} is the corresponding midpoint displacement and A denotes the cross-sectional area. In addition to the regular bending forces (linear term), there are also tensile forces acting on the fiber (cubic term). Note that Equation (7.4) describes a nonlinear, but still fully elastic behavior.

Experimentally, it is often difficult to achieve large deformations when loading the suspended fiber from the top due to a possible contact between fiber and substrate. Therefore, many studies that utilize large deformation measurements apply the load in the substrate plane and therefore, perpendicular to the slack direction.^{33–35} Hence, we investigated the difference between vertical loading (in the same direction as

the slack) and lateral loading (perpendicular to the slack) in the large deformation regime. To study the latter, we used a model with tetrahedral elements (Figure 7.8) since the quasi-2D beam element model does not allow the deformation modes induced by lateral loading. We compared the simulations for vertical loading between beam and volume element models and found no significant differences (Supporting Information SI 7.4).

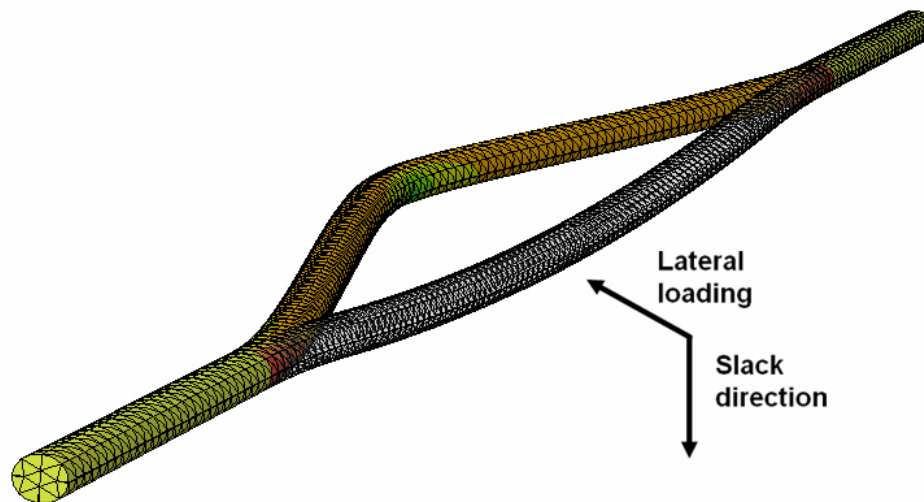
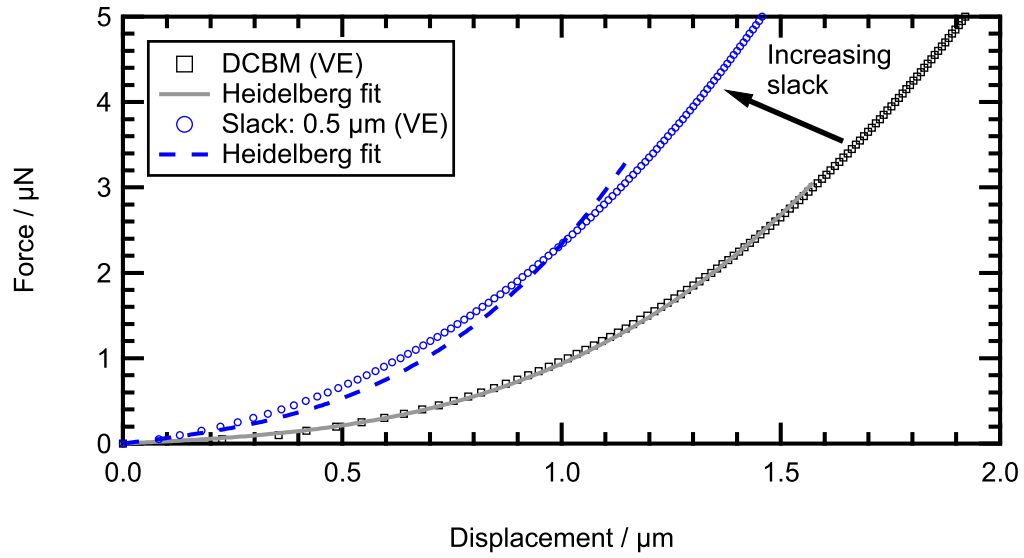


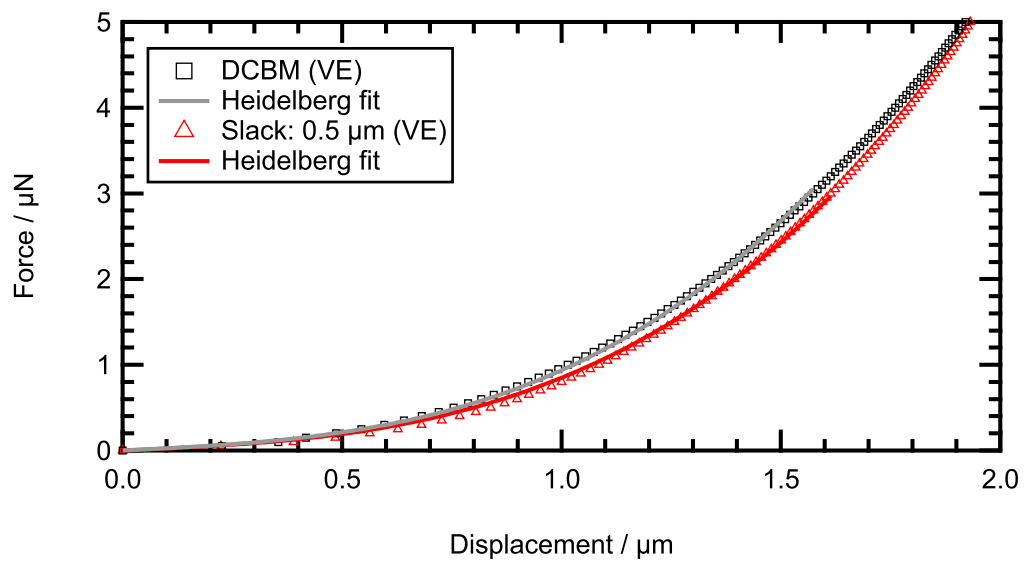
Figure 7.8 Volume element model used for studying the effect of loading the fiber in and perpendicular to the slack direction. The transparent geometry is the initial (undeformed) fiber and the colored geometry is the simulated deformed fiber. The colors indicate the stress distribution along the fiber axis, from maximum compressive (green) to maximum tensile (red).

The (approximate) solution proposed by *Heidelberg* et al. corresponded well with our simulations of a double clamped beam without slack, but produced an overestimation of Young's modulus by 16%, which is in the same range as the previously reported maximum error of 18%.³³ However, the inaccuracy present in Equation (7.4) was much smaller than the drastic influence of the slack.

When loaded vertically, increased slack resulted in a stiffening of the fiber and produced an overestimation of Young's modulus by roughly a factor of 3 (Figure 7.9(a)). With the slack, the force-displacement curve showed a small but clear deviation from the Heidelberg model, especially at very large displacements (i.e., displacement $> r$). This demonstrates that slack does not just affect the profile shape when performing small deformation measurements to obtain Young's modulus, but also the large deformation regime.



(a)



(b)

Figure 7.9 Results of the large-deformation simulations with the volume element (VE) model. (a) Vertical loading. (b) Lateral loading. The black curves represent the model without slack.

The results for the lateral loading, however, are very different. Despite a significant slackness of the fiber, the simulated force-displacement curves showed only little deviation from the DCBM behavior (Figure 7.9(b)). In fact, the apparent modulus was even 9% smaller than in the model without slack. The most likely explanation is that if a significantly curved beam is loaded perpendicular to the curvature plane, the deformation is no longer bending dominated, but rather involves significant amounts of torsion. For larger deformations, the cubic term in Equation (7.4) is again dominating the force-displacement behavior. Therefore, the slack has negligible influence when the fiber is loaded laterally. The same is true for the small-deformation stiffness profiles obtained by lateral loading that showed no significant slack influence and yielded a correct modulus (Supporting Information SI 7.5).

It has to be kept in mind that we performed the simulation with the assumption of an isotropic, linear elastic material. Therefore, although the deformation mode changes, it is not surprising that the results are consistent with the predictions of the analytical DCBM model. This may not be the case for many real samples, especially in the small deformation regime since a torsional deformation involves different material constants as the regular bending. In the large deformation regime, the differences will become less significant as the axial tension dominates the deformation. Therefore, although slack may be present, it will not be visible when performing large deformation measurements perpendicular to the curvature plane.

7.3 Conclusions

Herein, we have investigated the effect of a slack fiber on nanomechanical bending experiments using FE simulations. The results suggest that an increasing slack-to-radius ratio will lead to an apparent stiffening within the small- and large-deformation regime and therefore, to an overestimation of Young's modulus. In addition, the slack alters the shape of the stiffness profile, which is commonly used in bending experiments to determine the boundary conditions. This can lead to a misinterpretation of the boundary conditions which results in an overestimation of Young's modulus by over one order of magnitude. Since slack is difficult to identify experimentally, it is important to find characterization methods that are robust against such effects. Our simulations suggest that loading the fiber perpendicular to the slack direction might be an experimental solution to deal with samples where slack is an issue and to produce more reliable results.

7.4 Experimental Section

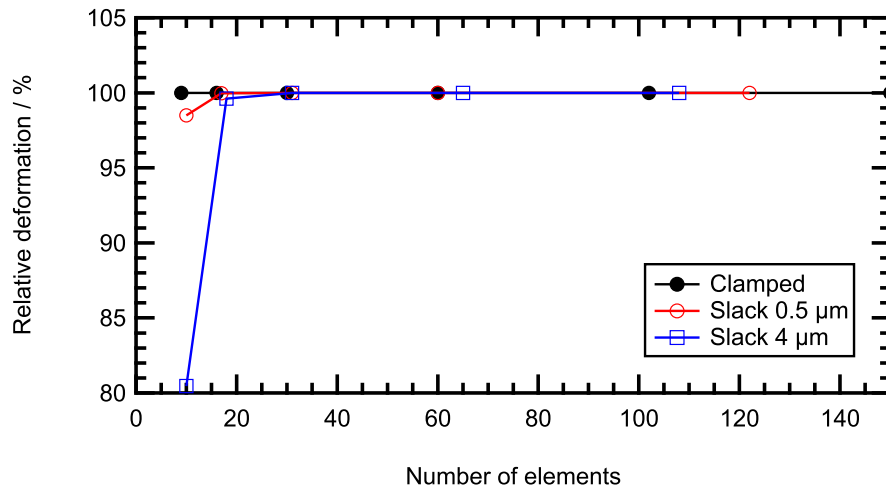
Small deformations. Finite element (FE) models of a typical fully clamped fiber having a circular cross section with a diameter of $0.5\ \mu\text{m}$ and a free-standing segment length (i.e., absolute distance between the clamping points) of $20\ \mu\text{m}$ were developed. Two different scenarios were considered: a reference case of a straight fiber without a slack and a parametric study where the slack depth (Figure 7.2) was varied from $0.1\ \mu\text{m}$ to $1\ \mu\text{m}$ in steps of $0.1\ \mu\text{m}$. For each slack depth, 5 simulations were performed where a point load of $100\ \text{nN}$ was applied at different positions along the fiber axis, equally spaced with an interval of 10% of the total fiber length L . Due to symmetry, only 5 positions (i.e., $0.1L$, $0.2L$, \dots , $0.5L$) were probed. The corresponding stiffness was calculated at each load application point by dividing the imposed load with the resulting FE displacement, as in the AFM experiments.^{8–10} For the evaluation, we focused on the experimentally relevant range from $0.2L$ to $0.8L$. All the FE simulations were performed with the commercial FE software Abaqus (Version 6.11; Providence, RI, USA). The FE mesh consisted of at least 80 second order Timoshenko beam elements (element B22 in Abaqus) and mesh density was checked to assure convergence of the results (Supporting Information SI 7.1). Additionally, the FE models were verified by a comparison with a very refined mesh of approx. 5000 second order tetrahedral elements (element C3D10 in Abaqus). The computed stiffness between the two meshing approaches varied less than 7% (Supporting Information SI 7.2). For all the simulations, an isotropic elastic modulus of $3\ \text{GPa}$ (comparable to previous studies^{8,9}) and a Poisson's ratio of 0.3 were used. To assess the interplay between the fiber aspect ratio and the slack, the slack/radius (s/r) and length/radius (L/r) ratios were also varied. Specifically, we kept the length of the free-standing segment constant and changed the radius and the slack depth to obtain L/r ranging from 25 to 200 and s/r from 0 to 2.

Large deformations. Simulations including geometric nonlinearities were performed using the above described FE model (beam elements) with a diameter of $0.5\ \mu\text{m}$ and an applied load of $5\ \mu\text{N}$ at the midpoint of the free-standing segment to achieve large deformations. The volume element (tetrahedral elements) model was also used to simulate a lateral loading (i.e., perpendicular to the slacking). The material was modeled to respond elastically over the whole deformation range.

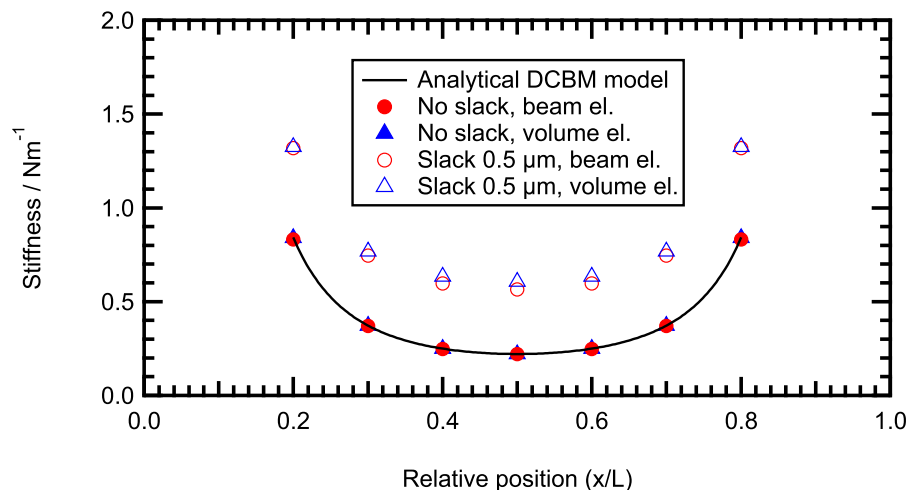
Acknowledgments

This work received financial support from the German Research Foundation (Deutsche Forschungsgemeinschaft) within the SFB 840, project B8. DK acknowledges the support of the Elite Network of Bavaria.

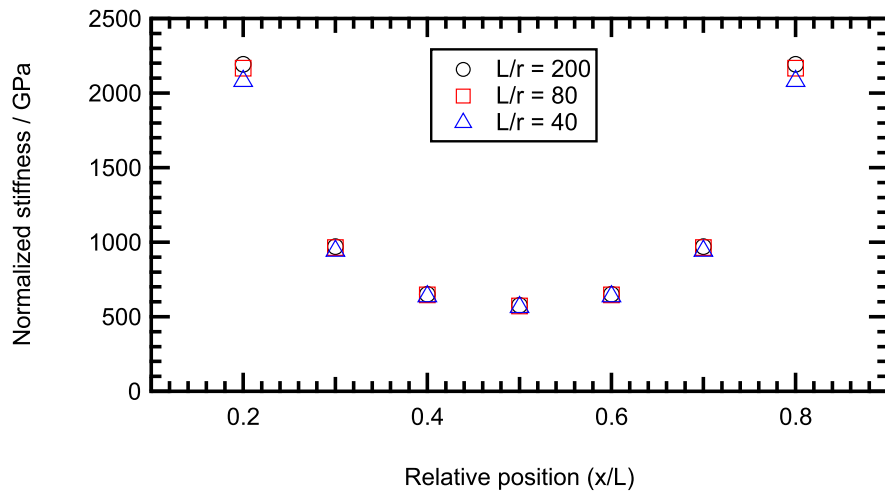
7.5 Supporting Information



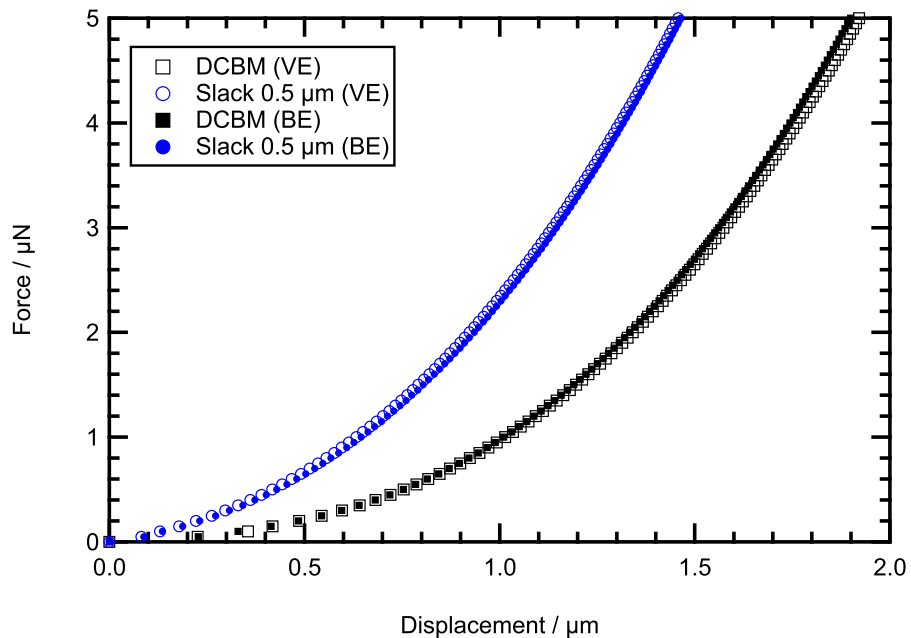
SI 7.1 Deformation at the midpoint of the beam for a double-clamped beam without slack, a beam with a slack of $0.5\ \mu\text{m}$ and a beam with a slack of $4\ \mu\text{m}$. Convergence was found in all cases above 65 elements. In combination with the overall low cost of the measurements we therefore decided to use a highly refined mesh with at least 80 elements for the parametric studies.



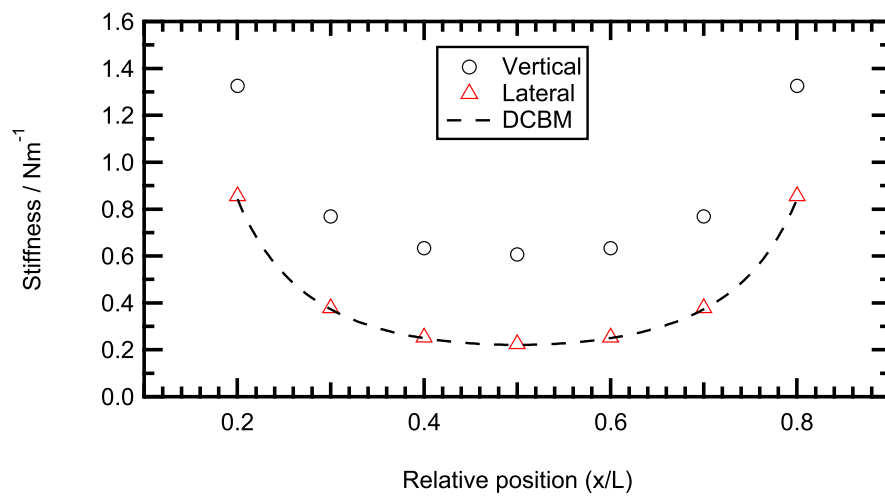
SI 7.2 Comparison of the results using tetrahedral and beam elements for a double-clamped beam without slack (closed symbols) and with a slack of $0.5\ \mu\text{m}$ (open symbols). It can be seen that the differences in stiffness (less than 7%) between tetrahedral and beam elements are insignificant compared to the effect of the slack. Therefore, beam elements were chosen for the parametric investigation due to the facilitation of the geometrical modeling.



SI 7.3 Normalized stiffness profiles without slack. The L/r ratio has no significant effect on the profile as long as $r \ll L$ to correspond with beam theory.



SI 7.4 Comparison of the volume element (open symbols) and beam element (closed symbols) models for large deformations without (black squares) and with slack (blue circles).



SI 7.5 Comparison of stiffness profiles with a slack of $0.5\ \mu\text{m}$ obtained by vertical and lateral loading. Lateral loading shows extremely good agreement with the regular DCBM.

7.6 References

- [1] S. Agarwal, J. H. Wendorff, A. Greiner, *Polymer* **2008**, *49*, 5603–5621.
- [2] B. E. Alaca, *International Materials Reviews* **2009**, *54*, 245–282.
- [3] Y. N. Xia, P. D. Yang, Y. G. Sun, Y. Y. Wu, B. Mayers, B. Gates, Y. D. Yin, F. Kim, Y. Q. Yan, *Advanced Materials* **2003**, *15*, 353–389.
- [4] M. P. Lutolf, J. A. Hubbell, *Nature Biotechnology* **2005**, *23*, 47–55.
- [5] T. P. J. Knowles, M. J. Buehler, *Nature Nanotechnology* **2011**, *6*, 469–479.
- [6] R. S. Barhate, S. Ramakrishna, *Journal of Membrane Science* **2007**, *296*, 1–8.
- [7] K. Jayaraman, M. Kotaki, Y. Z. Zhang, X. M. Mo, S. Ramakrishna, *Journal of Nanoscience and Nanotechnology* **2004**, *4*, 52–65.
- [8] D. Kluge, F. Abraham, S. Schmidt, H. W. Schmidt, A. Fery, *Langmuir* **2010**, *26*, 3020–3023.
- [9] D. Kluge, J. C. Singer, J. W. Neubauer, F. Abraham, H.-W. Schmidt, A. Fery, *Small* **2012**, *8*, 2563–2570.
- [10] D. Kluge, J. C. Singer, B. R. Neugirg, J. W. Neubauer, H.-W. Schmidt, A. Fery, *Polymer* **2012**, *53*, 5754–5759.
- [11] E. P. S. Tan, C. T. Lim, *Composites Science and Technology* **2006**, *66*, 1102–1111.
- [12] J. Gere, B. Goodno, *Mechanics of Materials*, Cengage Learning, London, 7th ed., **2008**.
- [13] Y. X. Chen, B. L. Dorgan, D. N. Mcilroy, D. E. Aston, *Journal of Applied Physics* **2006**, *100*, 104301.
- [14] W. J. Mai, Z. L. Wang, *Applied Physics Letters* **2006**, *89*, 073112.
- [15] D. Gangadean, D. N. Mcilroy, B. E. Faulkner, D. E. Aston, *Nanotechnology* **2010**, *21*, 225704.
- [16] D. A. Walters, L. M. Ericson, M. J. Casavant, J. Liu, D. T. Colbert, K. A. Smith, R. E. Smalley, *Applied Physics Letters* **1999**, *74*, 3803–3805.
- [17] Y. X. Chen, I. Stevenson, R. Pouy, L. D. Wang, D. N. Mcilroy, T. Pounds, M. G. Norton, D. E. Aston, *Nanotechnology* **2007**, *18*, 135708.
- [18] P. Zhou, C. W. Wu, X. D. Li, *Measurement Science & Technology* **2008**, *19*, 115703.
- [19] B. Bhushan, G. B. Agrawal, *Ultramicroscopy* **2003**, *97*, 495–507.
- [20] R. R. Lahiji, X. Xu, R. Reifengerger, A. Raman, A. Rudie, R. J. Moon, *Langmuir* **2010**, *26*, 4480–4488.
- [21] G. A. Zickler, D. Ruffoni, J. W. C. Dunlop, R. Elbaum, R. Weinkamer, P. Fratzl, T. Antretter, *Biointerphases* **2012**, *7*.
- [22] E. Celik, I. Guven, E. Madenci, *Theoretical and Applied Fracture Mechanics* **2011**, *55*, 185–191.

- [23] S. Sundararajan, B. Bhushan, *Sensors and Actuators a-Physical* **2002**, *101*, 338–351.
- [24] J. Yvonnet, A. Mitrushchenkov, G. Chambaud, Q. C. He, *Computer Methods in Applied Mechanics and Engineering* **2011**, *200*, 614–625.
- [25] C. Zou, G. Jing, D. Yu, Y. Xue, H. Duan, *Physics Letters A* **2009**, *373*, 2065–2070.
- [26] C. Fang, A. Kumar, S. Mukherjee, *Journal of Applied Mechanics - Transactions of the ASME* **2011**, *78*, 034502.
- [27] X. Guo, A. Y. T. Leung, X. Q. He, H. Jiang, Y. Huang, *Composites Part B-Engineering* **2008**, *39*, 202–208.
- [28] X. Y. Wang, X. Wang, *Composites Part B-Engineering* **2004**, *35*, 79–86.
- [29] S. Kasas, A. Kis, B. M. Riederer, L. Forro, G. Dietler, S. Catsicas, *Chemphyschem* **2004**, *5*, 252–257.
- [30] Z. P. Xu, R. Paparcone, M. J. Buehler, *Biophysical Journal* **2010**, *98*, 2053–2062.
- [31] M. Bathe, C. Heussinger, M. Claessens, A. R. Bausch, E. Frey, *Biophysical Journal* **2008**, *94*, 2955–2964.
- [32] C. Li, Z. J. Zheng, J. L. Yu, C. W. Lim, *Acta Mechanica Sinica* **2011**, *27*, 713–719.
- [33] A. Heidelberg, L. T. Ngo, B. Wu, M. A. Phillips, S. Sharma, T. I. Kamins, J. E. Sader, J. J. Boland, *Nano Letters* **2006**, *6*, 1101–1106.
- [34] E. W. Wong, P. E. Sheehan, C. M. Lieber, *Science* **1997**, *277*, 1971–1975.
- [35] B. Wu, A. Heidelberg, J. J. Boland, *Nature Materials* **2005**, *4*, 525–529.

Perspectives I: Beyond Small Deformations

8.1 Introduction

The previous chapters demonstrated that bending experiments are a powerful tool to reliably determine Young's modulus of a material. However, in the vertical bending direction (perpendicular to the substrate), the deformation is limited to a very small range. In order to investigate the mechanical properties of fibers beyond the linear elastic regime, the deformation mode has to be changed. One approach is to employ lateral force microscopy (LFM).¹⁻⁴ There are several successful reports in the literature where this technique was used for free-standing 1D samples like carbon nanotubes,⁵ various types of nanowires,⁶⁻¹¹ silicon(dioxide) nanobeams,¹² polymer composites,¹³ biopolymers,^{14,15} and biological samples.^{16,17} The setup is depicted in Figure 8.1.

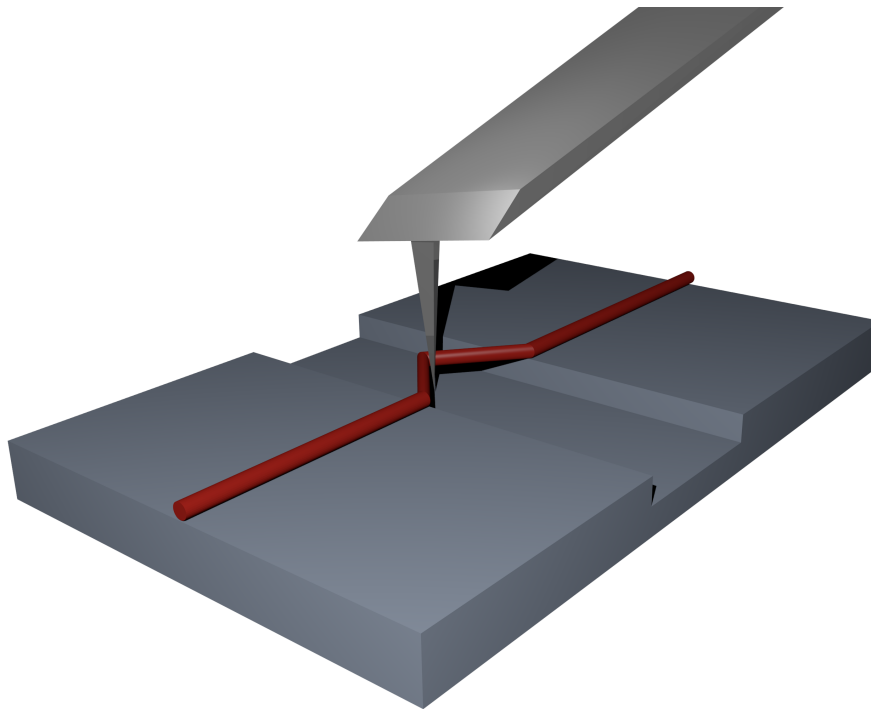


Figure 8.1 Schematic setup of a lateral AFM fiber bending experiment.

In this setup, the fiber experiences a combination of bending and tension (see Section 3.2.4). For small deformations, bending-type forces are dominant. For large deformations, the experiment can be considered as quasi-uniaxial stretching and tension forces are dominant. The full mathematical description of this interplay is rather complicated.^{5,7,13} For the sake of clarity, let us consider the approximate solution for the resulting force at the midpoint of the fiber by *Heidelberg et al.*⁷

$$F_{\text{center}} = \frac{192EI}{L^3} \Delta v_{\text{center}} + \frac{8EA}{L^3} \Delta v_{\text{center}}^3$$

The first term is the regular bending force. The second, cubic term is the tensile force acting on the fiber which becomes significant for deformations at the midpoint of the free-standing segment that are larger than the radius of the fiber. For all evaluations, this approximate solution is used. Although it has a maximum error of 18%,⁷ it is sufficient for a first estimate of the elastic properties at large deformations. In addition, it allows determining whether the plastic properties (such as yield stress and fracture strength, see Section 3.2.4) can still be evaluated with beam theory or if the additional stresses due to uniaxial tension have to be considered.

8.2 Results and Discussion

8.2.1 Calibration

The first step was finding or developing a suitable lateral calibration for our specific setup. In contrast to vertical measurements, the lateral calibration is more complicated, less precise, and although several approaches have been reported in the literature, there are no standard techniques so far (see also Section 3.3.5).³ We decided to perform the calibration in close analogy to the vertical experiments, i.e., determining the lateral sensitivity and lateral cantilever spring constant separately. The terms *lateral* (referring to an actual displacement of the cantilever tip in nm) and *torsional* (referring to an angular torsion of the cantilever in rad) are sometimes used inconsistently in the literature, and this work strictly follows the definition described in Section 3.3.5.

We determined the lateral sensitivity S_x in the same manner as the vertical sensitivity, using the slope of the measured signal in the constant compliance regime when applying forces to a hard substrate. Of course, for lateral measurements, this requires a vertical step. In addition, the distance of the contact point to the reflective side of the cantilever (i.e. the lever arm) plays a crucial role as already pointed out (see Section 3.3.5). We used the same glass substrates for the calibration as in the fiber bending experiments. The setup can be seen in Figure 8.2(a). This setup ensures that the cantilever hits the calibration substrate at almost the same position as it will afterward hit the fibers in the measurements. A corresponding calibration

curve can be seen in Figure 8.2(b). In the constant compliance regime, the lateral displacement of the cantilever tip is equal to the lateral displacement of the piezos. Therefore, the slope of the calibration curve directly yields the lateral sensitivity.

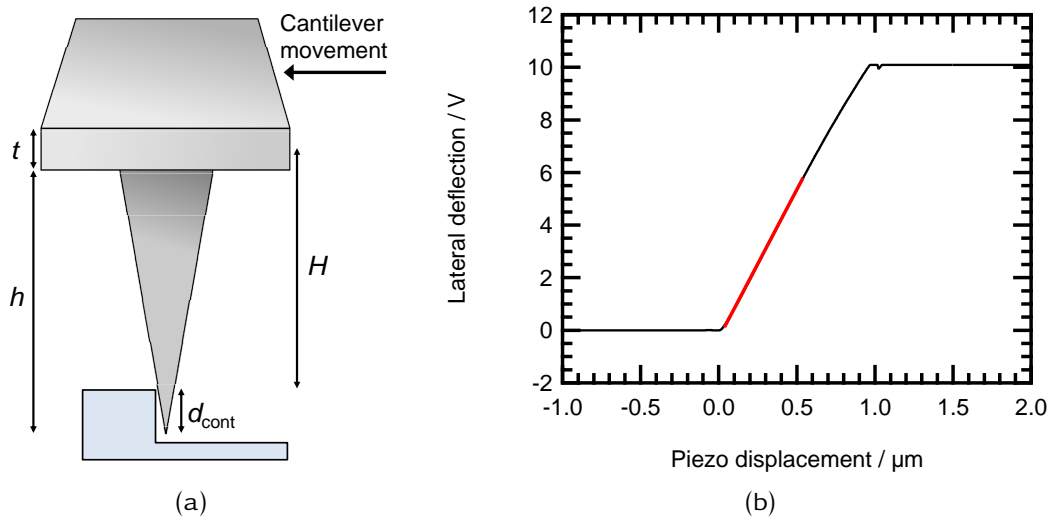


Figure 8.2 (a) Sketch of the lateral sensitivity calibration using the step of the structured glass substrates. (b) Lateral deflection-displacement curve obtained by pushing the cantilever against the undeformable substrate. Deflections larger than 10 V cannot be detected by the photodiode and hence lead to the plateau of the curve. The slight nonlinearity observed towards the end of the curve is most likely caused by the nonlinear response of the photodiode.¹⁸ The nonlinear region was only taken into account for the sensitivity calibration if very large deflections were needed to break the fibers.

This approach shares similarities with the method suggested by *Cannara et al.* who modified the cantilever with a colloidal probe and pushed against GaAs samples.¹⁹ However, the major advantage of our calibration is that we do not require a test probe but can use exactly the same setup as for the lateral force measurements, thus having precise control over the lever arm. This greatly enhances the reliability for our specific type of experiment. Control of the lever arm for lateral bending experiments can also be achieved via the approach recently reported by *Gestos et al.* who calibrated the cantilever against a free-standing glass fiber.¹⁸ However, since our approach uses a non-deformable substrate, knowledge of the reference sample's mechanical properties is not needed, thus eliminating another error source. The ongoing effort of developing a simple, fast and reliable calibration approach demonstrates the importance of large deformation AFM measurements for materials science.

In order to calibrate the lateral spring constant k_x , we used a semi-empirical approach. The vertical spring constant k_z of a rectangular cantilever can be calculated from its geometry:³

$$k_z = \frac{Ewt^3}{4l^3} \quad (8.1)$$

Where w , t and l are the width, thickness and length of the cantilever, respectively, and E is the elastic modulus of the cantilever material. The same can be done for the lateral spring constant k_x using the shear modulus G of the cantilever material:

$$k_x = \frac{Gwt^3}{3lH^2} \quad (8.2)$$

Here, H is the lever arm of the cantilever which is normally simply defined as the tip length h plus half of the cantilever thickness (see Section 3.3.5 and Figure 8.2), but of course in this case, the distance of the tip-fiber contact point to the tip end has to be subtracted:

$$H = h + \frac{t}{2} - d_{\text{cont}} \quad (8.3)$$

One can easily see that the lateral and normal spring constant are related by

$$k_x = \frac{4}{3} \frac{G}{E} \left(\frac{l}{H} \right)^2 k_z \quad (8.4)$$

Therefore, we calibrated the normal spring constant of the cantilever with the thermal noise method²⁰ and used the geometry of the cantilever to calculate the lateral spring constant based on the results of the vertical calibration.

It is important to note that this approach has limitations: First of all, it requires knowledge of the cantilever material properties. Although provided by the manufacturer, those can be inconsistent within different batches of cantilevers. In addition, determining the lever arm is not straightforward and even small deviations can have a large effect on the spring constant. It requires knowledge of the cantilever thickness and tip length. However, this is a problem for all lateral calibration approaches. For the majority of the experiments in this work, we used the values provided by the manufacturer which were confirmed by SEM imaging of selected

cantilevers. Despite these limitations, *Neugirg* could show in later work that the calibration employed here is consistent with more sophisticated techniques like the torsional Sader method.^{21–23}

8.2.2 Friction influence

In the described setup, the cantilever tip is in contact with the substrate during the lateral deformation. This leads to the occurrence of friction. *Amontons' 1st Law* states that the friction force is directly proportional to the applied load. We wanted to investigate if the vertical setpoint (which is directly proportional to the applied load) influences the lateral results. For that purpose, we performed repeated measurements on a test fiber with varied setpoint (Figure 8.3). While the absolute measured lateral force increases with increasing friction, the slope of the deflection-displacement curve does not change. Therefore, the friction does not affect the lateral measurement of the fiber stiffness. However, it leads to increased noise and reduced precision. Therefore, it would be beneficial to perform the measurements in a frictionless setup, i.e. without touching the substrate with the cantilever tip during the lateral movement.

The experimental realization of this approach was not straightforward and can be found in Section 8.4. Since the solution to this problem was achieved only late during the progress of the lateral experiments, it was only applied to few samples and shall only be briefly discussed here. In Figure 8.4, typical force-displacement curves of lateral bending and friction-free lateral bending can be seen. It is clear that friction-free experiments offer an enormous increase of the signal-to-noise ratio of the lateral measurements in the small-deformation regime.

In addition, the friction-free setup allows acquiring trace and retrace data if the measurement is aborted before plastic deformation occurs (Figure 8.5). This is not possible if tip and substrate are in contact during the measurement, since the tip-substrate friction causes the cantilever to snap in the opposite direction at the point of reversal and therefore to lose contact with the sample.

However, note that the advantages came at the prize of a less reliable calibration: Since the AFM was not designed for lateral measurements without feedback of the z-piezo, we developed a workaround where the cantilever was positioned in a way that it could no longer reach the bottom of the channel, even with fully extended piezos. The disadvantage is that in this setup, the exact distance between tip and

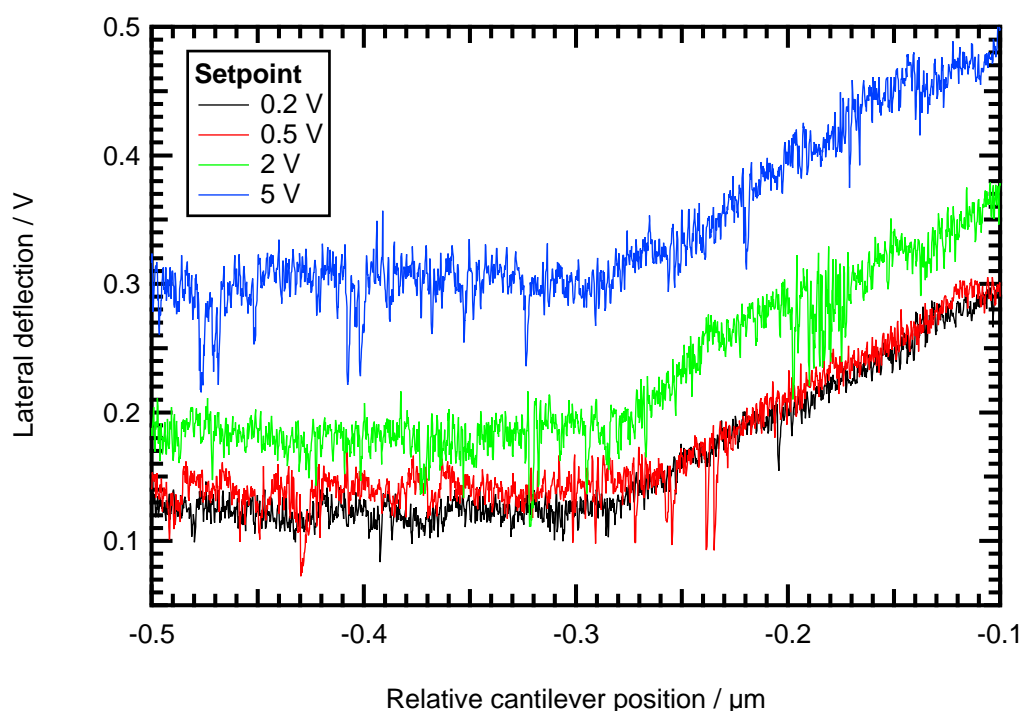


Figure 8.3 Repeated lateral measurements of the same test fiber with varied vertical setpoint (which corresponds to the vertical loading force). While the absolute lateral deflection increases with increasing load, the slope (which corresponds to the fiber stiffness) does not change significantly.

substrate cannot be determined and as a consequence the lever arm in the sensitivity calculation - and therefore also the cantilever spring constant - have an increased inaccuracy. This problem was later approached and solved by *Neugirg* in the course of his master's thesis.²² Concerning the following sections, the measurements in Section 8.2.3 were performed in a friction-free setup while the measurements in Section 8.2.4 were performed with a defined tip-substrate contact.

8.2.3 Small Deformation Measurements

We investigated two types of trisamides using lateral bending experiments, *N,N,N'*-tri(2,3-dimethyl-cyclohexyl)-1,3,5-benzenetricarboxamide **1** (Figure 8.6(b), see Chapter 5) and 1,3,5-tris(2,2-dimethylpropionylamino)-benzene **2** (Figure 8.6(a), see Chapters 4 and 5). The first step of the trisamide investigation was to establish a reference for the lateral bending experiments. For that purpose, we needed very precise lateral measurements and therefore used a friction-free setup. Since it was the best-studied system, we performed the measurements on fibers of compound **2**. We

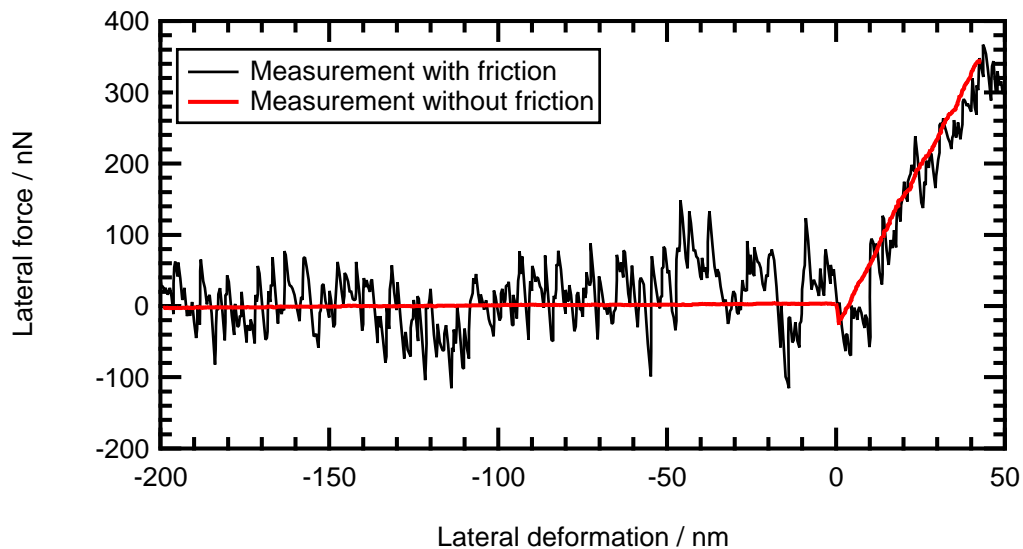


Figure 8.4 Comparison of lateral force curves with and without tip-substrate contact during the measurement. The signal-to-noise ratio is significantly improved. The measurements were performed on two different fibers with comparable stiffness in order to illustrate the difference and both measurements were aborted before any plastic deformation to the fibers occurred.

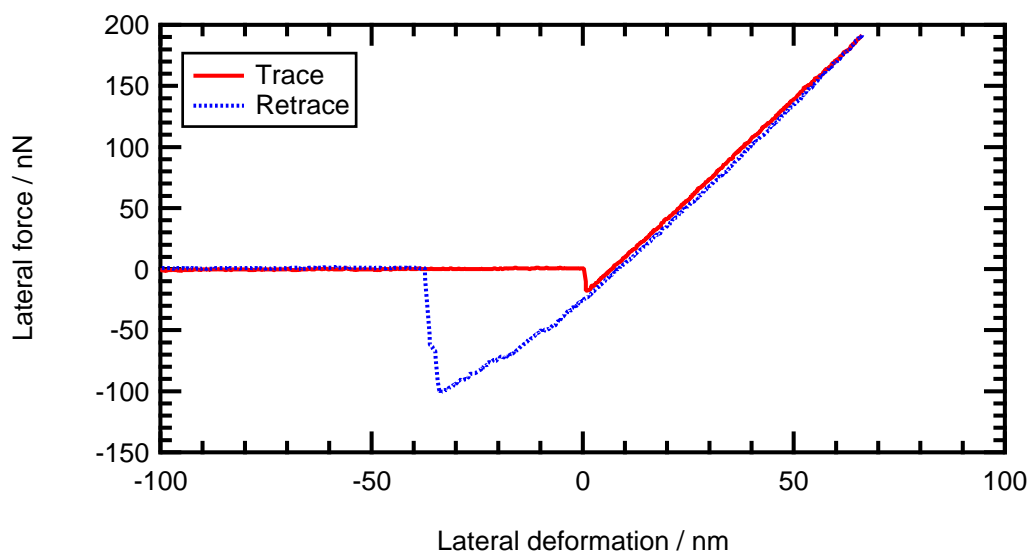


Figure 8.5 Exemplary lateral trace and retrace curves.

first acquired a vertical force map on a free-standing segment and afterward used a lateral setup with a very soft cantilever to perform sensitive small-deformation measurements (for more on the experimental procedure see Section 8.4) to produce a lateral force map on exactly the same position.

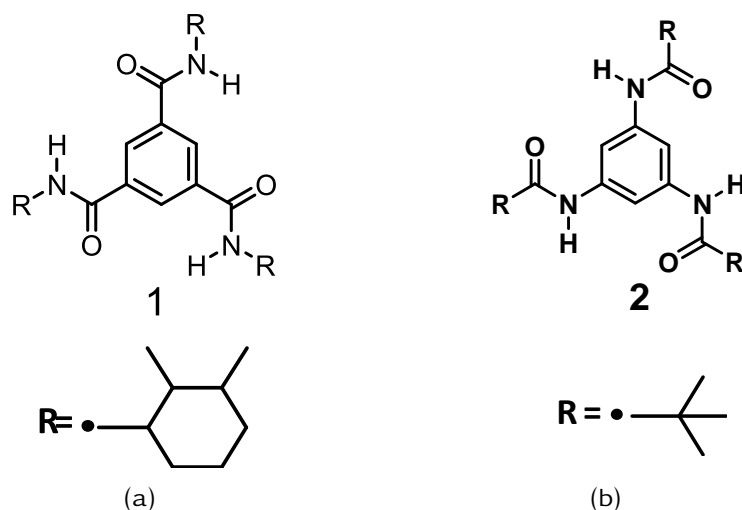


Figure 8.6 The structural formulas of (b) compound 1 and (a) compound 2.

A very good comparison can be seen in Figure 8.7. Although the lateral data showed a little more scatter, both results were in very good agreement with each other. Also, the corresponding moduli of these two measurements were comparable (3.5 GPa and 4.1 GPa, respectively). We compared several measurements of 2 in the same way and found a generally good agreement between both deformation modes, although the lateral measurements were much more prone to scatter. The main reason for deviations was most likely the uncertainty in the lateral calibration. In addition, since the lateral force maps had to be performed manually (instead of using the force mapping mode in the vertical case), there was an additional source of error when repositioning the cantilever. However, the experiments showed that the lateral measurements can be used for a mechanical characterization with reasonable reliability.

8.2.4 Large Deformation Measurements

Our goal was to perform large deformation measurements until failure. It was not possible to reliably break the fibers of 2 since the required forces were too high to be detected with the AFM photodiode even when using the stiffest cantilevers available. Therefore, we only investigated fibers of 1 for the large deformation experiments.

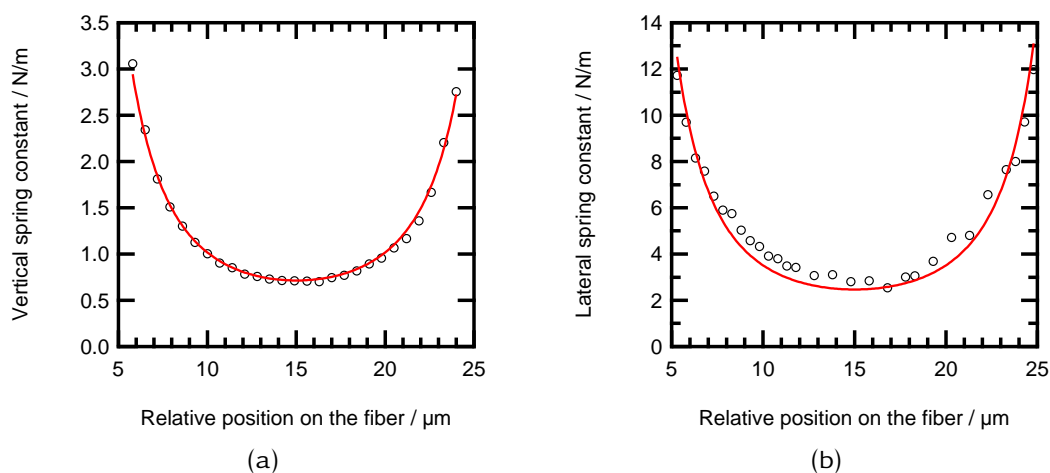


Figure 8.7 Vertical and lateral stiffness profiles measured on the same free-standing segment of a fiber of compound **2**. Although the lateral data shows more scatter, the shape of the profiles and the resulting Young's moduli are in good agreement.

Since they were thinner, they in turn also possessed a smaller flexural rigidity and smaller forces were needed to break them.²⁴

In Figure 8.8, two typical examples of lateral force-deformation curves can be seen. Figure 8.8(a) shows the most commonly observed case which was comparable to a brittle fracture: The force increased linearly with deformation until a sudden drop of the force indicated the failure of the material. The second case (Figure 8.8(b)), which rarely occurred, shows a nonlinear behavior. However, when applying the completely elastic model by *Heidelberg et al.*,⁷ the nonlinearity can clearly be identified as a purely geometric effect, the material itself is still within the linear elastic regime. Therefore, the curves essentially confirm the brittle behavior seen in the first case. We fitted the simplified *Heidelberg* model to all measurements and it described the fibers' behavior extremely well. For every investigated sample, the model predicted the correct shape of the force-deformation curve (linear or nonlinear) only based on the AFM-image of the fiber cross section.

We used Equation (8.1) to calculate Young's modulus from the elastic regime and again cross-checked the results with the vertical measurements reported in Chapter 5. The order of magnitude was generally in good agreement and the average values were consistent ($E_{\text{vert}} = 2.3 \pm 0.3 \text{ GPa}$ ²⁴ and $E_{\text{lat}} = 3.4 \pm 5.1 \text{ GPa}$), although the lateral data showed huge scatter that caused the extremely high standard deviation. The main reason was most likely a systematic error due the cantilever calibration,

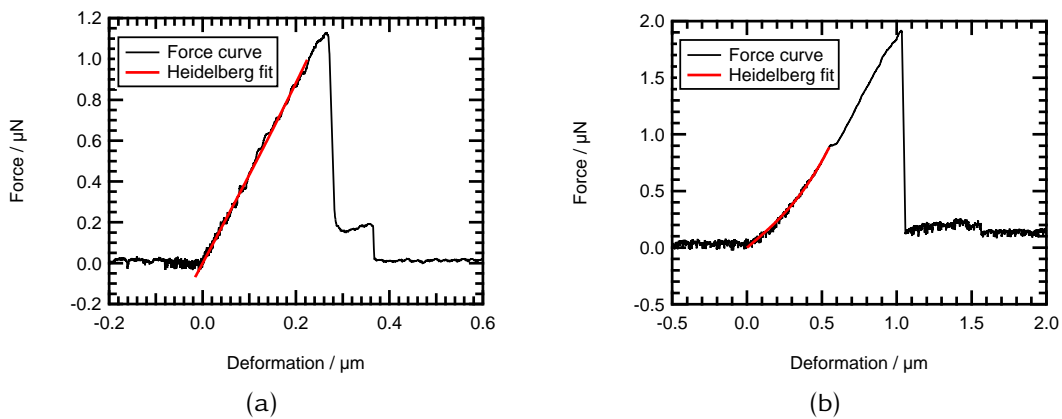


Figure 8.8 Exemplary lateral force curves and fit with the Heidelberg model. (a) The most common case with linear elastic deformation until fracture. (b) Example of a purely elastic behavior with geometric nonlinearities.

since sets of measurements that were performed within a short time frame and with the same cantilever calibration yielded very similar results. In addition, the applied model required a loading exactly at the midpoint of the fiber which could cause additional uncertainties if the cantilever tip contacted the fiber not exactly in the middle of the free-standing segment.

To determine the plastic properties of the fibers, one has to investigate the regime where the measured data starts to deviate from the behavior described by Equation (3.21). As discussed, most fibers showed a rather brittle behavior according to one of the two cases shown in Figure 8.8 without any pronounced signs of yield. There were only few samples where the behavior at large deformations significantly deviated from the elastic model. An extreme example can be seen in Figure 8.9.

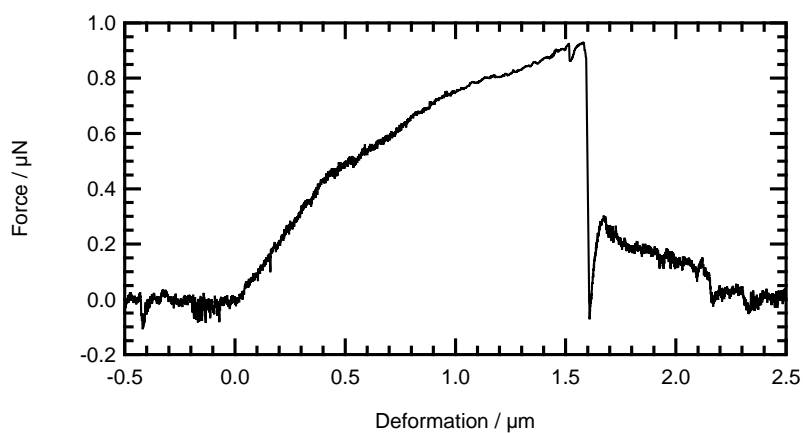


Figure 8.9 Exemplary lateral force curve. While the initial behavior is completely linear, slippage at higher loads leads to a steady decrease of the slope.

In these cases, the slope of the force-deformation curve constantly decreased after a certain point. However, it is questionable whether this point should be identified as a yield point: It is known that the adhesion of the trisamides on the glass substrate is sufficient to guarantee a firm fixation for small loads, but that detachment and slipping of the whole fiber occurs at high loads.²² Due to the small size of the fibers, however, a reliable observation with optical methods was not possible. In addition, vertical forces can occur during the lateral deformation due to the geometry of the contact between cantilever tip and fiber. These can push the cantilever upwards and cause instabilities of the contact. In summary, it is impossible to distinguish the individual contributions of material and slippage and the results concerning a possible yield point are ambiguous, especially considering that the crystalline microstructure of the self-assembled fibers only allows limited deformation mechanisms that could cause yielding.

While this complicates the determination of the bending strength, slippage can (to certain extent) be neglected when calculating the bending strength since the force at break F_b is not affected by any slippage or yield that occurs during the deformation. The only value that changes is the effective length of the free-standing segment. However, for small amounts of slippage this is only of minor importance. It has been shown in Section 3.2.4 that the bending strength $\sigma_{b,\max}$ of a fiber is given by:

$$\sigma_{b,\max} = \frac{FL}{8I} d_{n,\max}$$

Here, F is the applied load, L is the length of the free-standing segment, I is the area moment of inertia and $d_{n,\max}$ is the distance to the neutral axis. In case of the benzenetrisamides, the cross sections had a very irregular shape and therefore determining the distance to the neutral axis (which is equivalent to the distance to the centroid of the cross section)²⁵ is complicated. As a first approximation, we defined an effective radius r_{eff} calculated from the cross-sectional area of the fiber

$$r_{\text{eff}} = \sqrt{\frac{A}{\pi}} \quad (8.5)$$

which leads to the following expression for the bending strength:

$$\sigma_{b,\max} = \frac{FL}{8I} r_{\text{eff}} \quad (8.6)$$

However, since the fibers often had a flattened shape, the dimension in the direction of the bending is larger than the effective radius. Therefore, the bending strength will be underestimated. In addition, this approach neglects the homogeneously distributed tensile stresses that become significant at large deformations, which leads to an overestimation of the bending strength.^a A full theoretical treatment of these additional stresses is very complicated and can be found in the literature.⁹ However, our measurements were clearly dominated by bending. Therefore, we only estimated the effect of tension instead of performing a full theoretical evaluation.

To do so, we calculated the deformation based on the measured force at break assuming completely elastic behavior using Equation (8.1). This deformation allows calculating the ratio of bending and tensile forces. We calculated the corresponding maximum bending stresses according to Equation (8.6) and added the corresponding tensile stresses $\sigma_t = \frac{F_t}{A}$. However, it should be pointed out that for our experiments, neglecting the tension would only have led to an average overestimation of 4%.

The order of magnitude of the flexural strength ranged between 10 and 500 MPa with an average value of 102 ± 97 MPa. The main contributions to the large standard deviation are the uncertainty of the cantilever calibration and the error introduced by using the effective radius instead of the real distance to the neutral axis. In addition, local defects play a significant role for bending strength, since the stress is concentrated on small portions of the sample and therefore, the scatter is higher than for uniaxial tensile measurements. The measurements which showed the best agreement between vertical and lateral modulus can be assumed to be the most reliable ones and suggested a flexural strength of around 70 MPa, which is comparable to Nylon 6.²⁶

8.3 Conclusions

The work in this chapter demonstrates that LFM can be a powerful addition to the vertical bending setup, because it allows applying large deformations until failure to the fibers. These large deformations lead to a combination of bending and tension, which makes interpretation of the data more complicated than in a pure bending

^aIf a certain *force* is assumed and the pure bending stresses are calculated, it is neglected that a part of this force is also used to stretch the fiber. Since uniaxial stretching of the fiber causes significantly smaller maximum stresses than bending, the total *stress* is overestimated. If, in turn, a given *deformation* is used to calculate the force and the pure bending stresses, the additional uniaxial tension is neglected and the actual *force* is underestimated.

or uniaxial tension experiment. In the elastic regime, the lateral data showed good agreement with the vertical experiments. In addition, we could for the first time determine the bending strength of fibers of **1**, which was comparable to Nylon 6. However, there are also some drawbacks that have to be addressed in future work: The lateral calibration requires special care and is a major error source. In addition, performing the measurements without contact between cantilever tip and substrate is essential to eliminate the strong noise caused by friction. The most fundamental requirement in order to apply the lateral experiments to a wide variety of trisamide systems is a suitable approach for fixation of the fibers on the substrate. Once these issues are solved, the possibility to combine vertical and lateral bending on exactly the same position allows characterization of the mechanical properties within and beyond the linear elastic regime with outstanding reliability.

8.4 Experimental Section

Fiber preparation. The fibers of **1** and **2** were prepared as previously described in Chapters 4 and 5.^{24,27}

Vertical bending. All vertical bending measurements were performed as previously described in Chapter 5.²⁴

Lateral calibration. The method described herein was developed on a Nanowizard I apparatus (JPK Instruments AG, Berlin, Germany), combined with a Zeiss Axiovert 200 microscope and a Zeiss LD A-Plan® Ph1 objective lens (20x, numerical aperture 0.3, working distance 4.3 mm). We used a combination of the manipulation mode and the real-time scan (RTS). In manipulation mode, the cantilever follows a pre-determined path while keeping contact with the substrate at a defined load. The RTS was used to monitor the x -, y - and z -displacement of the piezos as well as the vertical and lateral deflection of the cantilever during the manipulation. In order to determine the lateral sensitivity, the cantilever (Nanosensors AdvancedTEC Cont by NanoWorld AG, Neuchâtel, Switzerland) was brought into contact with the structured glass substrates inside a channel (setpoint 0.2 V) and moved perpendicular to the ridges with 0.01 – 0.02 $\mu\text{m/s}$. When a significant deflection was achieved, the measurement was aborted by retracting the piezo to avoid damaging the tip. For the calibration of the friction-free measurements, we used the same procedure but reduced the z -range of the piezo so that the cantilever was separated 500 nm from the bottom of the channel.

Lateral bending. The measurements were performed by choosing an appropriate sample segment in the optical microscope (perpendicular to the channels and without visible defects) and imaging the segment in intermittent contact mode. The manipulation path was selected and the AFM data was recorded via RTS. The tip velocity was $0.02 - 0.05 \mu\text{m/s}$ (with a vertical setpoint of 0.2V for the in-contact measurements). In order to allow friction-free measurements, we again restricted the z -range of the piezo so that the measurements were performed at a distance of 500 nm above the bottom of the channel. The lateral force maps were acquired by repeatedly performing lateral bending experiments on several positions along the free-standing segment and aborting the measurements after a sufficient lateral deflection signal was reached to avoid damaging the fibers. The raw data was evaluated using self-written procedures in Igor Pro 6 (Wavemetrics Inc., Portland, USA). Additional time-lapse videos were obtained using an AxioCam (Zeiss, Jena, Germany) by acquiring individual microscope images in appropriate intervals (typically 250 ms) and processing the multidimensional images with the Zeiss AxioVision software.

8.5 References

- [1] C. M. Mate, G. M. McClelland, R. Erlandsson, S. Chiang, *Physical Review Letters* **1987**, *59*, 1942–1945.
- [2] G. Meyer, N. M. Amer, *Applied Physics Letters* **1990**, *57*, 2089–2091.
- [3] M. Munz, *Journal of Physics D: Applied Physics* **2010**, *43*, 063001.
- [4] U. D. Schwarz, P. Koster, R. Wiesendanger, *Review of Scientific Instruments* **1996**, *67*, 2560–2567.
- [5] D. A. Walters, L. M. Ericson, M. J. Casavant, J. Liu, D. T. Colbert, K. A. Smith, R. E. Smalley, *Applied Physics Letters* **1999**, *74*, 3803–3805.
- [6] V. Cimalla, C. C. Rohlig, J. Pezoldt, M. Niebelschutz, O. Ambacher, K. Bruckner, M. Hein, J. Weber, S. Milenkovic, A. J. Smith, A. W. Hassel, *Journal of Nanomaterials* **2008**.
- [7] A. Heidelberg, L. T. Ngo, B. Wu, M. A. Phillips, S. Sharma, T. I. Kamins, J. E. Sader, J. J. Boland, *Nano Letters* **2006**, *6*, 1101–1106.
- [8] Y.-J. Kim, K. Son, I.-C. Choi, I.-S. Choi, W. I. Park, J.-I. Jang, *Advanced Functional Materials* **2011**, *21*, 279–286.
- [9] L. T. Ngo, D. Almecija, J. E. Sader, B. Daly, N. Petkov, J. D. Holmes, D. Erts, J. J. Boland, *Nano Letters* **2006**, *6*, 2964–2968.
- [10] B. Wu, A. Heidelberg, J. J. Boland, *Nature Materials* **2005**, *4*, 525–529.

- [11] B. Wu, A. Heidelberg, J. J. Boland, J. E. Sader, X. M. Sun, Y. D. Li, *Nano Letters* **2006**, *6*, 468–472.
- [12] S. Sundararajan, B. Bhushan, *Sensors and Actuators a-Physical* **2002**, *101*, 338–351.
- [13] D. Almecija, D. Blond, J. E. Sader, J. N. Coleman, J. J. Boland, *Carbon* **2009**, *47*, 2253–2258.
- [14] C. R. Carlisle, C. Coulais, M. Guthold, *Acta Biomaterialia* **2010**, *6*, 2997–3003.
- [15] C. R. Carlisle, C. Coulais, M. Namboothiry, D. L. Carroll, R. R. Hantgan, M. Guthold, *Biomaterials* **2009**, *30*, 1205–1213.
- [16] L. Kreplak, H. Herrmann, U. Aebi, *Biophysical Journal* **2008**, *94*, 2790–2799.
- [17] L. Kreplak, L. R. Nyland, J. L. Contompasis, J. O. Vigoreaux, *Journal of Molecular Biology* **2009**, *386*, 1403–1410.
- [18] A. Gestos, P. G. Whitten, G. M. Spinks, G. G. Wallace, *Polymer Testing* **2013**, *32*, 655–664.
- [19] R. J. Cannara, M. Eglin, R. W. Carpick, *Review of Scientific Instruments* **2006**, *77*, 053701.
- [20] J. L. Hutter, *Langmuir* **2005**, *21*, 2630–2632.
- [21] C. P. Green, H. Lioe, J. P. Cleveland, R. Proksch, P. Mulvaney, J. E. Sader, *Review of Scientific Instruments* **2004**, *75*, 1988–1996.
- [22] B. R. Neugirg, “Nanomechanics of Fibers Beyond Linear Elasticity”, Bayreuth, **2012**.
- [23] J. E. Sader, J. W. M. Chon, P. Mulvaney, *Review of Scientific Instruments* **1999**, *70*, 3967–3969.
- [24] D. Kluge, J. C. Singer, J. W. Neubauer, F. Abraham, H.-W. Schmidt, A. Fery, *Small* **2012**, *8*, 2563–2570.
- [25] J. Gere, B. Goodno, *Mechanics of Materials*, Cengage Learning, London, 7th ed., **2008**.
- [26] Y. Kojima, A. Usuki, M. Kawasumi, A. Okada, Y. Fukushima, T. Kurauchi, O. Kamigaito, *Journal of Materials Research* **1993**, *8*, 1185–1189.
- [27] D. Kluge, F. Abraham, S. Schmidt, H. W. Schmidt, A. Fery, *Langmuir* **2010**, *26*, 3020–3023.

Perspectives II: Extending the Material Library - Spider Silks

9.1 Introduction

In recent years, silks have become very popular materials due to their impressive mechanical and biochemical properties.¹ Their good biocompatibility, biodegradability, antimicrobial activity, and low immune reaction make them a promising material for scaffolding in tissue engineering applications and as wound dressings.^{2–4} In terms of mechanical properties, especially spider silks possess an exceptional combination of stiffness, extensibility, and strength. In general, their remarkable mechanical properties are based on a combination of amorphous and crystalline regions on the scale of the fiber's nanostructure.⁵

It is important to keep in mind that spider silk fibers can be very different, depending on their role in the spider's web. The garden spider *Araneus diadematus* for example possesses seven gland-spinneret complexes that can produce fibers with unique properties.^{6,7} Amongst those, the *major ampullate* (MA) gland fibers that form the web frame and the spider's dragline have the most impressive mechanical properties and are best understood.^{8,9} To illustrate this, the MA silks have an initial stiffness comparable to bone combined with a ten times greater extensibility that is comparable to nylon and a strength that almost matches high-tensile steel.⁸

In contrast to silk worms, spiders cannot be farmed on a large scale due to their predatory and cannibalistic nature.¹⁰ An alternative is the identification of the relevant protein sequences and the recombinant production of genetically engineered silks.^{11–13} The fibers investigated in this work were prepared from the genetically engineered protein eADF4(C16). It consists of 16 repeats of a module termed C derived from the fibroin ADF4, one out of at least two MA silk proteins of *A. diadematus'* dragline silk.^{14–16} The engineered module comprises alanine-rich segments that are known to form crystalline β -sheet stacks in natural silks and increase their tensile strength.^{14,17} In addition, it also has glycine-rich segments that adopt flexible helices, providing elasticity.¹⁴ Thus, it mimics the natural silk's composite character.

In general, both natural and engineered silk proteins can be processed into a large variety of morphologies like spheres, films, foams, fibers and many more.¹⁷ In terms of fibers, the main processing pathways are solvent extrusion, microfluidics and electrospinning.¹⁸ The major advantages of electrospinning are that it requires only small amounts of protein and that it produces mats of extremely fine fibers that are well-suited for cell- and tissue-culture studies.¹⁸ Recently, *Leal-Egaña* et al. used

electrospinning to form nonwoven scaffolds of recombinant spider silks.¹⁵ Testing the mechanical properties of the individual electrospun fibers requires sensitive techniques like the bending experiments presented within this thesis.

9.2 Results and Discussion

9.2.1 Vertical Bending Measurements

Since this was a new class of materials, the first step was of course again to ensure that the fibers undergo pure bending without any indentation. We found no significant indentation when the fibers were supported by the substrate (Figure 9.1). In addition, the force-deformation curves on the free-standing segments showed a linear behavior, thus allowing an evaluation with common models of beam theory as described in Chapter 3.2.

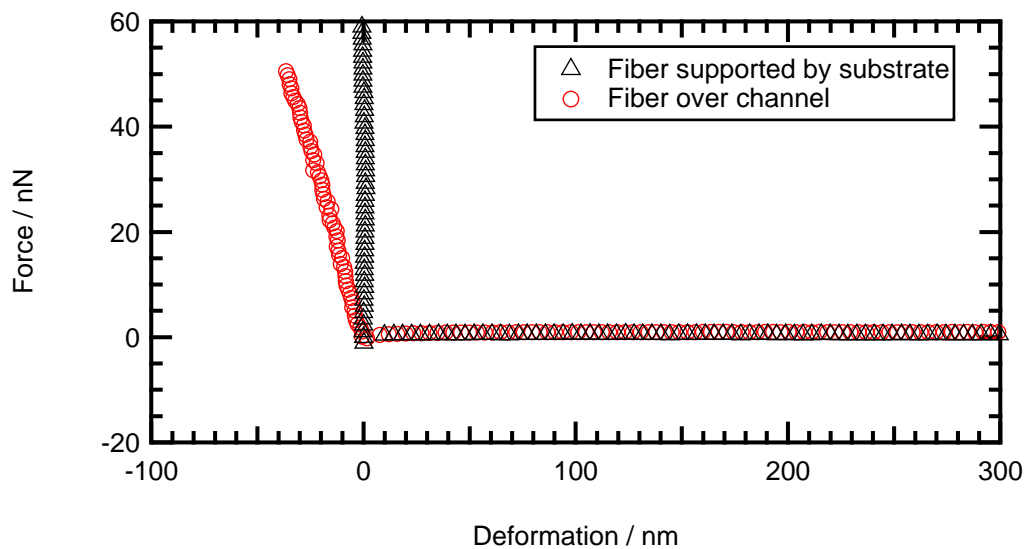


Figure 9.1 Force-deformation curves on a silk fiber segment supported by the substrate (black squares) and on a free-standing segment (red circles). The segment supported by the substrate showed no significant deformation for the maximum applied load during the measurements (50 nN).

However, the experiments produced very inconsistent results with large deviations between the individual fibers. Although the SSBM showed better agreement with the data, the majority of the profiles could not be described by any of the common beam theory models or by a mixture of those. In addition, the general tendency was that with increasing deviation from the DCBM shape, the determined apparent

modulus became unrealistically high, sometimes over one order of magnitude above the literature value for *A. diadematus*' dragline silk, 10GPa.⁸ This was true even if the experiments were evaluated in an extremely conservative way by excluding any measurements that showed a pronounced non-standard behavior. Of all 45 investigated samples, only very few measurements yielded at least reasonable stiffness profiles and moduli in a realistic range (around 1-10 GPa). Just one single profile showed a perfect DCBM behavior (Figure 9.2). This was completely contrary to the impression during handling of the samples under the optical microscope that suggested a firm fixation of the fibers on the substrate.

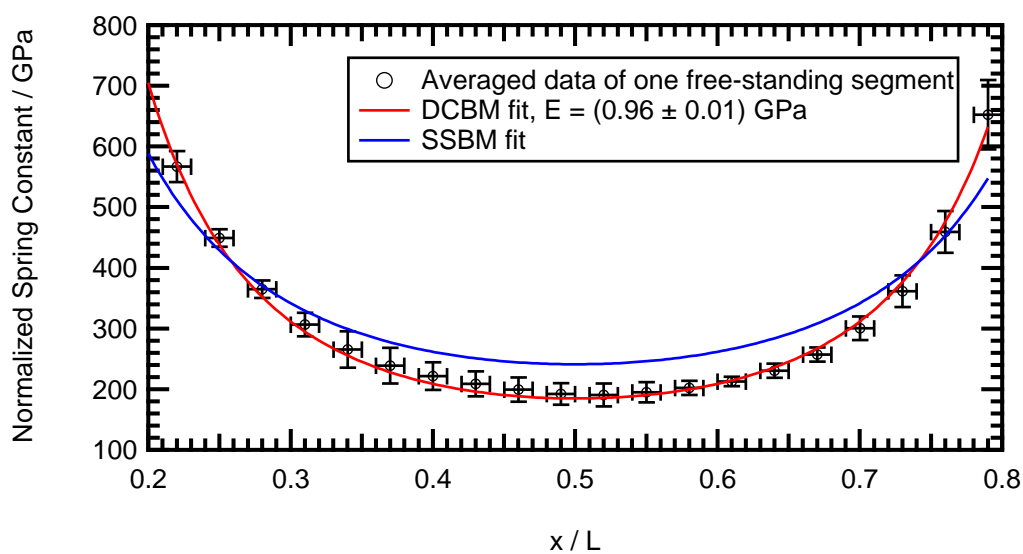


Figure 9.2 One of the few fiber segments that corresponded to the DCBM. The stiffness profile was obtained by averaging over 6 individual measurements on the same free-standing segment.

The results strongly suggests that the observed behavior must not be attributed to real supported boundary conditions, but rather to a to date inexplicable effect. To better compare the measurements on all free-standing segments, the profiles were normalized and averaged as previously described.¹⁹ Again, the SBM seemed to correspond best to the data, but fails to completely describe the shape of the averaged stiffness profile (Figure 9.3).

The important task was to identify the source of these issues. We investigated the fibers using SEM and found that many samples showed a flattened cross section on the segments that were supported by the substrate, while the cross section of the free-standing segment was circular (Figure 9.4). Since the cross section for evaluation of the data is determined on the supported segments (see Section 4), this will

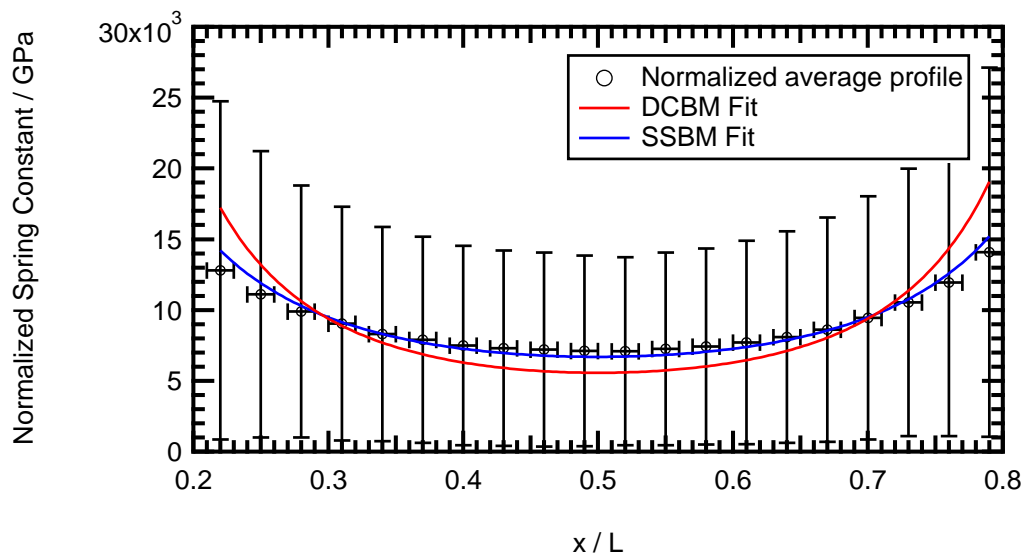


Figure 9.3 Averaged stiffness profile of tall investigated spider silk samples and the corresponding fits with the DCBM and SSBM. To allow a comparison, the individual measurements were normalized as previously described.¹⁹

lead to an underestimation of the fiber height and therefore to an overestimation of Young's modulus. However, since the change seemed to be very abrupt at the edge of the channel, it did not explain the shape of the stiffness profiles.

A reason for the inhomogeneous morphology of the fibers may have been the fact that they were directly electrospun on the structured glass substrates. The flattened shape may have been caused by the fiber hitting the substrate while the solvent was not completely evaporated. In order to produce fibers without these artifacts, we tested two approaches. The first was to prepare the fibers by collecting the fibers between two wires with a gap of ≈ 2 cm and bringing them into contact with the substrate after a certain time to ensure that the solvent was completely evaporated and the fiber morphology was stable (in the following termed ESW fibers). The second approach was to use dry spinning for the fiber preparation (in the following termed DS fibers). Both approaches yielded fibers with homogeneous cross sections along the fiber.

We performed control experiments on both types. For the ESW fibers, the shape of the stiffness profiles was comparable to our previous observations (Figure 9.5(a)). The apparent modulus showed a narrower distribution around smaller values, but still yielded a very high value (≈ 50 GPa) if evaluated with the SSBM (as suggested by the profile shape). The DS fibers also showed the SSBM-like shape of the stiffness profiles (Figure 9.5(b)), but yielded a significantly higher modulus (≈ 270 GPa

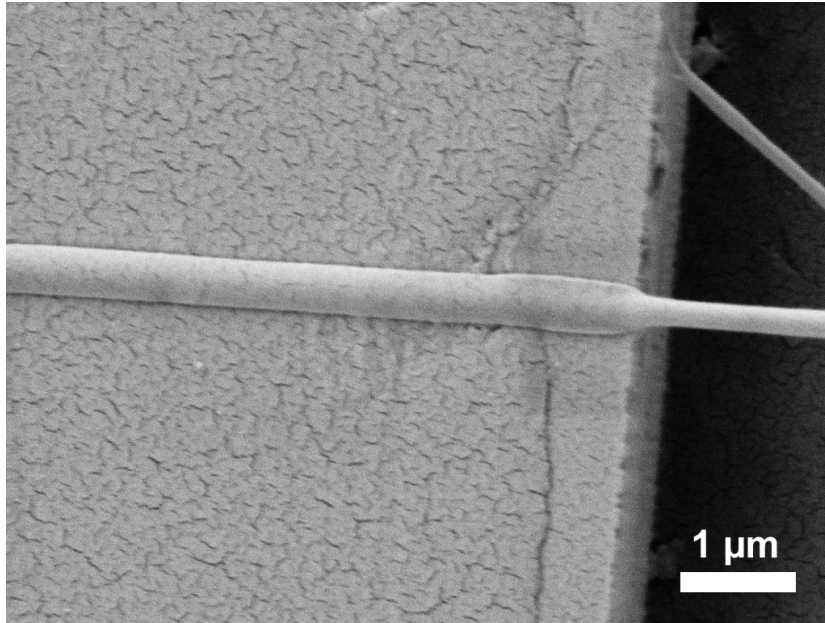


Figure 9.4 SEM image of a suspended spider silk fiber. It is clearly visible that the cross section is not homogeneous along the fiber axis, with a significant broadening where the fiber is in contact with the substrate.

if evaluated with the SSBM) than the ESW fibers. However, it is not possible to determine if the difference in modulus is a systematic effect due to the preparation or only a statistical effect because of the small number of specimens (6 segments of 5 ESW fibers, 4 segments of 3 DS fibers). In summary, while the effect of an inhomogeneous cross section due to the fiber preparation definitely is an issue, it does not explain the observed behavior.

It should be pointed out that the flattened stiffness profiles and overestimation of Young's modulus strongly resembles the effects of a slack fiber reported in Chapter 7. However, it is difficult to identify the source for such a slack. One possible explanation could be the influence of the relative humidity. It is known that humidity can have a pronounced effect on the properties of silks.²⁰ Changes in the relative humidity between preparation of the fibers on the substrate and the bending measurements could therefore lead to a swelling. However, significant swelling of the fibers, thus leading to an elongation and a possible slack, is not very likely.

Of course, also the opposite could happen. Natural silks show a phenomenon called supercontraction, which is a strong contraction of the fiber with increased humidity.^{21,22} This would lead to a prestress of the fiber and therefore also to an altered mechanical behavior. However, supercontraction has not yet been observed in the genetically engineered samples that we investigated (a reason could be that

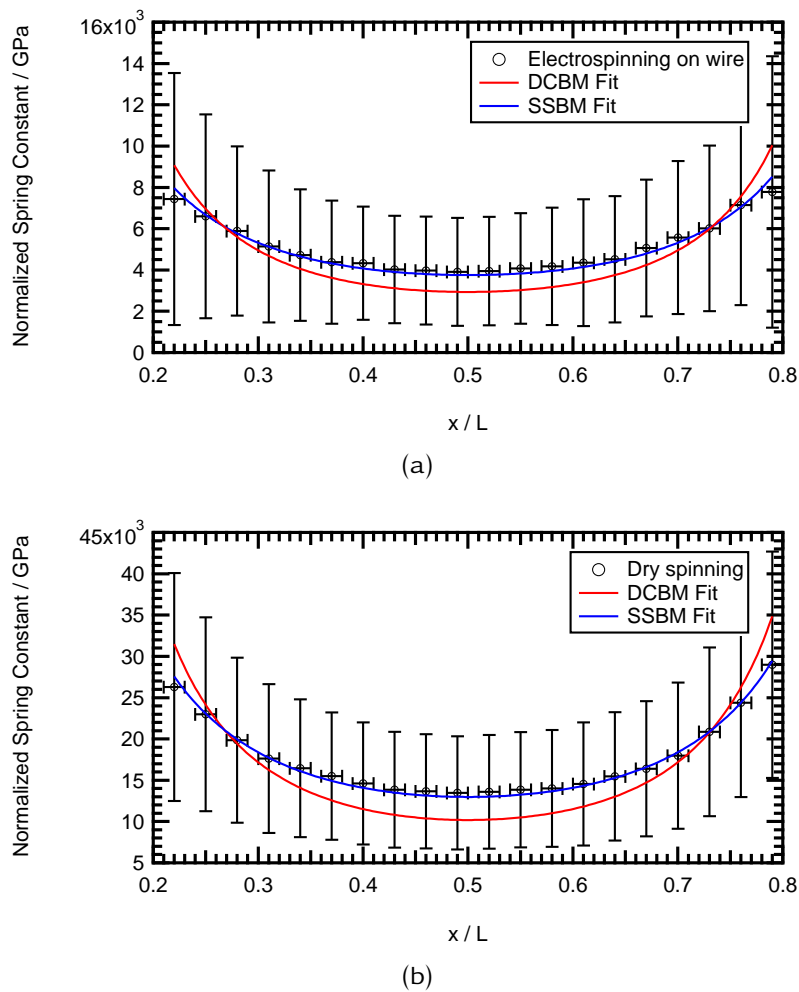


Figure 9.5 Normalized and averaged stiffness profiles of the control experiments on silk fibers that were not directly spun onto the substrate. (a) Fibers electrospun between two wires. (b) Dry spun fibers.

the fibers consist only of a single silk protein and do not possess the additional lipid layer of the natural silks) and hence, can be excluded as an explanation. In summary, no comprehensive and convincing model for the observed behavior was found to this date.

9.2.2 Lateral Bending Measurements

In addition to the vertical bending tests, we also employed a lateral setup as described in Chapter 8. An exemplary force-deformation curve can be seen in Figure 9.6. We evaluated the measurements with the simplified model of *Heidelberg et al.* in order to determine the elastic properties.²³ In contrast to the vertical bending

experiments that could not be correlated to any literature model, the lateral data showed a very good agreement with the predicted behavior (Figure 9.6). In addition, evaluation of the elastic properties yielded realistic values of Young's modulus with a reasonable amount of scatter. This again corresponds well to the findings of Chapter 7, which predicted only a minor influence of slack on lateral measurements (i.e., measurements perpendicular to the slack direction).

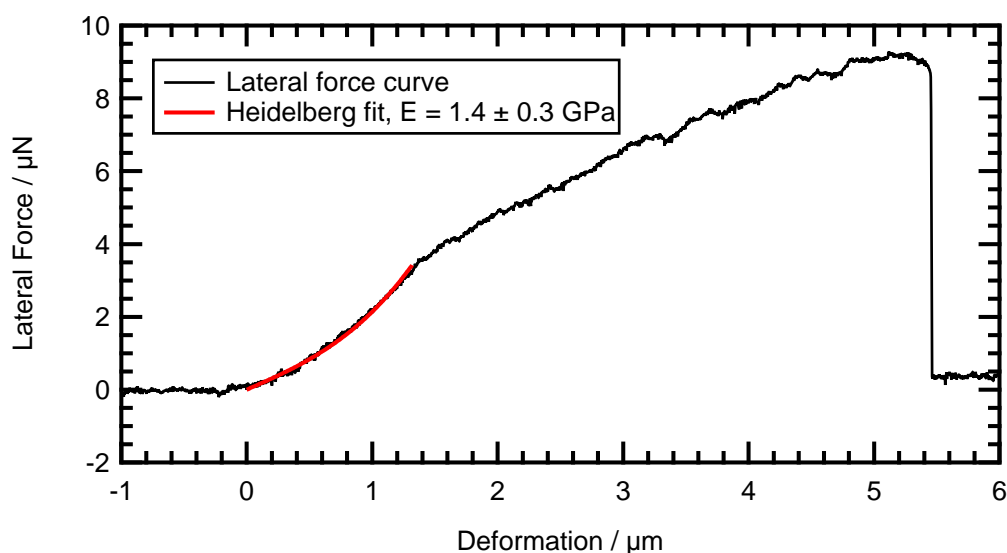


Figure 9.6 Exemplary lateral force-deformation curve and evaluation of Young's modulus using the Heidelberg model.

Although the results of the lateral measurements were obviously much more reliable than the vertical ones, it has to be kept in mind that there were still several limitations. Besides the uncertainties of the lateral measurements that were discussed in Chapter 8, especially concerning the cantilever calibration, the inhomogeneous cross section will strongly influence the results and lead to a systematic error. Consequently, the absolute values of the elastic modulus should be taken with care. However, the measurements are suited to compare different sets of samples and show relative differences.

Therefore, we used the lateral bending measurements to study the influence of a post-treatment on the single fiber mechanics. According to *Huemmerich et al.*, silk proteins that were processed from hexafluoroisopropanol (HFIP) solutions show predominantly α -helical secondary structures, but can be transformed into β -sheet rich structures by methanol treatment.²⁴ While this is mostly used to make the proteins water-insoluble, the structural change will of course also affect the mechanical properties. To investigate this influence, we performed lateral bending experi-

ments until fracture on several untreated and methanol treated eADF4(C16) fibers and evaluated their modulus by fitting the simplified Heidelberg model to the initial, elastic part of the curve. We saw a clear difference between untreated and methanol treated fibers, with a significant increase in modulus of the treated fibers (Figure 9.7).

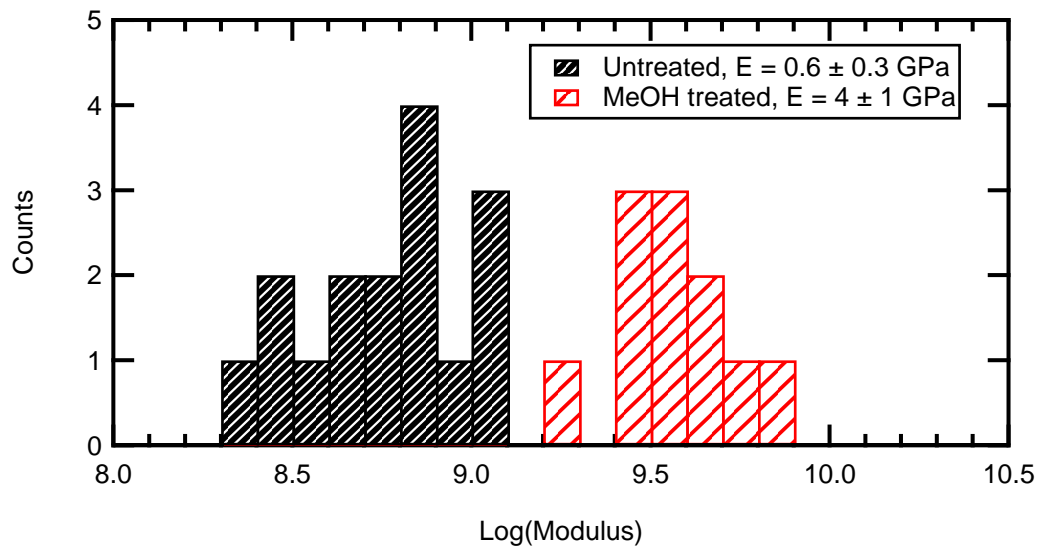


Figure 9.7 Distribution of Young's modulus determined from the lateral bending experiments for untreated (black) and methanol treated (red) silk fibers.

There were also qualitative differences in the deformation behavior between the treated and untreated fibers that were best visible under the optical microscope.²⁵ The treated fibers mostly showed a clear and sudden rupture and gave the impression of a rather brittle material, regardless of their extensibility. In addition, they often returned to their initial position after breaking. The untreated fibers, on the other hand, rather resembled a material with significant yielding at larger deformations, showed a higher extensibility (although not in all cases) and did not recover their initial shape after unloading. Unfortunately, these effects were difficult to quantify in the force curves, since at large deformations, a possible yielding of the material often was difficult to distinguish from instabilities of the cantilever-fiber contact. However, unlike the previous experiments on the BTA fibers (Chapter 8), the fiber-substrate contact remained stable in most cases and the silk fibers showed no pronounced slipping or detachment.

We also performed a preliminary evaluation of the silk fibers' bending strength. For that purpose, we determined the maximum force at which the fibers ruptured and applied Equation (8.6).

$$\sigma_{b,\max} = \frac{FL}{8I} r_{\text{eff}}$$

We could clearly see a difference between the treated ($\sigma_{\max} = 0.9 \pm 0.3$ GPa) and untreated ($\sigma_{\max} = 0.2 \pm 0.1$ GPa) fibers. Modulus and strength of the post-treated fibers were in good agreement with the literature values for *Araneus* MA silks ($E = 10$ GPa, $\sigma_{\max} = 1$ GPa).⁸ However, it again shall be stressed that this is only a very rough estimation due to the multitude of uncertainties that contribute to the final value. Especially the inhomogeneous cross section will largely affect the results, because the bending strength depends linearly on the area moment I and therefore, on the fourth power of the fiber radius. Since the actual thickness of the fiber in the direction of the applied load is smaller than suggested by the AFM image of the broadened cross section, thus leading to an overestimation of I_{zz} and an underestimation of the fibers' strength. This effect will most likely dominate any other errors that result from the assumptions and simplifications described in Section 8.2.4.

However, it is important to mention that in contrast to the BTA fibers, the silks showed a considerable elongation before breaking, thus leading to a significant contribution of tensile forces to the total measured force and therefore, an overestimation of the maximum stresses and $\sigma_{b,\max}$ which will likely be higher than for the BTAs. In addition, yield is not considered in this model which will lead to further inaccuracies. Another source of error that affects both modulus and strength is of course the lateral cantilever calibration. Furthermore, the noise due to cantilever-substrate friction made it sometimes difficult to determine the onset of force-deformation curve, but this was only a minor issue that did not significantly influence the results. Despite the problems and the resulting uncertainties of the absolute values, the tendency of a significant increase of fiber modulus and strength by post treatment is clear.

9.3 Conclusions

This chapter illustrates that the experimental approaches developed and refined within this thesis are not limited to the BTA fibers, which of course were the central topic, but can also be transferred to fibers of virtually any other material class. Here, we investigated the mechanical properties of electrospun fibers of genetically

engineered silk proteins, which are a promising building block for advanced functional materials due to the remarkable combination of biochemical and mechanical properties of natural silks. While vertical bending experiments were possible, the results were inconclusive. Most samples showed an apparent modulus that was unrealistically high and shapes of the stiffness profile that could not be explained by the classical beam theory boundary conditions. Although the source of this behavior could not be definitely identified, the fact that it could only be identified as an artifact by acquiring stiffness profiles demonstrates the importance of validating the boundary conditions and mechanical models for a reliable nanomechanical characterization.

Additional lateral bending experiments did not show such a dramatic deviation from the theoretical models and allowed to clearly identify the increase of Young's modulus and flexural strength by a post-treatment with methanol on the single fiber level. The results also strongly support the slack hypothesis of Chapter 7, as it provides a valid explanation for all of the observed effects. However, to provide a definitive answer on the role of slack for the observed behavior, further experimental verification is necessary. Regardless of the issues, this chapter demonstrates that in principle, a mechanical investigation of engineered silk fibers via bending experiments is possible, that it can identify non-ideal behavior and therefore, produce reliable results. Especially lateral large deformation experiments that include the improvements developed by Neugirg²⁶ are a promising approach for further mechanical studies.

9.4 Experimental Section

Fiber preparation. The electrospun fibers were prepared from a solution of 100 mg/ml eADF4(C16) in 1,1,1,3,3,3-hexafluoro-2-propanol (HFIP) as described in the literature.¹⁵ The fibers were directly spun onto the structured glass substrates (GeSiM GmbH, Großerkmannsdorf, Germany), which were fixed on a rotating cylinder to allow fiber alignment perpendicular to the channels of the substrate. The ESW fibers for the control experiments were prepared in the same way, but spun between two wires and deposited on the glass substrates afterward. The dry spun fibers were prepared from a solution of 250 mg/mL eADF4(C16) in HFIP. A droplet of the solution was brought between two glass slides, the solvent was allowed to evaporate until the concentration was high enough so that fibers formed upon separation of the glass slides. For the post-treatment, the electrospun fibers were subjected to methanol va-

por by heating a closed beaker that contained methanol and the electrospun fibers (which were not in contact with the methanol liquid) to 50 °C.²⁷

AFM measurements. All vertical AFM measurements were performed on a Nanowizard I (JPK Instruments AG, Berlin, Germany) as previously reported,¹⁹ using tipless NSC12/AIBS cantilevers (μ Masch, Tallinn, Estonia). The maximum applied load was 50 nN. The lateral measurements were performed using special tip-visible cantilevers (DP16/GP/AIBS, μ Masch, Tallinn, Estonia) at a vertical setpoint of 0.2 V and a deformation speed of 0.5 ms⁻¹. The detailed experimental procedure is described in Chapter 8.

9.5 References

- [1] G. H. Altman, F. Diaz, C. Jakuba, T. Calabro, R. L. Horan, J. S. Chen, H. Lu, J. Richmond, D. L. Kaplan, *Biomaterials* **2003**, *24*, 401–416.
- [2] L. Meinel, S. Hofmann, V. Karageorgiou, C. Kirker-Head, J. Mccool, G. Gronowicz, L. Zichner, R. Langer, G. Vunjak-Novakovic, D. L. Kaplan, *Biomaterials* **2005**, *26*, 147–155.
- [3] D. Liang, B. S. Hsiao, B. Chu, *Advanced Drug Delivery Reviews* **2007**, *59*, 1392–1412.
- [4] S. Wright, S. L. Goodacre, *BMC Research Notes* **2012**, *5*, 326.
- [5] L. Römer, T. Scheibel, *Chemie in Unserer Zeit* **2007**, *41*, 306–314.
- [6] J. M. Gosline, M. E. Demont, M. W. Denny, *Endeavour* **1986**, *10*, 37–43.
- [7] F. Vollrath, *Scientific American* **1992**, *266*, 70–76.
- [8] J. M. Gosline, P. A. Guerette, C. S. Ortlepp, K. N. Savage, *Journal of Experimental Biology* **1999**, *202*, 3295–3303.
- [9] M. Humenik, A. M. Smith, T. Scheibel, *Polymers* **2011**, *3*, 640–661.
- [10] J. G. Hardy, T. Scheibel, *Journal of Polymer Science Part A: Polymer Chemistry* **2009**, *47*, 3957–3963.
- [11] M. B. Hinman, J. A. Jones, R. V. Lewis, *Trends in Biotechnology* **2000**, *18*, 374–379.
- [12] C. Vendrely, T. Scheibel, *Macromolecular Bioscience* **2007**, *7*, 401–409.
- [13] C. Vendrely, C. Ackerschott, L. Romer, T. Scheibel, *Methods in Molecular Biology* **2008**, *474*, 3–14.
- [14] D. Huemmerich, C. W. Helsen, S. Quedzuweit, J. Oschmann, R. Rudolph, T. Scheibel, *Biochemistry* **2004**, *43*, 13604–13612.
- [15] A. Leal-Egaña, G. Lang, C. Mauerer, J. Wickinghoff, M. Weber, S. Geimer, T. Scheibel, *Advanced Engineering Materials* **2012**, *14*, B67–B75.

- [16] A. Heidebrecht, T. Scheibel, *Advances in Applied Microbiology Vol 82* **2013**, *82*, 115–153.
- [17] J. G. Hardy, L. M. Romer, T. R. Scheibel, *Polymer* **2008**, *49*, 4309–4327.
- [18] J. A. Kluge, U. Rabotyagova, G. G. Leisk, D. L. Kaplan, *Trends in Biotechnology* **2008**, *26*, 244–251.
- [19] D. Kluge, J. C. Singer, J. W. Neubauer, F. Abraham, H.-W. Schmidt, A. Fery, *Small* **2012**, *8*, 2563–2570.
- [20] T. Vehoff, A. Glisovic, H. Schollmeyer, A. Zippelius, T. Salditt, *Biophysical Journal* **2007**, *93*, 4425–4432.
- [21] I. Agnarsson, C. Boutry, S. C. Wong, A. Baji, A. Dhinojwala, A. T. Sensenig, T. A. Blackledge, *Zoology* **2009**, *112*, 325–331.
- [22] T. A. Blackledge, C. Boutry, S. C. Wong, A. Baji, A. Dhinojwala, V. Sahni, I. Agnarsson, *Journal of Experimental Biology* **2009**, *212*, 1980–1988.
- [23] A. Heidelberg, L. T. Ngo, B. Wu, M. A. Phillips, S. Sharma, T. I. Kamins, J. E. Sader, J. J. Boland, *Nano Letters* **2006**, *6*, 1101–1106.
- [24] D. Huemmerich, U. Slotta, T. Scheibel, *Applied Physics a-Materials Science & Processing* **2006**, *82*, 219–222.
- [25] B. R. Neugirg, “Nanomechanische Charakterisierung von Spinnenseidenproteinen”, Bayreuth, **2010**.
- [26] B. R. Neugirg, “Nanomechanics of Fibers Beyond Linear Elasticity”, Bayreuth, **2012**.
- [27] G. Lang, “Herstellung von Vliesstoffen aus Proteinen und Analyse ihrer Eignung als Scaffold für Zellkulturen”, Bayreuth, **2010**.

Danksagung

Mit diesen Zeilen beschließe ich ziemlich genau vier Jahre, die ich sowohl wissenschaftlich als auch privat als den erlebnisreichsten, oft anstrengendsten, alles in allem aber mit Abstand besten Abschnitt meines bisherigen Lebens empfunden habe. Dies ist vor allem den Menschen geschuldet, die diese Zeit begleitet haben. Bei diesen möchte ich mich hiermit bedanken.

An erster Stelle gilt mein Dank Prof. Andreas Fery, der diese Zeit erst möglich gemacht hat. Danke, Andreas, für die richtige Mischung aus viel kreativer Freiheit und der hin und wieder notwendigen Refokussierung auf das Wesentliche. Ich habe sehr viel von dir gelernt, habe immer gerne mit dir zusammengearbeitet und freue mich, dass so einiges deiner Arbeitsweise auf mich abgefärbt hat. Vielen Dank zudem für die Chance, an zahlreichen nationalen und internationalen Konferenzen teilzunehmen, da dies nicht nur meine Arbeit, sondern auch ganz stark mein Denken bereichert hat.

Ich danke Prof. Hans-Werner Schmidt und Prof. Thomas Scheibel für die Möglichkeit, spannende Kooperationsprojekte umzusetzen, die gute Zusammenarbeit und die zahlreichen Diskussionen. Many thanks to Davide Ruffoni for giving me the opportunity to learn a few things about finite elements (and to enjoy great Swiss food at the same time).

Mein ganz besonderer Dank gilt Ben, Julia, Gregor und Jens, die viele Höhen und Tiefen dieser Arbeit mit mir geteilt haben. Ich bin in der seltenen und glücklichen Situation, in euch nicht nur großartige Kooperationspartner, sondern auch gute Freunde gefunden zu haben. Ohne euch wäre diese Arbeit nicht das geworden, was sie ist. Danke!

Bei dem gesamten Team der PC II möchte ich mich für das (nicht zuletzt durch Sybille) fast schon familiäre Arbeitsumfeld, die stets spannenden wissenschaftlichen und nicht-wissenschaftlichen Diskussionen, die Abende in der Kaffeeküche und auf

der Terrasse, sowie die Mithilfe bei Problemen aller Art bedanken. Es war wirklich schön mit euch. Besonderer Dank gilt Meli und Johann sowie den ehemaligen Mitarbeitern Öznur, Eva und Alex.

Nadine, ich versuche es mal mit „*Ich gebe zu, dass ich dich mag, ich mein, wir kennen uns schon so lang...*“, aber du weißt ja selbst, wie defizitär Sprache sein kann.

Abschließend danke ich meiner Familie für die fortwährende Unterstützung.

Erklärung

Hiermit erkläre ich, dass ich die vorliegende Arbeit selbständig verfasst und keine anderen als die angegebenen Quellen und Hilfsmittel verwendet habe.

Ferner habe ich nicht versucht, anderweitig mit oder ohne Erfolg eine Dissertation einzureichen oder mich der Doktorprüfung zu unterziehen.

Bayreuth, 30. Juli 2013

Daniel Kluge